UNIVERSITÀ DEGLI STUDI DI TRIESTE

XXVIII CICLO DEL DOTTORATO DI RICERCA IN
SCIENZE E TECNOLOGIE CHIMICHE E
FARMACEUTICHE

Theoretical description of photoabsorption spectra: TDDFT development and applications

Settore scientifico-disciplinare: **CHIM/02**

DOTTORANDO
OSCAR BASEGGIO

COORDINATORE
PROF. MAURO STENER

SUPERVISORE DI TESI
PROF. MAURO STENER

ANNO ACCADEMICO 2014 / 2015

Contents

Overview of the thesis

This PhD thesis is focused on the theoretical simulation and the interpretation of photoabsorption spectra. Two lines of research have been followed: the calculation of Near Edge X-ray Absorption Fine Structure (NEXAFS) spectra at Density Functional Theory (DFT) level for molecules in the gas phase and the development of a new algorithm for the calculation of photoabsorption spectra at Time Dependent Density Functional Theory (TDDFT) level for large size systems (>100 atoms).

NEXAFS C1s and XPS spectra in the gas phase for two polycyclic aromatic hydrocarbons (PAHs) (Phenanthrene and Coronene) have been calculated, interpreted and compared to the experimental data. The electronic spectra calculated at ΔKS level exhibit significant differences with respect to the experiment, in particular for the intensity distribution. On the other hand vibrationally resolved spectra calculated at Frank-Condon level with linear coupling model. Simulate properly the experimental data. Furthermore, NEXAFS C1s and XPS spectra in the gas phase for a thiophenes series (Thiophene, Dithiophene and Terthiophene) have been calculated at ΔKS level, interpreted and compared to the experimental data.

The second part of this thesis concerns the development of a new TDDFT algorithm to calculate photoabsorption spectra. The aim of this project is to go beyond the intrinsic limits of the actual codes, which employ the Casida algorithm and the Davidson diagonalization. In fact, for large size systems (typically >100 atoms), e.g. metallic clusters, the density of states is so high that, with conventional algorithms based on the Davidson diagonalization, it is not possible to calculate the spectrum over on energy range wide enough to cover the optical region of practical interest, say up at least 5 eV. The new algorithm solves the TDDFT equations in the space of the density fitting auxiliary basis set and extracts the spectrum point by point from the imaginary part of polarizability. The original idea, which made the present scheme very efficient, consists in the simplification of the double sum over occupied-virtual pairs in the definition of the dielectric susceptibility, allowing for an easy and efficient calculation of such matrix as a linear combination of constant matrices with photon energy dependent coefficients.

This method has been applied to several systems, different for nature and size (from H_2 to $[Au_{147}]^-$). The new algorithm shows, in all cases, a good agreement with respect to the results obtained with the Amsterdam Density Functional (ADF) code (maximum deviation 0.2 eV). Furthermore, the analysis of the results in terms of transition contribution maps (TCM), the Jacob plasmon scaling factor and the induced density analysis have been implemented and successfully employed in the application.

The new algorithm has been employed to study different systems consisting of metal clusters, simulating both the plasmonic resonance phenomena and the trend with respect to the dimensions and the nature of ligands. In particular, we studied two series of icosahedra of gold and silver (M_{13}, M_{55}, M_{147}, M_{309}) and $Au_{30}S(S\text{-}tBu)_{18}$ cluster. It has been also possible to analyze different systems characterized by large dimensions and low symmetry, e.g. $Au_{144}(SH)_{60}$.

Finally, the new TDDFT algorithm has been extended, in order to describe the Circular Dichroism effect in chiral molecules. New expressions for the calculation of the optical rotation tensor have been developed, and the rotatory strength evaluation has been implemented as well. Preliminary calculation on a chiral silver chain (Ag_8) furnished nice agreement with ADF for two different response schemes in both length and velocity gauge.

1 Introduction

1.1 Core Spectroscopy

The core – level spectroscopy, or X-Ray Absorption Spectroscopy (XAS), is based on formation of a core – hole, which can be defined like the absence of one electron from a core level, i.e. from an inner orbital.

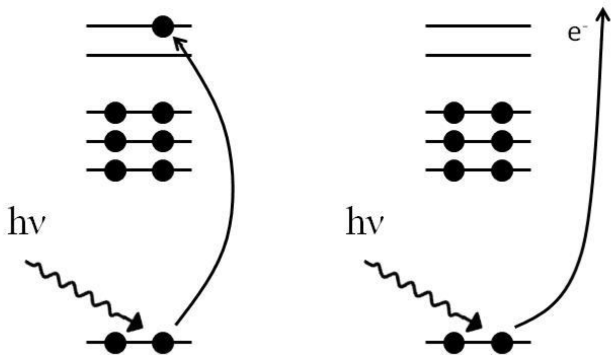

***Figure 1.1** The x-ray absorption phenomena*

When a core electron is hit by a radiation with a opportune energy (soft x-ray: 100eV – 3KeV), two phenomena may happen (**Figure 1.1**): the excitation of the electron to a unoccupied bound state, or the excitation of the electron to a continuum state; i.e. with an energy higher than the ionization threshold: in this case the energy excess with respect to the ionization energy remains as the photoelectron kinetic energy.

The earliest x-ray absorption investigations were reported at the beginning of the last century, however the main advances for these studies are related to the development of x-ray sources, and in particular to the introduction of the synchrotron light (electron synchrotron sources, with $E < 1GeV$ in the 1960s and early 1970s, and electron storage rings, with $E > 1GeV$, in the 1970s)[1.1].

More specifically, XAS studies the behavior of the absorption coefficient μ, which gives the probability of x-ray to be absorbed by the matter, as a function of the incident photon energy:

$$I = I_0 \cdot e^{-\mu \cdot x} \tag{1.1.1}$$

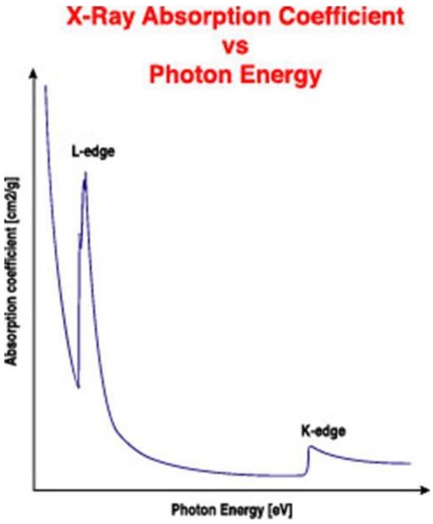

***Figure 1.2** example of XAS spectrum*

Where I_0 is the intensity of incident x-ray, I is the intensity transmitted through the sample and x is the sample thickness. When the incident x-ray photon energy is equal to the binding energy of a core electron, a sharp rise in absorption is observed, called absorption edge, corresponding to the ejection of this core electron into the continuum (photoelectric effect). XAS is involved in the study of μ just around these absorption edge.

In **Figure 1.2** a typical XAS spectrum is reported, which displays two edges: the K-edge and the L-edge, relative to the ionization potential from 1s and 2s, 2p orbitals respectively.

In fact the core spectrum nomenclature is based to on the orbital of the excited electron. The edge is named in crescent energy order: K, L_{I}, L_{II}, L_{III}, M_{I}, …; where the letter indicates the principle quantum number n, that is $1, 2, 3, \ldots \rightarrow K, L, M, \ldots$; and the number indicates the orbital angular momentum l, and total angular momentum j, that is $s_{1/2}, p_{1/2}, p_{3/2}, \ldots \rightarrow I, II, III, \ldots$.

The x-ray absorption spectrum is commonly divided into two great regimes, depending on the photon energy and following on the distinct interpretation of the spectral features and on the kind of information they can provide: they are respectively addressed to as NEXAFS and EXAFS.

- The Near Edge X-ray Absorption Fine Structure (NEXAFS) region covers the energy range from few eV below the ionization threshold (pre-edge region) up to few tens of eV above it (early known as “Kossel structure”).

The NEXAFS profile is sensitive to the atomic geometrical arrangement around the absorbing atom, and provides “local” information, such as oxidation state and coordination chemistry of the excited atom. The acronyms XANES and NEXAFS should be interchangeable, even if over the year “NEXAFS” has become the main terminology for low-Z molecules absorbed on surfaces[1.2], while the term “XANES”, has been more often employed for solids and inorganic complexes[1.1]. Currently “NEXAFS” is by far the most used terminology, and the term “XANES”, survives only to indicate the lower NEXAFS region (up to 10 eV above the edge).

- The Extended X-ray Absorption Fine Structure (EXAFS) region start from the upper limit of NEXAFS and spreads for hundreds of eV in the continuum (for many years it has been referred to as the “Kronig structure”). The EXAFS is due to single scattering of the ejected photoelectron, which now has a very high kinetic energy, so this part of the XAS spectrum permits the determination of interatomic distances, coordination numbers and species of neighbors surrounding the absorbing atom.

The boundary energy between NEXAFS and EXAFS corresponds approximately to the wavelength that equals the distance between the absorbing atom and its first neighbors [1.3].

The NEFAFS spectrum comes out to be a powerful local probe of the chemical environment of the absorbing atom; in fact the probability of a transition is proportional to the square of the transition moment, which is the integral of electric dipole moment operator between initial and final state wave functions:

$$P_{if} \propto \left|\langle \Psi_i | \hat{\mu} | \Psi_f \rangle\right|^2 \tag{1.1.2}$$

In atoms, the transition moment is strictly governed by the dipole selection rules: $\Delta l = \pm 1$, $\Delta j = \pm 1$ and $\Delta s = 0$, where l is the orbital angular momentum quantum number, j is the total angular momentum quantum number and s is the spin quantum number, consequently only the transitions $s \to p$, $p \to d$,$p \to s$, … are allowed.

Non-dipolar effects can be important for dipole forbidden transitions, which may gain intensity from higher order terms, like for example electric quadrupole or magnetic dipole moments. These features are very important, for example, in transition metal K-edge excitations, giving rise to typical excitonic features described to metal 1s→3d dipole forbidden transitions [1.4].

The NEXAFS spectrum is usually in turn subdivided into two energy ranges:

- The low energy pre-edge region, whose features are caused by electronic transitions to empty bound states, that are controlled by the dipolar selection rules, as discussed above. This narrow energy range (extending for about 8 eV [1.1] up to the ionization threshold) is rich in information on the local geometry around the absorbing atom, on oxidation state and binding characteristic. The physical origin of the absorption features in the edge region is different in different classes of materials, many-body singularities in metals, bond atom-like localized excitation in solid [1.5].
- The high energy region, whose features are essentially explained by means of multiple-scattering resonances (with large cross sections) of the photoelectrons ejected at low kinetic energy [1.6]; information is provided about the atomic position of the neighbors of the absorbing atom, both for interatomic distances and bond angles.

This distinction directly involves the concept of absorption threshold, which can be defined in a threshold manner [1.1]:

- The “absorption threshold”, that is the energy of the lowest state reached by the core excitation;
- The “absorption jump edge” or “rising edge”, that is the energy where the absorption coefficient is at half-height of the atomic absorption jump; because the dipole selection rule can suppress a number of the lowest

transitions, the energy of the absorption jump edge can be much larger than the absorption threshold;

- The “continuum threshold” or “ionization threshold”, that is the energy at which the electron is ejected into the continuum.

If we limit our discussion, for the sake of simplicity, to K shell excitation spectra (but the following considerations have more general validity) the 1s Ionization Potential (IP) or Binding Energy (BE) is defined as the minimum energy necessary to excite a 1s electron to the continuum of states above the vacuum level, i.e. the third definition of absorption edge presented above; it is conveniently measured by x-ray photoelectron spectroscopy (XPS) as the difference between the exciting photon energy ($h\nu$) and the Kinetic Energy of the photoelectron (KE), i.e. the energy position of the corresponding peak in the XPS spectrum:

$$IP = BE = h\nu - KE \tag{1.1.3}$$

An alternative experimental technique for the investigation of the electronic structure, as concerns the conduction band, especially for solids is represented by the high-energy Electron Energy-Loss Spectroscopy (EELS) in transmission [1.7]. It consists in exposing the sample to a beam of electrons with a known, narrow range of kinetic energies; some electrons will undergo inelastic scattering (interaction between the beam electron and an electron in the sample) and consequently will lose energy; the measurement of the scattered electron energies gives the distribution of energy loss, i.e. the EELS spectrum. EELS and XAS provide similar information about the conduction band; among the EELS advantages one has the opportunity to use smaller samples and to increase the momentum transfer so that other than dipole selection rules apply.

1.2 NEXAFS theoretical approach

NEXAFS is considerably hard to fully interpret; for this reason precise and accurate calculations are mandatory for a correct and non-ambiguous interpretation of the spectral features. The theoretical description of NEXAFS spectra represents a big challenge due to the difficulty to calculate both the pre-edge and post-edge energy regions. A customary general theoretical approach explains the NEXAFS structures as arising from a multiple scattering process, where the excited electron is resonantly scattered by the surrounding atoms in the molecules. This has the advantage to provide the MS-Xα computational method which can estimate both the bound and the above edge transitions [1.8]. This approach, which is at present the only widely employed scheme to describe the above edge region, is however limited by the crude muffin-tin approximation.

Alternatively the near-edge absorption structures can be investigated at theoretical level in terms of discrete below edge transitions of the core electron into the unoccupied orbitals of the molecule characterized by well defined excitation energies and oscillator strengths, and the continuum transitions which generate the photoionization cross section profiles above the ionization limit. The LCAO Molecular Orbital (MO) approach is particularly convenient to describe below edge excitations in terms of one-electron transitions which are known to make usually the largest contribution to the discrete structure of the XAS spectra. The calculations of bound excited states can be performed at various levels of approximation in the framework of accurate theoretical schemes, however these methods are based on localized orbitals, therefore they are not a suitable tool to describe states in the continuum. For the present, discrete transitions evaluated above the edge, although partly basis set dependent, may be qualitatively associated with the prominent resonances in the spectrum, in particular in the lowest energy range [1.9]. Such approximation can be further refined in the rigorous framework provided by Stieltjes moment theory [1.10].

A very powerful typology of NEXAFS spectra is represented by angular resolved NEXAFS, which consists of studying by the system under analysis of polarized x-rays. The use of the polarization dependence of the absorption cross section in the NEXAFS spectra of anisotropic sites allows to select the multiple-scattering contributions due to a set of atoms placed in a particular direction or on a particular plane; consequently, the orientation and angular distribution of neighboring atoms can be easily determined by changing the relative position of the incident beam and the sample.

Obviously, resolved NEXAFS is of practical important only when the molecule orientation is fixed in the laboratory frame, which happens when the molecules is absorbed over a surface, so that polarization direction is fixed with respect to the molecule. On the other hand, when the molecule is in the gas phase and therefore free to rotate, the NEXAFS spectrum will be a rotational average of all possible mutual orientations between molecule and polarization.

In MO approach the polarization dependence of the resonance intensities can be correlated to the spatial displacement of the final orbital [1.2]: the resonance intensity associated with a specific molecular orbital final state is largest if the electric field is parallel to the direction of that molecular orbital, and the intensity vanishes if the electric field is perpendicular to that direction. The main application of this technique is the determination of the orientation of the molecules chemisorbed on surfaces.

1.3 Peculiar proprieties of metallic nanoparticles

The study of nanoscaled metallic particles is nowadays strongly motivated by their unusual physical and chemical properties with respect to bulk materials [1.11]. In the last 20 years, the extensive production of scientific works related to the synthesis, characterization and technological applications of metallic nanoparticles gave rise to revolution in terms nanoelectronics, catalysis and sensing [1.12][1.13][1.14]. In particular, noble metals nanoparticles, such as gold, have played a central role in material science research due to their optical, electronic and chemical properties as well as biomedical applications [1.15].

The nanoscale is so interesting for metal nanoparticles because the electronic structure of these kind of systems is no longer the one of the molecular case, such as inorganic clusters, but neither the one of the bulk metals. Most of the metallic nanoparticles keep a discrete distribution of the energy levels, however these levels approach to degeneracy while the dimension of the cluster grows, becoming an almost continuos distribution of the states like a band structure of a macroscopic crystal. Not only the size plays an important role in influencing the electronic properties of small metal cluster, but also the shape [1.16]. These systems can be produced in various shapes of different sizes such as spheres, rods, plates, prisms, cube, different polyhedral and wires. By varying the aspect ratio of the geometrical shape of the cluster (e.g. the ratio between the height and the dimension of the base of a prism) it is possible to generate confinement effects, reducing the mobility of the electron gas in quasi-2, 1 and even 0 dimensions. This direct dependence of the electronic structure to the size and shape of the nanoclusters is commonly related to their optical behavior.

1.4 Surface Plasmon Resonance

As noble metals are reduced in size of tens of nanometers a strong absorption due to the collective oscillations of the electrons between two opposite regions of the particle surface is observed. This effect is not relevant in the bulk case because of the low surface/volume ratio. In particular as gold and silver nanoparticles, this absorption occurs in the visible region, becoming very useful for several technological applications. The phenomenon is called Surface Plasmon Resonance (SPR) [1.16]. It has been confirmed both experimentally and theoretically that the plasmonic absorption is strongly related to structure (size and shape) of the nanomaterials. The main feature observed, is a general redshift and enhancement of the absorption peak while increasing the size of the cluster.

Under specific size conditions (e.g. spherical NPs with less than 15 nm of radius), where the scattering processes are negligible, the metallic nanoparticles generally absorb radiation through three main mechanisms:

1. collective excitations of the free electrons which determine surface modes and SPRs directly connected to shape, size, chemical environment and composition
2. single excitations of bound electrons from occupied to empty bulk bands of different indexes, also called interband transitions
3. surface dispersion or scattering of the free electrons with a mean free path comparable to the dimensions of the nanoparticle.

The first two mechanisms are mostly the fundamental way of absorption, while the last one is the main mechanism to dissipate the energy absorbed by plasma oscillations. It is important to notice that bound electrons excitations are not involved in the collective motion of the electron gas, so they have not reasonable influence on the nature of SPRs. Furthermore, surface dispersion effects do not change the position of the SPRs bands but have effects on the absorption spectra, making them wider and less intense due to coupling of the proper modes to the applied field [1.17].

Metals like copper, silver and gold absorb visible light by means of plasma oscillation mechanisms, whereas most other transition metals show only a broad and poorly resolved band in the UV region. This important difference is attributed to the strong coupling between the plasmon transition and the interband excitation. In addition, the conduction band electrons of the noble metals can move freely, independently from the ionic background, and the ions act only as scattering centers. This gives the electrons in the noble metals a higher polarizability, which shifts the plasmon resonance to lower frequencies with a sharp bandwidth.

The SPR was theoretically explained by Mie in 1908, including linear optical properties such as extinction and scattering of small metal particles. Mies’s theory and experimental spectra agree well in the size regime > 20 nm. But when the size of nanoparticles is much smaller than < 20 nm and even much smaller than the wavelength of the incident light, the Mie’s theory cannot reproduce experimental results, because the plasmon band shows still a size dependence and even seems to disappear completely for nanoparticles of size < 2 nm.

1.5 Theoretical description

One of the most interesting spectral features of noble metal clusters are their optical response in the interaction with a radiating source. In the previous section the “plasmon” have been introduced, which is a collective excitation of the conduction electrons: a joined motion of the nearly-free electrons, induced by the light, within the mean positively charged field of the ionic cores.

This feature has been discovered and then explained by classical electrodynamics models based on the Mie theory, where the cluster is assumed as an homogeneous conduction sphere. Since the optical properties are sensitive to the dimension of the system, even at the classic or semi-classic level, with Discrete Dipole Approximation (DDA), this is a difficult problem to deal with.

The problem becomes even more tricky when the cluster size is smaller than the electron mean path: in this case quantum confinement effects must be introduced in the model, since the band structure has been replaced by discrete energy levels.

So, a quantum mechanical treatment is required to approach this problem and, at the moment, the most practical method is the Time Dependent Density Functional Theory (TDDFT) which formally includes the coupling of mono-excited configurations, necessary to describe the “collective” plasmonic behavior of MNP.

There are two main different implementations of the TDDFT:

- the first adopts the formalism based on molecular orbitals, following the Casida procedure[1.18];
- the second studies the temporal evolution of the system, employing plane waves or Cartesian grids to solve the TDDFT equations.

The first approach is advantageous because it allows a detailed analysis of the transitions in terms of molecular orbitals involved, so the nature of these transitions can be inferred. On the other hand, this procedure allows to study the optical properties in only a limited range of energy, because a limited number of eigenvalues can be extracted by the diagonalization algorithm commonly employed in the procedure [1.19].

2 Theory

2.1 Density Functional Theory

The Density Functional Theory (DFT) is an alternative approach to ab-initio method; it is a rigorous method but it is necessary to introduce some approximations, with minor computational cost than ab-initio methods.

The density functional theory[2.1] is based on the idea, that the electronic structure of atoms, molecules and solids can be rigorously described by the electronic density $\rho(\bar{r})$ instead of the wave function in N particles $\Psi(x_1, x_2, \dots, x_N)$. In this way the energy of the system will be a functional of the electron density.

In the ’60 Hohenberg and Kohn[2.2] have demonstrated two theorems that are the background of DFT. First consider the definition of a functional: it is an application from a vector space into its underlying scalar field, or more specifically an application from a set of functions to the real number $f \rightarrow \mathbb{R}$..

In the non-relativistic case and assuming the Born-Oppenheimer approximation, the generic Hamiltonian for N electrons is given by:

$$\hat{H} = \sum_{i=1}^{N}\left(-\frac{1}{2}\nabla_i^2\right) + \sum_{i<j}^{N}\frac{1}{r_{ij}} + \sum_{i=1}^{N} V_{ext}(\bar{r}_i) = \hat{T} + \hat{V}_{ee} + \hat{V}_{\mathrm{ext}} \qquad (2.1.1)$$

Where the first term $\hat{T}$ is the kinetic energy of the electrons, the second $\hat{V}_{ee}$ is the potential energy contribution for the repulsion between electrons pairs, and the last $\hat{V}_{ext}$ is the external potential due interactions between nuclei and electrons.

At this time the functional $F[\rho]$ is defined as the minimum of the integral for the first two Hamiltonian contributions.

$$F[\rho] = \min_{\Psi \to \rho} \langle \Psi | T + V_{ee} | \Psi \rangle \tag{2.1.2}$$

Where Ψ are the antisymmetric wave function that correspond to the density ρ

$$\rho(\bar{r}) = N \int \Psi(\bar{x}_1, \bar{x}_2, \dots, \bar{x}_N)\, \Psi^*(\bar{x}_1, \bar{x}_2, \dots, \bar{x}_N) d\omega_1 d\bar{x}_2, \dots , d\bar{x}_N \tag{2.1.3}$$

The first variable is integrated only in the spin coordinate ω, so the expression gives the electronic density at the point $\bar{r}$. The functional F[ρ] is universal because it doesn't depend on V_{ext}, so it depends only on the number of electrons i.e. on the density.

Now another functional $E[\rho]$ is defined:

$$E[\rho] = F[\rho] + \int V_{ext}(\bar{r})\rho(\bar{r})d\bar{r} \tag{2.1.4}$$

Where the classical potential energy contribution for the nuclei-electrons interactions is introduced, indeed it's possible to demonstrate that this classic expression is equivalent to the quantum mechanical one.

Now it can be shown that a variational principle based on the electronic density ρ rather than on the wave function Ψ holds:

$$E[\rho] \geq E_{GS} \tag{2.1.5}$$

$$E[\rho_{GS}] = E_{GS} \tag{2.1.6}$$

Where E_{GS} and ρ_{GS} are respectively the exact energy and density of the ground state. Therefore E[ρ] has the minimum value when the density is that of ground state.

At this point, minimizing the energy E means minimizing the functional E[ρ], moreover since F[ρ] associates ρ to the wave functions Ψ_{min}^{ρ}, then it is possible to define a functional for each term of Hamiltonian:

$$E[\rho] = T[\rho] + V_{ee}[\rho] + \int V_{ext}(\bar{r})\rho(\bar{r})d\bar{r} \tag{2.1.7}$$

There are two possible approaches to deal with this problem:

- Direct Method (Thomas-Fermi approach or more recent Orbital Free (OF) method[2.3]): the electronic density ρ is taken as independent variable.
- Indirect Method (Kohn-Sham approach[2.4]): which refers to a non-interacting system, with the same electronic density of the real one, and where the molecular orbitals are taken as independent variables instead of the density.

2.2 The Kohn-Sham method

In the fictitious non-interacting system, the interaction potential between electrons is absent $V_{ee} = 0$. Such system has a simpler Hamiltonian, the so called Kohn-Sham Hamiltonian:

$$\hat{H}_{KS} = \sum_{i=1}^{N}\left(-\frac{1}{2}\nabla_i^2\right) + \sum_{i=1}^{N} V_{KS}(\bar{r}_i) \tag{2.2.1}$$

The $V_{KS}(\bar{r}_i)$ is the Kohn-Sham potential and it must be determined. It is a local mono-electronic potential that has to be chosen so that the density of the KS system is equal to the electronic density of the interacting one.

The wave function Ψ_{KS} is the solution of the non-interacting system, and therefore it can be described with a single Slater Determinant

$$\Psi_{KS} = \frac{1}{\sqrt{N!}} \det[\varphi_1 \varphi_2 \dots \varphi_N] \tag{2.2.2}$$

Therefore the problem can be separated in N mono-electronic equations

$$\left[-\frac{1}{2}\nabla^2 + V_{KS}\right] \varphi_i = \varepsilon_i \varphi_i \;\; i = 1,2, \dots, N \tag{2.2.3}$$

Now the value of the kinetic energy for the non-interacting system can be calculated from the spin-orbitals, with a very good approximation of the real system

$$T_0[\rho] = \sum_{i=1}^{N} \left\langle \varphi_i \middle| -\frac{1}{2}\nabla_i^2 \middle| \varphi_i \right\rangle \tag{2.2.4}$$

This is the essential reason why the Kohn-Sham method is superior with respect to the Thomas-Fermi scheme which gives very large errors in the kinetic energy. Now the energy functional for the interacting system can be defined like sum of different contributions

$$E[\rho] = T_0[\rho] + J[\rho] + E_{xc}[\rho] + \int V_{ext}(\bar{r})\rho(\bar{r})d\bar{r} \tag{2.2.5}$$

Where $T_0[\rho]$ is the kinetic energy functional for the non-interacting system, $J[\rho]$ is the functional of the classic Coulomb repulsion energy:

$$J[\rho] = \frac{1}{2}\iint \frac{\rho(\bar{r})\rho(\bar{r}')}{|\bar{r} - \bar{r}'|} d\bar{r} d\bar{r}' \tag{2.2.6}$$

$E_{xc}[\rho]$ is the exchange-correlation functional, and it contains all terms to correct the first two terms to the real system, it is defined as:

$$E_{xc}[\rho] = T[\rho] - T_0[\rho] + V_{ee}[\rho] - J[\rho] \tag{2.2.7}$$

The $E_{xc}[\rho]$ is unknown, therefore it must be approximated using some model, for example the electron gas, anyway it is a good approximation because this term represents small contribution in the whole expression of the energy.

The energy functional has to be minimized with respect to the electronic density, but the minimum has to be constrained because the number of electrons is constant:

$$\int \rho(\bar{r})d\bar{r} = N \tag{2.2.8}$$

Now the Lagrangian multiplier μ that operates on the constrain is introduced and the following Lagrangian function is obtained:

$$L = E[\rho] - \mu\left(\int \rho(\bar{r})d\bar{r} - N\right) \tag{2.2.9}$$

The minimum condition corresponds to zero functional derivative:

$$\frac{\delta}{\delta\rho}\left[E[\rho] - \mu\left(\int \rho(\bar{r})d\bar{r} - N\right)\right] = 0 \tag{2.2.10}$$

Performing the functional derivatives, the minimum condition for the real system is

$$\frac{\delta T_0}{\delta\rho} + \int \frac{\rho(\bar{r}')}{|\bar{r} - \bar{r}'|}d\bar{r}' + \frac{\delta E_{XC}}{\delta\rho} + V_{ext}(\bar{r}) = \mu \tag{2.2.11}$$

While for the non-interactive system

$$\frac{\delta T_0}{\delta \rho} + V_{KS}(\bar{r}) = \mu \tag{2.2.12}$$

Requiring that the two systems have the same electronic density ρ, an expression of the $V_{KS}(\bar{r})$ can be found requiring that equations (2.2.11) and (2.2.12) are equal:

$$V_{KS}(\bar{r}) = \int \frac{\rho(\bar{r}')}{|\bar{r} - \bar{r}'|} d\bar{r}' + \frac{\delta E_{XC}}{\delta \rho} + V_{ext}(\bar{r}) \tag{2.2.13}$$

Where the first term is the electronic potential generated by the electron density of the system, the second is the functional derivative of the exchange-correlation energy:

$$V_{xc}[\rho(\bar{r})] = \frac{\delta E_{XC}}{\delta \rho} \tag{2.2.14}$$

And the third is the external potential.

Now it is possible define the Kohn-Sham equations which are one-electron Schrödinger type equations, consequently the orbitals are the solutions of the N mono-electronic equations.

$$\hat{H}_{KS}\varphi_i = \varepsilon_i \varphi_i \;\; i = 1,2,\dots,N \tag{2.2.15}$$

The electronic density is defined by the orbitals (φ_i):

$$\rho(\bar{r}) = \sum_{i}^{occ} \sum_{s}^{spin} n_i |\varphi_1(r,s)|^2 \tag{2.2.16}$$

The Hamiltonian depends on the density and therefore is defined by the solutions, consequently self-consistent field (SCF) method is necessary. This approach is rigorous only for the ground state, but it is possible to choose a different occupation number set with respect to the ground state, and apply this method for the excited states as well.

2.3 The Transition State (TS) Method

The simplest and pragmatic approach to calculate excitation or ionization processes by DFT consists to neglect of relaxation effects by means of a frozen-orbital [2.5] assumption: excitation energies are simply calculated as the differences between the energy eigenvalues relative to the initial occupied level and the final virtual level:

$$\Delta E_{i\to f} = \varepsilon_f - \varepsilon_i \tag{2.3.1}$$

While the IP is directly obtained following Koopmans' like theorem as the opposite eigenvalue of the initial level:

$$IP_i = -\varepsilon_i \tag{2.3.2}$$

In other words this approximation assumes that, upon removal of an electron from some initial orbital φ_i, none of the other φ_k ones change.

The intensity of the transition is proportional to the square module of electric dipole moment between final and initial states:

$$I \propto \left|\langle\Psi_i|\hat{\mu}|\Psi_f\rangle\right|^2 \tag{2.3.3}$$

Where $\hat{\mu}$ is the dipole operator; at this point the wave functions are described by the Kohn-Sham determinants (GS and one-electron excited configuration), and in particular the intensity is represented by the oscillator strength:

$$f_{i\to f} = \frac{2}{3}\Delta E_{i\to f} n_i \left|\langle \varphi_i | \hat{\mu} | \varphi_f \rangle\right|^2 \tag{2.3.4}$$

Where n_i is the occupation number of the initial state. This form is used when the radiation isn't polarized or when the sample is randomly oriented in gas phase. For the polarized spectra the form is the following:

$$f_{i\to f} = \frac{2}{3}\Delta E_{i\to f} n_i \left|\langle \varphi_i | \vec{e} \cdot \vec{\mu} | \varphi_f \rangle\right|^2 \tag{2.3.5}$$

Where $\vec{e} \cdot \vec{\mu}$ is the scalar product between the electric field and the dipole operator.

The ΔSCF scheme, as suggested by the name itself, consists in performing two different SCF calculations, one for the N-electron GS and one for the ion, or the excited state that is for the (N-1)-electron configuration or for the N-electron excited configuration obtained by properly fixing the occupation numbers; the corresponding excitation or ionization energy is obtained as the difference in total energy between the ground state and the excited or ionized state:

$$\begin{gathered} \Delta E_{i\to f} = E_i^f - E_{GS} \\ IP_i = E_{\mathrm{i}} - E_{GS} \end{gathered} \tag{2.3.6}$$

It clearly follows that such procedure for the calculation of excitation energies is rather cumbersome, as it requires a different calculations for each unoccupied final orbital.

The Transition State (TS) method, formulated by J.C. Slater [2.6], consists in performing one SCF calculation for the electronic configuration in which half an electron is promoted from the initial to the final level. Slater analyzed the eigenvalues of excited states, and observed that SCF calculations of non-physical states that are in between the ground state and the excited state, are good approximations to excitation energies calculation.

To justify the choice of fractional occupation numbers, it is useful to expand the total energy E in Taylor series as a function of occupation numbers [2.7]:

$$E_{(n_i)} = \bar{E} + \sum_i \bar{E}_i(n_i - \bar{n}_i) + \frac{1}{2}\sum_i \sum_j \bar{E}_{ij}\,(n_i - \bar{n}_i)(n_j - \bar{n}_j) + \cdots \qquad (2.3.7)$$

Where $\bar{E}$ is the total energy when the occupations are $n_i = \bar{n}_i$; using Janak theorem[2.8][2.9], the $\bar{E}_i$ are the first derivatives of total energy with respect to the occupation numbers and are equal to mono-electron equation eigenvalues.

$$\bar{E}_i = \frac{\partial E_{tot}}{\partial n_i} = \varepsilon_i \qquad (2.3.8)$$

While $\bar{E}_{ij}$ are the second derivatives of total energy.

At this point, we consider the total energy for a second electronic configuration n_i' and again expand in Taylor series. The difference between total energies for occupations n_i and n_i' is equal to the eigenvalue difference, obtained with a single SCF calculation using the occupation:

$$\bar{n}_i = \frac{(n_i + n_i')}{2} \qquad (2.3.9)$$

This is the Transition State method according to Slater, and the result is simply formulated in this way[2.9]:

$$E(n_i') - E(n_i) = \sum_i \bar{E}_i\,(n_i' - n_i) + third\ order\ terms \cong \varepsilon_f - \varepsilon_i \qquad (2.3.10)$$

The third order term is very small and can be neglected with good approximation, and the excitation energy is determined with good approximation by the difference between eigenvalues of a state that is in between the two configurations.

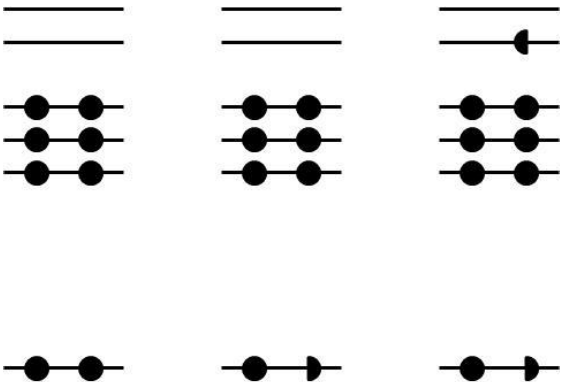

Figure 2.1 *Ground state and transition state occupations*

In **Figure 2.1** the occupations for three different cases are reported: the first case reports the occupation for the ground state, the second and third show the scheme of transition state, the central scheme consist in electronic configuration that resulted by removing a half electron from initial state and leaving the virtual states unoccupied [2.11], this scheme is used to calculate the ionization energy, the right scheme shows the electronic configuration for the promotion a half an electron from the initial state to the final state [2.12], this last scheme is used to calculate a specific transition.

At this point, to calculate a spectrum, the Kohn-Sham equations are solved using the transition state occupations:

$$H_{KS}^{TS}\varphi_i^{TS} = \varepsilon_i^{TS}\varphi_i^{TS} \quad i = 1,2,\dots,N \tag{2.3.11}$$

Where H_{KS}^{TS} is the Kohn-Sham Hamiltonian built whit transition state electronic configurations: $(i)^{-1/2}(a)^{0}$ or $(i)^{-1/2}(a)^{+1/2}$ for ionization and excitation respectively. The ionization potentials and the excitation energies can be obtained by solution of these equations. In fact the ionization potential correspond to the initial orbital's opposite eigenvalue $IP_i = -\varepsilon_i^{TS}$, and the excitation energies are the difference between to final virtual orbital and initial orbital eigenvalues $\Delta E_{i\to f} = \varepsilon_f^{TS} - \varepsilon_i^{TS}$. In practice, TS is not practical when many excitations are needed. In that case it is much more convenient to use the ionization configuration $(i)^{-1/2}(a)^0$ for the excitation as well, this scheme is called Transition Potential (TP).

2.4 Response Theory

DFT furnishes a rigorous electronic structure description only for the ground state of a given system. Therefore, when dealing with electronic excited states, the only rigorous theoretical approach is the Time – Dependent Density Functional Theory (TDDFT). It is convenient to start from general Response Theory [2.13].

Let us consider a system of N electrons which obeys the time-dependent Schrödinger equation:

$$H\Psi = i\frac{\partial \Psi}{\partial t} \tag{2.4.1}$$

When the TD perturbation is small, the perturbed Hamiltonian can be expressed as follows:

$$H(t) = H^0 + \lambda H^{(1)}(t) \tag{2.4.2}$$

The unperturbed wave function can be factorized in two parts, one spatial and the other time dependent; and assuming that $H^0\Psi_n^0 = E_n\Psi_n^0$ has already been solved:

$$\Psi_n^0(\bar{x},t) = \Psi_n^0(\bar{x})e^{-iE_nt} \tag{2.4.3}$$

Therefore the solution of the perturbed system can be expressed as follows:

$$|\Psi_0\rangle' = \Psi'_0(\bar{x},t)e^{-iE_0t} = \Psi_0^0(\bar{x})e^{-iE_0t} + \lambda\sum_{n\neq 0} c_n(t)\,\Psi_n^0(\bar{x})e^{-iE_nt} \tag{2.4.4}$$

Setting $\omega_{0n} = E_n - E_0$ so:

$$\Psi'_0(\bar{x}, t) = \Psi_0^0(\bar{x}) + \lambda \sum_{n\neq 0} c_n(t)\, \Psi_n^0(\bar{x}) e^{-i\omega_{0n}t} \tag{2.4.5}$$

Introducing (2.4.5) in (2.4.1), considering the first order in the expansion series, and collecting the exponential terms one obtains:

$$H^{(1)}\Psi_0^0 = i \sum_{n\neq 0} \dot{c}_n\, \Psi_n^0 e^{-i\omega_{0n}t} \tag{2.4.6}$$

After the introducing the bra element $\langle \Psi_k^0 |$, the coefficients c_k can be found resolving:

$$c_k(t) = \int_{-\infty}^{t} \dot{c}_k dt = -i \int_{-\infty}^{t} \langle \Psi_k^0 | H^{(1)} | \Psi_0^0 \rangle e^{i\omega_{0n}t'} dt' \tag{2.4.7}$$

Where $H^{(1)}(t) = AF(t)$, where A is only space dependent and $F(t)$ only time dependent. Therefore the integral above can be split in two parts: a spatial one which gives the shape of the perturbation; and one then time dependent. The coefficients count for the contribution of the excited state, due to the perturbation, on the first order perturbed wave function.

Usually, it is more interesting to consider the effect of the perturbation on some properties of the wave function, the actual response of the system. This can be seen from the differences in the expectation value $\langle B \rangle$, generated by a perturbation A, and the first order result will determine the linear response (linear in F(t)).

$$\delta B = \langle B \rangle - \langle B \rangle_0 \tag{2.4.8}$$

Using the expression above for the wave function:

$$\delta B = \langle \Psi | B | \Psi \rangle - \langle \Psi_0 | B | \Psi_0 \rangle \tag{2.4.9}$$

$$\delta B = -i \sum_{n \neq 0} \langle 0 | B | n \rangle \langle n | A | 0 \rangle \int_{-\infty}^{t} F(t') e^{-i\omega_{0n}(t-t')} dt' + c.c. \tag{2.4.10}$$

Introducing the "time-correlation function" K, the expression can be simplified

$$\delta B = \int_{-\infty}^{t} K(BA|t-t') F(t') dt' + c.c. \tag{2.4.11}$$

The perturbation A at time t' is related to the oscillations $\langle B \rangle$ at time t; in according with the causality principle it must be that $t > t'$ unless $K(BA|t-t')$ isn't defined.

At this point it is convenient to consider the function $F(t)$, with all its frequency components with the Fourier transform $f(\omega)$. Consequently the first order perturbed Hamiltonian is expressed:

$$H'(t) = \frac{1}{2\pi} \int_{-\infty}^{+\infty} f(\omega) \frac{1}{2} \left[A_{\omega} e^{-i\omega t} - A_{-\omega} e^{i\omega t} \right] d\omega \tag{2.4.12}$$

Considering the simplest case of a monochromatic perturbation $H'(t) = \frac{1}{2}\left[A_{\omega} e^{-i\omega t} - A_{-\omega} e^{i\omega t}\right]$ and introducing an attenuating convergence factor ($e^{\varepsilon t}$) with $\varepsilon \to 0^{+}$ that is zero for $t = -\infty$ and is equal to one for $t = t'$. Now the coefficients of the perturbed wave function can be expressed in frequency term by the Fourier anti-transform.

$$c_n(t) = -\frac{i}{2} \int_{-\infty}^{t} \langle n | A_{\omega} | 0 \rangle e^{i(\omega_{0n} - \omega - i\varepsilon)t'} dt' + term_{\omega \to -\omega} \tag{2.4.13}$$

The integral gives:

$$c_n(t) = \left(-\frac{1}{2}\right)\left[\langle n|A_\omega|0\rangle \frac{e^{i(\omega_{0n}-\omega+i\varepsilon)t}}{\omega_{0n}-\omega-i\varepsilon} + term_{\omega\to-\omega}\right] \tag{2.4.14}$$

Since this expressions are taken to the limit $\varepsilon \to 0^+$, this factor is important only at the denominator, and it can be interpreted as the imaginary part of the photon frequency. Moreover when $\omega_{0n} = \omega$ (resonance condition, photon energy equal to transition energy) the expression tends to ∞ and a discrete line spectrum is obtained. If instead a small but finite ε is employed, the excitations are described as Lorentzian shape functions.

Therefore, turning back to the oscillations of $\langle B\rangle$, and expressing them as a function of the frequency oscillations:

$$\delta B_\omega = \frac{1}{2}\left[\alpha(BA_\omega|\omega)e^{-i\omega t} + \alpha(BA_{-\omega}|-\omega)e^{i\omega t}\right] \tag{2.4.15}$$

We obtain an expression for the dynamic polarizability α, which consists of the Fourier transform of the time correlation function K:

$$\alpha(BA_\omega|\omega) = \sum_{n\neq 0} \frac{\langle 0|B|n\rangle\langle n|A_\omega|0\rangle}{-\omega_{0n}+\omega+i\varepsilon} - \frac{\langle 0|A_\omega|n\rangle\langle n|B|0\rangle}{\omega_{0n}+\omega+i\varepsilon} \tag{2.4.16}$$

It is worth noting that when the system is resonant $\omega = \omega_{0k}$ the first term denominator tends to zero and the whole expression blows up for the resonance state k, while the others $n \neq k$ elements of the sum remain finite and therefore negligible. Being $\hat{A}$ and $\hat{B}$ both electronic dipole components, so:

$$\alpha(BA_\omega|\omega) \propto \frac{|\langle 0|z|k\rangle|^2}{i\varepsilon} \tag{2.4.17}$$

The dynamic polarizability is proportional to the transition moment and on the resonance it is an imaginary number.

From this expression the problem can be solved in different method:

- Solving the response matrix with a diagonalization, and obtaining a discrete spectra.
- Calculating the spectrum point by point from the imaginary part of the polarizability, setting the value of ε as a finite number.

We obtained formal exact expressions with the only limitation imposed by the first order perturbation. However such expressions are not practical since involved infinite summations on all the exact excited states, which are not accessible in practice.

So it is desirable to apply such formalism on simplified, model descriptions of the system (Kohn-Sham), in order to obtain a method that can be implemented and used in practice.

2.5 Random Phase Approximation (RPA) and Time dependent Density Functional Theory (TDDFT)

In the previous section, devoted to the linear response theory, we have obtained formal exact expressions (2.4.16) with the limitation imposed by the first order perturbation. However such expressions are not practical since involve infinite summations on all the exact excited states, which are not accessible in practice.

So it is desirable to apply such formalism on simplified, model descriptions of the system, namely Hartree-Fock (HF) or Kohn-Sham (KS), in order to obtain a method that can be implemented and used in practice.

Although the rigorous to introduce the TDDFT consist in the demonstration of the Runge – Gross theorem [2.14], we have followed a different path. Since in this work we are interested in the reformulation of the TDDFT algorithm, we have considered more convenient to follow the conventional linear – response formalism.

Referring to the first order Time Dependent Perturbation Theory (TD-PT) (2.4.12) and considering a perturbing term with ω frequency:

$$H^{(1)}(t) = A_{\omega} e^{-i\omega t} + A_{-\omega} e^{i\omega t} \tag{2.5.1}$$

So the time dependent Schrödinger equation will be:

$$\begin{aligned}\left[H^{(0)} + \lambda\left(A_{\omega} e^{-i\omega t} + A_{-\omega} e^{i\omega t}\right)\right]\left[\Psi_0^{(0)}(\bar{x}) e^{-iE_0 t} + \lambda\left(\Psi^{(1,-)}(\bar{x}) e^{-i(E_0+\omega)t} + \Psi^{(1,+)}(\bar{x}) e^{-i(E_0-\omega)t}\right)\right] \\ = i\frac{\partial}{\partial t}\left[\Psi_0^{(0)}(\bar{x}) e^{-iE_0 t} + \lambda\left(\Psi^{(1,-)}(\bar{x}) e^{-i(E_0+\omega)t} + \Psi^{(1,+)}(\bar{x}) e^{-i(E_0-\omega)t}\right)\right]\end{aligned} \tag{2.5.2}$$

The expression (2.5.2) has been written assuming that the first order perturbed wave-function has only two different “time behaviors”: $e^{-i(E_0+\omega)t}$ and $e^{-i(E_0-\omega)t}$, this is due to the two different terms which appear in $H^{(1)}$ (2.5.1).

The zero order equation corresponds to the time independent equation:

$$H^{(0)}\Psi_0^{(0)}(\bar{x}) e^{-iE_0 t} = E_0 \Psi_0^{(0)}(\bar{x}) e^{-iE_0 t} \tag{2.5.3}$$

The first order terms can be grouped in two linear independent, time dependent contributions: one for $e^{-i(E_0+\omega)t}$ and the other for $e^{-i(E_0-\omega)t}$.

$$e^{-i(E_0+\omega)t}\left[H^{(0)}\Psi^{(1,-)}(\bar{x}) + A_{\omega}\Psi_0^{(0)} - (E_0 + \omega)\Psi^{(1,-)}\right] + \tag{2.5.4}$$

$$e^{-i(E_0-\omega)t}\left[H^{(0)}\Psi^{(1,+)}(\bar{x}) + A_{-\omega}\Psi_0^{(0)} - (E_0 - \omega)\Psi^{(1,+)}\right] = 0 \tag{2.5.5}$$

Since the whole expression must be zero identically, both expressions in brackets must be zero.

So far the expressions have always been general, now instead the special case of Hartree-Fock will be considered: so $H^{(0)} \equiv \hat{F}$ and Ψ_0 will correspond to all occupied orbitals $\Psi_0 = \varphi_i \;\; i = 1, \dots, N.$

$\Psi_i^{(1,-)}$ and $\Psi_i^{(1,+)}$ are perturbations of the occupied orbitals, therefore they also have been labelled with the index i.

The perturbed wave functions must preserve the orthonormality condition, $\langle \varphi_i | \varphi_j \rangle = \delta_{ij}$ where i, j sign up for the occupied orbitals, so:

$$\langle \delta\varphi_i | \varphi_j \rangle + \langle \varphi_i | \delta\varphi_j \rangle = 0 \tag{2.5.6}$$

Therefore each term is zero, this means that the perturbed function is orthogonal to all the occupied orbitals, then it must be a linear combination of virtual orbitals:

$$|\delta\varphi_i\rangle = \sum_b^{Virt} c_{ib} |\varphi_b\rangle \tag{2.5.7}$$

The expression (2.5.7) must hold for both the “time behaviors” of the perturbed wave function, which can be expressed as follows:

$$\varphi_i^{(1,-)} = \sum_b^{Virt} X_{ib}\varphi_b \quad \varphi_i^{(1,+)} = \sum_b^{Virt} Y_{ib}^* \varphi_b \tag{2.5.8}$$

Resuming the general equations of the first order TD-DP, making the proper substitutions and doing a scalar product on the left with a virtual orbital $\langle \varphi_a |$ the following expressions are obtained:

$$\sum_b \langle \varphi_a | F | \varphi_b \rangle X_{ib} + \langle \varphi_a | A_\omega | \varphi_i \rangle - (\varepsilon_i + \omega) \sum_b \langle \varphi_a | \varphi_b \rangle X_{ib} = 0 \tag{2.5.9}$$

$$\sum_b \langle \varphi_a | F | \varphi_b \rangle Y_{ib}^* + \langle \varphi_a | A_{-\omega} | \varphi_i \rangle - (\varepsilon_i - \omega) \sum_b \langle \varphi_a | \varphi_b \rangle Y_{ib}^* = 0 \tag{2.5.10}$$

where equation (2.5.9) corresponds to equation (2.5.4), while (2.5.10) corresponds to (2.5.5).

In both expressions the sum reduces to one term only, which correspond to $b = a$, and transforming the second equation in its conjugated complex other two simpler expression are found:

$$(\varepsilon_a - \varepsilon_i - \omega) X_{ia} + \langle \varphi_a | A_\omega | \varphi_i \rangle = 0 \tag{2.5.11}$$

$$(\varepsilon_a - \varepsilon_i + \omega) Y_{ia} + \langle \varphi_a | A_\omega | \varphi_i \rangle = 0 \tag{2.5.12}$$

The TD external field, whose strength corresponds to the A_ω operator that contains its dipole components, does affect the orbitals and consequently also the Fock operator will change.

Therefore in order to evaluate the $\langle \varphi_a | A_\omega | \varphi_i \rangle$ term, $\langle \varphi_a | F^{(1)} | \varphi_i \rangle = \langle a | F^{(1)} | i \rangle = \sum_j (\langle a\delta j \| ij \rangle + \langle aj \| i\delta j \rangle)$ should be considered first, where $F^{(1)} = \sum_j^{Occ} (\langle\, \delta j \|\, j \rangle + \langle\, j \|\, \delta j \rangle)$ and both j and δj are expressed with their TD components; so

$$\begin{aligned} \langle a | F^{(1)} | i \rangle = \sum_{j,b} e^{-i\omega t} \left[Y_{jb} \langle ab \| ij \rangle + X_{jb} \langle aj \| ib \rangle \right] \\ + \sum_{j,b} e^{i\omega t} \left[X_{ib}^* \langle ab \| ij \rangle + Y_{jb}^* \langle aj \| ib \rangle \right] \end{aligned} \tag{2.5.13}$$

Therefore $\langle\varphi_a|A_\omega|\varphi_i\rangle = \langle a|z|i\rangle + \sum_{j,b}\langle aj\|ib\rangle X_{jb} + \langle ab\|ij\rangle Y_{jb}$, where the coefficients X and Y are unknown.

At this point the expressions (2.5.11) and (2.5.12) can be rewritten as follows:

$$(\varepsilon_a - \varepsilon_i - \omega)X_{ia} + \sum_{j,b}\langle aj\|ib\rangle X_{jb} + \langle ab\|ij\rangle Y_{jb} = -\langle a|z|i\rangle \tag{2.5.14}$$

$$(\varepsilon_a - \varepsilon_i + \omega)Y_{ia} + \sum_{j,b}\langle ib\|aj\rangle Y_{jb} + \langle ij\|ab\rangle X_{jb} = -\langle i|z|a\rangle \tag{2.5.15}$$

And they can be both represented in matrix form:

$$\begin{pmatrix} A & B \\ B^* & A^* \end{pmatrix}\begin{pmatrix} X \\ Y \end{pmatrix} - \omega\begin{pmatrix} 1 & 0 \\ 0 & -1 \end{pmatrix}\begin{pmatrix} X \\ Y \end{pmatrix} = \begin{pmatrix} -V \\ -V \end{pmatrix} \tag{2.5.16}$$

Where $A_{ia,jb} = \delta_{ij}\delta_{ab}(\varepsilon_a - \varepsilon_i) + \langle aj\|ib\rangle$ and $B_{ia,jb} = \langle ab\|ij\rangle$.

The equations give the coefficients X and Y for a given ω; and when the frequency corresponds to an excitation energy then the polarizability goes to infinite.

The response of the system is manifest looking at the expectation value oscillations δB, like already seen in the previous section, the (2.4.8) expression should be observed and in this case is:

$$\delta B = \sum_i \langle\delta\varphi_i|\hat{B}|\varphi_i\rangle + \langle\varphi_i|\hat{B}|\delta\varphi_i\rangle = \sum_i \langle\delta\varphi_i|z|\varphi_i\rangle + \langle\varphi_i|z|\delta\varphi_i\rangle \tag{2.5.17}$$

Which, referring to (2.5.7) becomes:

$$\delta B = \sum_{i,a} e^{-i\omega t}[Y_{ia}\langle a|z|i\rangle + X_{ia}\langle i|z|a\rangle] + \sum_{i,a} e^{i\omega t}[X_{ia}^{*}\langle a|z|i\rangle + Y_{ia}^{*}\langle i|z|a\rangle] \quad (2.5.18)$$

And by comparison with the expression (2.4.15) a new expression is found:

$$\alpha(BA_{\omega}|\omega) \equiv \sum_{ia} Y_{ia}\langle a|z|i\rangle + X_{ia}\langle i|z|a\rangle \quad (2.5.19)$$

The oscillations of the expectation value δB, so expression (2.5.17), goes to infinite when X and Y are the solutions to the pseudo-eigenvalues equations:

$$\begin{pmatrix} A & B \\ B^{*} & A^{*} \end{pmatrix} \begin{pmatrix} X \\ Y \end{pmatrix} = \omega \begin{pmatrix} 1 & 0 \\ 0 & -1 \end{pmatrix} \begin{pmatrix} X \\ Y \end{pmatrix} \quad (2.5.20)$$

The expression above is the well known Random Phase Approximation (RPA) equation.

The problem can be simplified when:

- Orbitals are real, so $A = A^{*}$ and $B = B^{*}$
- B matrix can be neglected, this is called the Tamm Dancoff Approximation (TDA) which leads to the more common eigenvalues equation $AX = \omega X$.

If, instead of HF Hamiltonian $\hat{F}$, $\hat{H}_{KS}$ is employed as $H^{(0)}$, starting again from equations (2.5.16) is possible to switch from RPA to TDDFT equations. The matrix elements of A and B differs from RPA ones for bi-electronic term only, since in the KS approach V_{XC} must be included.

- RPA:

$$A_{ia,jb} = \delta_{ij}\delta_{ab}(\varepsilon_a - \varepsilon_i) + \langle aj\|ib\rangle = \delta_{ij}\delta_{ab}(\varepsilon_a - \varepsilon_i) + \langle aj|ib\rangle - \langle aj|bi\rangle \quad (2.5.21)$$

$$B_{ia,jb} = \langle ab \| ij \rangle = \langle ab | ij \rangle - \langle ab | ji \rangle \tag{2.5.22}$$

- TDDFT

$$\begin{aligned} A_{ia,jb} &= \delta_{ij}\delta_{ab}(\varepsilon_a - \varepsilon_i) + \langle aj \| ib \rangle \\ &= \delta_{ij}\delta_{ab}(\varepsilon_a - \varepsilon_i) + \langle aj | ib \rangle - \langle aj | K_{xc} | ib \rangle \end{aligned} \tag{2.5.23}$$

$$B_{ia,jb} = \langle ab \| ij \rangle = \langle ab | ij \rangle - \langle ab | K_{xc} | ij \rangle \tag{2.5.24}$$

Assuming that both A and B are real matrices, then $\langle aj | ib \rangle = \langle ab \| ij \rangle$ because they are real objects and the (2.5.16) equations turn into a simpler equations system:

$$\begin{cases} AX + BY - \omega X = -V \\ BX + AY + \omega Y = -V \end{cases} \tag{2.5.25}$$

Deducing the value of $(X - Y) = \omega(A - B)^{-1}(X + Y)$ and rehashing the equations, the following equation is found:

$$(A + B) - \omega^2 (A - B)^{-1}(X + Y) = -2V \tag{2.5.26}$$

Where $(A - B)^{-1}$ is diagonal in TDDFT and can be redefine as $\mathcal{E}^{-1}$ where $\mathcal{E}_{ia,jb} = \delta_{ij}\delta_{ab}(\varepsilon_a - \varepsilon_i)$.

At the end the final expression leads to the Casida formulation of TDDFT:

$$\Omega F = \omega^2 F \tag{2.5.27}$$

Where $\Omega \equiv \mathcal{E}^{-1/2}(A + B)\mathcal{E}^{1/2}$ and $F \equiv \mathcal{E}^{-1/2}(X + Y)$.

A this point the problem reduces to an eigenvalues equation that, with the proper transformations, gives $(\Omega-\omega^2)^{-1}=F_p\left(\frac{1}{\omega_p^2-\omega^2}\right)F_p^\dagger$ and looking at the result of this perturbation on a system property:

$$\delta B=V^\dagger(X+Y)=V^\dagger\mathcal{E}^{1/2}F=V^\dagger\mathcal{E}^{1/2}(-2)F_p\left(\frac{1}{\omega_p^2-\omega^2}\right)F_p^\dagger\mathcal{E}^{1/2}V \tag{2.5.28}$$

The oscillations of the expectation value $\langle B\rangle$ lead to the familiar expression, when the frequency of the external potential is resonant with one of the excited state energy $(\omega\to\omega_p)$.

$$\begin{aligned}\delta B &\cong \left|\left(V^\dagger\mathcal{E}^{1/2}F_p\right)\right|^2\frac{(-2)}{\omega_p^2-\omega^2}\cong\frac{\left|\left(V^\dagger\mathcal{E}^{1/2}F_p\right)\right|^2(-2)}{(\omega_p-\omega)2\omega}=\frac{\left|\left(V^\dagger\mathcal{E}^{1/2}F_p\right)\right|^2}{(\omega-\omega_p)\omega}\\ &=\frac{|\langle p|z|0\rangle|^2}{\omega-\omega_p}\end{aligned} \tag{2.5.29}$$

With $\omega|\langle p|z|0\rangle|^2=\left|\left(V^\dagger\mathcal{E}^{1/2}F_p\right)\right|^2$.

So, in the Casida formalism, the solutions to the TDDFT problem is to be found in the diagonalization of the matrix Ω, and its matrix elements are the folloing:

$$\Omega_{ia\sigma,jb\tau}=\delta_{\sigma\tau}\delta_{ij}\delta_{ab}(\varepsilon_a-\varepsilon_i)^2+2\sqrt{\varepsilon_a-\varepsilon_i}\mathrm{K}_{ia\sigma,jb\tau}\sqrt{\varepsilon_b-\varepsilon_j} \tag{2.5.30}$$

Where $\mathrm{K}_{ia\sigma,jb\tau}$ is called Coupling Matrix and it is:

$$\mathrm{K}_{ia\sigma,jb\tau} = \int dr \int dr' \, \varphi_{i\sigma}(r)\varphi_{a\sigma}(r) \left[\frac{1}{r-r'} + f_{xc}^{ALDA}(r)\delta(r-r')\right] \varphi_{j\tau}(r')\varphi_{b\tau}(r') \tag{2.5.31}$$

Concerning the intensity of the spectral lines, corresponding to the excitation energies given by ω_p, it is expressed by the oscillator strengths that are extracted from the eigenvectors F_p.

$$\begin{aligned} f_{pI} &= \frac{2}{3}\omega(|\langle p|x|0\rangle|^2 + |\langle p|y|0\rangle|^2 + |\langle p|z|0\rangle|^2) \\ &= \frac{2}{3}\left(x^\dagger \mathcal{E}^{1/2} F_p + y^\dagger \mathcal{E}^{1/2} F_p + z^\dagger \mathcal{E}^{1/2} F_p\right) \end{aligned} \tag{2.5.32}$$

And $x^\dagger$ is defined as $x^\dagger = (\dots \langle i|x|a\rangle \dots)$.

Until now the Spin coordinate hasn't been discussed; in this approach adding the Spin contribution is simplified because spin flip is not allowed: the excited electron keeps the same spin it had in its ground state.

So the Ω matrix can conveniently count also for the spin value of the electrons involved in the transitions, therefore the matrix elements will have two more labels $\Omega_{ia\sigma,jb\tau}$:

- σ is the spin state of i and a; (which can be both α or β)
- τ is the spin state of j and b; (which can be both α or β)

Introducing the spin state, the exchange-correlation contribution is the only term which is changed by this new contribution.

This formulation is practical restricted by the very large dimension of the matrix Ω in the equations, so the calculation of the spectra for the very large system is difficult.

For this reason we think to enveloped a new algorithm to calculate a spectra point by point from the imaginary part of the dynamical polarizability

2.6 The new TDDFT algorithm [2.15]

As already mentioned before this formulation is based on calculation of the photoabsorption spectrum $\sigma(\omega)$ point by point from the imaginary part of the dynamical polarizability $\alpha(\omega)$

$$\sigma(\omega) = \frac{4\pi\omega}{c}\Im[\alpha(\omega)] \tag{2.6.1}$$

This expression is of practical interest when the polarizability is calculated for complex frequency, i.e., $\omega = \omega_r + i\omega_i$, where the real part ω_r is the scanned photon frequency (energy) and ω_i is the imaginary part which corresponds to a broadening of the discrete lines and can be interpreted as a pragmatic inclusion of the excited states finite lifetime.

Now it will be shown that it is possible to calculate efficiently the complex $\alpha(\omega)$ introducing some approximations. First let us start with the definition:

$$\alpha_{zz}(\omega) = \int \rho_z^{(1)}(\omega, \bar{r}) z d\bar{r} \tag{2.6.2}$$

Where $\alpha_{zz}(\omega)$ is the z-th diagonal term of the polarizability tensor, $\rho_z^{(1)}(\omega, \bar{r})$ stands for the Fourier component of a given frequency of the first order time dependent induced density by the external time dependent electromagnetic field. For the calculation of the spectrum, the isotropic part of the tensor is actually extracted from the trace: $\alpha(\omega) = \frac{1}{3}\sum_{i=1}^{3} \alpha_{ii}(\omega)$ where the index i runs on the three components x, y and z.

For the TDDFT the induced density can be calculated from the Kohn-Sham dielectric susceptibility $\chi_{KS}(\omega, \bar{r}, \bar{r}')$ of a reference system of non-interacting electrons under the effect of an effective perturbing potential $V_{SCF}^{z}(\omega, \bar{r})$ sum of the external potential plus the Coulomb and XC response potential.

This is summarized by the following coupled linear equations:

$$\rho_z^{(1)}(\omega, \bar{r}) = \int \chi_{KS}(\omega, \bar{r}, \bar{r}') V_{SCF}^{z}(\omega, \bar{r}') d\bar{r}' \tag{2.6.3}$$

$$V_{SCF}^{z}(\omega, \bar{r}) = V_{EXT}^{z}(\omega, \bar{r}) + \int \frac{\rho_z^{(1)}(\omega, \bar{r}') d\bar{r}'}{|\bar{r} - \bar{r}'|} + \left. \frac{\partial V_{XC}}{\partial \rho} \right|_{\rho^0} \rho_z^{(1)}(\omega, \bar{r}) \tag{2.6.4}$$

In last expression the Adiabatic Local Density Approximation (ALDA)[2.16] has been employed (XC kernel local in time and additionally also in space, V_{XC} is the same for the Casida formulation) and $V_{EXT}^{z}(\omega, \bar{r})$ corresponds in practice to the z dipole component.

Now rewrite expressions for the induced density and the perturbing potential in operatorial form:

$$\rho_z^{(1)} = \chi_{KS} V_{SCF}^{z} \tag{2.6.5}$$

$$V_{SCF}^{z} = V_{EXT}^{z} + K \rho_z^{(1)} \tag{2.6.6}$$

Where in expression (2.6.6) K stands for the sum of the Coulomb and the XC kernels:

$$K(\bar{r},\bar{r}') = K_C(\bar{r},\bar{r}') + K_{XC}(\bar{r},\bar{r}') = \frac{1}{|r-r'|} + \delta(r-r')\left.\frac{\partial V_{XC}}{\partial \rho}\right|_{\rho^0} \qquad (2.6.7)$$

Due to the linearity of (2.6.5) and (2.6.6) it is possible to eliminate V_{SCF}^{z} and to obtain an equation for, $\rho_z^{(1)}$ which reads:

$$[1 - \chi_{KS}K]\rho_z^{(1)} = \chi_{KS}V_{EXT}^{z} \qquad (2.6.8)$$

Now it is convenient to represent equation (2.6.8) over a basis set and since the unknown term corresponds to the induced density, it is natural to choose the auxiliary density fitting functions f_μ as basis set. More precisely it is even better to choose such basis as a subset of the fitting set, since the induced density will be affected mainly by valence orbitals so all the functions needed to fit the core density should be excluded without loosing of accuracy. With this representation $\rho_z^{(1)}(\omega,\bar{r}) = \sum_\mu^K f_\mu(\bar{r})b_\mu(\omega)$, the following non-homogeneous system of linear algebraic equations is obtained, which written in matrix formulation reads:

$$[\boldsymbol{S} - \boldsymbol{M}(\boldsymbol{\omega})]\boldsymbol{b} = \boldsymbol{d} \qquad (2.6.9)$$

Where **S** is the overlap matrix between fitting functions, **b** is the unknown vector with the expansion coefficients $b_\mu(\omega)$ of $\rho_z^{(1)}$, **d** is the frequency dependent vector corresponding to the known non-homogeneous term, whose components are:

$$d_\mu = \langle f_\mu | \chi_{KS}(\omega) | z \rangle \qquad (2.6.10)$$

and finally the elements of the frequency dependent matrix **M** are:

$$M_{\mu\nu} = \langle f_\mu | \chi_{KS}(\omega) K | f_\nu \rangle \tag{2.6.11}$$

Now, let us analyse the efforts needed to build the frequency dependent $\boldsymbol{M}(\omega)$ matrix: apparently this is a prohibitive task for a practical calculation, since it should be repeated for each frequency. The original characteristic of the present new method is the introduction of a simple approximation which should enable the construction of $\boldsymbol{M}(\omega)$ as a linear combination of frequency independent matrices $\boldsymbol{G}^k$ with frequency dependent coefficients $s_k(\omega)$, with this expression:

$$\boldsymbol{M}(\omega) = \sum_k s_k(\omega) \boldsymbol{G}^k \tag{2.6.12}$$

with this idea a set of matrices $\{\boldsymbol{G}^k\}$ is calculated and stored once at the beginning, then the matrix $\boldsymbol{M}(\omega)$ is calculated very rapidly at each photon energy ω.

Now let us justify the expression (2.6.12), starting with the expression of the KS dielectric susceptibility:

$$\begin{aligned} \chi_{KS}(\omega, \bar{r}, \bar{r}') &= \sum_i^{Nocc} \sum_a^{Nvirt} \varphi_i(\bar{r}) \varphi_a(\bar{r}) \frac{4\varepsilon_{ia}}{\omega^2 - \varepsilon_{ia}^2} \varphi_i(\bar{r}') \varphi_a(\bar{r}') \\ &= \sum_i^{Nocc} \sum_a^{Nvirt} \Theta_{ia}(\bar{r}) \lambda_{ia}(\omega) \Theta_{ia}(\bar{r}') \end{aligned} \tag{2.6.13}$$

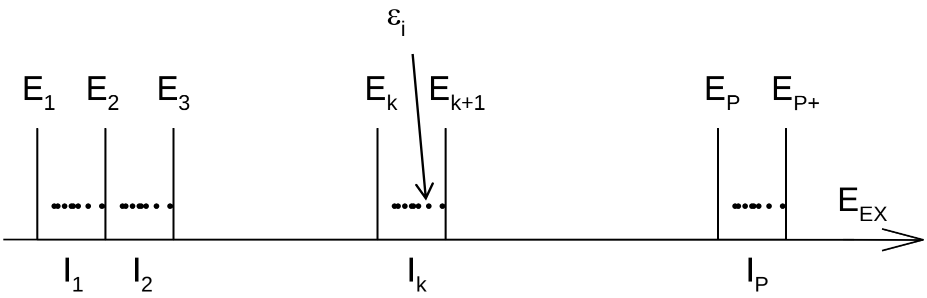

Figure 2.2 *Grid of the energy axis to place* $\boldsymbol{\varepsilon_{ia}}$ *to simplify the dielectric susceptibility expression.*

where in (2.6.13) we have assumed real KS occupied φ_i and virtual φ_a orbitals and $\varepsilon_{ia} = \varepsilon_a - \varepsilon_i$ are differences between virtual and occupied KS eigenvalues. Now consider carefully the right hand side of expression (2.6.13): the frequency dependence enters only in the $\lambda_{ia}(\omega)$ factor, which is 'almost' constant for all the pairs of index *i*- and *a*- for which $\varepsilon_a - \varepsilon_i$ is almost constant. This happens when many ε_{ia} are close together, that is when the density of 'zero order' excitation energies is high. This important observation allows to profitably change the double sum in expression (2.6.13).

In fact, let us consider the distribution of all the ε_{ia} on the excitation energy axis, like in the next **Figure 2.2**, and define an energy grid over this axis, starting from the minimum ε_{ia} which corresponds to $\varepsilon_{LUMO} - \varepsilon_{HOMO}$. The energy grid consists of P+1 knots $\{E_k\}_{k=1,\dots,P+1}$ and P intervals I_k.

Now it is possible to change the double sum of previous equation (2.6.13) as follows:

$$\chi_{KS}(\omega,\bar{r},\bar{r}') = \sum_{k=1}^{P} \sum_{\varepsilon_{ia} \in I_k} \Theta_{ia}(\bar{r}) \lambda_{ia}(\omega) \Theta_{ia}(\bar{r}') \qquad (2.6.14)$$

the advantage of this new double sum is that, if the energy knots are dense enough, the values of ε_{ia} within each interval can be considered, with good approximation, almost constant and equal to the average $\bar{E}_i = \frac{E_i+E_{i+1}}{2}$: this allows to bring the $\lambda_{ia}(\omega)$ factor outside the inner sum:

$$\chi_{KS}(\omega,\bar{r},\bar{r}') = \sum_{k=1}^{P} \frac{4\bar{E}_k}{\omega^2 - \bar{E}_k^2} \sum_{\varepsilon_{ia}\in I_k} \Theta_{ia}(\bar{r})\Theta_{ia}(\bar{r}') \tag{2.6.15}$$

so in expression (2.6.15) the frequency dependent dielectric susceptibility is a linear combination of frequency independent objects (the inner sum) while only the coefficients are frequency dependent. Moreover, if one is interested in the lowest part of the spectrum as usually it happens, the sum in (2.6.15) can be safely truncated at a maximum energy cut-off, which can be chosen checking the convergence of the results with respect to such energy cut-off.

This re-summation is the central idea of the present algorithm. Now we will use this approach to build the matrix $\boldsymbol{M}(\omega)$. From equation (2.6.11) and using expression (2.6.15) we get:

$$M_{\mu\nu} = \sum_{k=1}^{P} s_k(\omega) \sum_{\varepsilon_{ia}\in I_k} \langle f_\mu|\Theta_{ia}(\bar{r})\rangle\langle\Theta_{ia}(\bar{r}')|K|f_\nu\rangle = \sum_{k=1}^{P} s_k(\omega) G_{\mu\nu}^k \tag{2.6.16}$$

which now justifies previous expression (2.6.12), defines the matrix $G_{\mu\nu}^k$ and the coefficients:

$$s_k(\omega) = \frac{4\bar{E}_k}{\omega^2 - \bar{E}_k^2} \tag{2.6.17}$$

The construction of each $G_{\mu\nu}^k$ matrix corresponds to a matrix-matrix product:

$$G_{\mu\nu}^{k} = \sum_{\varepsilon_{ia}\in I_k} \langle f_\mu | \Theta_{ia}(\bar{r}) \rangle \langle \Theta_{ia}(\bar{r}') | K | f_\nu \rangle = \sum_{\varepsilon_{ia}\in I_k} A_{\mu,ia}^{k} B_{ia,\nu}^{k} \tag{2.6.18}$$

Where the matrices **A** and **B** are:

$$A_{\mu,ia}^{k} = \langle f_\mu | \Theta_{ia}(\bar{r}) \rangle \tag{2.6.19}$$

$$B_{ia,\nu}^{k} = \langle \Theta_{ia}(\bar{r}') | K | f_\nu \rangle = \left\langle \Theta_{ia}(\bar{r}') \middle| \frac{1}{|\bar{r}' - \bar{r}''|} \middle| f_\nu \right\rangle + \left\langle \Theta_{ia}(\bar{r}') \middle| \frac{\partial V_{XC}}{\partial \rho} \middle| f_\nu \right\rangle \tag{2.6.20}$$

Finally from the coefficients b_μ, solution to the equation (2.6.9), we can be possible calculate the dynamic polarizability:

$$\alpha_{zz}(\omega) = \sum_{\mu} b_\mu \int f_\mu z d\bar{r} \tag{2.6.21}$$

Having the components of the complex dynamic polarizability the first order TD density perturbation, i.e. the spectrum, is obtained.

2.7 Basis sets

Since DFT is commonly used for solid states problems, plane waves are the most commonly function adopted as basis set functions for condensed matter. In quantum chemistry instead, more localized functions are regularly employed: for example Gaussian functions or Slater Type Orbitals (STO).

In the Amsterdam Density Functional (ADF) program[2.17][2.18], which is a commercial molecular DFT code, the STO functions are employed as basis set.

ADF employs a second auxiliary basis set to fit the electronic density. In fact, in order to reduce the computational effort of the Coulomb term in the Hamiltonian, it is useful to expand $\rho(\bar{r})$ by the auxiliary basis set functions $f_i(\bar{r})$:

$$\tilde{\rho}(\bar{r}) = \sum_i a_i f_i\,(\bar{r}) \tag{2.7.1}$$

The fit functions $f_i(\bar{r})$ are provided by a data base included in ADF, while the coefficients a_i are obtained minimizing the error:

$$D = \int [\rho(\bar{r}) - \tilde{\rho}(\bar{r})]^2 d\bar{r} \tag{2.7.2}$$

With the constrain $\int \tilde{\rho}(\bar{r})\,d\bar{r} = N$

Once the electron density has been fitted with such procedure, the Coulomb term of the KS Hamiltonian matrix is calculated by Gaussian quadrature between the basis function pair and the Coulomb potential generated by $\tilde{\rho}(\bar{r})$, the latter being analytical.

2.8 Relativistic effects

When relativistic effects are not considered in the theoretical description of heavy atoms compounds anomalies between the expected properties and the theoretical results are found[2.19]. It is well known that, gold compounds, in particular, must be treated with the relativistic theory in order to describe properly their electronic structure.

The relativistic effects concern mainly the core orbitals (1s), anyway the whole electronic structure is affected as a consequence. All the s-type orbitals, in fact, must be orthonormals to the 1s orbital; therefore the relativistic contraction in the 1s orbital whose average speed is comparable with that of light, produces a contraction in all the s-type orbitals. Moreover, the valence orbitals feel a minor attraction towards the nucleus as a result of the increased shield of the contracted core orbitals, so they raise in energy. These two effects combined reduce the energy gap between the 5d and 6s bands.

The theoretical description of the electronic structures including the relativistic effects means that the Dirac equation must be solved, which can be difficult because the solution furnishes also eigenvalues with negative energy since the equation is not bound from below.

Some approximations of the Dirac Hamiltonian H_{Dirac} are therefore necessary: H_{Dirac} has four components: the so called large and small components which are each split in two spin components. The small and large components can be approximately decoupled, so two approximated Hamiltonian with two components (spatial and spin coordinates) are found. And when the Spin-Orbit coupling can be neglected the Hamiltonian has one component only and gives a Scalar Relativistic description of the electronic structure.

The STOs of the basis set used in ADF code have exponents which have been optimized for the use in Scalar Relativistic Zeroth-Order Regular Approximated (SR-ZORA) equations [2.20].

Excitation energies based on the scalar-ZORA TDDFT method has, in fact, shown to afford accurate results [2.21]. The ZORA method is obtained by rewriting the energy expression and expanding in the term ${}^{E}\!/_{(2mc^2 - V)}$, which remains small even close to the nucleus.

Retaining only the zeroth order term one gets:

$$E = \frac{p^2c^2}{2mc^2 - V} + V \tag{2.8.1}$$

which gives the following Hamiltonian:

$$H_{ZORA} = \sigma \cdot p \frac{c^2}{2c^2 - V} \sigma \cdot p + V \tag{2.8.2}$$

where σ is the Pauli spin matrix vector, c is the speed of light, p is the moment operator and V is the total potential that equals the sum of the nuclear-attraction potential, the electronic repulsion potential and the XC potential.

Spin-Orbit coupling affects the electronic structure when the two component H_{ZORA} is employed, which has an additional term: the spin-orbit H_{SO}. Employing the SO coupling should provide all the most relevant physical effects involved in the photoabsorption, ranging from the configuration mixing of TDDFT to the SO coupling itself, which can be applied to the cluster of moderate size and high symmetry with reasonable efforts.

SO coupling results from the interaction of the electron magnetic moments with the magnetic field generated by its own orbital motion. The computation becomes more involved with respect to the SR term because the spin-orbit term reduces and makes more involved the treatment of the molecular symmetry.

In practice, when the SO is included in the calculation, both the electronic structure and the electronic excitation undergo more or less pronounced complications, because now the non-s molecular orbitals $(l \neq 0)$ generate doubly-split states.

The electronic structure is therefore described in term of spinors: this induces a reduction of the degeneracy going from molecular orbitals to SO spinors. The latter are one electron functions as well and are expressed as the sum of two products between a spatial and a spin function:

$$\chi(r, \omega) = \varphi_\alpha(r)\alpha(\omega) + \varphi_\beta(r)\beta(\omega) \tag{2.8.3}$$

r corresponds to the electron spatial coordinates and ω to the spin coordinate.

2.9 The exchange-correlation potential V_{xc}

The V_{XC} potential is the only unknown term in the KS equations therefore to find the solutions to the equations, an approximated form of this potential has to be employed. Since there are many different V_{XC} models available in literature, here will be presented the main properties of the exact exchange-correlation potential to have a better understanding of the different levels of approximation.

Considering the equation (2.2.14) it can possible write:

$$E_{xc}[\rho] = \Delta T[\rho] + \Delta E_{ncl}[\rho] \tag{2.9.1}$$

Since the potential is derived from the functional, its different contributions will be analyzed individually:

- Correlation term of the kinetic energy ΔT
- E_{ncl} incorporates all the non-classic electron-electron interaction, that are: Exchange energy h_x (antisymmetric or Pauli exclusion principle), Coulomb correlation energy h_c, Self Interaction Correction (SIC)

The correlation effects condition the probability to find one electron in r_2 while another is already in r_1:

- In case there isn't any interaction

$$\gamma_2(x_1, x_2) = \frac{N-1}{N}\gamma_1(x_1)\gamma_1(x_2) \tag{2.9.2}$$

- With the electronic interaction

$$\gamma_2(x_1, x_2) = \gamma_1(x_1)\gamma_1(x_2)[1 + f(x_1, x_2)] \tag{2.9.3}$$

where $\gamma_1(x_1)$ and $\gamma_1(x_2)$ are the individual probabilities for the electrons to be found in x_1, x_2 respectively and $\gamma_2(x_1, x_2)$ is the joint probability. The (2.9.3) expression, when the electrons aren't correlated and $f(x_1, x_2) = 0$, gives back the (2.9.2) expression but it doesn't normalize to the correct number of electron pairs and includes the unphysical self-interaction. $f(x_1, x_2) = 0$ strictly for the non interacting system for 2 electrons of opposite spin, when the spin is parallel the motion is correlated due to the "exchange-correlation" as a consequence of the antisymmetry or Pauli exclusion principle.

For the non-interacting system, the joint density is the simple product of the individual probabilities; in the real system instead, the electrons are charged and therefore are affected by a repulsive potential, furthermore they are also fermions and must obey the Pauli exclusion principle.

To consider the correlation effects, the conditioned probability can be defined:

$$g(x_1, x_2) = \frac{\gamma_2(x_1, x_2)}{\gamma_1(x_1)} \tag{2.9.4}$$

$$\int g(x_1, x_2)dx_2 = N - 1 \tag{2.9.5}$$

The difference between $g(x_1, x_2)$ and the unconditioned probability γ_1 is the exchange-correlation hole:

$$h_{xc}(x_1, x_2) = \frac{\gamma_2(x_1, x_2)}{\gamma_1(x_1)} - \gamma_1(x_2) \tag{2.9.6}$$

so this term contains all the correlation effects due to both exchange and Coulomb repulsion, plus the SIC. It's important to notice that the expression integrated gives -1 as result: the hole contains the exact charge of one electron.

With this new considerations and identifying the individual probabilities γ_1 with the electron density ρ, the electron-electron repulsive potential con be re-written:

$$\langle V_{ee} \rangle = \frac{1}{2} \iint \frac{\rho(r_1)\rho(r_2)}{r_{12}} dr_1 dr_2 + \frac{1}{2} \iint \frac{\rho(r_1) h_{xc}(r_1, r_2)}{r_{12}} dr_1 dr_2 \tag{2.9.7}$$

where the first term is the classic interaction between two electronic densities, which contains also a self-interacting term which can cause some issues in case of one-electron systems. The second term instead, concerns the interaction between the electron density and the XC hole, introducing the correlation effects and the correction to the self-interaction.

The exchange-correlation hole can be divided in two parts:

$$h_{xc}(r_1, r_2) = h_X^{S_1, S_2}(r_1, r_2) + h_C^{S_1, S_2}(r_1, r_2) \tag{2.9.8}$$

the first term is the Fermi hole which states the Pauli exclusion principle, and affects electrons with the same spin value; the second term is the Coulomb hole and is due to electrostatic effects and all electrons are affected independently from their spin value. Anyway only the overall expression of the hole has a physical meaning.

The effective potential that acts on the system in the Kohn-Sham approach is therefore:

$$v_{eff}(r_i) = -\sum_A \frac{Z_A}{r_{iA}} + \int \frac{\rho(r_j)}{r_{ij}} dr_j + v_{xc}(\rho, r_i) \tag{2.9.9}$$

where $\nu_{xc}(\rho, r_i)$ explicitly counts for the exchange-correlation effects. It is a local potential and therefore is different from the ab-initio exchange operator of the method of Hartree-Fock where the operator $\hat{k}$ is non-local.

$$\hat{k}_b \chi_a(\bar{x}_1) = \int \frac{\chi_b^*(\bar{x}_2)\chi_a(\bar{x}_2)}{r_{12}} d\bar{x}_2 \chi_b(\bar{x}_1) \tag{2.9.10}$$

From the potential expression it is possible to infer one of the most important characteristic of the V_{xc}.

In fact, for a neutral molecule $(\sum_A Z_a = N)$, referring to expression (2.9.9), when the system is far from the center of the atom or molecule which correspond to the limit $\lim_{|r|\to\infty} \nu_{eff}(r)$, it is apparent that $\nu_{Ne} \to -\frac{N}{r}$ and $\nu_C = \int \frac{\rho(r)}{r_{ij}} dr_i \to \frac{N}{r}$; which cancel mutually.

The limit of the V_{xc} when r tends to infinite can be easily shown from the expression of the Fock operator:

$$\hat{f} = \hat{h} + \sum_b^N (\hat{j}_b - \hat{k}_b) \tag{2.9.11}$$

$$\langle a|\hat{f}|a\rangle = \langle a|\hat{h}|a\rangle + \sum_b^N \langle ab|ab\rangle - \langle ab|ba\rangle \tag{2.9.12}$$

the bi-electronic operators run all over the occupied spin-orbitals. In fact when $a = b$ the two terms in the last expression are identical: there are no self-interacting contributions. Therefore the electron in the a orbital feels the Coulomb repulsion of the other $N - 1$ electrons, since the self-interaction is exactly cancelled by the exchange term.

So it should be that $\lim_{|r|\to\infty} V_{xc}(r) = -\frac{1}{r}$, and since the other terms cancel mutually for neutral systems the limit of the whole effective potential (2.9.9) is:

$$\lim_{|r|\to\infty} v_{eff}(r) = -\frac{1}{r} \tag{2.9.13}$$

The V_{xc} potential in the KS approach replaces the role of the exchange operator in the HF method.[2.22]

Aside the correct asymptotic behavior, there are other requirements that an approximate exchange-correlation potential must satisfy.

2.10 Computational Details of new TDDFT algorithm

The new TDDFT algorithm is based on the resolution of the system of linear algebraic equations:

$$[\boldsymbol{S} - \boldsymbol{M}(\boldsymbol{\omega})]\boldsymbol{b} = \boldsymbol{d} \tag{2.10.1}$$

Now the construction for the all terms of equation (2.10.1) will be outlined.

This algorithm has been developed starting from the Amsterdam Density Functional (ADF) code [2.17][2.18], in fact many integrals are already calculated by ADF, so the code has been only modified to save these integrals on an external file which will be read by a different program which will complete the calculations.

The ADF code calculates and saves the following analytic integrals:

- The fitting function overlapping integrals matrix S:

$$S_{\mu\nu} = \langle f_\mu | f_\nu \rangle \tag{2.10.2}$$

- Coulomb integrals between fitting functions F:

$$F_{\mu\nu} = \left\langle f_\mu \middle| \frac{1}{|\bar{r}' - \bar{r}''|} \middle| f_\nu \right\rangle \tag{2.10.3}$$

- The integrals between two basis functions and one fitting functions (pair fitting):

$$\langle f_\mu | \sigma\tau \rangle \tag{2.10.4}$$

- Dipole integrals between basis functions:

$$\langle \sigma | z | \tau \rangle \tag{2.10.5}$$

It also saves the eigenvalues of the molecular orbitals and the molecular orbital expansion coefficients.

Finally we had to implement in ADF also the calculation of new integrals, between fitting functions and the ALDA exchange correlation Kernel:

$$Z_{\mu\nu} = \left\langle f_\mu \middle| \frac{\partial V_{XC}}{\partial \rho} \middle| f_\nu \right\rangle \tag{2.10.6}$$

The new program (independent by ADF) reads the files, selects the fitting functions, builds all the needed matrices and solves the TDDFT equation (2.10.1), calculates the spectrum and performs the analysis.

The new program first builds the energy grid, distributes the difference of eigenvalues between occupied and virtual molecular orbitals, and selects the fitting functions. Then it builds the matrix A^k:

$$A^k_{\mu,ia} = \langle f_\mu | \varphi_i \varphi_a \rangle = \sum_{\sigma\tau}^{basis} \langle f_\mu | \sigma\tau \rangle c_{\sigma i} c_{\tau a} \tag{2.10.7}$$

The complete calculation of (2.10.7) would be far prohibitive, but in ADF a very efficient “pair fitting” technique has been already developed so the run of the basis indexes is not free but limited such that at least one basis function lies on the same center of the fit function. This step will be the most expensive in the matrix construction. The similar procedure is used to calculate the matrix B^k.

$$B^k_{ia,\nu} = \left\langle \varphi_i\varphi_a \middle| \frac{1}{|\bar{r}' - \bar{r}''|} \middle| f_\nu \right\rangle + \left\langle \varphi_i\varphi_a \middle| \frac{\partial V_{XC}}{\partial \rho} \middle| f_\nu \right\rangle \tag{2.10.8}$$

Now it considers the first term of equation (2.10.8):

$$\begin{aligned} \left\langle \varphi_i\varphi_a \middle| \frac{1}{|\bar{r}' - \bar{r}''|} \middle| f_\nu \right\rangle &= \sum_{\gamma\eta} \langle \varphi_i\varphi_a | f_\gamma \rangle S^{-1}_{\gamma\eta} \left\langle f_\eta \middle| \frac{1}{|\bar{r}' - \bar{r}''|} \middle| f_\nu \right\rangle \\ &= ((A^k)^+ S^{-1} F)_{ia,\nu} \end{aligned} \tag{2.10.9}$$

The second term in (2.10.8) can be calculated in a similar fashion:

$$\left\langle \varphi_i\varphi_a \middle| \frac{\partial V_{XC}}{\partial \rho} \middle| f_\nu \right\rangle = \sum_{\gamma\eta} \langle \varphi_i\varphi_a | f_\gamma \rangle S^{-1}_{\gamma\eta} \left\langle f_\eta \middle| \frac{\partial V_{XC}}{\partial \rho} \middle| f_\nu \right\rangle = ((A^k)^+ S^{-1} Z)_{ia,\nu} \tag{2.10.10}$$

Therefore from (2.10.8), (2.10.9), and (2.10.10) we get:

$$B^k_{ia,\nu} = ((A^k)^+ S^{-1}(F + Z))_{ia,\nu} \tag{2.10.11}$$

In Theory chapter we define matrix G^k in this way:

$$G^k = A^k B^k \tag{2.10.12}$$

In fact we don’t directly calculate B^k, but we determine matrices D^k and L that are defined:

$$D^k = A^k (A^k)^+ \tag{2.10.13}$$

$$L = S^{-1}(F + Z) \tag{2.10.14}$$

It possible observe that matrix L is independent from k index (interval energy), so now G^k is defined in this way:

$$G^k = D^k L \tag{2.10.15}$$

Also in this case the matrix G^k isn’t directly calculated, because it isn’t computational convenient, because matrix $M(\omega)$ is defined:

$$M(\omega) = \sum_{k=1}^{P} s_k(\omega) G^k = \sum_{k=1}^{P} s_k(\omega) D^k L = \left(\sum_{k=1}^{P} s_k(\omega) D^k \right) L \tag{2.10.16}$$

Where the coefficients s_k corresponds to:

$$s_k(\omega) = \frac{4\bar{E}_k}{\omega^2 - \bar{E}_k^2} \tag{2.10.17}$$

We have still to calculate the d vector of equation (2.10.1), i.e. the non-homogeneous term, taking advantage of previously describes technique, it is straightforward:

$$d_\mu = \langle f_\mu | \chi_{KS}(\omega) | z \rangle = \sum_{k=1}^{P} s_k(\omega) \sum_{\varepsilon_{ia} \in I_k} A_{\mu,ia}^k \langle \varphi_i | z | \varphi_a \rangle \tag{2.10.18}$$

The dipole moment integrals are calculated with linear combination from integrals (2.10.5)

$$\langle\varphi_i|z|\varphi_a\rangle = \sum_{\sigma\tau}^{basis} \langle\sigma|z|\tau\rangle c_{\sigma i} c_{\tau a} \tag{2.10.19}$$

So vector d is easily calculated at each frequency as a linear combination of frequency independent vectors, accessible from A matrix and conventional dipole matrix elements.

Finally the complex dynamic polarizability components are calculated:

$$\alpha_{zz}(\omega) = \int \rho_z^{(1)}(\omega,\bar{r}) z d\bar{r} = \sum_\mu b_\mu \int f_\mu z d\bar{r} = \sum_\mu b_\mu n_\mu \tag{2.10.20}$$

Where the vector b in (2.10.20) is the solution of equation (2.10.1) and the elements of the n vector are integrals which are easily calculated analytically.

This step concludes the calculation of the dynamic polarizability, and therefore of the spectrum, and furnished the first order TD density which can be used to analyze and rationalize the results. However our goal is to get also a more complete analysis of the spectrum, namely in terms of linear combination of one-electron excited configurations or in terms of Transition Contribution Maps (TCM) [2.23]. To obtain this, it is convenient adopt the Modified Sternheimer Approach (MSA) formulation [2.24] of linear response, which furnished the first order perturbation of the KS orbitals:

$$\begin{gathered}[H_{KS}^0 - \varepsilon_i - \omega]\varphi_i^{(1,-)} = -V_{SCF}\varphi_i \\ [H_{KS}^0 - \varepsilon_i + \omega]\varphi_i^{(1,+)^*} = -V_{SCF}\varphi_i\end{gathered} \tag{2.10.21}$$

And from the perturbed orbitals the perturbed density is obtained:

$$\rho^{(1)} = 2\sum_{i}^{occ} \varphi_i \left(\varphi_i^{(1,-)} + \varphi_i^{(1,+)^*}\right) \tag{2.10.22}$$

It is worth noting that, for convenience, the second inhomogeneous equations (2.10.21) is actually the complex conjugate with respect to that reported in ref. [2.24] for $\varphi_i^{(1,+)}$. Equations (2.10.21) and (2.10.22) in the past were used to calculate self-consistently the V_{SCF} (see the theory chapter) in old TDDFT implementations [2.25][2.26], but in the present context they are useful to easily get the analysis in terms of one-electron configurations once the TDDFT equations have been already solved. In fact if the perturbed orbitals are expanded in terms of virtual KS orbitals the term in brackets is diagonal:

$$\begin{aligned} [\varepsilon_a - \varepsilon_i - \omega]c_i^{a-} &= -\langle\varphi_a|V_{SCF}|\varphi_i\rangle \\ [\varepsilon_a - \varepsilon_i + \omega]c_i^{a+^*} &= -\langle\varphi_a|V_{SCF}|\varphi_i\rangle \end{aligned} \tag{2.10.23}$$

The polarizability is then expressed by:

$$\alpha_{zz}(\omega) = 2\sum_{i}^{occ}\sum_{a}^{virt}\langle\varphi_i|z|\varphi_a\rangle\left(c_i^{a+^*} + c_i^{a-}\right) = \sum_{i}^{occ}\sum_{a}^{virt}\langle\varphi_i|z|\varphi_a\rangle P_i^a \tag{2.10.24}$$

Where in equation (2.10.24), the density matrix (dipole amplitudes) P_i^a is introduced. From equation (2.10.23) and using the definition of $s_k(\omega)$, we obtain:

$$P_i^a = s_k(\omega)\langle\varphi_i|V_{SCF}|\varphi_a\rangle \tag{2.10.25}$$

In practice from imaginary part of equation (2.10.24) the absorption spectrum is obtained and therefore from imaginary part of expression (2.10.25) the analysis in term of one-electron excited configurations and TCM is obtained.

The dipole amplitudes are actually calculated as follows:

$$P_i^a = s_k(\omega)\left[\langle\varphi_i|z|\varphi_a\rangle + \sum_{\mu\tau}^{fit}(A^k)^+_{ia,\mu}L_{\mu\tau}b_\tau\right] \qquad (2.10.26)$$

We have decided to implement the new code in a separate program independent by ADF in order to exploit more easily the parallelization, with the goal to obtain a code which were massively parallel and easily portable on different architectures. For this reasons we have used standard Message Passing Interface (MPI), BLACS and ScaLAPACK libraries. The general scheme of the parallel calculation consists of four points: first is the initialization the BLACS grid, second the distribution of the matrix among the grid processes (typically cyclic block distribution), third the call to ScaLAPACK routines (matrix product, matrices sum, etc.), fourth the harvest of the results. However, the inclusion of the complete program within the ADF suite is under consideration and will be available in a future release of ADF.

The new program allows a simple choice of a subset of the ADF fitting functions, in order to save computer time when some fitting functions are not necessary for an accurate description of the photoabsorption spectrum. The strategy to choose a properly reduced fitting subset consists to perform some preliminary TDDFT test calculations on simple systems (typically biatomic molecules) increasing gradually the number of fit functions. Typically this procedure converges rather rapidly, giving calculated spectra that match better and better with those obtained with a standard TDDFT calculation by ADF. When a good match is obtained, the fitting subset of the corresponding atoms can be used for more complicated or larger system.

Equation (2.10.1) must be solved for each non-equivalent dipole component, and the induced density $\rho^{(1)}$ must integrate to zero over space due to orthogonally of occupied-virtual orbitals. This condition is naturally satisfied when the dipole component is not totally symmetric, on the other hand when the symmetry is low and one or more dipole components are totally symmetric, such constrain must be imposed this is easily done by Lagrange multipliers technique after equation (2.10.1) is solved. So to rewrite the equation in matrix form

$$\begin{pmatrix} S-M & \cdots & \bar{n} \\ \vdots & \ddots & \vdots \\ \bar{n} & \cdots & 0 \end{pmatrix} \begin{pmatrix} b \\ \vdots \\ -\lambda \end{pmatrix} = \begin{pmatrix} d \\ \vdots \\ 0 \end{pmatrix} \tag{2.10.27}$$

Where $\bar{n}$ is the vector of the integrals of fitting functions:

$$\bar{n} = \int f_\mu d\bar{r} \tag{2.10.28}$$

In practice the vector of expansion coefficients b of $\rho^{(1)}$ is calculated in this way:

$$\bar{b} = \bar{t} - \frac{\langle n|t\rangle}{\langle n|q\rangle}\bar{q} \tag{2.10.29}$$

Where $\bar{t}$ is the solution of the linear equation (2.10.1) without constrain, instead $\bar{q}$ is defined:

$$\bar{q} = (S-M)^{-1}\bar{n} \tag{2.10.30}$$

While ADF employ the fully symmetry in both SCF and TDDFT parts, in the present method the symmetry is only partially exploited: the density fitting basis functions are not symmetrized by now, however only the pairs of occupied (φ_i) and virtual (φ_a) orbitals involved in allowed dipole selection rules are actually considered.

We have implemented in the present method also the plasmon analysis according to Jacob et al.[2.27]: they suggested to study the evolution of the TDDFT photoabsorption spectra by changing a scaling factor $0 \leq \lambda \leq 1$ used to “turn on” the coupling matrix K. In present implementation this can be easily done multiplying the matrix L (equation (2.10.14)) by the scaling factor λ. This scaling factor analysis has proven successful in previous studies on silver chains[2.28] and polyacenes[2.29].

3 Vibrationally resolved high-resolution NEXAFS and XPS spectra of phenanthrene and coronene

G. Fronzoni, O. Baseggio, M. Stener, W. Hua, G. Tian, Y. Luo, B. Apicella, M. Alfé, M. de Simone, A. Kivimäki, and M. Coreno, The Journal of Chemical Physics 141, 044313 (2014);

We performed a combined experimental and theoretical study of the C1s Near-Edge X-ray Absorption Fine-Structure (NEXAFS) spectroscopy and X-ray Photoelectron Spectroscopy in the gas phase of two polycyclic aromatic hydrocarbons (phenanthrene and coronene), typically formed in combustion reactions. In the NEXAFS of both molecules, a double-peak structure appears in the C1s → LUMO region, which differ by less than 1 eV in transition energies. The vibronic coupling is found to play an important role in such systems. It leads to weakening of the lower-energy peak and strengthening of the higher-energy one because the $0 - n\,(n > 0)$ vibrational progressions of the lower-energy peak appear in nearly the same region of the higher-energy peak. Vibrationally resolved theoretical spectra computed within the Frank-Condon (FC) approximation and linear coupling model agree well with the high-resolution experimental results. We find that FC-active normal modes all correspond to in-plane vibrations.

3.1 Introduction

Spectroscopic techniques related to core electron excitations are very appealing to study complex systems, because the localization of the core hole on a specific atomic site allows one to obtain precious information on the electronic structure at that site, in particular on the contribution of the atomic functions to the virtual molecular orbitals involved in the excitation. In this respect Near Edge X-ray Absorption Spectroscopy

(NEXAFS)[3.1] represents the spectral interval of absorption near the inner-shell (or core) threshold (within 30–40 eV) where the transitions from the core orbitals to valence virtual orbitals give rise to distinct spectral features. These features are strictly related to the electronic structure of the system under study; however, their interpretation is usually not straightforward. Therefore it is very useful to employ theoretical calculations to rationalize and assign the experimental spectra. Up to now, many theoretical schemes have been proposed and widely employed to simulate NEXAFS spectra of large systems, in particular with ab initio methods such as static-exchange [3.2], Density Functional Theory (DFT) [3.3][3.4], and Time Dependent DFT (TDDFT)[3.5][3.6]. In these approaches, the simplest way to obtain the intensity is to calculate it from electric dipole transition moments between the initial and final bound states.

On the other hand, with the continuous improvement of spectral resolution in synchrotron facilities, it is now routinely possible to identify vibrational features in NEXAFS spectra. Such vibrational fine structures are well known since long ago, with the pioneering studies of ethylene by electron yield [3.7] and by energy loss spectra [3.8]. Vibrational features present in high resolution NEXAFS have proven very useful also to gain important information on the geometrical structure of the excited state [3.9]. The theoretical description of the vibrational structure in NEXAFS has been developed by Ågren and co-workers [3.10], and is usually performed at the linear coupling level, which assumes only linear terms in the expansion of the final state potential around the equilibrium geometry of the initial state.

Closely related with NEXAFS is X-ray Photoelectron Spectroscopy (XPS), which furnishes the Binding Energies (BE) of the core electrons. BE are very sensitive to the chemical environment of the ionized atomic site, in terms of electron density (initial state effect) or relaxation (final state effect) which are the two main contributions to the BE chemical shifts and which can also be very well reproduced by ab initio [3.11] and DFT calculations [3.12]. At variance with NEXAFS, in XPS it is difficult to calculate the intensity of the primary lines since in the final ionic state the unbound photoelectron wavefunction obeys boundary conditions which are not supported by conventional basis sets employed in quantum chemistry like Gaussian or Slater functions. Therefore, if the photoelectron energy is not too low, the relative intensity among different primary lines is simply assumed to be proportional to the number of equivalent atoms of the same type.

The first photoelectron spectra which showed vibrational excitation in molecular inner shell photoionization (CH4, CO, and N2) were recorded by excitation with an Al Kα x-ray tube, and collecting the electrons with a spherical sector-type analyser [3.13], while starting in the 1990s synchrotron radiation started to be employed to study vibrational fine structure in core photoionization [3.14]. At present, the instrumental resolution is usually limited by the lifetime broadening (around 100 meV) and not by apparatus factors, so the vibrational spacing related, for example, to C-H stretching (3200 cm^{-1} corresponding to 400 meV) are accessible.

The present work consists of a combined experimental and theoretical analysis of the NEXAFS and XPS spectra of two Polycyclic Aromatic Hydrocarbons (PAH), namely phenanthrene and coronene. For these systems vibrational effects have been found to play an important role in the description of the spectra, so that a theoretical study is necessary for a robust assessment of the observed features.

In general, PAH are of concern as they are formed from incomplete combustion of a wide range of combustion sources for heating, transportation and energy production. They are believed to be hazardous to human health and to be soot precursors. However, their role in the soot formation process is not fully understood even though soot inception has a rich literature [3.15][3.16][3.17][3.18] and contributes significantly in round-table discussions [3.19].

The current European legislation provides PAH monitoring from exhaust through time-consuming sampling by condensation, washing by solvent, filtration and off-line mass spectrometric analysis. Continuous on-line measurement of PAH inside and at the exhaust of combustion systems is still challenging. This is due to the small concentrations and limited selectivity of available measurement methods. Therefore a deeper analysis of their electronic structure and spectra in gas phase may be helpful for developing new analytical methods and to understand better chemical reactions that are involved, for example, in the production of atmospheric soot.

3.2 Computational model

3.2.1 Electronic spectra

Within the dipole approximation for soft X-ray photon, the oscillator strength for excitation from the ground state (GS) $\left|\Psi_g\right\rangle$ to excited state $|\Psi_e\rangle$ is given by (atomic units used),

$$f_{g\to e} = \frac{2\Delta E_{g\to e}}{3}\left|M_{g\to e}\right|^2 \tag{3.2.1}$$

$$M_{g\to e} = \left\langle\Psi_g\middle|\hat{\mu}\middle|\Psi_e\right\rangle \tag{3.2.2}$$

Where $M_{g\to e}$ denotes the transition dipole moment with $\hat{\mu} = \sum_i r_i$ being the dipole operator. $\Delta E_{g\to e} = E_e - E_g$ is the total energy difference. According to the final-state rule [3.20][3.21][3.22][3.23]] and the sudden approximation [3.1], Eq. (3.2.1) is further approximated in a single-particle fashion and the oscillator strength is estimated in terms of two molecular orbitals (MOs) ψ_{1s} and ψ_a of the final state,

$$f_{g\to e} = \frac{2\Delta\varepsilon_{1s\to a}}{3}|\langle\psi_{1s}(1)|r_1|\psi_a(1)\rangle|^2 \tag{3.2.3}$$

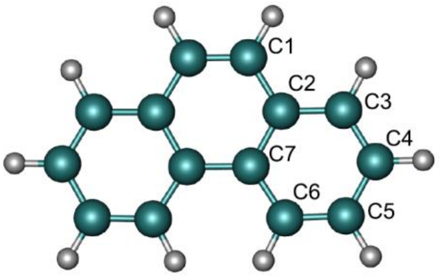

Phenanthrene ($C_{14}H_{10}$)

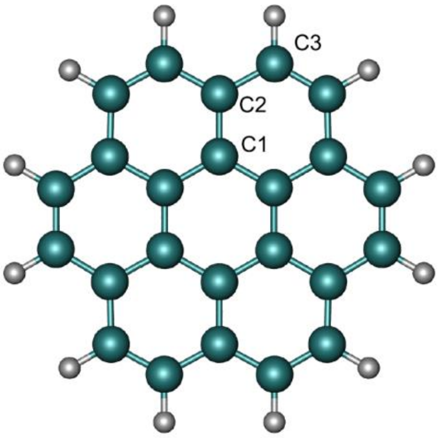

Coronene ($C_{24}H_{12}$)

Figure 3.1 *Schematic illustration of phenanthrene and coronene with nonequivalent carbon atoms labeled.*

Where $\Delta\varepsilon_{1s\rightarrow a} = \varepsilon_a - \varepsilon_{1s}$ denotes the orbital energy difference. Structures of all hydrocarbons are first relaxed at the density functional theory (DFT) level with the B3LYP functional [3.24][3.25][3.26] and the 6-311G** basis set by using the Gaussian 09 package [3.27]. The C1s NEXAFS spectra are then computed at the spin-restricted DFT level with the BP86 functional [3.24][3.28] by a locally modified version of the ADF program [3.29][3.30][3.31]. The core hole at each non-equivalent carbon center is modeled by the half core hole (HCH, also referred as the transition potential) approximation [3.4]. Taking phenanthrene (**Figure 3.1**) as an example, the influence of DFT functionals and core hole methods have been verified, employing two functionals (BP86 and B3LYP) in conjunction with two approximations [HCH and the full core hole (FCH)].

The basis functions employed consist of Slater Type Orbitals (STO). A very extended basis set is chosen for the core-excited carbon atom, consisting of an even tempered Quadruple Zeta with 3 polarization and 3 diffuse functions (designated as ET-QZ3P-3DIFFUSE in the ADF database) while the DZP basis set has been employed for the remaining ones. No symmetry is enforced. Fine integration grid of 5.0 is used. The raw spectra are calibrated by aligning the first transition energy $\Delta\varepsilon_{1s\rightarrow LUMO}$ (LUMO: lowest unoccupied MO) to that obtained from the ΔKohn-Sham (ΔKS) scheme [3.32][3.33], as difference between the total energy of the excited state $\left(E_{e_1}\right)$ and the total energy of the GS (E_g): $\Delta E_{g\rightarrow e_1} = E_{e_1} - E_g$. In order to get a pure singlet first core-excited state, E_{e_1} is computed as [3.34]

$$E_{e_1} = 2E(|1s\alpha^1 \dots LUMO\beta^1|) - E(|1s\alpha^1 \dots LUMO\alpha^1|) \tag{3.2.4}$$

Here $E(|1s\alpha^1 \dots LUMO\beta^1|)$ and $E(|1s\alpha^1 \dots LUMO\alpha^1|)$ denote the total energies of two spin-polarized single-determinants with unpaired electrons in the 1s and LUMO orbitals (antiparallel and parallel, respectively). In addition, we also calculate the core ionization potential (IP) in the following way:

$$IP_{1s} = E(|1s\alpha^1 \dots |) - E_g \tag{3.2.5}$$

where $E(|1s\alpha^1 \dots |)$ represents the total energy of a spin-polarized FCH state.

The NEXAFS transition energies and IPs reported in **Figure 3.3** and **Figure 3.4** are further shifted by +0.2 eV to account for the relativistic effects [3.4]. The stick spectra are broadened by using a Gaussian lineshape $\Phi(\omega; \Delta\varepsilon_{1s\rightarrow a}, \gamma)$ with half-width-at-half-maximum (hwhm) γ = 0.1 eV. Finally, the atom-specific spectrum of each nonequivalent carbon center is weighted by their relative abundance and summed to get the total spectrum.

The simulation of the XPS spectra reported in **Figure 3.7** and **Figure 3.8** has been performed calculating the BE at ΔSCF level with Eq. (3.2.5), employing the BP86 functional and a TZ2P basis set without any energy shift. As stated in the introduction, it is rather difficult to calculate the intensity of the XPS lines since the unbound photoelectron wavefunction should be employed in the dipole transition moment. Therefore we simply assumed that the intensity of each C1s line is proportional to the number of equivalent carbon atoms. For a better comparison with the experiment, each line has been broadened with a Gaussian function with FWHM = 150 meV, in line with experimental resolution.

3.2.2 Vibrational Structure

Vibrational structure is studied for both phenanthrene ($C_{14}H_{10}$) and coronene ($C_{24}H_{10}$) (**Figure 3.1**). They have a C_{2v}/D_{6h} symmetry in the ground state respectively and contain totally 7/3 non-equivalent carbons. Vibrational frequencies are first computed at the same level as for geometrical optimization by using Gaussian 09. Then the vibrationally-resolved C1s NEXAFS spectra are computed within the Condon approximation and the linear coupling model (LCM) [3.35] by using our Dynavib package [3.36]. The absorption cross section at photon energy ω is given by:

$$\sigma_{abs}(\omega) = \sum_{N}\sum_{e}\left[f_{g\to e}\sum_{n}\Big(\langle 0|n\rangle^{2}\Phi\big(\omega;\Delta E_{g0\to en},\gamma\big)\Big)\right] \tag{3.2.6}$$

Here N represents the summation over all carbon centers, e is the summation over electronic excited states. $\Delta E_{g0\to en} = \Delta E_{g\to e} + \sum_k n_k \nu_k$ denotes the energy difference between the excited state $|e,n\rangle$ and the ground state $|g,0\rangle$, where k denotes the index of normal mode, n_k is the vibrational quantum number and ν_k the vibrational frequency (the same frequency is assumed for the ground and core-excited states within the LCM model). $\langle 0|n\rangle = \prod_k \langle 0|n_k\rangle$ stands for the nuclear overlap integral (also often referred as the Frank-Condon (FC) amplitude) with the integral of each mode given by [3.37]:

$$\langle 0|n_k\rangle = \frac{(-1)^{n_k}}{\sqrt{n_k!}} exp\left(-\frac{S_k}{2}\right) S_k^{n_k/2} \tag{3.2.7}$$

$$S_k = \frac{1}{2}\nu_k d_k^2 \tag{3.2.8}$$

Here S_k is the Huang-Rhys factor and d_k the displacement of the two sets of normal coordinates. d_k's are computed numerically by fitting the core-excited Potential Energy Surfaces (PESs) to quadratic equation [3.38][3.39]

$$U(Q_k) = \frac{1}{2} a_k (Q_k - d_k)^2 + b_k \tag{3.2.9}$$

The advantage of such a procedure is that it allows us to validate the harmonicity of the PESs. Five different structures shifted by 0, $\pm\delta_k$ and $\pm 2\delta_k$ in the direction of the GS normal coordinates are sampled. Different δ_k (between 0.1 and 4.0a.u.) are employed for different vibrational modes aiming to get a balance between the numerical accuracy (requiring larger δ_k) and the harmonicity of the oscillator (requiring smaller δ_k). γ in Eq. (3.2.6) is set to 0.05 eV to broaden the stick spectra. Other alternative schemes to calculate the displacements from numerical or analytical gradients are given in, e.g., Refs [3.37][3.40][3.41][3.42]

3.3 Experimental setup

The core-level photoelectron spectroscopy measurements were performed at the GAs PHase (GAPH) beamline of the Elettra synchrotron, in Trieste [3.43]. The electron spectrometer used to obtain the spectra has been described in detail in Ref. [3.44]. Briefly, it consists of a four-element electrostatic lens system and a VG 150 mm hemispherical electrostatic analyzer, equipped with six channel electron multipliers. The analyzer was mounted at 54.7◦ with respect to the electric vector of the linearly polarized light, making the measurements insensitive to the β asymmetry parameter.

Samples were purchased from Fluka, with declared 95% minimum purity (phenanthrene) and from Sigma-Aldrich, with declared minimum purity of 99% (coronene), and introduced in experimental chamber without further purification. Samples were sublimated using a custom built resistively heated furnace, based on a stainless steel crucible, a Thermocoax® heating element and a type K thermocouple. The evaporation temperature for phenanthrene was 45 ◦C, while for coronene it was about 180–190 ◦C. During the experiment the quality of vaporization was monitored by measuring the valence photoelectron spectrum of the heated sample at 120 eV photon energy and by comparing it with the reference He(I) photoelectron spectra known from literature [3.45][3.46][3.47][3.48]. During the whole experiment, the pressure in the ionization region remained constant and no evidence of contamination or thermal decomposition was found.

The Core-level photoelectron spectrum of phenanthrene was measured with a total resolution (photon + analyzer) of 100 meV at 338 eV photon energy. For coronene, the carbon 1s photoelectron spectrum was recorded at the photon energy of 353 eV, with an overall experimental resolution of 150 meV. The binding energy scale of the C 1s photoelectron spectra was calibrated by admitting into the ionization chamber a small amount of CO_2 whose C1s BE is 297.7 eV [3.49].

The photoabsorption spectra at the C K-edges of the two samples were acquired by measuring the total ion yield with a channel electron multiplier placed near the ionization region, with a photon energy resolution of 50 meV. Spectra were calibrated using CO_2 as calibration gas [3.50][3.51].

3.4 Results and discussion

3.4.1 Influence of the DFT functionals and the core hole methods for NEXAFS

Figure 3.2 shows the C1s NEXAFS spectra of phenanthrene measured in the gas phase and calculated with different methods. The theoretical spectra roughly reproduce the main features of experiment but differ in details. In order to have a key for the interpretation of the spectra, it is very useful to give a brief description of the virtual molecular orbitals involved in the dipole allowed core electron excitations. As expected, at lower energy only empty π^* orbitals are found, more precisely all the four spectral features up to 287 eV in the calculated BP86-HCH spectrum are ascribed to empty π^* orbitals. In particular the first two features (denoted by the letters a and b in the experiment) both correspond to $C1s \rightarrow LUMO$ transitions, peak a from $C1s$ belonging to carbon atoms directly bound to H atoms (C1, C3, C4, C5, and C6), while peak b comes from C1s belonging to carbon atoms which are not bound to H (C2 and C7). The next feature at 286 eV in the BP86-HCH spectrum is ascribed to $C1s \rightarrow LUMO + 2$ transitions (experimental peak c) and the next one at 286.7 eV (experimental peak d) to $C1s \rightarrow LUMO + 4$ transitions. Only beyond this point (starting with LUMO + 5), the σ^* orbitals start to play a role in the absorption spectrum. It is interesting to observe that the LUMO + 1 orbital always has a very low C2p contribution on the C1s excitation site, therefore we do not find any line of appreciable intensity ascribable to transitions to the LUMO + 1 orbital.

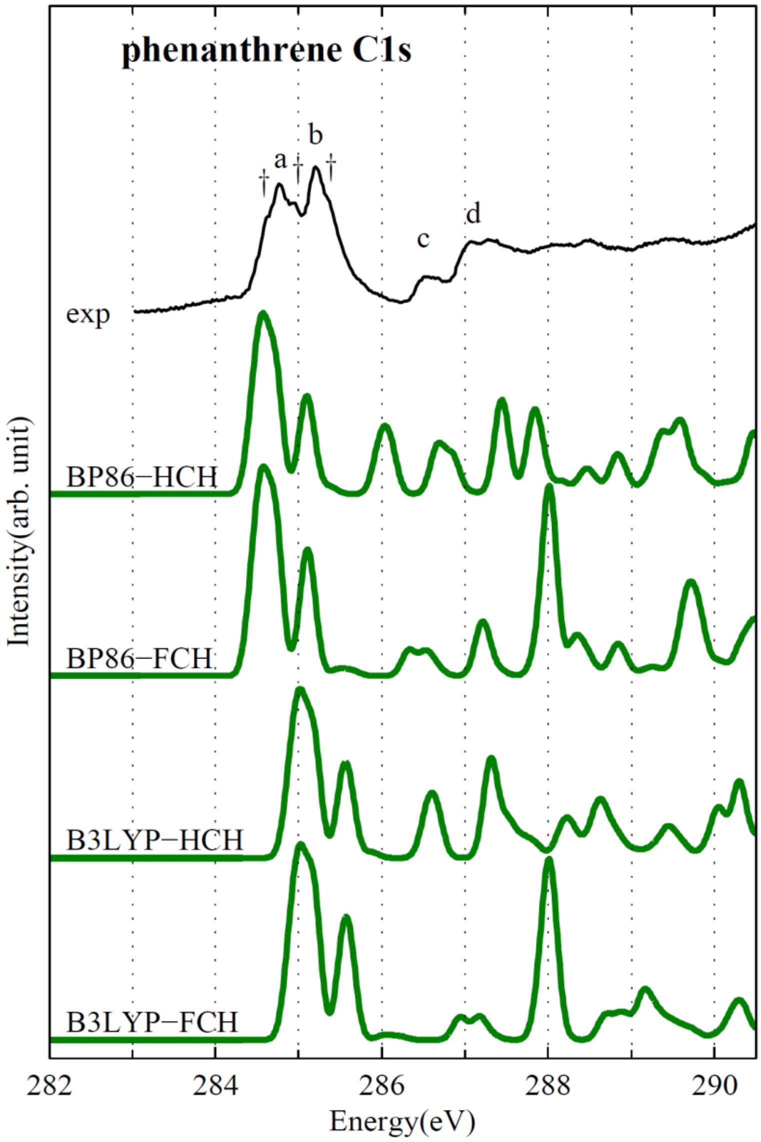

Figure 3.2 *Phenanthrene C1s NEXAFS spectra. Top: Experimental result (black line) with main features labelled. Middle: Calculated total electronic spectra (green lines) by using the B3LYP and BP86 DFT functionals as well as the FCH and HCH models. The calculated 1s ionization potentials of all carbons are around 290 eV.*

In the experimental curve, the two peaks a (284.8 eV) and b (285.2 eV) ($C1s \rightarrow LUMO\ \pi^*$) have almost identical intensities and additionally contain two (284.6 and 285.0 eV) or one (285.4 eV) shoulders, respectively (shoulders labelled by daggers). In the region beyond, the two peaks c and d appear at 286.5 and 287.1 eV, respectively. On the other hand, all theoretical spectra also produce two $C1s \rightarrow LUMO\ \pi^*$ peaks but with different intensity ratios: the peak b at a higher energy is always much weaker than peak a. Shoulder structures are also lost. FCH and HCH methods present similar spectra in the C1s→LUMO π^* region but differ in the $C1s \rightarrow LUMO + 2\ \ \pi^*$ and $C1s \rightarrow (LUMO + 3)\ \pi^*$ regions. The spectra are less sensitive to different DFT functionals, in agreement with previous findings in other systems [3.52][3.53]. In summary the disagreement between theory and experiment cannot be removed by changing the DFT exchange-correlation energy functional or the core-hole scheme. This suggests that such disagreement is not related to a deficiency in the description of the electronic structure but rather to effects not included in the computational model, such as those related to the nuclear motion.

3.4.2 Vibrational effects in NEXAFS

Incorporation of the vibronic coupling al LCM level in the BP86-HCH electronic spectrum significantly improves the theoretical photoabsorption of phenanthrene and bridges the gap with experiment, as illustrated in **Figure 3.3**. Not only does the intensity ratio of the $C1s \rightarrow LUMO\ \pi^*$ features a and b agree well with the experiment, but the three shoulder fine-structures (labelled by daggers) are also clearly reproduced with almost the same absolute transition energies. Results show that the vibronic coupling plays an important role for core-hole excitations of this molecule. Furthermore, the atomic-specific spectra show that the first two $\pi*$ peaks originate from the $C1s \rightarrow LUMO$ electronic transitions: more precisely, C2 and C7 contribute to peak b (as already found in the pure electronic spectra) and the remaining carbon atoms to peak a. Although Frank-Condon vibrational progressions are dominated by the 0-0 transitions, the 0-1 and 0-2 transitions (and even 0-3 transitions for some carbons) also have significant contributions which leads to the redistribution of the oscillator strengths and tends to average the intensity of the two $C1s \rightarrow LUMO\ \pi^*$ peaks. The vibronic coupling also shows considerable effects in the $C1s \rightarrow LUMO + 2$ and $C1s \rightarrow LUMO + 3$ regions. The peaks c and d are also better reproduced except a red shift of 0.2–0.5 eV.

Figure 3.4 shows the C1s NEXAFS spectra of coronene measured in the gas phase and calculated with and without vibronic coupling. In the experimental profile two $C1s \rightarrow LUMO\ \pi^*$ peaks a and b appear at 284.5 and 285.2 eV, respectively, where the latter displays a much stronger intensity. Similarly to phenanthrene, the calculated electronic spectra do not reproduce properly the intensity ratio between the two $C1s \rightarrow LUMO\ \pi^*$ peaks a and b of the experiment. Such a discrepancy is effectively reduced when the vibronic coupling is turned on. Also in this case the peak a is ascribed to the $C1s \rightarrow LUMO$ transition from the C atom bound to H (C3), while peak b is ascribed to the $C1s \rightarrow LUMO$ excitation from the C atom not bound to H (C1 and C2). This finding shows that very tiny inductive effects (like the electron donation of H) produce energy shifts on C1s excitation energies which are important for a proper assessment of the spectrum.

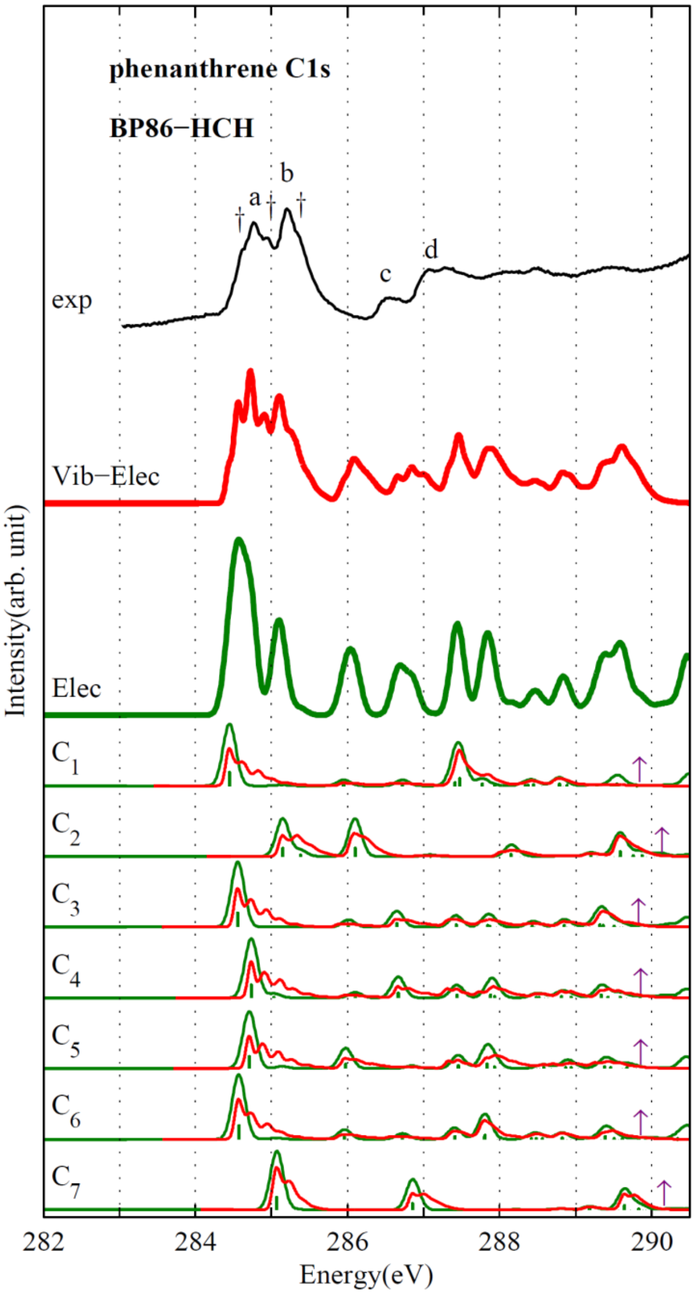

Figure 3.3 *Phenanthrene C1s NEXAFS spectra. Top: Experimental result (black line) with main features labelled. Middle: Calculated total spectra with (red) and without (green) considering the vibronic coupling. Bottom: Atomspecific contributions of each non-equivalent carbon with (red) and without (green) the vibronic coupling. IP positions are denoted by arrows. Theoretical spectra are calculated with the BP86-HCH method.*

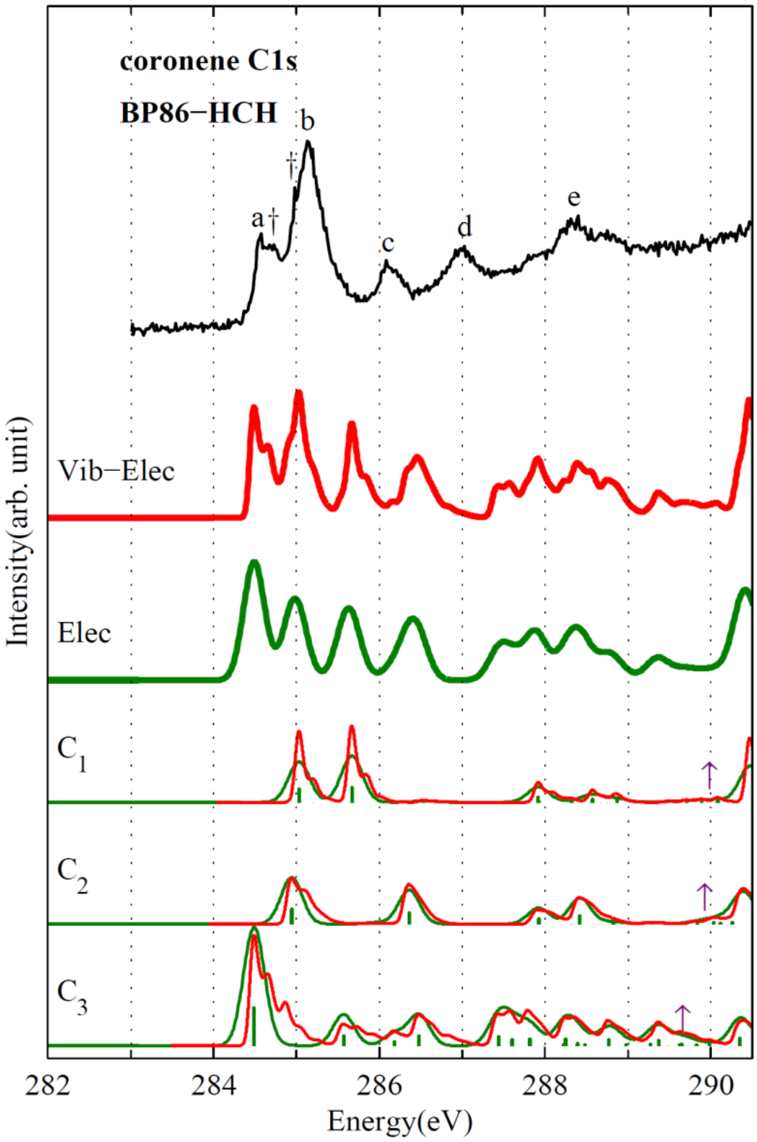

Figure 3.4 *The same as in Fig. 3 for coronene. Here the sticks and curves denoted by "C1," "C2," "C3" have already included the weights (6:6:12) of non-equivalent atoms.*

The vibronic coupling is also responsible for the two shoulder structures at ∼284.7 and 285.0 eV, respectively (daggers). In the higher energy region, theory reproduces the three peaks c, d, e except for a red shift of ∼0.4 eV in energy.

From the analysis of the virtual orbitals involved in the excitations, experimental peak c is assigned to $C1s \rightarrow (LUMO + 2)\ \pi^*$ transitions and the next peak d to $C1s \rightarrow$

$(LUMO + 4)$ π^* and $C1s \rightarrow (LUMO + 5)$ π^* transitions. Beyond this point (starting with peak e and with LUMO + 6), the σ^* orbitals start to play a role in the absorption spectrum. It is interesting to observe that the LUMO + 2 and LUMO + 4 orbitals always have a very low C2p contribution on the C1s excitation site, therefore we do not find any lines of appreciable intensity ascribable to transitions to the these two orbitals.

To further understand the individual modes that govern the vibronic coupling effects in phenanthrene and coronene, we take the 1s → LUMO transition of each carbon as an example, and analyze mode-specific contributions. In **Figure 3.5**, the vibronic coupling strength $\left(\lambda_k \equiv \sqrt{S_k}\right)$ of each mode k is visualized versus the corresponding vibrational frequency. The number of modes that make considerable contributions (with a threshold of $\lambda_k \geq 0.1$) vary among different carbon sites, and range from 14–34 (17–27) for coronene (phenanthrene) out of the total number of 102 (66). All these modes correspond to in-plane vibrations. For each carbon excitation, a wide frequency range and different mode types are covered. For instance, in coronene, 34 modes make considerable contributions to the first core-excited state of C3. They cover from the low-frequency fingerprint modes of ~400 cm^{-1} to the C-H stretching of ~3200 cm^{-1}; selected vibrational modes among these 34 ones are also illustrated in **Figure 3.6**.

3.4.3 XPS

In **Figure 3.7** and **Table 3.1** the experimental C1s XPS of phenanthrene is reported, together with a simulation produced using the calculated BE and assuming intensity proportional to the multiplicity of the carbon atom, in the present case seven atoms have all the same multiplicity of 2. From the calculation, it is possible to define two different groups of carbon atoms: the first one give rise to lines at lower binding energy and statistical weight equal to 10, which correspond to external carbons bound to hydrogen atoms, while the second group of carbons are those not bound to any hydrogen atom and give rise to lines at higher binding energy and statistical weight equal to 4. So, theoretical statistical ratio is equal to 5/2 = 2.5 and the energy difference between the

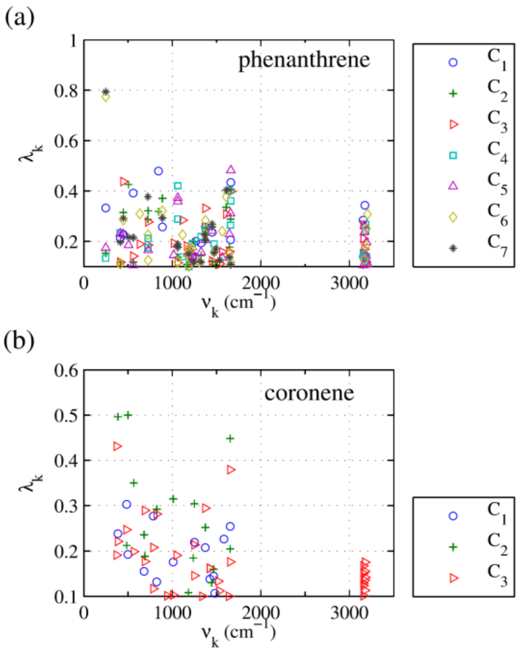

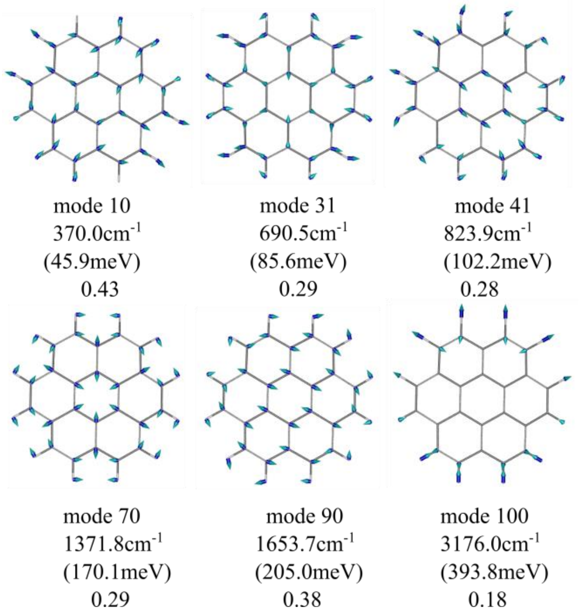

***Figure* 3.5** *left: Normal mode analysis of the first core-excited state of each nonequivalent carbon for (a) phenanthrene and (b) coronene: vibronic coupling strengths λ_k versus the corresponding vibrational frequencies ν_k. For each electronic state, only those modes with considerable contributions (with a threshold of $\lambda_k \geq 0.1$) are plotted.*

***Figure* 3.6** *right: Selected normal modes of coronene that have considerable vibronic coupling effect to the first core-excited state of C3. Vibrational frequencies (in cm^{-1}) and corresponding vibronic coupling strengths are also listed below each mode index. Cartoons have been generated by Gabedit [3.55].*

two groups is around 0.26 eV. The features of the C 1s experimental spectrum have been fitted by fixed Voigt functions with the Gaussian component of FWHM = 100 meV, for the photon energy of 338 eV, and Lorentzian component of FWHM = 95 meV. The energies and intensities were allowed to change freely in the fit. In **Table 3.1** and **Table 3.2** experimental relative energies are given with three decimal digits, while only one decimal digit is given for the absolute energy of the lowest peak, in order to be consistent with the accuracy of the calibration energy (that is ±0.1 eV).

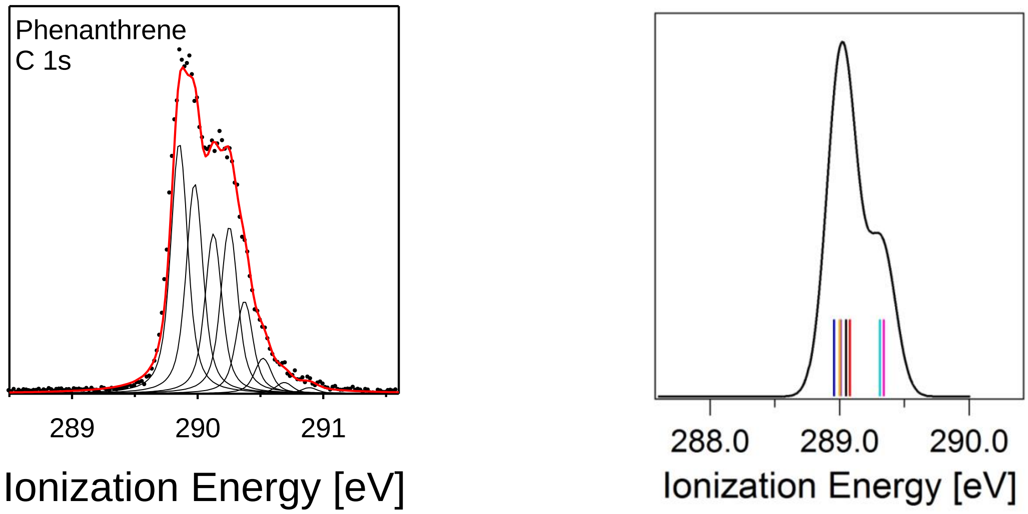

Figure 3.7 *Phenanthrene C1s XPS spectra. Left: Experimental data and results of the fitting procedure. Peak numbers 1–8, running from left to right, are referred to in* ***Table 3.1*** *Right: Simulated spectra taking one line for each BE calculated at the ΔKS level (BP86 functional and TZ2P basis set) with intensity proportional to multiplicity of C atom.*

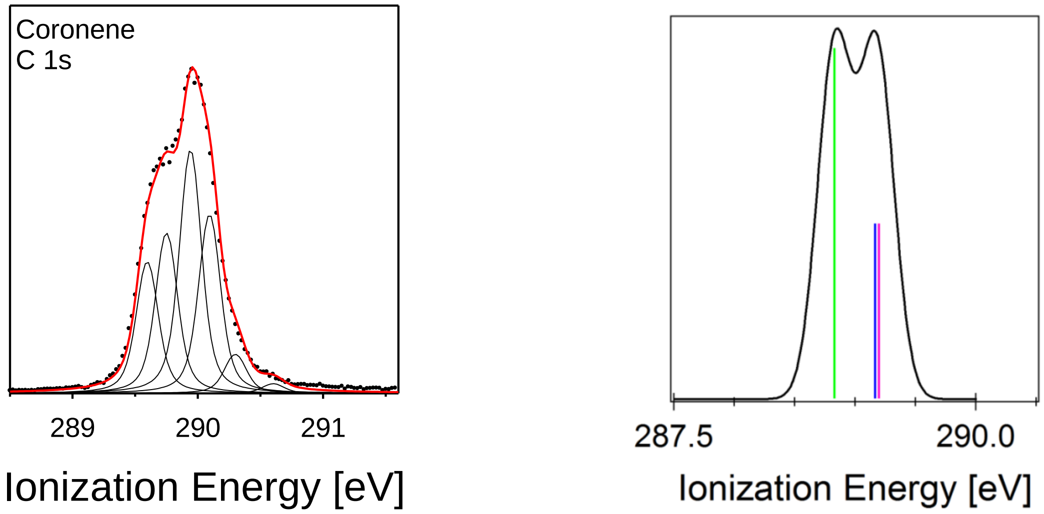

Figure 3.8 *Coronene C1s XPS spectra. Left: Experimental data and results of the fitting procedure. Peak numbers 1–6, running from left to right, are referred to in* ***Table 3.2****. Right: Simulated spectra taking one line for each BE calculated at the ΔKS level (BP86 functional and TZ2P basis set) with intensity proportional to multiplicity of C atom.*

Carbon site	Calculated BE (eV)	Relative weight
C1	289.29	2
C3	289.30	2
C6	289.31	2
C5	289.33	2
C4	289.33	2
C2	289.57	2
C7	289.57	2

Peak	Experimental BE (eV)	Assignment
1	0 (289.9)	C_{I} (= C1,C3-C6) 1s
2	+0.122	C_{I} 1s + vib(C-C)
3	+0.272	C_{II} (=C2,C7) 1s
4	+0.398	C_{I} 1s +vib(C-H), C_{II} 1s + vib(C-C)
5	+0.519	C_{I} 1s +vib(C-C)+vib(C-H)
6	+0.667	C_{II} 1s +vib(C-H)
7	+0.84	
8	+1.04	

Table 3.1 *Calculated (upper data, TZ2P basis set) BE with corresponding carbon site and relative weight. Experimental (lower data) relative BE with respect to the lowest peak (absolute energy in parentheses) from deconvolution of experimental data for phenanthrene and tentative assignment.*

Carbon site	Calculated BE (eV)	Relative weight
C3	289.02	12
C2	289.26	6
C1	289.30	6

Peak	Experimental BE (eV)	Assignment
1	0 (289.6)	C_{I} (= C3) 1s
2	+0.154	C_{I} 1s + vib(C-C)
3	+0.345	C_{II} (=C1,C2) 1s
4	+0.497	C_{II} 1s + vib(C-C)
5	+0.70	
6	+1.01	

Table 3.2 *Calculated (upper data, TZ2P basis set) BE with corresponding carbon site and relative weight. Experimental (lower data) relative BE with respect to the lowest peak (absolute energy in parentheses) from deconvolution of experimental data for coronene and tentative assignment.*

In order to give an interpretation of the phenanthrene XPS, it is useful to recall briefly the analysis of Myrseth et al. on C1s XPS of C6H6 [3.54], whose vibrational structure may be expected, to some extent, to resemble those of phenanthrene and coronene. In C_6H_6 it was found that the adiabatic primary line was followed by a manifold of rather strong vibrational states, the intensity of the strongest line being the 48% of the adiabatic line, in the energy range 125–150 meV, ascribed to C-C stretching and CCH bending modes. Then a rather intense line was predicted around 264 meV ascribed to an overtone transition relative to a C-C stretching and CCH bending mode.

Finally at 417 meV the C-H stretching was found. With this scheme in mind, we consider the Voigt fit of the phenanthrene spectrum (**Figure 3.7**) which gives an energy difference of 122 meV between peaks 1 and 2. Peak 2 should therefore be assigned to a vibrational excitation (probably a mostly C-C stretch-like vibration). The energy difference between peaks 1 and 3, on the other hand, was fitted to be 0.27 eV, which is very close to the splitting calculated (0.26 eV) between the groups (C2, C7) and all the other C atoms. Peak 4 should then be a combination of C-H stretch vibration related to peak 1 (about 400 meV) and a lower energy vibration ascribed to C-C stretching (about 120 meV) of the peak 3. Peak 5 could be a composite vibration of C-H stretch (~400 meV) + the lower energy vibration (~120 meV) related to peak 1. Peak 6 may tentatively be attributed to the C-H stretch related to the atoms C2, C7 (i.e., to peak 3).

For coronene, the experimental XPS spectrum fitted with Voigt curves performed over the experimental data points together with the calculated results are shown in **Figure 3.8** and **Table 3.2**. In this case, fixed Voigt functions with the Gaussian component of FWHM = 150 meV for the photon energy of 353 eV and Lorentzian component of FWHM = 99 meV have been employed. The energies and intensities were allowed to change freely in the fit.

The interpretation of the C1 PES of coronene is less clear than that of phenanthrene, which may also be due to the worse experimental resolution. A tentative assignment is given in the following; it should be taken with caution. Peak 1 is due to the adiabatic transition from the C3 atoms (weight 12); this assumption is based on present calculations. The most intense peak 3 should then be the analogous transition for the C1 and C2 atoms, giving the splitting of 0.345 eV between C3 and (C1, C2), which is slightly larger than the calculated splitting (~0.26 eV). The energy difference between peaks 1 and 2 is ~154 meV, which is larger than in phenanthrene but could still be due to similar vibrations (mostly C-C stretch). This would also mean that the intensity of the vibrational line (peak 2) is larger than the vibrationless transition (peak 1): a different behaviour with respect to benzene which could suggest a strong structural relaxation of coronene upon core hole formation. The difference between the peaks 3 and 4 is again about 150 meV, attributable to the C-C stretch-like vibrations. The intensity of the C-H vibrations may be smaller than in phenanthrene, this is not surprising since there are proportionally less C-H bonds than C-C bonds in coronene than in phenanthrene.

3.5 Conclusion

We have carried out a combined experimental and theoretical study of C1s NEXAFS and XPS spectra of phenanthrene and coronene in the gas phase. Vibrationally resolved spectra are calculated for phenanthrene and coronene within the Condon approximation and the linear coupling model. When the vibrational effects are included in the calculations, a good agreement between theory and experiment is obtained. In both molecules, strong vibronic coupling is responsible for the peak intensity redistribution among the two main π^* peaks and the shoulder structures. Only in-plane vibrational modes make effective contributions. For the out-of-plane modes, the potential energy surfaces of the ground and core-excited states have almost no displacement. Our high-resolution study offers an in-depth understanding of the electronic structure of the PAHs as well as the interplay of the electronic and vibrational transitions.

In XPS it is possible to discriminate the different carbon sites according to whether they are bound to hydrogen or not. In fact carbons bound to hydrogen have lower BE and displays a chemical shift of about 0.3–0.4 eV with respect to C not bound to hydrogen, which can be resolved by the experiment and are nicely reproduced by theory. The inclusion of vibrational structures is mandatory to properly fit the experimental spectral shape. Low energy vibrations in the range of 120–150 meV appear particularly strongly excited – they are probably mostly due to C-C vibrations – whereas C-H stretching modes are less intense.

4 Experimental and theoretical NEXAFS and XPS spectra for Thiophene, Bithiophene and Terthiophene

4.1 Introduction

Five-membered heterocyclic compounds show promising technological applications especially for their high electrical conductivity, environmental stability, and redox properties which make them good organic electronic systems for electronic devices [4.1][4.2][4.3]. Although inorganic materials are more popular for such applications, organic electronics are more attractive for their lightweight, low cost manufacture, ease of synthesis and mechanically flexibility [4.4].

Oligomers consist of covalently linked monomer units giving small chain length polymers which are highly appealing because of further potential applications in electronic and optoelectronic devices. These have been extensively studied in order to provide insights of the more complex polythiophene systems' properties. In particular, there is a considerable interest in the basic electronic structure of thiophene-based oligomers since these have been demonstrated to be among the most active components on optoelectronics due to their charge generating and charge transporting properties [4.5]. As a consequence, they have been widely used in photovoltaic cells, light-emitting diodes and field-effect transistors. The extent of their charge delocalization depends either on the size of the overlap between the π orbitals of neighbouring carbon atoms or any hindrance to this conjugation which can affect the properties. With this regard, thiophene-based polymers have received a great deal of attention because of their highly π-conjugated bonding systems, chemical stability and tunable electronic properties [4.6][4.7]. The band gap of a polymer is one of the most important features which can enhance the efficiency of optoelectronic devices. For instance, molecular conductivity depends on the HOMO-LUMO band gap and this value is determined by factors such as the polymer substituents, the torsion angles among species and the length of conjugation of the chain. So far, thiophene-based oligomers and polymers have been considered in many theoretical studies [4.8]-[4.12], due to their chemical stability and large number of already available experimental data.

The gas phase electronic structure of thiophene (T), 2,2'-bithiophene (2T) and 2,2′:5′,2″-terthiophene (3T), which represent, respectively, the monomer, dimer and trimer of polythiophene, have been here characterized. The chemical structures of these three molecules (**Figure 4.1**) has been therefore reported. In particular X-ray Photoelectron Spectroscopy (XPS) at the C1s core-level and valence band (VB) spectra together with X-ray Absorption Near Edge Structure (XANES) at the carbon K-edge have been performed together with theoretical calculations of their most stable computed conformation.

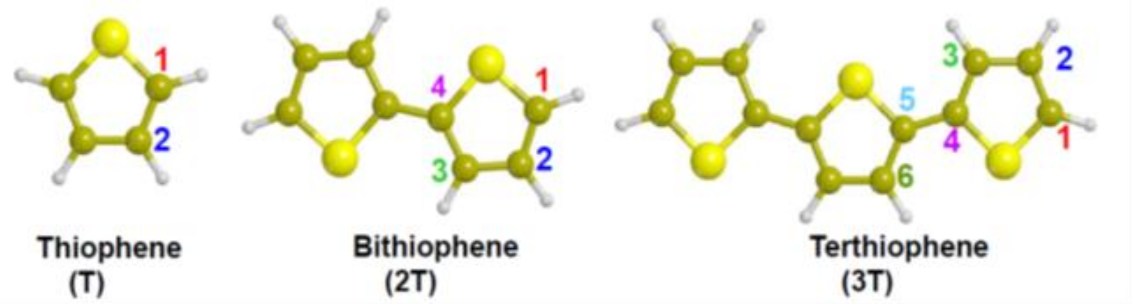

Figure 4.1 *Schematic illustration of thiophene (T), bithiophene (2T) and terthiophene with nonequivalent carbon atoms labeled.*

4.2 Experimental section

The photoemission measurements on the gas-phase sample were performed at the GAs-PHase (GAPH) beamline of the Elettra synchrotron in Trieste [4.13] and 2T are liquid at room temperature and after several freeze-pump-thaw cycles of purification they were inserted in vacuum and dosed via a stainless steel variable leak valve. 3T sample was sublimated in vacuum using a custom built resistively heated furnace after a purification treatment at 30°C for 12 hours. Electron spectra were measured using a Scienta SES-200 electron analyzer [4.14], mounted at 54.7 deg with respect to the electric vector of the linearly polarized incident light, and in the same plane as the beam propagation direction. In this geometry the electron analyzer is set at the (pseudo) magic angle, so measurements are almost insensitive to the photoelectron asymmetry parameter. XANES spectra at the C K-edge were acquired by measuring the total ion yield (TIY) with an electron multiplier placed near the ionization region. The photon flux was measured simultaneously with a calibrated Si photodiode for the spectra normalization. The energy scale of the spectra was calibrated by taking simultaneous spectra of the samples and of CO2, with the characteristic transition at 290.77 eV (C 1s $\rightarrow \pi^*$, CO2) [4.15][4.16]. The photon energy resolution was 70 meV. 1T and 2T are liquid at room temperature and after several freeze-pump-thaw cycles of purification they were inserted in vacuum and dosed via a stainless steel variable leak valve. 3T sample was sublimated in vacuum using a custom built resistively heated furnace set at T=66° degrees after a purification treatment at 30°C for 12 hours.

4.3 Computational details

The geometrical structures of thiophene, bithiophene and terthiophene have been optimized at the density functional theory (DFT) level whit the LDA VWN functional [4.1] and the Triple Zeta Polarized (TZP) basis set of Slater type orbitals (STO) by the using ADF package [4.18][4.19][4.20]. Bithiophene and terthiophene have been considered in the *all-trans* conformations with a planar structure (with C_{2h} and C_{2V} symmetry in the GS, respectively).

The C1s NEXAFS spectra have been then calculated at the spin-restricted DFT level with the GGA PW86xPerdew functional [4.21] by the ADF program. The core hole at each non-equivalent carbon center is modeled by the half core hole (HCH) also referred as the Transition Potential (TP) approximation [4.22]. In the TP computational technique half an electron is removed from the 1s orbital of the excited C atom, relaxing all the orbitals until self-consistency is obtained. This scheme includes most of the relaxation effects following the core hole formation and provides a single set of orthogonal orbitals useful for the calculation of the transition moments. The basis functions employed in the DFT-TP calculations consist of a very extended STO set for the core-excited carbon atom, in particular an even tempered Quadruple Zeta with three polarization and three diffuse functions (designed as ET-QZ3P-3DIFFUSE set in the ADF database), while the TZP basis set has been employed for the remaining atoms. Symmetry is properly reduced allowing core-hole localization.

The raw spectra are so calculated: the excitation energies are obtained as the differences between the eigenvalue of the virtual orbital and that of the 1s orbital calculated with TP configuration:

$$\Delta\varepsilon_{1s\to a} = \varepsilon_a - \varepsilon_{1s} \tag{4.3.1}$$

The excitation intensity is calculated with the oscillator strength that, within the dipole approximation, for excitation from the ground state (GS) $|\Psi_g\rangle$ to excited state $|\Psi_e\rangle$, is given by (atomic units used),

$$f_{g\to e} = \frac{2\Delta E_{g\to e}}{3}\left|M_{g\to e}\right|^2 \tag{4.3.2}$$

$$M_{g\to e} = \langle\Psi_g|\hat{\mu}|\Psi_e\rangle \tag{4.3.3}$$

where $M_{g\to e}$ is the transition dipole moment with $\hat{\mu} = \sum_i r_i$ being the dipole operator, and $\Delta E_{g\to e} = E_e - E_g$ is the total energy difference. Taking into account the final-state rule [4.23][4.24] and the sudden approximation [4.25], Equation(4.3.2) can be formulated at one-electron level, so that the oscillator strength is evaluated in terms of two molecular orbitals (MOs) ψ_{1s}(core) and ψ_a of the final state, obtained with the DFT-TP scheme:

$$f_{g\to e} = \frac{2\Delta\varepsilon_{1s\to a}}{3} |\langle\psi_{1s}(1)|r_1|\psi_a(1)\rangle|^2 \tag{4.3.4}$$

The TP approach leads to a less attractive potential and the absolute transition energies are generally too large. In order to correct the NEXAFS energies, the raw spectra are calibrated by aligning the first transition energy $\Delta\varepsilon_{1s\to LUMO}$ (LUMO: lowest unoccupied MO) to that obtained from ΔKohn-Sham (ΔKS) scheme [4.26], as difference between the total energy of the excited state (E_{e_1}) and the total energy of the ground state(E_g): $\Delta E_{g\to e_1} = E_{e_1} - E_g$. In order to get a pure singlet first core excited state, E_{e_1} is calculated as [4.26]:

$$E_{e_1} = 2E(|1s\alpha^1 \dots LUMO\beta^1|) - E(|1s\alpha^1 \dots LUMO\alpha^1|) \tag{4.3.5}$$

where $E(|1s\alpha^1 \dots LUMO\beta^1|)$ and $E(|1s\alpha^1 \dots LUMO\alpha^1|)$ are the total energies of two spin-polarized single-determinants with unpaired electrons in the 1s and LUMO orbitals (antiparallel and parallel, respectively). Moreover, the core Ionization Potential (IP) is determined in the following way:

$$IP_{1s} = E(|1s\alpha^1 \dots |) - E_g \tag{4.3.6}$$

Where $E(|1s\alpha^1 \dots |)$ represents the total energy of a spin-polarized Full Core-Hole(FCH) state.

The excitation spectrum at each non-equivalent Carbon site of the molecule is obtained as a single calculation, then it is weighted by relative abundance and finally the total C1s NEXAFS spectrum is obtained by summing up the different contributions. In order to facilitate the comparison with the experiment, the raw spectra have been broadened by using a Gaussian lineshape with Full-Width-at-Half-Maximum (FWHM) of 0.4eV for thiophene and terthiophene and of 0.3eV for bithiophene.

4.4 Results and discussion

4.4.1 C1s NEXAFS

The thiophene (T), bithiophene (2T) and terthiophene (3T) molecules are shown schematically in **Figure 4.1** with our labeling of the non equivalent C atoms.

Peak	Site	E (eV)	fx10^2	Assignment
A	C1	285.64	5.86	LUMO (1π*)
	C2	285.65	3.50	
B	C1	286.93	3.12	σ*(S-C)
	C2	287.11	4.73	2π*(C=C)
C	C1	287.73	0.89	2π*(C=C)
	C2	287.88	0.97	Rydberg
	C1	288.13	0.79	
D	C2	288.53	1.15	Rydberg + σ*(CH)
	C1	288.68	2.17	
	C1	288.84	1.05	

***Table 4.1** Calculated excitation energies (eV) and oscillator strengths of Thiophene. Only the main transitions are reported.*

The results of the computed C 1s NEXAFS spectra are collected in **Table 4.1** and reported in **Figure 4.2** where the calculated lines and profile of the total spectrum are shown in black while the colored profiles refer to the partial contributions of the Carbon non-equivalent sites. **Figure 4.3** reports the comparison of the calculated total C1s spectra with the experimental ones. The theoretical C1s ionization thresholds are also reported in the figures; they are useful to distinguish the below-edge region of the spectrum, where the present discrete orbital description is adequate, from the above-edge region, where such an approach determines a discretization of the non-resonant continuum that is in part an artifact of the calculation, so that only qualitative information could be extracted above the ionization threshold. The site-resolved excitation spectra showed in **Figure 4.2** substantially represent a deconvolution of the experimental spectrum into components which allow a great flexibility in analysis of the transitions and facilitate the attribution of the spectral features to specific portions of the molecule.

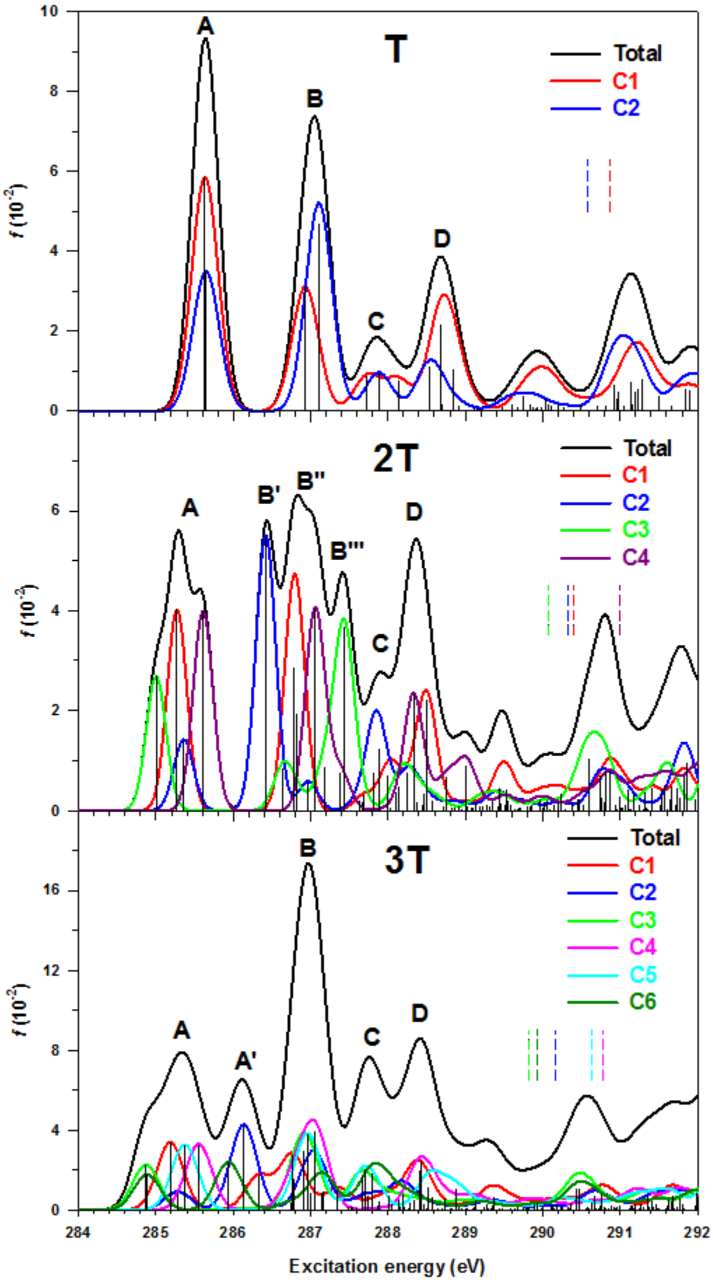

Figure 4.2 *Calculated C 1s NEXAFS spectra of thiophene (upper panel), bithiophene (central panel) and terthiophene (lower panel): total spectra (black line), and partial contributions (colored lines). The ΔKS C 1s ionization thresholds are also shown.*

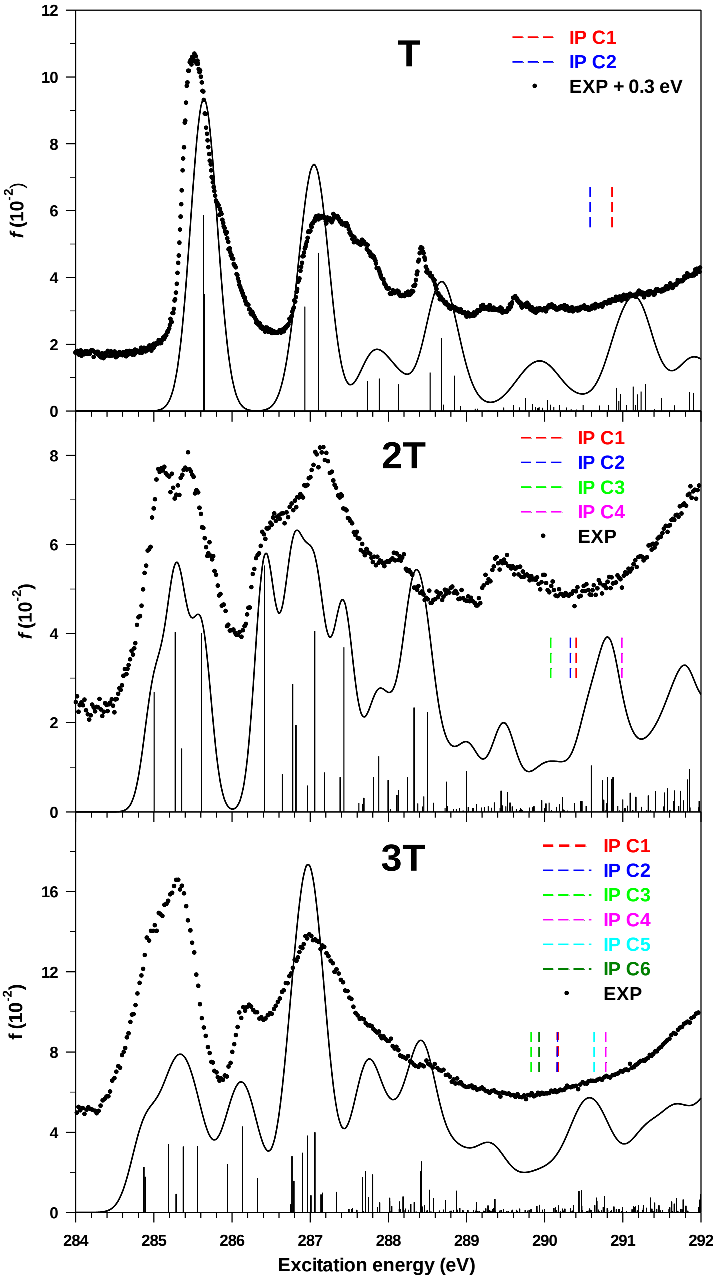

Figure 4.3 *C 1s NEXAFS spectra of thiophene (upper panel), bithiophene (central panel) and terthiophene (lower panel): experimental data (circles) and calculated DFT-TP results (solid line and vertical bars). Experimental energy scale of thiophene has been shifted of +0.3 eV in order to match the first calculated peak. The ΔKS C 1s ionization thresholds are also reported.*

The calculated total C1s spectrum of the thiophene molecule (**Table 4.1** and upper panel of **Figure 4.2**) is characterized by a first sharp peak (A, at 285.65eV) which is assigned to the two C1s → LUMO transitions from both C1 and C2 carbon sites. The LUMO orbital (1π*) is appreciably localized at the Sulphur atom, because of the considerable aromatic character of thiophene, and this is reflected in the lower intensity of the C2 1s→1π* compared to the C1 1s→1π* transition. These two calculated 1π* transitions are degenerate therefore do not reproduce the relative binding energy (BE) of the core orbitals, for which the calculations provide the C1 binding energy higher compared to C2 due to the higher electronegativity of the sulfur, close to C1, compared to carbon. The calculated BE shift is 0.28 eV, in good agreement with the value extracted from the experimental spectrum (0.3 eV). The degeneracy of the two 1π* transitions is therefore due to a final state effect, in particular a differential relaxation effect on the LUMO virtual orbital: when the half-hole is created on C1 the relaxation of the LUMO is stronger compared to C2. The second calculated peak B is a superposition of two excitations: from C1 (at 286.93 eV) towards a σ* (S-C) virtual orbital, which is largely contributed by the S lone pairs with a smaller $2p_x$ in plane (x) component of C1, and from C2 into the 2π* orbital (at 287.11 eV), which is localized on the four carbon atoms. The analogous 1s→2π* transition from C1 is weaker and lies at 287.7 eV, therefore above the corresponding transition from C2, and contributes to the small peak C. The lower intensity of C1 1s→2π* compared to C2 1s→2π* transition is due to the higher localization of the 2π* final orbital on the C atoms not directly bonded to the Sulphur. The other two weak transitions contributing to peak C derive from two equivalent C1 and C2 transitions into diffuse orbitals. The last peak before threshold (peak D at 288.7 eV) corresponds to transitions to final C3p Rydberg MOs with some σ*(C-H) contribution; the mixed valence-Rydberg nature of these transitions is consistent with their significant intensity. The assignment of the features substantially agrees with that previously published [4.27][4.28].

The bithiophene spectrum (**Table 4.2** and middle panel of **Figure 4.2**) shows an increased complexity due to the presence of four carbon non-equivalent sites as well as of the increased number of low-lying virtual π* orbitals. The first structure (A, around

285.5 eV) is assigned to transitions from the four C1s non equivalent carbon atoms into the LUMO orbital, which is contributed by the valence C 2pz and S3pz components and therefore comparable in nature to the LUMO orbital of thiophene. These transitions cover an energy range of about 0.6 eV due to the splitting of the C1s binding energies and their convolution gives rise to a double-peak shape. The relative excitation energies reflect only partly the relative energy of the core orbitals; in particular, each C1s α-carbon atom (C4), connecting the two thiophene rings, feels the proximity of the S atom and of two C atoms with a stronger depletion of electron density than the other C atoms of the rings. The C4-1s orbitals are therefore less shielded and a larger excitation energy is predicted for them which contribute to the higher energy side of peak A. The two C2-1s and C1-1s LUMO excitations are very close in energy and give rise to the lower energy side of peak A together with the C3-1s LUMO excitation, which is the lowest in energy and accounts for the most shielded C1s orbital compared to other carbon atoms, in agreement with the calculated binding energies. The C1 and C4 C1s→LUMO transitions are the most intense partial contributions of the A peak: this is a consequence of the localization of the LUMO on C1 and C4 atoms which are directly bonded to the sulfur atom.

The second calculated feature (B), around 287 eV, has a three peaked shape (denoted as B', B" and B"') as a result of the convolution of the many intense transitions falling in this energy range. The nature of these transitions roughly corresponds to those contributing to the thiophene B peak, namely towards the second π*(2π*) and the σ* (S-C) antibonding orbitals. The 2π* orbital resembles the LUMO composition maintaining a significant S 3pz component consistent with an increased aromatic character compared to thiophene. In particular, the B' component of the peak B derives from the second π* transition from the C2 site (at 286.42 eV) while analogous transitions from the C1 and C3 sites (at 286.77 eV and 287.43 eV) contribute to the B" and B"' components respectively. The strongest π* transitions still involve the C atoms not directly bonded to the Sulphur atom, as in the thiophene. The excitations to the σ* (S-C) antibonding orbitals contribute significantly to B" component and derive from the C1and C4 carbon sites directly bonded with sulphur atom (at 286.77 eV and 287.06 eV respectively). The assignment of the main features substantially agrees with that proposed in ref. [4.28].

Peak	Site	E (eV)	f x10^2	Assignment
A	C3	285.00	2.68	LUMO (1π*)
	C1	285.27	4.03	
	C2	285.36	1.42	
	C4	285.61	4.00	
B’	C2	286.42	5.52	π*
	C1	286.78	2.86	σ*(S-C)
B”	C1	286.82	1.94	π*
	C4	287.06	4.05	σ*(S-C)
B”’	C3	287.43	3.69	π*
C	C2	287.81	0.80	Rydberg
	C2	287.88	1.24	π*
	C1	287.99	0.71	Rydberg
	C4	288.33	2.34	π*
D	C1	288.50	2.23	Rydberg + σ*(CH)

Table 4.2 *Calculated excitation energies (eV) and oscillator strengths of Bithiophene. Only the main transitions are reported.*

Peak C and D should be characterized as superposition of valence and Rydberg excitations. The most intense transitions are towards final orbitals of π* character (from C2 site at 287.88 eV, peak C and from C4 site at 288.33 eV, peak D), their reduced intensity compared to the lower energy π* transitions reflects the decrease of the valence C2pz contribution of the C1s excited site in the higher π* virtual MO. The less intense lines are assigned to transitions into diffuse orbitals of mainly C3p-Rydberg character.

Peak	Site	E (eV)	f x10^2	Assignment
A	C3	284.87	2.26	LUMO (1π*)
	C6	284.88	1.77	
	C1	285.18	3.38	
	C2	285.28	0.92	
	C5	285.37	3.27	
	C4	285.55	3.29	
A’	C6	285.94	2.39	2π*
	C2	286.13	4.27	
	C1	286.32	1.70	
B	C1	286.77	2.80	σ*(S-C)
	C4	286.79	1.56	2π*
	C3	286.90	2.96	π*
	C5	286.96	3.81	σ*(S-C)
	C2	287.05	2.44.	π*
	C4	287.06	3.99	σ*(S-C)
	C6	287.15	0.97	π*
	C1	287.34	1.01	π*
C	C3	287.67	1.75	π*
	C5	287.70	2.05	π*
	C6	287.80	1.88	π*
D	C1	288.41	2.03	Rydberg
	C4	288.42	2.52	π*
	C5	288.53	1.11	π*
	C5	288.87	1.07	π*

Table 4.3 *Calculated excitation energies (eV) and oscillator strengths of Terthiophene. Only the main transitions are reported.*

The complexity further increases in the terthiophene spectrum (lowest panel of **Figure 4.2** and **Table 4.3**); in this molecule there are six non equivalent C atoms and even greater number of low-lying π* orbitals. The peak A arises from the C1s→LUMO transitions from all the six carbon sites whose contributions are highlighted in **Figure 4.2**. The larger excitation energies are predicted for the C4 and C5 carbon sites which are less shielded being directly bounded to the sulfur atoms and connecting two rings, as already found for the 2T molecule, and in agreement with the energy position of the calculated IPs. However, the differential relaxation effects on the π* low-lying orbitals, depending on the localization of the carbon core hole, prevent an analysis of the following features based on a regular energy shift of the site-resolved excitation spectra following the energy position of the IPs. The feature A’ corresponds to transitions to the second π* orbital (2π*) from C6, C2 and C1 sites while the transition from C4 site is shifted at higher energy (286.79 eV, peak B). We do not observe analogous transitions from C3 and C5 sites because the 2π* relative final orbitals have a negligible C2pz contribution of the carbon excited site. The B peak arises from several transitions to π* orbitals overlapped on the stronger σ* (S-C) transitions from the C1, C4 and C5 sites; this attribution confirms the mixed nature of peak B found also for thiophene and bithiophene. The C and D peaks are still contributed by transitions to virtual orbitals with π* character; the calculations indicate that these higher energy π* orbitals are mostly localized on carbon atoms with a reduction of the S3pz contribution as well as of the conjugation among the rings. The progressive intensity decrease of these transitions reflects the general reduction of the C2pz valence character of the final MOs; in the region of peak D also transitions to diffuse MOs with Rydberg C3p components are present with lower intensity.

In **Figure 4.3** the C 1s NEXAFS spectra computed by the TP-DFT scheme are compared with the gas phase experiments. The thiophene experimental profile (upper panel) has been shifted on the energy scale (+0.3eV) to match the first peak of the calculation. In this way, the relative energy shift among the calculated transitions, which actually represents the most significant observables, is preserved. A general good agreement is reached between experiment and theory, in particular the theoretical results correctly describe the main features of the experiment curves and the energy separation among the peaks. A clear correspondence between calculated and experimental peaks is apparent in the thiophene spectrum; the major discrepancy concerns the broad shape of the second experimental feature, assigned to the calculated B and C peaks, which is not reproduced by the calculations. Such disagreement should be caused by vibronic effects, which have been found to influence also the XPS C1s profile in the thiophene [4.29] but are not included in the present computational model. Such effects could be also responsible also for other discrepancies between theory and experiment in the bithiophene and terthiophene spectra, in particular as concerns the first peak. The intensity distribution of the experimental double-peak feature of the bithiophene spectrum is not properly reproduced by the calculation while in the terthiophene spectrum the theory underestimates the first peak intensity with respect to the second peak. We would underline that also the conformational flexibility of bithiophene [4.30] and terthiophene [4.31] should be kept in mind when comparing theoretical results and experimental spectroscopic data, due to possible contaminations of the conformers employed in the experimental measurements.

In summary, a comparison between the TP-DFT electronic calculations and experiment is fully satisfactory as far as the relative excitation energies are concerned, while the intensity distribution is less quantitative. We tend to ascribe this problem to the neglect of vibrational effects in the computational approach, also on the basis of our previous vibrationally resolved studies on NEXAFS C1s spectra of both simple aromatic molecules [4.32] and polycyclic aromatic hydrocarbons [4.33]. It is worth noting that the present electronic calculations are suitable for an unambiguous assignment of the experimental features despite the vibrational effects can play a role in the intensity distribution.

We finally address the evolution of the spectral features of the oligothiophenes when increasing the number of thiophene rings. The lower energy features (A and B) maintain their nature along the series, despite the increasing complexity and the enlargement of the peaks. The first π* peak (C 1s transitions to the LUMO) shifts to lower energy (about 0.5 eV) from thiophene to bithiophene while it does not change anymore from bithiophene to terthiophene: this trend can explain a stabilizing effect due to the aromaticity, which is stronger in passing from one to two rings than in adding a third ring. The σ* (S-C) transitions maintain their energy almost constant along the series because the involvement of a single bond is not influenced by aromaticity and always falls in the region of peak B together with the π* transitions. The number of overlapping transitions increases at higher energies (peaks C and D) preventing a strict correspondence along the series.

4.4.2 C 1s XPS

In **Figure 4.4** and **Table 4.4** the calculated ΔKS binding energies (BE) of thiophene, bithiophene and terthiophene are reported together with the experimental C 1s XPS spectra. It would be too difficult to calculate the absolute intensity of the XPS lines since the unbound photoelectron wavefunction should be employed in the dipole transition moment. Therefore we simply assumed that the intensity of each C1s line is proportional to the number of equivalent carbon atoms (in each of the present molecules all the C atoms have the same multiplicity of 2). Note that the experimental profiles of thiophene and bithiophene are shifted in energy (+0.2eV) to facilitate the comparison. Following the calculated BE, it is possible to define two different groups of carbon atoms: the first one at lower binding energies corresponds to the carbon atoms not bonded with sulfur atom, while the second group at higher energies identifies the carbons adjacent to the sulfur. We can also note that in bithiophene and terthiophene the highest BE are relative to carbons bound to S atom and connecting two rings.

The higher BE of the carbons neighbouring the S atom is consistent with the higher electronegativity of sulfur compared to carbon as well as charge transfer from sulfur to C atom not bonded with it through resonance in the π system. The further BE increase for the C atom connecting the rings reproduces a trend already observed in polycyclic aromatic hydrocarbons for which the calculations provides higher BE for C atoms non bound to any hydrogen atom compared to external carbons bound to hydrogen atoms [4.33]. Starting from the thiophene spectrum, the measured spectrum can be obviously interpreted as derived from the two chemically shifted carbon lines: the part at higher energy assigned to C1, atom close to sulfur, separated by 279 meV from the C_2 subspectrum. The theoretical statistical ratio of the carbon atoms (2:2) is not able to account for the intensity distribution between the two observed peaks which is affected by complex vibrational effects not included in the present computational scheme. The most pronounced vibrational components, in particular deriving from the S-C_1 bond stretching, are present in the C_1 1s spectrum compared to C_2, as analyzed by Giertz *et al.* [4.29].

Thiophene	
Carbon Site	BE (eV)
C1	290.862
C2	290.583
Bithiophene	
Carbon Site	BE (eV)
C4	290.987
C1	290.404
C2	290.330
C3	290.078
Terthiophene	
Carbon Site	BE (eV)
C4	290.781
C5	290.633
C1	290.167
C2	290.166
C6	289.929
C3	289.828

Table 4.4 *Calculated BE with corresponding carbon site and relative weight.*

For bithiophene, the calculation assign the higher energy peak to the C1s α-carbon atom (C4), connecting the two thiophene rings; the energy shift with the other C atom (C1), bound to sulfur and also to an hydrogen atom, is quite significative (583 meV) so the calculated C1 line contributes to the lower energy peak together with the lower energy lines relative to the C atom not bonded to sulfur (C2 and C3). The lowest binding energy of C3 compared to C2 can be ascribed to an addition of valence electron charge on the C3 site as a result of changes in bonding for the aromaticity induced by the second ring. The theoretical statistical ratio of these two groups of C atoms is equal 2:6 and qualitatively accounts for the relative height of the two experimental peaks. We note also the significant decrease of the energy shift between C1 and C2, 74 meV to be compared with 279 meV of thiophene. A similar trend is found also for the calculated BE of terthiophene : the higher BE refer to the two C atoms (C4, C5) which connect the rings and lose their equivalence in this molecule, while the lowest BE are found for the C atoms not bonded to S atom (C2, C3 and C6 respectively). The energy separation between C1 and C2 reduces to such an extent that the two BE are almost degenerate while the energy shift between the (C4, C5) group and the (C1, C2) one (540 meV) is similar to that found in bithiophene as well as the lowest BE calculated for the C3 and C6 sites. The presence of second and third rings introduces slight different aromaticity effects so that the C1 and C3 sites are destabilized by an increase of charge density, in line with the calculated decrease of C1 and C2 binding energies along the series. The first peak is therefore assigned to the binding energies of C4, C5 sites while all the other carbon lines contribute to the lowest energy experimental peak. The statistical ratio is therefore 4: 8 which apparently does not match the relative heights of the experimental peaks. Also in this case the complex vibrational structures affecting the spectral peaks prevent therefore a correct description of the XPS spectral shape.

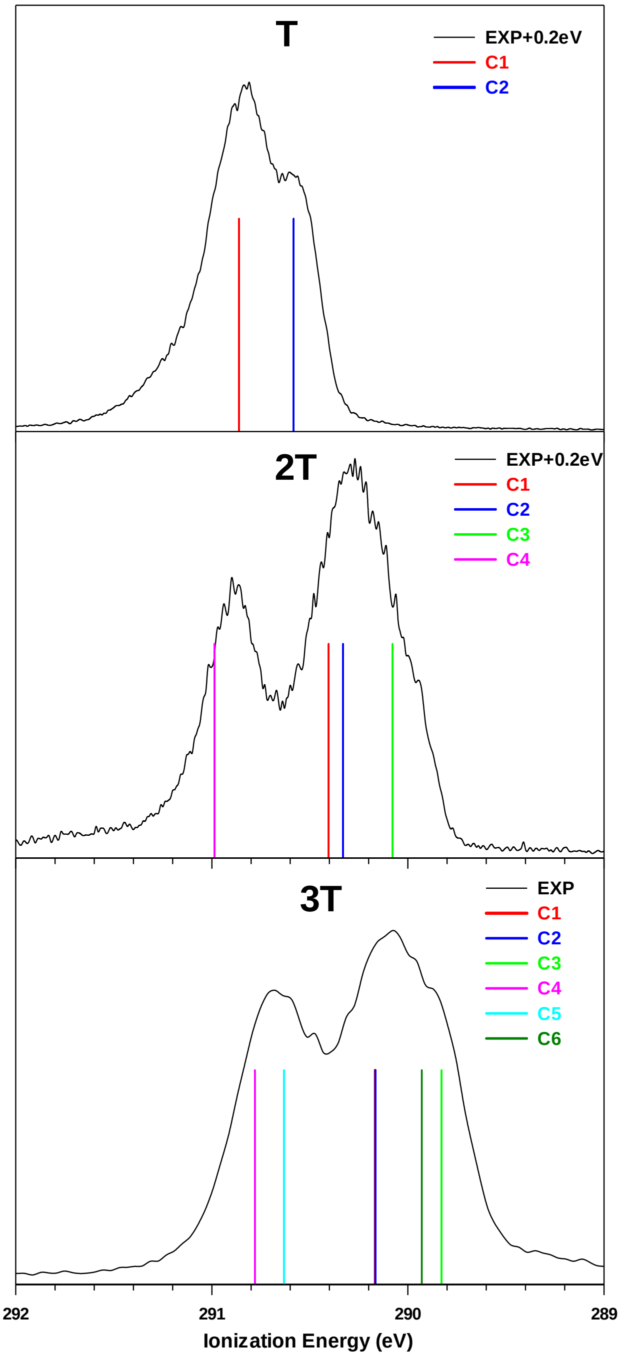

Figure 4.4 *C 1s XPS spectra of thiophene (upper panel), dithiophene (central panel) and terthiophene (lower panel): experimental data (solid line) and BE calculated at the ΔKS level (vertical colored lines). The line intensity is proportional to the multiplicity of the C atom. Experimental energy scale of thiophene and bithiophene has been shifted by +0.2 eV.*

5 A new time dependent density functional algorithm for large systems and plasmons in metal clusters

O. Baseggio, G. Fronzoni, M. Stener, The Journal of Chemical Physics 143, 024106 (2015);

A new algorithm to solve the Time Dependent Density Functional Theory (TDDFT) equations in the space of the density fitting auxiliary basis set has been developed and implemented. The method extracts the spectrum from the imaginary part of the polarizability at any given photon energy, avoiding the bottleneck of Davidson diagonalization. The original idea which made the present scheme very efficient consists in the simplification of the double sum over occupied-virtual pairs in the definition of the dielectric susceptibility, allowing an easy calculation of such matrix as a linear combination of constant matrices with photon energy dependent coefficients. The method has been applied to very different systems in nature and size (from H_2 to $[Au_{147}]^-$). In all cases, the maximum deviations found for the excitation energies with respect to the Amsterdam density functional code are below 0.2 eV. The new algorithm has the merit not only to calculate the spectrum at whichever photon energy but also to allow a deep analysis of the results, in terms of transition contribution maps, Jacob plasmon scaling factor, and induced density analysis, which have been all implemented.

5.1 Introduction

The calculation of optical spectra for large molecules has become a routine task, thanks to efficient implementations of the Time Dependent Density Functional Theory (TDDFT) method. More specifically, various approaches are available in computer codes which allow the treatment of large molecular systems.

In particular, it is worth mentioning the “standard” quantum chemistry approach, where molecular Kohn-Sham (KS) orbitals are expanded as linear combination of atomic functions, and the TDDFT equations are recast to a diagonalization of a matrix Ω according to the density matrix formulation of Casida [5.1]. The problem consists in extracting a set of eigenvalues and eigenvectors ofΩ, whose dimension is Nocc × Nvirt. Such method is efficiently implemented in many quantum chemistry codes, like, for example, Amsterdam Density Functional(ADF) code [5.2][5.3][5.4], which takes advantages of the molecular symmetry (employing the Wigner-Eckart theorem for the TDDFT part), of the Davidson diagonalization algorithm, of efficient fitting techniques of the first order density through the use of auxiliary basis functions to improve matrix-vector multiplication within the Davidson algorithm, and finally of the parallelization of the code which can exploit modern supercomputer architectures. Despite all these efforts, it is very difficult to calculate valence photoabsorption spectra over a wide excitation energy range when very large systems are considered. In fact, the Davidson iterative algorithm is very efficient on largeΩmatrices, but it is limited to the extraction of a relatively small number of lowest eigenvalues and eigenvectors; such diagonalization algorithm is generally employed in all the TDDFT codes which use the Casida method, like, for example, TURBOMOLE [5.5].

Therefore, the Casida TDDFT algorithm remains very efficient on large systems only when few low energy transitions are extracted but cannot be employed in practice to calculate a photoabsorption spectrum over a wide energy range, often necessary for a complete simulation of an experiment. Of course as the molecule/cluster size increases such problem will become more and more pathological, preventing any calculation of the spectrum. Moving from this practical consideration, it would be very appealing to find an alternative TDDFT algorithm to avoid the bottleneck of the Davidson diagonalization, capable to calculate the spectrum without limitations on the value of the maximum excitation energy.

Before describing the new algorithm, it is worth mentioning other recent alternative TDDFT strategies, which are promising for applications to large systems.

The first one is based on the explicit time-propagation technique. This scheme was introduced in the seminal work of Yabana and Bertsch [5.6] and is now implemented usually over real space grids, like in the OCTOPUS program [5.7], which has been recently applied to study the photoabsorption of large biomolecules [5.8] and large metal clusters, clusters up to 147 atoms [5.9] and 263 atoms [5.10].

The second one consists in a superoperator formulation of the TDDFT, which allows the calculation of the dynamical polarizability by means of a very efficient Lanczos method, implemented with plane waves basis set [5.11]; it has been applied to systems like C60, C70, zinc tetraphenylporphyrin, and chlorophyll a [5.12][5.13][5.14]. The Lanczos method is quite appealing for large systems since it furnishes the whole excitation spectrum, at variance with Davidson diagonalization which is limited to the lower part of the spectrum. A third very recent scheme has been developed by Grimme and consists in a simplified Tamm Dancoff Approximation (TDA) [5.15] and TDDFT [5.16], while a linear-scaling TDDFT has been developed by Zuehlsdorff [5.17].

A very promising recent method for large systems is the TDDFT time-propagation with Transition Contribution Map (TCM) by Hakkinen [5.18], which has been employed to calculate the spectrum of clusters containing up to 314 gold atoms protected by ligands. Very recently, Nobusada has developed a massively parallel implementation of TDDFT based on real-time and real-space [5.19], which allowed to consider clusters containing up to 1414 gold atoms [5.20]. It is worth noting that each of these algorithms has its different pros and cons which must be taken into account. In particular, the Casida algorithm suffers for the already mentioned problem of extracting of a large number of eigenvalues, but it has the great advantage to allow a very detailed assignment of the spectral features in terms of one-electron (1h1p) excited configurations. On the other hand, the TDDFT algorithms based on the time-evolution allow the calculation of the spectrum on a wide energy range without any problem; however, they do not give information regarding the nature of the transitions involved in the spectral feature. The only possibility is the inspection of the first order perturbed density whose nature is useful for a qualitative description but the information gained is too limited to allow a detailed assignment in terms of electronic transitions. At the moment, to the best of our knowledge, the only method which does not suffer energy limitation and is able to give a detailed assignment is the TDDFT time-propagation with TCM by Hakkinen [5.18].

Despite already Linear Response (LR) TDDFT implemented codes, it is worth mentioning also the subsystem formulation of LR-TDDFT [5.21][5.22], which is a very promising new idea for future applications on very large systems.

Finally, it must be considered that also the development of highly parallel ab initio and density functional theory (DFT) codes like NWCHEM [5.23] is an alternative way to describe large systems with respect to the proposal of new TDDFT algorithms. This way appears very practical, thanks to availability of massively parallel supercomputers.

In the present work, we propose a new TDDFT algorithm for the efficient calculation of photoabsorption spectra without the need of the diagonalization and therefore at any given energy. The necessary approximations introduced in the scheme can be safely kept under control. Moreover, the present algorithm allows a detailed analysis of the spectrum both in terms of 1h1p excited configuration which can be represented by TCM as well as in terms of the first order perturbed density. The method has been implemented within the ADF suite of codes and has been parallelized with standard Message Passing Interface (MPI); therefore, it is suitable to run on very large supercomputers.

5.2 Theoretical method and implementation

The first requirement of the new algorithm must be to avoid the diagonalization of the large Ω matrix, which is the main bottleneck of most implementations. This can be formally obtained if the photoabsorption spectrum $\sigma(\omega)$ is calculated point by point, from the imaginary part of the dynamical polarizability $\alpha(\omega)$,

$$\sigma(\omega) = \frac{4\pi\omega}{c} Im[\alpha(\omega)] \tag{5.2.1}$$

This expression is of practical interest when the polarizability is calculated for complex frequency, i.e., $\omega = \omega_r + i\omega_i$, where the real part ω_r is the scanned photon frequency (energy) and ω_i is the imaginary part which corresponds to a broadening of the discrete lines and can be interpreted as a pragmatic inclusion of the excited states finite lifetime. The introduction of a small imaginary part in the frequency is well established, for example, in the Lanczos method [5.11] and, more recently, in the damped response [5.24] formalism. This procedure introduces the arbitrary quantity ω_i and prevents the analysis of the spectrum by discrete lines. This is not a problem when the excited state density is so high that the analysis state-by-state would be impractical.

It will be shown in the following that it is possible to calculate efficiently the complex dynamical polarizability $\alpha(\omega)$ introducing some approximations. First, let us start with the definition

$$\alpha_{zz}(\omega) = \int \rho_z^{(1)}(\omega, \bar{r}) z d\bar{r} \tag{5.2.2}$$

of the z-th diagonal term of the polarizability tensor, where $\rho_z^{(1)}(\omega, \bar{r})$ stands for the Fourier component of the given frequency of the first order time dependent induced density by the external time dependent scalar potential. For the calculation of the spectrum, the isotropic part of the tensor is actually extracted from the trace: $\alpha(\omega) = \frac{1}{3}\sum_{i=1}^{3} \alpha_{ii}(\omega)$, where the index i runs on the three components x, y, and z.

Following the TDDFT theory, the induced density can be calculated from the dielectric susceptibility $\chi_{KS}(\omega, \bar{r}, \bar{r}')$ of a reference system of non-interacting electrons under the effect of an effective perturbing potential $V_{SCF}^{z}(\omega, \bar{r})$ sum of the external potential plus the Coulomb and the exchange-correlation (XC) response potential.

This is summarized by the following coupled linear equations:

$$\rho_z^{(1)}(\omega,\bar{r}) = \int \chi_{KS}(\omega,\bar{r},\bar{r}')V_{SCF}^{z}(\omega,\bar{r}')d\bar{r}' \tag{5.2.3}$$

$$V_{SCF}^{z}(\omega,\bar{r}) = V_{EXT}^{z}(\omega,\bar{r}) + \int \frac{\rho_z^{(1)}(\omega,\bar{r}')d\bar{r}'}{|\bar{r}-\bar{r}'|} + \left.\frac{\partial V_{XC}}{\partial\rho}\right|_{\rho^0} \rho_z^{(1)}(\omega,\bar{r}) \tag{5.2.4}$$

The Adiabatic Local Density Approximation (ALDA) [5.25] has been employed in expression (5.2.4) (XC kernel local in time and additionally also in space) and $V_{SCF}^{z}(\omega,\bar{r})$ corresponds in practice to the z dipole component. The present implementation is limited to ALDA and possible extensions to gradient corrected kernels are not expected to give any problem; on the other hand, in the present formulation, it is not possible to employ non-local kernels from hybrid functionals, as also specified after Equation (5.2.24).

Now, expressions (5.2.3) and (5.2.4) can be written in operatorial form

$$\rho_z^{(1)} = \chi_{KS}V_{SCF}^{z} \tag{5.2.5}$$

$$V_{SCF}^{z} = V_{EXT}^{z} + K\rho_z^{(1)} \tag{5.2.6}$$

where in expression (5.2.6), K stands for the sum of the Coulomb and the XC kernels,

$$K(\bar{r},\bar{r}') = K_C(\bar{r},\bar{r}') + K_{XC}(\bar{r},\bar{r}') = \frac{1}{|r-r'|} + \delta(r-r')\left.\frac{\partial V_{XC}}{\partial\rho}\right|_{\rho^0} \tag{5.2.7}$$

Due to the linearity of (5.2.5) and (5.2.6), it is possible to eliminate V_{SCF}^{z} and to obtain an equation for $\rho_z^{(1)}$, which reads as

$$[1-\chi_{KS}K]\rho_z^{(1)}=\chi_{KS}V_{EXT}^{z} \tag{5.2.8}$$

Now, it is convenient to represent Equation (5.2.8) over a basis set and since the unknown term corresponds to the induced density, it is natural to choose the auxiliary density fitting functions f_μ as basis set. More precisely, it is even better to choose such basis as a subset of the fitting set, since the induced density will be affected mainly by valence orbitals so all the functions needed to fit the core density should be excluded without losing accuracy. This is true only when valence excitations are considered (like in the present work); if core electron excitations are considered, the algorithm remains valid, but the fitting functions must be selected in a different way, allowing flexibility in order to properly describe products between a core and a virtual orbital. With this representation $\rho_z^{(1)}(\omega,\bar{r})=\sum_{\mu}^{K}f_\mu(\bar{r})b_\mu(\omega)$, the following non-homogeneous system of linear algebraic equations is obtained, which written in matrix formulation reads as

$$[\boldsymbol{S}-\boldsymbol{M}(\boldsymbol{\omega})]\boldsymbol{b}=\boldsymbol{d} \tag{5.2.9}$$

In Equation (5.2.9), $\boldsymbol{S}$ is the overlap matrix between fitting functions, $\boldsymbol{b}$ is the unknown vector with the expansion coefficients $b_\mu(\omega)$ of $\rho_z^{(1)}$, and $\boldsymbol{d}$ is the frequency dependent vector corresponding to the known non-homogeneous term, whose components are

$$d_\mu=\langle f_\mu|\chi_{KS}(\omega)|z\rangle \tag{5.2.10}$$

and finally, the elements of the frequency dependent matrix $\boldsymbol{M}$ are

$$M_{\mu\nu} = \langle f_\mu | \chi_{KS}(\omega) K | f_\nu \rangle \tag{5.2.11}$$

Now, let us consider the computational effort needed to solve Equation (5.2.9): (i) the construction of the matrices $\boldsymbol{S}$, $\boldsymbol{M}$, and vector $\boldsymbol{d}$ and (ii) the resolution of linear system (5.2.9). First, consider the resolution of the linear system: it will scale with N^3 where N is the dimension of the matrix corresponding to the number of the fitting functions. Although this part scales with the third power, it will be shown that the dimension N can be kept in practice rather low, for example, for Au atom, 44 functions are enough to give accurate results, so a cluster of 1000 Au atoms will give a matrix of dimension 44000, which is tractable with moderate efforts on a medium size computer cluster. This simple observation shows that as it concerns the linear system, the approach is competitive since it would allow to calculate much larger systems without the limitation of the Davidson algorithm, if a proper selection of the fit set is performed.

Let us now analyse the effort needed to build the frequency dependent $\boldsymbol{M}(\boldsymbol{\omega})$ matrix: apparently, this is a prohibitive task, since it should be repeated for each frequency. The original characteristic of the present new method is the introduction of a simple approximation which should enable the construction of $\boldsymbol{M}(\boldsymbol{\omega})$ as a linear combination of frequency independent matrices G_k with frequency dependent coefficients $s_k(\omega)$, with this expression,

$$\boldsymbol{M}(\omega) = \sum_k s_k(\omega) \boldsymbol{G}^k \tag{5.2.12}$$

with this idea, a set of matrices $\{\boldsymbol{G}^k\}$ is calculated and stored only once at the beginning; then, the matrix $\boldsymbol{M}(\omega)$ is calculated very rapidly at each photon energy ω. To justify expression (5.2.12), we start with the expression of the KS dielectric susceptibility [5.26],

$$\begin{aligned}\chi_{KS}(\omega,\bar{r},\bar{r}') &= \sum_{i}^{Nocc}\sum_{a}^{Nvirt} \varphi_i(\bar{r})\varphi_a(\bar{r})\frac{4\varepsilon_{ia}}{\omega^2-\varepsilon_{ia}^2}\varphi_i(\bar{r}')\varphi_a(\bar{r}') \\ &= \sum_{i}^{Nocc}\sum_{a}^{Nvirt} \Theta_{ia}(\bar{r})\lambda_{ia}(\omega)\Theta_{ia}(\bar{r}')\end{aligned} \tag{5.2.13}$$

In (5.2.13) we have assumed real KS occupied (φ_i) and virtual (φ_a) orbitals while $\varepsilon_{ia} = \varepsilon_a - \varepsilon_i$ are differences between virtual and occupied KS eigenvalues. Let us consider now carefully the right hand side of expression (5.2.13): the frequency dependence enters only in the $\lambda_{ia}(\omega)$ factor, which is "almost" constant for all the pairs of index $i-$ and $a-$ for which $\varepsilon_a - \varepsilon_i$ is almost constant. This happens when many ε_{ia} are close together, that is, when the density of "zero order" excitation energies is high. This important observation allows to profitably change the double sum in expression (5.2.13). In fact, let us consider the distribution of all the ε_{ia} on the excitation energy axis, like in **Figure 5.1**, and define an energy grid over this axis, starting from the minimum ε_{ia} which corresponds to $\varepsilon_{LUMO} - \varepsilon_{HOMO}$. The energy grid consists of P + 1 knots $\{E_k\}_{k=1,\dots,P+1}$ and P intervals are defined as $I_k = [E_k, E_{k+1}), k = 1, \dots, P$.

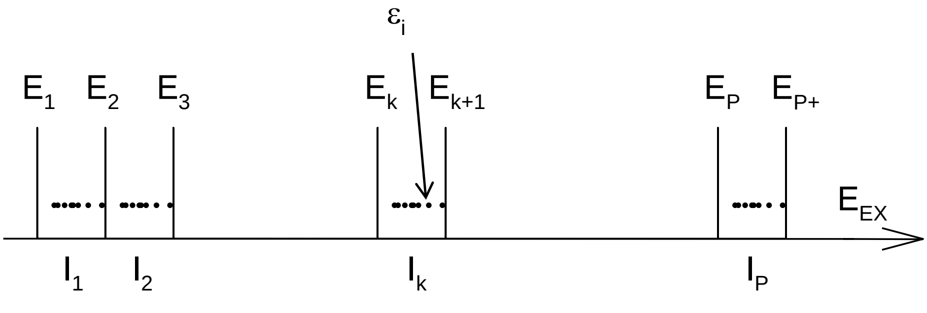

Figure 5.1 *Discretization of the energy axis to accommodate eigenvalue differences for the efficient calculation of the dielectric susceptibility. See text for details.*

It is possible to change the double sum of previous Equation (5.2.13) as follows:

$$\chi_{KS}(\omega,\bar{r},\bar{r}') = \sum_{k=1}^{P}\sum_{\varepsilon_{ia}\in I_k}\Theta_{ia}(\bar{r})\lambda_{ia}(\omega)\Theta_{ia}(\bar{r}') \tag{5.2.14}$$

The advantage of this new double sum is that, if the energy knots are dense enough, the values of ε_{ia} within each interval can be considered, with good approximation, almost constant and equal to the average $\bar{E}_i = \frac{E_i+E_{i+1}}{2}$: this allows to bring the $\lambda_{ia}(\omega)$ factor outside the inner sum,

$$\chi_{KS}(\omega,\bar{r},\bar{r}') = \sum_{k=1}^{P}\frac{4\bar{E}_k}{\omega^2-\bar{E}_k^2}\sum_{\varepsilon_{ia}\in I_k}\Theta_{ia}(\bar{r})\Theta_{ia}(\bar{r}') \tag{5.2.15}$$

so in expression (5.2.15), the frequency dependent dielectric susceptibility is a linear combination of frequency independent objects (the inner sum) while only the coefficients are frequency dependent. Moreover, if one is interested in the lowest part of the spectrum as it usually happens, the sum in (5.2.15) can be safely truncated at a maximum energy cutoff, which can be chosen checking the convergence of the results with respect to such energy cutoff. This re-summation is the central idea of the present algorithm and is quite general irrespective to the introduction of the auxiliary basis set for the density fitting. We will now use this approach to build the matrix $\boldsymbol{M}(\omega)$. From Equation (5.2.11) and using expression (5.2.15), we get

$$M_{\mu\nu} = \sum_{k=1}^{P}s_k(\omega)\sum_{\varepsilon_{ia}\in I_k}\big\langle f_\mu\big|\Theta_{ia}(\bar{r})\big\rangle\langle\Theta_{ia}(\bar{r}')|K|f_\nu\rangle = \sum_{k=1}^{P}s_k(\omega)G_{\mu\nu}^{k} \tag{5.2.16}$$

Which, now justifies previous expression (5.2.12), defines the matrix G^k and the coefficients,

$$s_k(\omega) = \frac{4\bar{E}_k}{\omega^2 - \bar{E}_k^2} \tag{5.2.17}$$

The construction of each G^k matrix corresponds to a matrix-matrix product,

$$G^k_{\mu\nu} = \sum_{\varepsilon_{ia} \in I_k} \langle f_\mu | \Theta_{ia}(\bar{r}) \rangle \langle \Theta_{ia}(\bar{r}') | K | f_\nu \rangle = \sum_{\varepsilon_{ia} \in I_k} A^k_{\mu,ia} B^k_{ia,\nu} \quad \boldsymbol{G^k} = \boldsymbol{A^k B^k} \tag{5.2.18}$$

The matrices $\boldsymbol{A}$ and $\boldsymbol{B}$ must be built, formally with the following expansions:

$$A^k_{\mu,ia} = \langle f_\mu | \varphi_i \varphi_a \rangle = \sum_{\sigma\tau}^{basis} \langle f_\mu | \sigma\tau \rangle c_{\sigma i} c_{\tau a} \tag{5.2.19}$$

in expression (5.2.19), σ and τ refer to orbital basis functions and c are the molecular orbital expansion coefficients (KS eigenvectors).

The calculation of (5.2.19) would be far prohibitive, but in ADF, a very efficient “pair fitting” technique has been already developed, so the run of the basis indexes is not free but limited so that at least one basis function lies on the same center of the fit function. This step is the most expensive in the matrix construction. In expression (5.2.19), the integrals between a fit function and two basis functions are already available in ADF between primitive (not symmetrized) functions. Actually, we have also implemented the calculation of the $\langle f_\mu | \sigma\tau \rangle$ integrals when the functions lie on three different centres. Since Slater type orbitals (STOs) functions are employed, these integrals are not analytical but can be easily calculated by fitting the products of two basis functions with the auxiliary density fitting functions. This does not change the dimension of Equation (5.2.9) but increases the computational effort to build matrix $\boldsymbol{A^k}$ (Equation (5.2.19)). However, we have noticed in preliminary test calculations that this does not change the results appreciably, and therefore, we have always neglected the $\langle f_\mu | \sigma\tau \rangle$ integrals when the functions are on three different centres.

For the matrix $\boldsymbol{B}$, the procedure is the same

$$B^k_{ia,\nu} = \left\langle \varphi_i\varphi_a \middle| \frac{1}{|\bar{r}' - \bar{r}''|} \middle| f_\nu \right\rangle + \left\langle \varphi_i\varphi_a \middle| \frac{\partial V_{XC}}{\partial \rho} \middle| f_\nu \right\rangle \tag{5.2.20}$$

The first term in (5.2.20) can be calculated using the Resolution of the Identity (RI),

$$\begin{aligned} \left\langle \varphi_i\varphi_a \middle| \frac{1}{|\bar{r}' - \bar{r}''|} \middle| f_\nu \right\rangle &= \sum_{\gamma\eta} \langle \varphi_i\varphi_a | f_\gamma \rangle S^{-1}_{\gamma\eta} \left\langle f_\eta \middle| \frac{1}{|\bar{r}' - \bar{r}''|} \middle| f_\nu \right\rangle \\ &= ((A^k)^+ S^{-1} F)_{ia,\nu} \end{aligned} \tag{5.2.21}$$

where in (5.2.21), the matrix F is defined as follows:

$$F_{\mu\nu} = \left\langle f_\mu \middle| \frac{1}{|\bar{r}' - \bar{r}''|} \middle| f_\nu \right\rangle \tag{5.2.22}$$

The second term in (5.2.20) can be calculated in a similar fashion:

$$\left\langle \varphi_i\varphi_a \middle| \frac{\partial V_{XC}}{\partial \rho} \middle| f_\nu \right\rangle = \sum_{\gamma\eta} \langle \varphi_i\varphi_a | f_\gamma \rangle S^{-1}_{\gamma\eta} \left\langle f_\eta \middle| \frac{\partial V_{XC}}{\partial \rho} \middle| f_\nu \right\rangle = ((A^k)^+ S^{-1} Z)_{ia,\nu} \tag{5.2.23}$$

and the matrix Z in (5.2.23) is defined as follows:

$$Z_{\mu\nu} = \left\langle f_\mu \middle| \frac{\partial V_{XC}}{\partial \rho} \middle| f_\nu \right\rangle \tag{5.2.24}$$

Equations (5.2.20), (5.2.23) and (5.2.24) are limited to ALDA and cannot be used in the present formulation for non-local kernels.

Therefore, from (5.2.20),(5.2.21) and (5.2.23), we get

$$B^k = (A^k)^+ S^{-1}(F+Z) \tag{5.2.25}$$

Finally, from Equations (5.2.18) and (5.2.25),

$$G^k = D^k L \tag{5.2.26}$$

where the following two new matrices are introduced:

$$D^k = A^k (A^k)^+ \tag{5.2.27}$$

$$L = S^{-1}(F+Z) \tag{5.2.28}$$

In practice, all the integrals (Equations (5.2.20)-(5.2.23)) needed to calculate the G^k matrices are already available in ADF, except the matrix $\boldsymbol{Z}$ (Eq. (5.2.24)) which has been implemented numerically. Then, each G^k matrix is calculated by expression (5.2.26).

We have still to calculate the $\boldsymbol{d}$ vector of Equation (5.2.10), i.e., the non-homogeneous term of Equation (5.2.9). Taking advantage of previously described technique, it is straightforward that

$$\begin{aligned} d_\mu = \langle f_\mu | \chi_{KS}(\omega) | z \rangle &= \sum_{k=1}^{P} s_k(\omega) \sum_{\varepsilon_{ia}\in I_k} \langle f_\mu | \Theta_{ia}(\bar{r}) \rangle \langle \Theta_{ia}(\bar{r}) | z \rangle \\ &= \sum_{k=1}^{P} s_k(\omega) \sum_{\varepsilon_{ia}\in I_k} A^k_{\mu,ia} \langle \varphi_i | z | \varphi_a \rangle \end{aligned} \tag{5.2.29}$$

so vector $\boldsymbol{d}$ is easily calculated at each frequency as a linear combination of frequency independent vectors, accessible from $\boldsymbol{A}$ matrix and conventional dipole matrix elements.

Finally, the complex dynamic polarizability components are calculated as

$$\alpha_{zz}(\omega) = \int \rho_z^{(1)}(\omega, \bar{r}) z d\bar{r} = \sum_{\mu} b_{\mu} \int f_{\mu} z d\bar{r} = \sum_{\mu} b_{\mu} n_{\mu} \tag{5.2.30}$$

the vector b in (5.2.30) is the solution of Equation (5.2.9), and the elements of the n vector are integrals which are easily calculated analytically.

This step concludes the calculation of the dynamic polarizability and therefore of the spectrum and furnished the first order TD density which can be used to analyze and rationalize the results. However, our goal is to get also a more complete analysis of the spectrum, namely, in terms of linear combination of one-electron excited configurations or in terms of Transition Contribution Maps (TCM) [5.18]. To obtain this, it is convenient adopt the Modified Sternheimer Approach (MSA) formulation [5.27] of linear response, which furnished the first order perturbation of the KS orbitals:

$$\begin{gathered} [H_{KS}^0 - \varepsilon_i - \omega]\varphi_i^{(1,-)} = -V_{SCF}\varphi_i \\ [H_{KS}^0 - \varepsilon_i + \omega]\varphi_i^{(1,+)^*} = -V_{SCF}\varphi_i \end{gathered} \tag{5.2.31}$$

From the perturbed orbitals, the perturbed density is obtained as

$$\rho^{(1)} = 2\sum_{i}^{occ} \varphi_i \left(\varphi_i^{(1,-)} + \varphi_i^{(1,+)^*}\right) \tag{5.2.32}$$

It is worth noting that, for convenience, the second inhomogeneous equations in (5.2.31) is actually the complex conjugate with respect to that reported in ref. [5.27] for

$\varphi_i^{(1,+)}$. Equations (5.2.31) and (5.2.32) were used in the past to calculate self-consistently the V_{SCF} via Equation (5.2.6) in old TDDFT implementations [5.28][5.29][5.30], but in the present context, they are useful to easily get the analysis in terms of one-electron configurations. In fact, if the perturbed orbitals are expanded in terms of virtual KS orbitals, the term in brackets in Equation (5.2.31) is diagonal. Moreover, the V_{SCF} is already available from Equations (5.2.9) and (5.2.6), so the following equations are obtained:

$$\begin{gathered}[\varepsilon_a - \varepsilon_i - \omega]c_i^{a-} = -\langle\varphi_a|V_{SCF}|\varphi_i\rangle \\ [\varepsilon_a - \varepsilon_i + \omega]c_i^{a+^*} = -\langle\varphi_a|V_{SCF}|\varphi_i\rangle\end{gathered} \tag{5.2.33}$$

The polarizability is then expressed by:

$$\alpha_{zz}(\omega) = 2\sum_i^{occ}\sum_a^{virt}\langle\varphi_i|z|\varphi_a\rangle\left(c_i^{a+^*} + c_i^{a-}\right) = \sum_i^{occ}\sum_a^{virt}\langle\varphi_i|z|\varphi_a\rangle P_i^a \tag{5.2.34}$$

the density matrix (dipole amplitudes) P_i^a is introduced in (5.2.34). From equation (5.2.33) and using the definition of $s_k(\omega)$ (Equation (5.2.18)), we obtain:

$$P_i^a = s_k(\omega)\langle\varphi_i|V_{SCF}|\varphi_a\rangle \tag{5.2.35}$$

In practice, the absorption spectrum is obtained from imaginary part of Equation (5.2.34) (like in expression (5.2.30)), and therefore, the analysis in term of one-electron excited configurations and TCM is obtained from imaginary part of expression (5.2.35).

Using Equations (5.2.6) and (5.2.28), dipole amplitudes are actually calculated as follows:

$$P_i^a = s_k(\omega)\left[\langle\varphi_i|z|\varphi_a\rangle + \sum_{\mu\tau}^{fit}(A^k)^+_{ia,\mu}L_{\mu\tau}b_\tau\right] \tag{5.2.36}$$

5.3 Computational Details

The method has been implemented in a local version of the ADF code, and more precisely, ADF has been modified in order to save on external files, all the needed integrals, and matrix elements, which were already calculated by ADF with the only exception of matrix Z (Equation (5.2.24)); this matrix has been implemented by the Gaussian numerical integration scheme of ADF. Then, a new program (independent by ADF) reads the files, builds all the needed matrices, solves TDDFT equation (5.2.9), calculates the spectrum, and performs the analysis. We have decided to implement the new code in a separate program independent by ADF in order to exploit more easily the parallelization, with the goal to obtain a code which was massively parallel and easily portable on different architectures. For this reason, we have used standard MPI and ScaLAPACK libraries. However, the inclusion of the complete program within ADF is under consideration and will be available in a future release of ADF.

In all calculations, we have employed the LB94 exchange-correlation model potential [5.31] to obtain the KS orbitals and eigenvalues from the KS equations, while the exchange-correlation kernel is approximated by ALDA [5.25] in the TDDFT part taking the derivative of the Vosko Wilk Nusair (VWN) [5.32] LDA XC potential. The basis sets employed consist of STOs included in the ADF database, as well as the auxiliary density fitting functions. The new program allows a simple choice of a subset of the ADF fitting functions, in order to save computer time when some fitting functions are not necessary for an accurate description of the photoabsorption spectrum. The strategy to choose a properly reduced fitting subset consists to perform some preliminary TDDFT test calculations on simple systems (for example, diatomic molecules) increasing gradually the number of fit functions. Typically, this procedure converges rather rapidly, giving calculated spectra that match better and better with that obtained with a standard TDDFT calculation by ADF. When a good match is obtained, the fitting subset of the corresponding atoms can be used for more complex or larger systems, as it will be shown in details in Sec. 5.4.

Equation (5.2.9) must be solved for each non-equivalent dipole component with the constraint that the integral of the induced density $\rho^{(1)}$ must be zero over space due to the orthogonality of occupied-virtual orbitals. This condition is naturally satisfied when the dipole component is not totally symmetric; on the other hand, when the system symmetry is low and one or more dipole components are totally symmetric, such constraint can be easily imposed by Lagrange multipliers after Equation (5.2.9) is solved. Most of the computational effort is spent in the resolution of complex algebraic linear system (5.2.9), which is managed by ScaLAPACK parallel library and should be portable on very large supercomputers.

While the ADF code fully exploits symmetry, this is only partially done in the present method: the density fitting basis functions are not symmetrised by now; however, only the pairs of occupied (φ_i) and virtual (φ_a) orbitals involved in allowed dipole selection rules are actually considered.

We have implemented the plasmon analysis in the present method according to Jacob et al. [5.33]: they suggested to study the evolution of the TDDFT photoabsorption spectra by changing a scaling factor $0 \leq \lambda \leq 1$ used to “turn on” the coupling matrix K. This can be easily done in present implementation multiplying the matrix L (Equation (5.2.28)) by the scaling factor λ. This scaling factor analysis has proven successful in previous studies on silver chains [5.34] and polyacenes [5.35].

It is worth noting that the dynamic polarizability and therefore the spectrum can be in principle calculated equivalently by expression (5.2.30) or (5.2.34); however, we have found that expression (5.2.34) is much more accurate and less demanding in terms of density fitting size. This is not surprising since the dipole integrals in expression

(5.2.34) are analytical while expression (5.2.30) requires a fitting able to accurately fit the occupied-virtual orbital product. For this reason, all the spectra reported in this work have been calculated with expression (5.2.34).

5.4 Results and Discussion

We have tested the performance of the new TDDFT algorithm implemented in this work, on a series of small but rather different systems (diatomic H_2, Na_2 Au_2, and triatomic H2O) and finally on two rather large gold clusters Au_{86} [5.36] and $[Au_{147}]^-$ [5.37]. The goal is to achieve a firm assessment of the accuracy of the method on small systems as well as of an accurate choice of the density fitting set. Finally, the large metal clusters have been selected since they have been already treated by standard TDDFT and offer therefore a good chance to compare the performances of the new method and test its numerical economy. It must be considered that the program is now installed only on a small HP ProLiant ML350p Gen8 server (with 16 cores Intel® Xeon® CPU E5-2650 2 GHz), on which the present calculations were run. The porting to a supercomputer and therefore the applications to much larger systems will be considered as the next step of a future work.

5.4.1 H_2

In **Figure 5.2**, we have reported the TDDFT photoabsorption spectrum of H_2 with the polarization along the bond, calculated by ADF and by present method employing a DZ basis set. An interatomic distance of 0.7414Å has been used. The photoabsorption corresponds to the $1\sigma_g \rightarrow 1\sigma_u$ valence transition. In order to have an easier comparison between the results of the two algorithms, the discrete lines obtained by ADF have been convoluted by Lorentzian functions with Half-Width Half Maximum (HWHM) η = 0.3eV according to the following expression:

$$f(\omega) = \sum_{I}^{N} \frac{\eta^2 f_I}{(\omega - \omega_I)^2 + \eta^2} \tag{5.4.1}$$

ω_I and f_I in (5.4.1) are the excitation energies and oscillator strengths, respectively, while the presence of η^2 in the numerator guarantees that the maximum of the Lorentzian for $\omega = \omega_I$ corresponds to the value of f_I when only one line is present. For the new algorithm, the imaginary part of the polarizability is calculated by Equation (5.2.34) for complex photon energy and in **Figure 5.2**, the plotted curves correspond to

$$f(\omega_r) = \frac{2\omega_r \omega_i}{3} Im[\alpha(\omega)] \tag{5.4.2}$$

ω_r and ω_i in (5.4.2) are the real and the imaginary part of the photon energy, respectively, and it must also be $\omega_i = \eta$ in order to have the same convolution as in ADF.

An excellent agreement between the two methods emerges from the figure. Four different curves have been obtained with the new algorithm employing different reduced density fitting sets in the TDDFT part. The ADF DZ density fitting set of H consists of 4s, 3p, 2d, 1f, and 1g Slater functions (39 in total), which is much larger than needed; in fact, the absorption is well described already with only 2 s fitting functions, with an error in the energy of the maximum of only 0.12 eV. The match is excellent with 4 s fitting functions both for energy and intensity. Already at this level, it is evident that fitting set can be strongly reduced with respect to the original one.

To check the algorithm performance also for the real part of the dynamic polarizability, the comparison with ADF is reported in **Figure 5.3**. The agreement is excellent and the new algorithm is very accurate to reproduce quantitatively the behaviour of the polarizability with only 4 s density fitting functions.

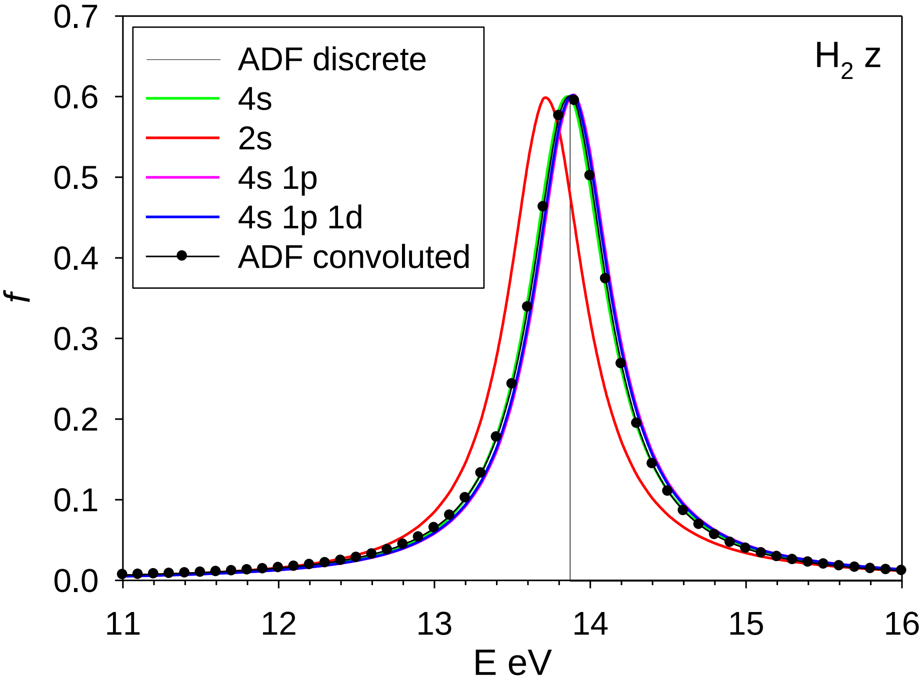

Figure 5.2 *Calculated TDDFT valence photoabsorption spectra of H_2 for polarization along the bond (Z direction). ADF results compared with present algorithm with various choices for the auxiliary basis for the density fitting.*

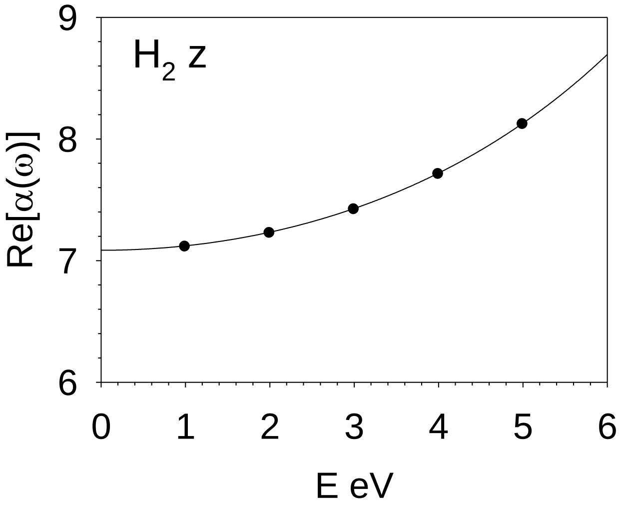

Figure 5.3 *Calculated TDDFT real part of the dynamical polarizability of H_2 for polarization along the bond (Z direction). ADF results (circles) compared with present algorithm (solid line).*

5.4.2 Na_2

H_2 is a very simple molecule, so it is important to test the algorithm on systems which become more and more complex in order to gradually identify possible pitfalls of the method and to get acquainted with its performances. In this respect, Na_2 is interesting because both s and p atomic functions are important to describe valence molecular orbitals; moreover, we have employed a DZP basis set in order to include also d functions in the calculation. An interatomic distance of 2.9997Å has been used. The original density fitting set of ADF for Na consists of 88 functions (14s 7p 6d 2f 1g); after some preliminary test calculations, we have identified a much smaller set (7s 5p) containing only 22 functions which has been employed in the TDDFT calculation for Na_2 with the new algorithm.

The photoabsorption of Na_2 is considered in **Figure 5.4**, with convolution $\omega_i = \eta = 0.15\text{eV}$ and bond direction along the Z axis: the upper panel considers the photoabsorption with parallel polarization (along Z) and the lower panel with perpendicular polarization (along X). Taking into account, the electronic structure of Na_2,

$$(1\sigma_g)^2(1\sigma_u)^2(2\sigma_g)^2(2\sigma_u)^2(3\sigma_g)^2(3\sigma_u)^2(1\pi_u)^4(1\pi_g)^4(4\sigma_g)^2(4\sigma_u)^0(2\pi_u)^0$$

the absorption with X polarization at 3.38 eV is ascribed to the $4\sigma_g \rightarrow 2\pi_u$ transition while the other one with Z polarization at 2.35 eV is ascribed to the $4\sigma_g \rightarrow 4\sigma_u$ transition. The match of the new algorithm with ADF is quantitative even with a fitting set which is 4 times smaller than the original one.

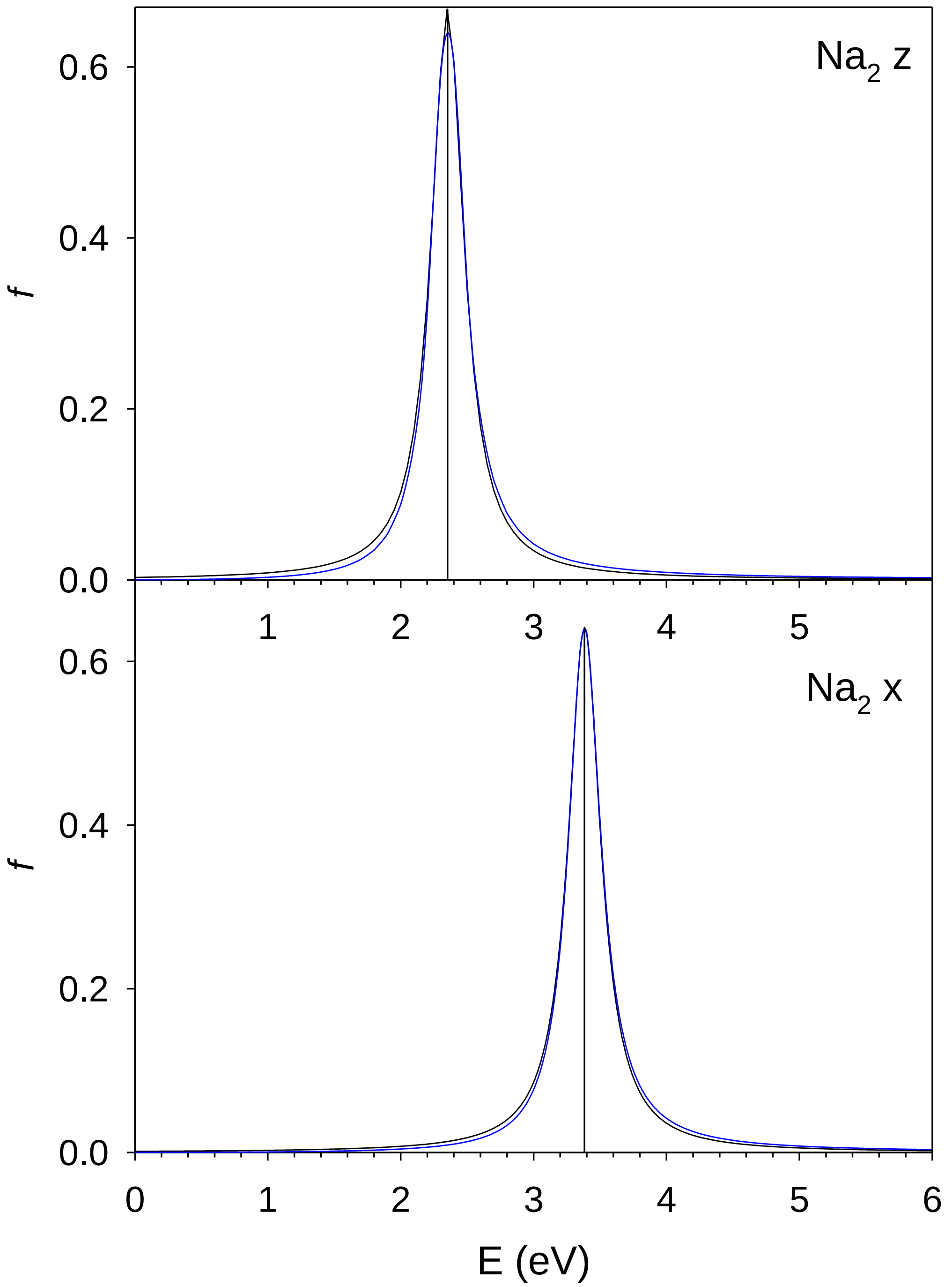

Figure 5.4 *Calculated TDDFT valence photoabsorption spectra of Na$_2$ for polarization along the bond (Z direction, upper panel) and perpendicular to the bond (X direction, lower panel). ADF results (black lines) compared with present algorithm (blue line).*

5.4.3 Au_2

We have considered gold dimer for two reasons: first its spectrum is quite complicated, with many transitions involving mixing of several one-electron excited configurations. The valence molecular orbitals are contributed by functions up to 4f and the density fitting set is quite rich, so its reduction must be carefully tested. Second, gold clusters are expected to be one of the most important applications of the present method in future works; therefore, it is very important to properly assess and to validate a robust choice of the density fitting for Au atom to be employed on larger systems.

The calculations have been performed at scalar relativistic level with Zero Order Relativistic Approximation (ZORA). The interatomic distance of 2.47Å has been employed, and both DZ and TZ2P basis sets (with frozen core up to Au 4f) have been tested. The photoabsorption of Au_2 calculated with the DZ basis set is considered in **Figure 5.5**, with convolution $\omega_i = \eta = 0.30eV$: the upper panel shows the photoabsorption with polarization parallel (Z) to the bond direction and the lower panel with perpendicular (X) polarization. The corresponding transitions calculated by ADF have been reported in **Table 5.1**, together with their nature in terms of one-electron excited configurations. For the new algorithm, the density fitting set has been reduced to 5s 4p 4d 1f for a total of 44 functions, with respect to the original set of 25s 15p 12d 8f 7g for a total of 249 functions, with a reduction of almost a factor of 6. Starting with the Z dipole absorption spectrum (Σ_u transitions), the most intense line is found at 8.50 eV; its nature consists in a mixing of two configurations: 62% $8\pi_g \rightarrow 9\pi_u$ and 17% $14\sigma_g \rightarrow 9\pi_u$, and the molecular orbitals involved are contributed by Au 5d and Au 6p for the initial and final states, respectively. The new algorithm simulates very well the ADF results in terms of intensity, although the excitation energy is underestimated by 0.2 eV. The other two transitions at lower energy are very well described in terms of excitation energy; the only observed discrepancy is a slight intensity overestimate of the band at 3.23 eV. Similar agreement is found for the X dipole component (subspecies of Π_u transitions), with only minor discrepancies in the intensity for the weaker transition at

7.30 eV and in the excitation energy of the transition at 11.40 eV an error of only 0.1 eV.

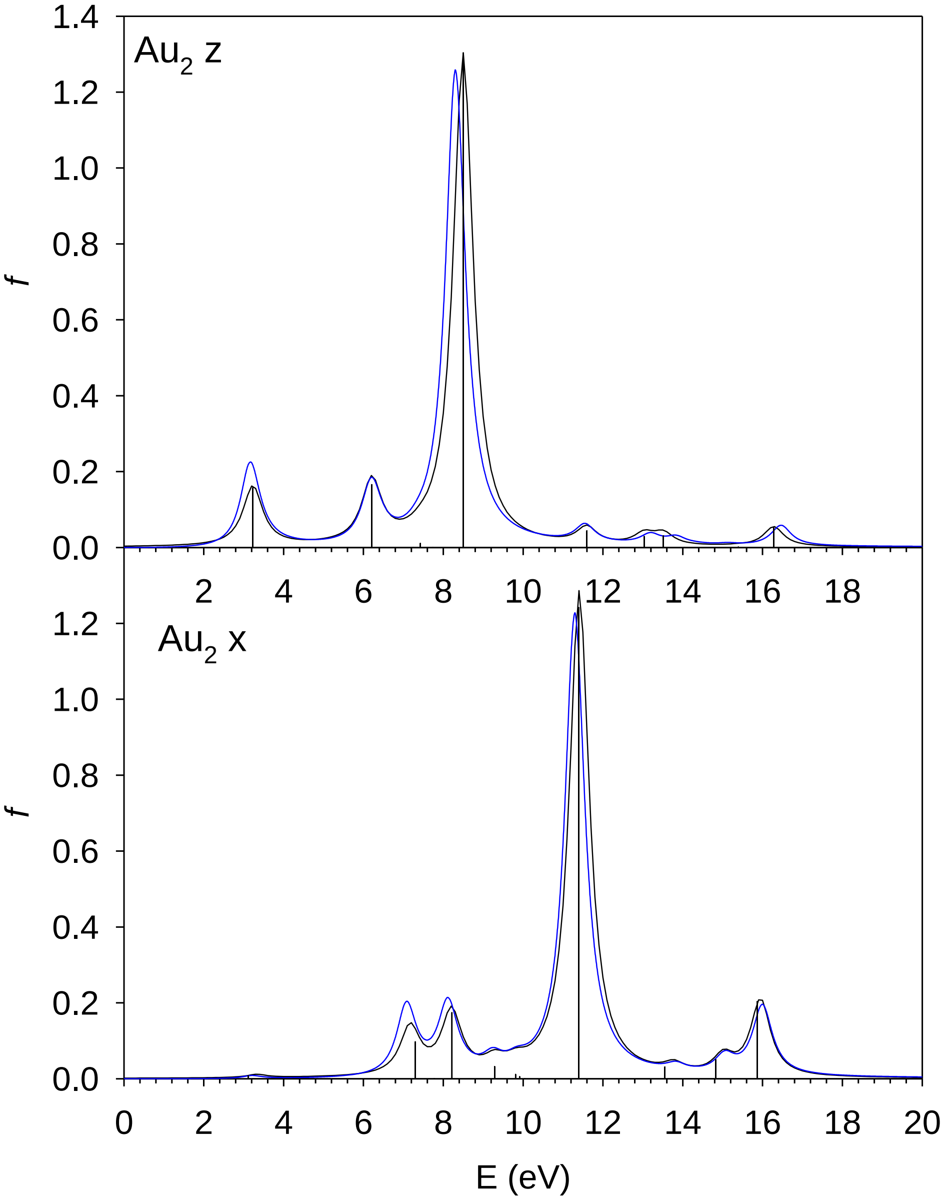

Figure 5.5 *Calculated TDDFT valence photoabsorption spectra of Au$_2$ for polarization along the bond (Z direction, upper panel) and perpendicular to the bond (X direction, lower panel) with DZ basis set. ADF results (black lines) compared with present algorithm (blue line).*

Transition	E (eV)	*f*	assignment
$1\Sigma_u$	3.23	0.157	100% $14\sigma_g$ (86% 6s 14% $5d_{z^2}$) $\rightarrow$ $14\sigma_u$ (78% 6s 18% $6p_Z$)
$3\Sigma_u$	6.21	0.165	78% $13\sigma_g$ (85% $5d_{z^2}$ 14% 6s) $\rightarrow$ $14\sigma_u$
$7\Sigma_u$	8.50	1.299	62% $8\pi_g$ (100% $5d_{xz}$) $\rightarrow$ $9\pi_u$ (100% $6p_{x,y}$)
			17% $13\sigma_u$ (99% $5d_{z^2}$) $\rightarrow$ $15\sigma_g$ (95% $6p_z$)
$2\Pi_u$	7.30	0.097	69% $14\sigma_g$ $\rightarrow$ $9\pi_u$
			28% $4\delta_g$ (100% $5d_{xy,x^2-y^2}$)$\rightarrow$ $9\pi_u$
$4\Pi_u$	8.22	0.174	62% $4\delta_g$ (100% $5d_{xy,x^2-y^2}$)$\rightarrow$ $9\pi_u$
			17% $14\sigma_g$ $\rightarrow$ $9\pi_u$
$9\Pi_u$	11.40	1.241	44% $4\delta_u$ (100% $5d_{xy,x^2-y^2}$)$\rightarrow$ $9\pi_g$ (98% $6p_{x,y}$)
			20% $13\sigma_u$ 99z2 (99% $5d_{z^2}$)$\rightarrow$ $9\pi_g$ (98% $6p_{x,y}$)
$12\Pi_u$	15.87	0.204	98% $8\pi_g$ $\rightarrow$ $16\sigma_u$ (84% $6p_z$)

***Table 5.1** Relevant TDDFT dipole allowed excitations of Au_2 (DZ basis set, LB94 potential, and ZORA scalar relativistic) calculated by ADF.*

In **Figure 5.6**, the Z component has been calculated with the TZ2P basis set; a reduced density fitting set of 5s 4p 4d 1f 2g functions has been employed for the new algorithm. The quality of the agreement is comparable with that obtained with the DZ basis set, and it is worth noting that the main effect of an enlarged basis set in the ADF calculations consists in a shift to lower energy (by 0.5 eV at most) and a moderate intensity reduction. Both of them are very well reproduced by the new algorithm as well.

As a general statement, we can say that the new TDDFT complex polarizability algorithm performs very well on Au_2 if compared with the standard TDDFT Casida implementation of ADF, with expected deviations limited to few tenths of eV for the excitation energies and robust intensity reproduction and with modest deviations found for the weaker transitions.

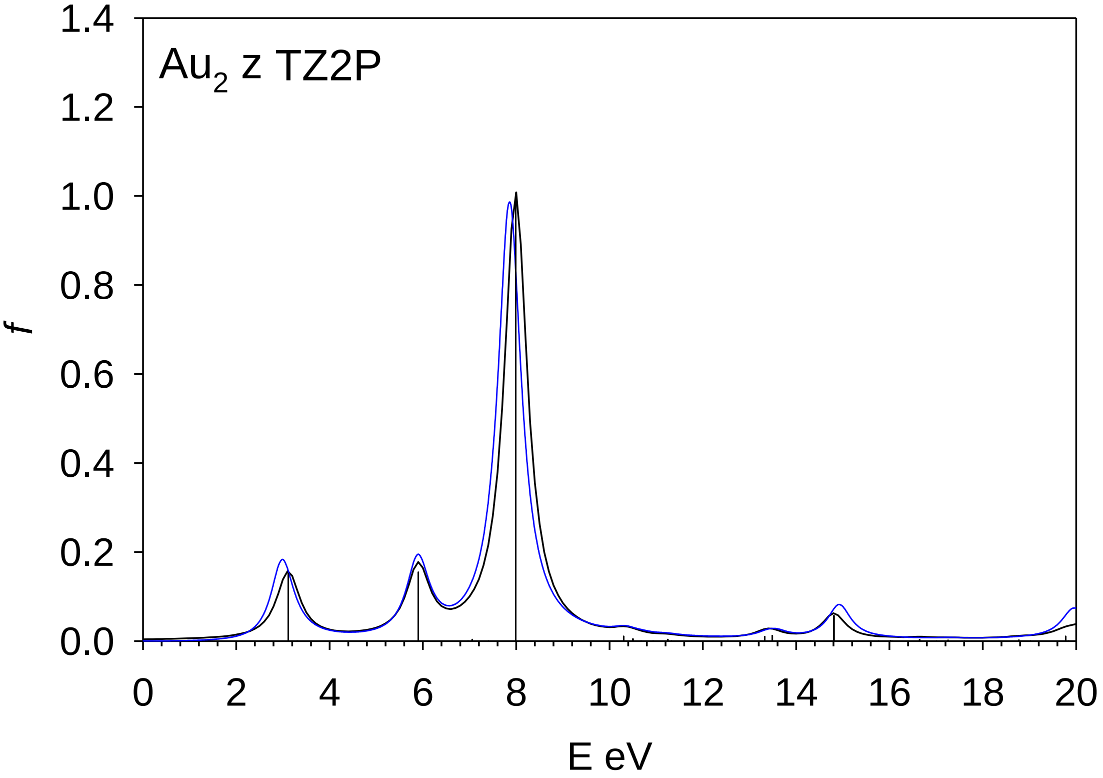

Figure 5.6 *Calculated TDDFT valence photoabsorption spectra of Au$_2$ for polarization along the bond (Z direction) with TZ2P basis set. ADF results (black lines) compared with present algorithm (blue line).*

5.4.4 H$_2$O

Water molecule has been calculated at DZP level. The absorption spectrum for both Y direction (in the molecular plane) and Z direction (C2 axis) is considered in **Figure 5.7**, with convolution $\omega_i = \eta = 0.30\ eV$. The original density fitting auxiliary basis set for O atom, consisting of 68 functions (10s 5p 4d 2f 1g), has been reduced to 24 functions (2s 4p 2d) while for H atom; the original set of 39 functions (4s 3p 2d 1f 1g) has been reduced to 5 functions (2s 1p). Two transitions are found when the polarization is along Y (b_2), a weaker one at 12.63 eV ascribed to a 100% $3a_1 \rightarrow 2b_2$ transition, and a stronger one at 14.08 eV (100% $1b_2 \rightarrow 4a_1$). The spectrum calculated by complex polarizability algorithm is in good agreement with ADF for both transition energy (with deviations around 0.1 eV) and intensity; only for the weaker transition, the intensity appears slightly overestimated. When the Z dipole component is considered, a single transition is found at 10.24 eV assigned as a 100% $3a_1 \rightarrow 4a_1$ excitation; this time the new algorithm overestimates the transition energy by 0.15 eV and the intensity by 10%. The discrepancies with respect to ADF are limited to 0.15 eV also for H2O, and therefore, they are of the same size as found for previous biatomic systems.

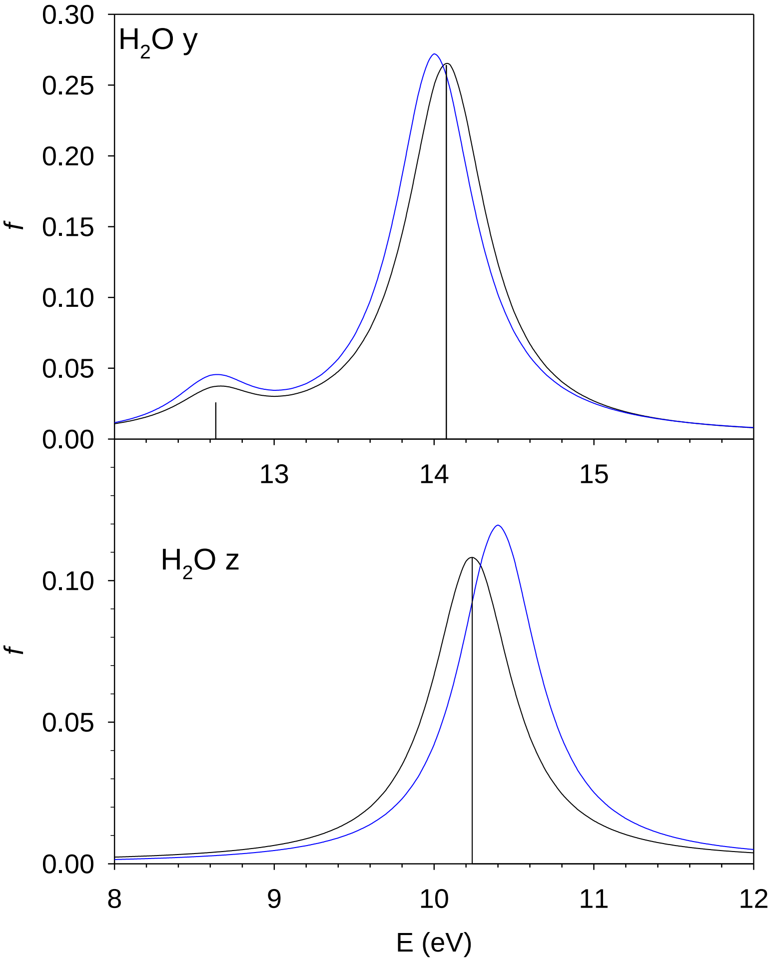

Figure 5.7 *Calculated TDDFT valence photoabsorption spectra of* H_2O *for polarization along the Y (upper panel) and Z (lower panel) directions. ADF results (black lines) compared with present algorithm (blue line).*

5.4.5 Au$_{86}$

Since, up to now, the complex polarizability algorithm has been validated on simple small systems of different nature comparing individual transitions with respect to ADF, it is now necessary to assess its performances in terms of accuracy and computational economy also on larger systems, which we expect should represent the target of its future applications. We have taken into account first the Au$_{86}$ gold nanowire, which has been already considered in our previous work, employing a DZ basis set and LB94 exchange correlation potential and displays a strong longitudinal plasmon around 2.35 eV [5.37]. Plasmons are photoabsorption features which start to appear when the metal (typically gold or silver) cluster size is beyond 2 nm for gold and are associated to free (collective) oscillations of the conduction band electrons and give rise to the so-called Surface Plasmon Resonance (SPR). Note that the longitudinal size of Au$_{86}$ is 2.59 nm.

In **Figure 5.8**, the calculated spectra with both ADF and complex polarizability methods are compared: the new algorithm performs very well and the maximum absorbance at 2.35 eV is quantitatively reproduced. Moreover, it allows to calculate the spectrum at higher energy. In the figure, we have reported the photoabsorption up to 5 eV calculated truncating the expression of Equation (5.2.15) with an energy cutoff of 7 eV, a value which is high enough to display the opening of the deeper excitations arising from the Au 5d band, which start to show up around 4.5 eV. In the inset of the upper panel, we reported a sketch of an isosurface of the imaginary part of the perturbed density, calculated from the ***b*** vector solution of Equation (5.2.8) at 2.35 eV: the dipolar shape is indicative of a typical plasmonic behaviour. Its nature can be further analysed by means of the TCM plot reported in the lower panel of **Figure 5.8**: the “spots” are indicative of contribution from one-electron configuration associated with a pair of orbital energies (occupied on the X axis (ε_i) and virtual on the Y axis(ε_a)). The solid black diagonal line corresponds to an eigenvalue difference equal to the excitation energy (2.35 eV) while the dashed black diagonal line corresponds to the maximum (cutoff) energy of 7 eV presently considered in sum (5.2.15), corresponding to the EP+1 knot in **Figure 5.1**. In order to properly discuss TCM and extract maximum information from it, it is useful to analyze the KS electronic structure of such cluster: the Fermi energy is at -10.02 eV, and the s band lies in the interval from -11 to -10 eV, while the d band is mainly located below -12 eV for occupied orbitals, while virtual orbitals are all mixed 6s-6p, with 6p contribution gradually increasing with energy. The maximum contribution to the absorption is given by intra-band 6s → 6s 6p transitions, in line with strong plasmonic behaviour, while the 5d → 6s 6p contribution is very low. It is well known that the plasmon intensity of gold is screened by intra-band 5d → 6s 6p response [5.18], such screening is weak in present case, and therefore, the plasmon gains intensity and appears rather strong. The TCM analysis is also very useful since it shows that the contributions from energy configurations decrease rapidly as the difference between the occupied-virtual eigenvalues moves away from the excitation energy (solid line), so the cutoff at 7 eV is justified a posteriori. Of course, if one would be interested to analyse the spectrum also above the plasmon, such cutoff should be shifted at higher and higher energy. However, the TCM analysis allows easily to check if the cutoff has been properly chosen or needs to be further shifted at higher energy. It is worth noting that if very high excitation energy were considered, a lower cutoff would be chosen as well, for example, in the case of core electron excitations [5.38].

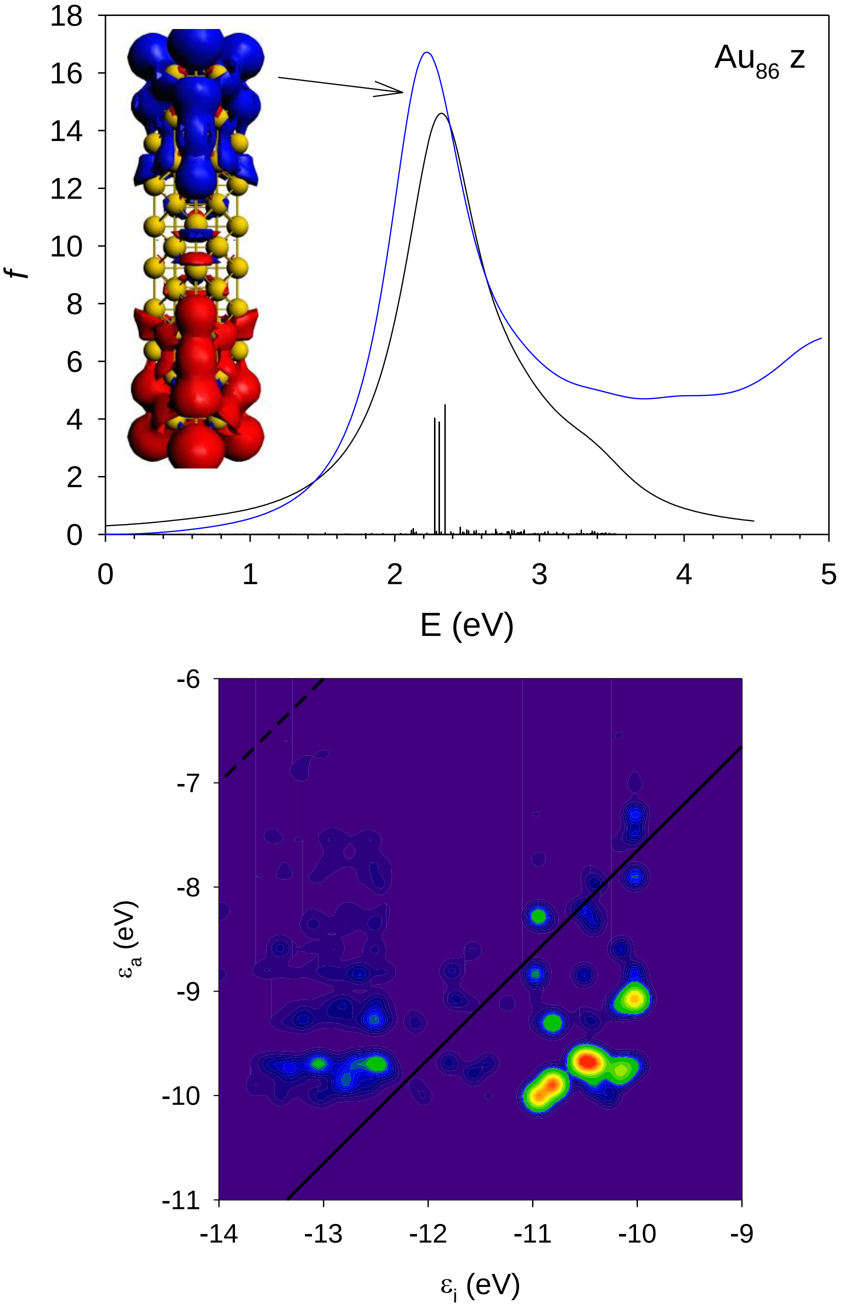

Figure 5.8 *Calculated TDDFT valence photoabsorption spectra of* Au_{86} *for polarization along the longitudinal direction (upper panel). ADF results (black lines) compared with present algorithm (blue line), inset: imaginary induced density at 2.35 eV. Lower panel: TCM analysis at 2.35 eV, x and y axes refer to occupied and virtual eigenvalues, respectively.*

5.4.6 [Au_{147}]$^-$

In Au_{86}, the plasmon is very strong because the long longitudinal cluster size (2.59 nm) allows the collective effects to be prevailing with respect to the screening of the Au 5d band. However, if the cluster is larger but more spherical, the plasmon is less easy to be identified, due to its lower intensity and also because it is overwhelmed by the very intense 5d → 6s 6p interband transitions. For this reason, we have considered the [Au_{147}]$^-$ cluster in a previous study [5.37], whose structure was optimized starting by from an icosahedral symmetry with a D5d symmetry constraint, the relaxed structure was only slightly distorted with respect to *Ih*. The negative charge is chosen in order to have a closed-shell electronic structure. Due to the relaxed reduced D_{5d} symmetry constraint, the dipole allowed symmetries are A_{2u} and E_{1u} and the absorption spectrum is their sum. Since we are interested to compare the present complex polarizability algorithm with respect to ADF, we have limited the analysis to the A_{2u} symmetry alone; since for such representation, it is possible to extract safely 300 roots up to 3.78 eV, while for the E_{1u} one, it has proven impossible to reach such excitation energy due to the already mentioned problems of the Davidson algorithm. The results concerning the only A_{2u} dipole component are reported in **Figure 5.9**; it is worth noting that all the spectral features calculated by ADF (in particular the maximum at 3.45 eV) are very well reproduced by the new algorithm in terms of excitation energy, while the intensity is overestimated by a factor of two. It is worth noting, however, that the complex polarizability includes excitations up to 7 eV, so we attribute the disagreement to a kind of “background” intensity deriving from the “tail” of the higher energy excitations, which is correctly included in the complex polarizability but is missing in ADF. In this case, we have also tested if the calculation of the $\langle f_\mu | \sigma\tau \rangle$ three centres integrals of Equation (5.2.19) would have improved the agreement between ADF and the new complex polarizability algorithm. However, also in this case, the contribution of the three centres integrals has proven irrelevant, so this approximation is not the origin of the found disagreement. The inset in the upper panel refers to the induced density calculated at the photon energy of the maximum. Also in this case, a typical dipolar shape is obtained, as expected for a SPR. In general, it is not easy to identify, with other computational schemes, a weak spectral feature like the present one at 3.45 eV over a monotonic increasing background, since it may happen that the resonant intensity is washed up and becomes confused with the background. For example, the truncated octahedral Au_{140} cluster did not show any feature at TDDFT level calculated with a time-evolution algorithm, although a weak plasmon would have been expected [5.9].

In the lower panel of **Figure 5.9**, the TCM analysis is reported, performed at a photon energy of 3.45 eV which corresponds to the maximum of absorption. In this case, the Fermi energy is at -7.90 eV, the Au 6s band lies between -9 and -8 eV, and the Au 5d lies between -10 eV and -12 eV for occupied orbitals while virtual orbitals are all of mixed 6s-6p nature. This time, the leading contributions come from the intra-band Au 5d → Au 6s 6p configurations (around -11 eV in the occupied eigenvalues scale) and from the Au 6s → Au 6s 6p ones (around -8 eV in the occupied orbital scale), both of them are placed very near to the diagonal corresponding to the eigenvalue difference equal to 3.45 eV. At variance with Au_{86}, in $[Au_{147}]^-$, the plasmon appears damped by the strong screening from the intra-band Au 5d → Au 6s 6p response. Such TCM analysis is consistent with the ADF one: such comparison is relatively easy in this case because in ADF there are two lines at 3.37 eV and 3.47 eV which are much more intense than the other ones, so analysis can be restricted only to these lines. In other circumstances, namely, when one band corresponds to the convolution of many transitions of comparable intensity, TCM is much more convenient, since it can be performed by just taking the excitation energy of the maximum. On the other hand, in ADF, such situation would be almost impracticable, since one should analyse one by one, all the transitions which lie in the energy interval centred on the band maximum with wideness comparable to the FWHM employed for the convolution.

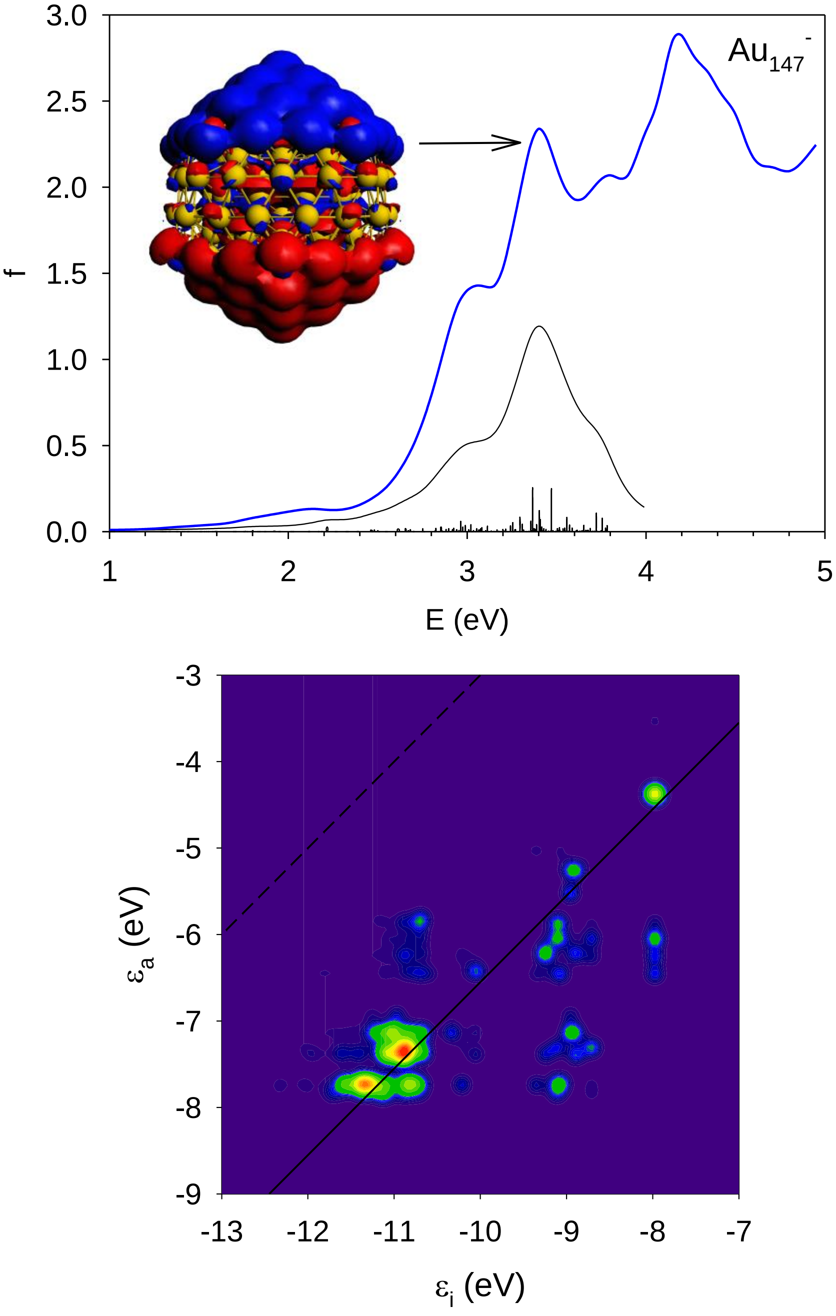

Figure 5.9 *Calculated TDDFT valence photoabsorption spectra of* D_{5d} $[Au_{147}]^-$ *for polarization along the* C_5 *axis (*A_{2u} *dipole component). ADF results (black lines) compared with present algorithm (blue line), inset: imaginary induced density at 3.45 eV. Lower panel: TCM analysis at 3.45 eV, x and y axes refer to occupied and virtual eigenvalues, respectively.*

The plasmonic nature of the absorption can be also investigated by means of the scaling factor method suggested by Jacob [5.33], which consists to follow the excitation energies evolution with respect to the scaling factor λ (as outlined in previous Sec. **5.3**): plasmonic excitations are characterized by a strong sensitivity of the excitation energy with respect to λ. In **Figure 5.10**, we have reported such analysis for both Au_{86} and $[Au_{147}]^-$, calculating the spectra with λ from 0 to 1 with step 0.2. The position of the maximum changes dramatically with respect to λ, in particular the maximum shifts to higher energy by 0.6 eV in $[Au_{147}]^-$ and by 0.4 eV in Au_{86} on going from $\lambda = 0$ to $\lambda = 0.2$. Interestingly, the energy shift is followed by a strong intensity reduction for the former and by a substantial intensity conservation for the latter. Due to the Thomas-Reiche-Kuhn (TRK) sum rule which states that the integral of oscillator strengths over the whole electronic spectrum must be equal to the number of electrons, we expect that the intensity for $[Au_{147}]^-$ will show up at higher energy.

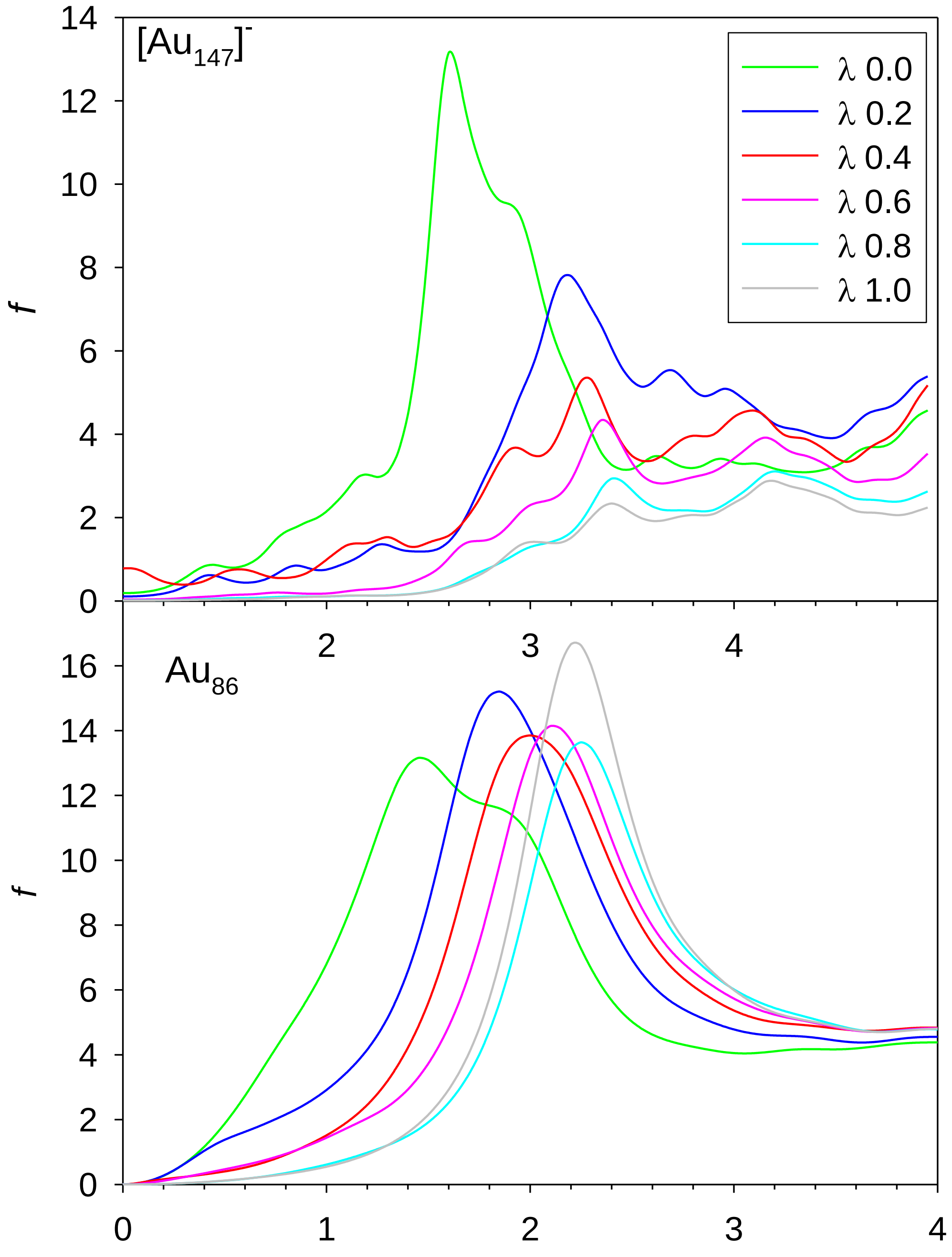

Figure 5.10 *Plasmon analysis according to Jacob. Upper panel: D_{5d} $[Au_{147}]^-$ (A_{2u} dipole component) and lower panel: Au_{86} longitudinal dipole component. Spectra calculated with present complex polarizability algorithm with different values of scaling factor parameter λ.*

5.5 Conclusions

In this work, we have developed and implemented a new algorithm within the ADF code, to solve the TDDFT equations in the space of the density fitting auxiliary basis set. The method extracts the spectrum from the imaginary part of the polarizability at any given photon energy, so the numerical part consists to solve a non-homogeneous system of linear algebraic equations, which can be managed by ScaLAPACK parallel library, avoiding the bottleneck of Davidson diagonalization. The original idea, which makes the present scheme very efficient, consists in the simplification of the double sum over occupied-virtual pairs in the definition of the dielectric susceptibility, allowing an easy calculation of such matrix as a linear combination of constant matrices with photon energy dependent coefficients. The method has been applied to very different systems in nature and size (from H_2 to $[Au_{147}]^-$) in order to gain a global sensitivity about its accuracy and efficiency. In all cases, the maximum deviations observed with respect to ADF are below 0.2 eV, making the present algorithm a well balanced compromise, sacrificing some accuracy in favour of the efficiency and the capability to calculate the spectrum up to high energy together with wide analysis possibilities. In fact, the new algorithm has the merit not only to calculate the spectrum at whichever photon energy (at variance with the Casida formulation) but also to allow a deep analysis of the results, in terms of TCM, Jacob plasmon scaling factor, and induced perturbation analysis, which have been all implemented. Further applications to large non symmetric metal clusters are under study.

A possible extension of the method may include an automatic selection of the fitting functions, which must be done by the user at the moment.

It is worth noting that, although the point symmetry group is only partially exploited in the present implementation, the computational effort needed to treat large gold clusters has proven to be even lower than by ADF, which exploits instead the full symmetry. Therefore, we expect that the present scheme would be very efficient to treat also large systems with low symmetry, a typical situation met for metal clusters protected by ligands. In summary, we believe that the present method can represent a general and efficient way to apply TDDFT to very large systems, allowing specific applications on large metal clusters protected by ligands, which represents a rapidly developing field where theory can help to simulate optical properties of new materials and rationalize them in terms of electronic structure.

6 Crystal Structure and Theoretical Analysis of Green Gold $Au_{30}(S\text{-}tBu)_{18}$ Nanomolecules and its Relation to $Au_{30}S(S\text{-}tBu)_{18}$

Amala Dass, Tanya Jones, Milan Rambukwella, David Crasto, Kevin J. Gagnon, Luca Sementa, Martina De Vetta, Oscar Baseggio, Edoardo Aprà, Mauro Stener, Alessandro Fortunelli, The Journal of Physical Chemistry C, DOI: 10.1021/acs.jpcc.6b00062

We report the complete X-ray crystallographic structure as determined through single crystal X-ray diffraction and a thorough theoretical analysis of the green gold $Au_{30}(S\text{-}tBu)_{18}$. While the structure of $Au_{30}S(S\text{-}tBu)_{18}$ with 19 sulfur atoms has been reported, the crystal structure of $Au_{30}(S\text{-}tBu)_{18}$ without the μ_3-sulfur has remained elusive until now, though matrix-assisted laser desorption ionization mass spectrometry (MALDI-MS) and electrospray ionization mass spectrometry (ESI-MS) data unequivocally shows its presence in abundance. The $Au_{30}(S\text{-}tBu)_{18}$ nanomolecule is not only distinct in its crystal structure but has unique temperature dependent optical properties. Structure determination allows a rigorous comparison and an excellent agreement with theoretical predictions of structure, stability, and optical response.

6.1 Introduction

Gold-thiolate nanomolecules, $Au_n(SR)_m$ are compounds with a fixed number n of gold atoms which are stabilized by passivating organic thiolate ligands *m* [6.1]. For instance, $Au_{25}(SR)_{18}^{-1,0}$, $Au_{38}(SR)_{24}$, and $Au_{144}(SR)_{60}$, are some of the most commonly studied nanomolecules, with size dependent and unique chemical and physical characteristics [6.2][6.3][6.4][6.5]. Griffin and coworkers and others showed that self-assembled monolayers on a Au (111) substrate with mixed tert-butanethiol and n-octadecanethiol ligands were prepared, revealed less-densly packed monolayers (SAMs) with increasing amount of tert-butanethiol, demonstrating that the bulkiness of the thiolate ligand modifies the packings of the SAMs [6.6]. Less common nanomolecules such as Au_{30}, Au_{39}, Au_{41}, Au_{65} and other clusters, have in fact been reported [6.7][6.8][6.9][6.10][6.11][6.12], synthesized using sterically hindered bulky ligands. Aromatic thiolate ligands have also been shown to lead to uncommon altered cluster sizes [6.13][6.14][6.15][6.16]. Aromatic thiols introduce an additional complication as aromaticity and bulkiness are coupled in an intricate way, so that it is not possible to attribute the changes in geometric and electronic structure to bulkiness only. Because of this complex panorama, structural and geometric studies are highly reliant on the identification of crystallographic structure of the nanomolecules.

In this study we follow this line of research. We focus on a specific compound: $Au_{30}(S\text{-}tBu)_{18}$, which had been identified so far only through mass spectrometry (MALDI-MS) and electrospray ionization mass spectrometry (ESI-MS) [6.9] but whose crystallographic structure had remained elusive until now, and determine its crystallographic data. Its properties can so be thoroughly compared with that of a homologous $Au_{30}S(S\text{-}tBu)_{18}$ compound, whose structure had been previously reported [6.10], thus providing an in-depth analysis on the composition, electronic, optical, and chiroptical properties. In addition to reporting the first crystallographic structure of the $Au_{30}(S\text{-}tBu)_{18}$ nanomolecule in two distinct packing structures, (space groups $P2_1/n$ and P-1), determined through the use of single crystal X-ray diffraction, we detail the unique temperature-dependent optical properties of $Au_{30}(S\text{-}tBu)_{18}$ and compare these optical properties with theoretical predictions obtained using time-dependent density-functional theory (TDDFT).

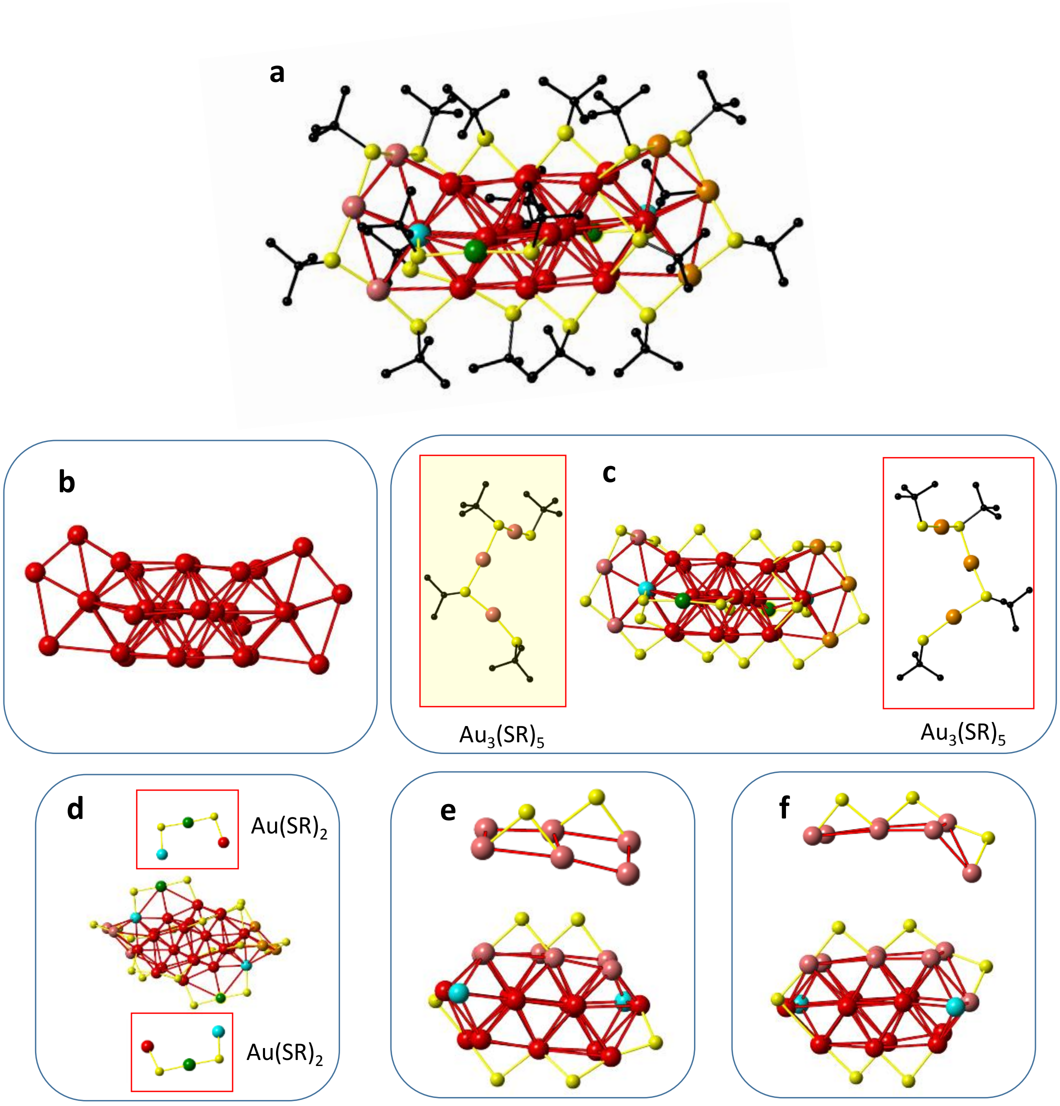

***Figure 6.1** Single crystal XRD structure of $Au_{30}(S\text{-}tBu)_{18}$. (a) Total structure of $Au_{30}(S\text{-}tBu)_{18}$ (hydrogen atoms are omitted for clarity); (b) Au_{30} skeleton showing an interpenetrating bicuboctahedral core geometry; (c) $Au_{30}S_{18}$ geometry showing the two trimeric [-SR-Au-SR-Au-SR-Au-SR-] units, highlighted in the red boxes inset; (d) $Au_{30}S_{18}$ geometry showing the two monomeric [-SR-Au-SR-] units, highlighted in the red box as inset (carbon atoms are omitted in (c) and (d) for clarity); (e and f) the positions of the rest of the SR groups on the Au_{22} bicuboctahedral substructure.*

6.2 Results and Discussion

$Au_{30}(S\text{-}tBu)_{18}$ was synthesized in a one-pot THF method (see Experimental Section for details), and crystallization was performed via vapor / vapor diffusion of hexane into a toluene solution of $Au_{30}(S\text{-}tBu)_{18}$. Small green needle-like crystals were obtained after 4-7 days. These needle-like crystals are different than the rhombic shaped plate-like crystals of $Au_{30}S(S\text{-}tBu)_{18}$.

6.2.1 Experiment: Structure

Figure 6.1.a presents the total structure of the bicuboctahedron $Au_{30}(S\text{-}tBu)_{18}$ cluster, which crystallizes in the space group $P2_1/n$. The structure was refined to a resolution of 1.06 Å, and to value of R1 = 10.93%. **Figure 6.1.b** shows the Au_{30} skeleton with an interpenetrating bicuboctahedral core. The geometry, shown in **Figure 6.1.c** represents the Au-SR staples and bond structures of $Au_3(SR)_4$. **Figure 6.1.d** represents the $Au_{30}S_{18}$ geometry highlighting the two monomeric [-SR-Au-SR-] units. The structure of $Au_{30}(S\text{-}tBu)_{18}$ is an oblate configuration composed of a Au_{20} polytetrahedral core with its tips symmetrically capped by two $Au_3(S\text{-}tBu)_4$ units and its central body wrapped by four $Au(S\text{-}tBu)_2$ units and two S-tBu groups in bridge sites between two Au atoms, see **Figure 6.1**. A second synthesis resulted in a different crystal structure containing the same bicuboctahedron $Au_{30}(S\text{-}tBu)_{18}$ cluster. It crystallizes in the space group *P-1* and refined to a resolution of 0.81 Å, and to a value of R_1 = 5.26%. The local structure in the cluster is the same between the two structures; however, the *P-1* structure contains more pronounced terminal S-Au-S disorder. The poor quality of the $P2_1/n$ structure did not allow for anisotropic refinement of the carbon atoms in the t-butyl thiol groups. In both structures, the external solvent contents could not be identified and were removed utilizing the SQUEEZE [6.17] program as implemented in the program PLATON [6.18].

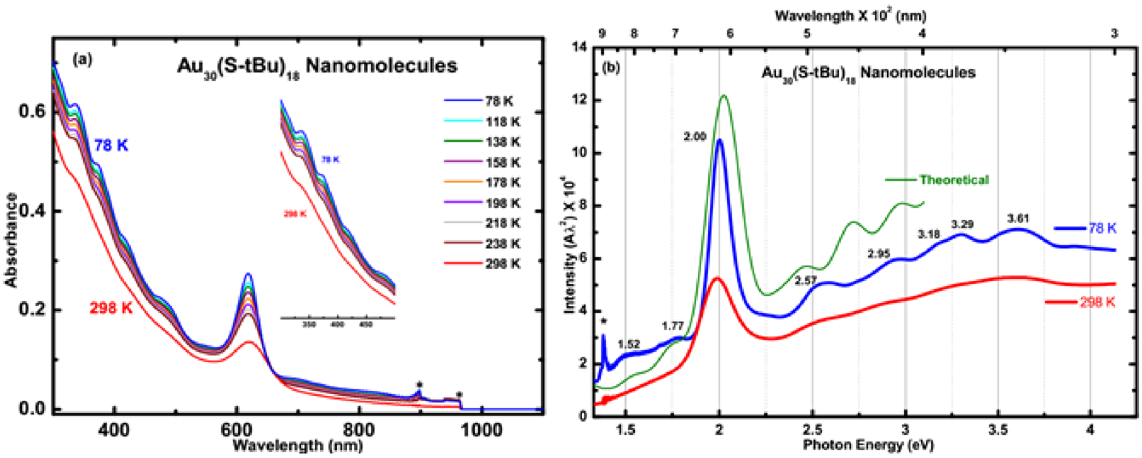

Figure 6.2 *(a) Temperature-dependent UV-vis-NIR absorption spectra of* $Au_{30}(S\text{-}tBu)_{18}$ *nanomolecules in 3-methyl-tetrahydrofuran solvent. (b) Temperature-dependent UV-vis-NIR* $Au_{30}(S\text{-}tBu)_{18}$ *nanomolecules plotted as photon energy where peaks marked by asterisk shows an instrumental artifact.*

6.2.2 Experiment: optical spectroscopy

UV-vis-NIR absorption response of $Au_{30}(S\text{-}tBu)_{18}$ is measured in 2-metyltetrahydrofuran at predetermined temperatures upon equilibrating at each temperature for 3-5 minutes as shown in **Figure 6.2.a**. Temperature dependent optical absorption spectra of the nanomolecules showed increased absorption features, with no shift of absorption maxima, and well resolved new vibronic peaks at lower wavelengths (~300 to ~550) nm. **Figure 6.2.b**, absorption intensity spectra plotted against photon energy, shows ~ five distinct peaks in between 2.25 eV and 3.75 eV range and two new peaks in low energy region.

6.2.3 Theory: structural analysis

Local geometry relaxation employing density-functional theory (DFT) and the Perdew–Burke–Ernzerhof (PBE) exchange-correlation (xc-) functional [6.19] were performed on the crystallographic determined structural model of $Au_{30}(S\text{-}tBu)_{18}$, reporting the full Cartesian coordinates in the Supplementary Information. It is interesting to compare the $Au_{30}(S\text{-}tBu)_{18}$ atomistic arrangement here determined for the

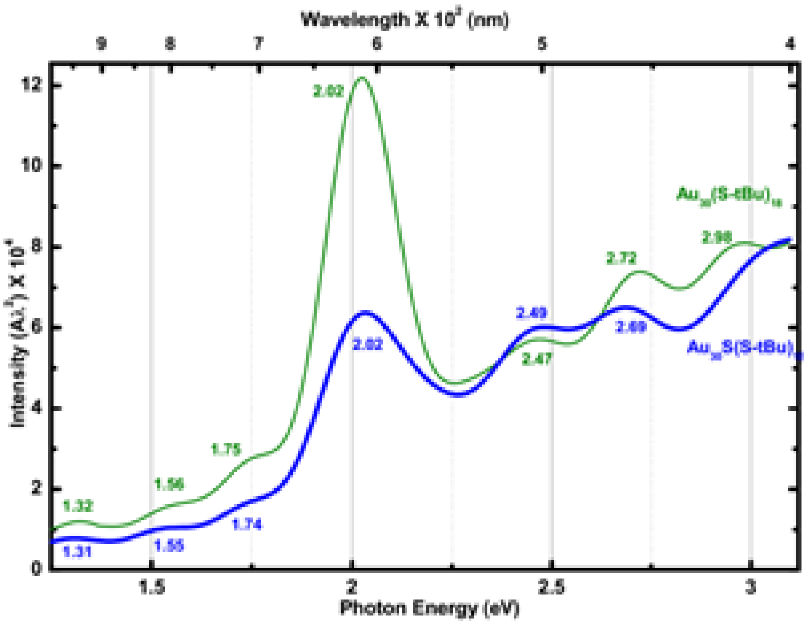

Figure 6.3 *Theoretical UV-vis-NIR of $Au_{30}(S\text{-}tBu)_{18}$ and $Au_{30}S(S\text{-}tBu)_{18}$ nanomolecules plotted as photon energy.*

first time with that of the homologous $Au_{30}S(S\text{-}tBu)_{18}$ compound whose stoichiometry differs only by addition of a S atom, determined in previous work [6.10]. We recall that in the $Au_{30}(S\text{-}tBu)_{18}$ structure a Au_{20} oblate core is protected by two $Au_3(S\text{-}tBu)_4$ and four $Au(S\text{-}tBu)_2$ units and two bridge S-tBu groups, see **Figure 6.1**. The insertion of an S anion on a hollow site of a Au_3 facet provokes a local swelling of the coordination environment, with the added S anion-like species pushing away the S atoms of one $Au_3(S\text{-}tBu)_4$ unit, while the other atoms approximately preserve their configuration, as can be appreciated by comparing **Figure 6.4.a** and **Figure 6.4.c** (see especially the top part of the cluster). A previously proposed structural model of $Au_{30}(S\text{-}tBu)_{18}$ was obtained by erasing the added S atom in $Au_{30}S(S\text{-}tBu)_{18}$ and performing a local geometry relaxation [6.10], a procedure which has been reproduced here and leads to the structure shown in **Figure 6.4.b**. The local geometry relaxation maintains the swelling caused by the added S anion, so that in the structural model of **Figure 6.4.b**, one of the $Au_3(S\text{-}tBu)_4$ units is somewhat detached from the rest of the cluster. A more compact and thus energetically more favorable coordination (lower in energy by 0.39 eV) is restored in the $Au_{30}(S\text{-}tBu)_{18}$ crystal structure illustrated in **Figure 6.4.c**, proving the structural fluxionality of these monolayer-protected systems. Knowledge of the correct structure improves the comparison of experimental and simulated optical absorption spectrum, vide infra.

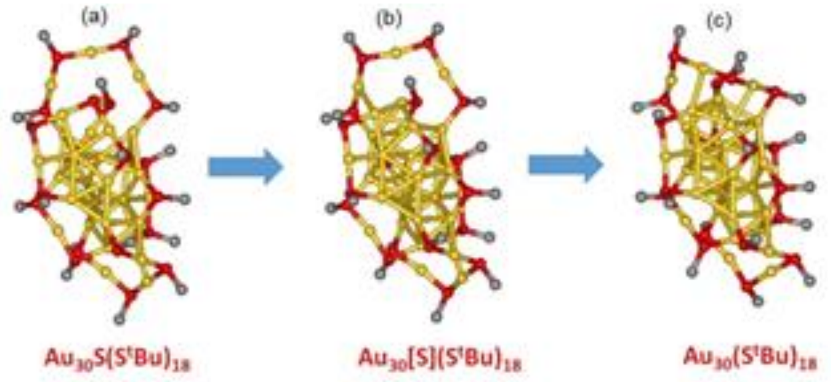

Figure 6.4 *Schematic depiction of the clusters investigated in the present work: (a) $Au_{30}S(S\text{-}tBu)_{18}$ with an arrow highlighting the additional S atom; (b) $Au_{30}S(S\text{-}tBu)_{18}$ as obtained by a local relaxation of $Au_{30}S(S\text{-}tBu)_{18}$ after erasing the additional S atom; (c) $Au_{30}(S\text{-}tBu)_{18}$;. The methyl atoms are not shown for clarity of illustration.*

6.2.4 Theory: optical spectroscopy

The optical absorption spectrum of $Au_{30}(S\text{-}tBu)_{18}$ was simulated via time-dependent DFT (TDDFT) using two different xc-functionals: B3LYP [6.20][6.21] and SAOP [6.22], see the Method section for more details. This allows us to compare the result of a hybrid (B3LYP) xc-functional and a semi-local Coulomb-corrected (SAOP) one, where a hybrid xc-functional is here employed to the best of our knowledge for the first time to predict the optical response of monolayer-protected clusters. In **Figure 6.2.b** the TDDFT/B3LYP spectrum is reported together with the experimental one. The agreement between experimental and simulated optical absorption spectra is excellent, and is here improved by the use of the correct structural model with respect to previous work, see **Figure 6.4.a** of ref. [6.10]. The intense peak at 2 eV in the experiment is predicted at 2.04 eV by theory, while minor features between 2.45 and 3 eV are also present which parallel the experimental ones in the same energy range. The TDDFT/SAOP spectrum is also reported in the Supplementary Information and compares well with both the TDDFT/B3LYP and experimental spectra. As the

TDDFT/B3LYP simulation is obtained by a real time propagation of the electronic density, an analysis of the excitation components is not possible. This is instead readily available via the TDDFT/SAOP approach. Focusing on the band around 2 eV, which is the counterpart of the experimental peak at 620 nm in **Figure 6.2.a**, we find that is contributed by many discrete transitions (see **Figure S5** in the Supplementary Information), of which two are the most prominent:

- one at 1.92 eV with main single-particle components: 42% HOMO→LUMO+2; 18% HOMO-3→LUMO ; 14% HOMO-4→LUMO
- one at 1.98 eV with main single-particle components: 43% HOMO→LUMO+4; 22% HOMO-5→LUMO ; 12% HOMO→LUMO+2

where HOMO is the Highest-Occupied Molecular Orbital and LUMO is the Lowest-Unoccupied Molecular Orbital. The molecular orbitals involved in such transition are illustrated in **Figure 6.5**. It is interesting to note that : (i) the occupied orbitals display contribution from both gold and sulfur, while in the virtual orbitals the sulfur contribution is marginal (i.e., both excitations can be classified as transitions from the Au-S bonds to the Au 6s-6p conduction band), and (ii) the HOMO belongs essentially to the metal Au 6s band and therefore is very delocalized, whereas the other occupied orbitals are more located on the Au-S bonds, with the 5d contribution the largest one on the gold atom.

6.3 Conclusions

Determination of crystal structure of monolayer-protected gold clusters is a crucial step to achieve in-depth understanding and control of the properties and functionalities of this class of materials. In the present work we were able to determine the crystallographic structure of $Au_{30}(S\text{-}tBu)_{18}$, a compound exhibiting peculiar optical absorption in the visible region of the spectrum conferring it a characteristic color and making it a unique "green gold" species, whose structure had remained elusive until

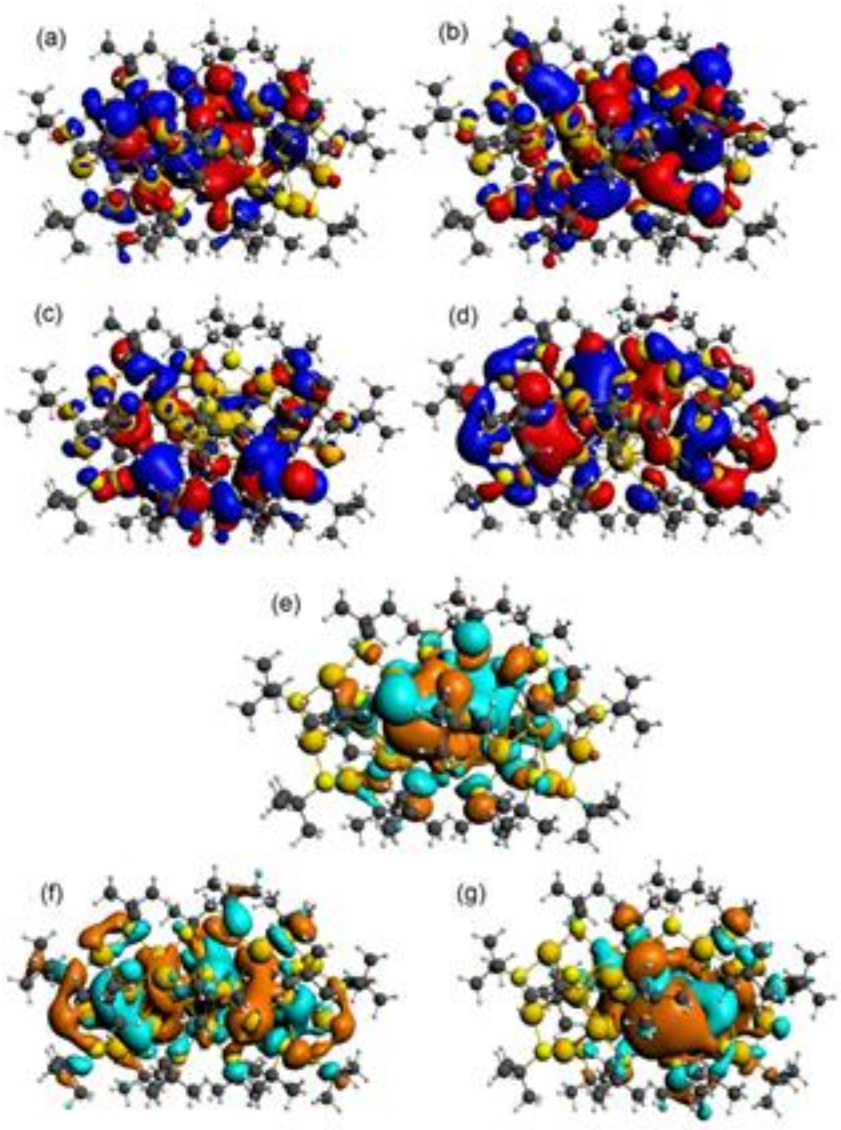

Figure 6.5 *Plot of the orbitals mainly involved in the peak around 2 eV: (a) HOMO-5; (b) HOMO-4; (c) HOMO-3; (d) HOMO; (e) LUMO; (f) LUMO+2; (g) LUMO+4. Red/orange and blue/light-blue, respectively, correspond to opposite signs of the wave function. Red/blue and orange/light-blue correspond to occupied and virtual orbitals, respectively.*

now despite its presence in massive form had been demonstrated via mass spectrometric techniques. Structure determination then allows us to pursue a stringent comparison between theory and experiment for this species, from which three major conclusions can be drawn: (i) a great structural fluxionality with the existence of low-energy, subtly different isomers, (ii) an extreme sensitivity of optical response to geometrical details, (iii) the possibility of achieving, through advanced computational tools, an excellent agreement between simulated and observed quantities. The present achievement opens the way to further investigations aimed at exploiting the unique optical features of this compound and tuning them to e.g. biochemical and opto-electronic applications.

6.4 Experimental Section

6.4.1 Materials

Sodium borohydride (Acros, 99%), tertiary butylthiol (Acros, 99%), and trans-2-[3[(4-tertbutyl-phenyl)-2-methyl-2-propenylidene] malononitrile (DCTB matrix) (Fluka≥99%) were purchased and used as received. HPLC grade solvents such as tetrahydrofuran, toluene, methanol, butylated hydroxytoluene stabilized tetrahydrofuran and acetonitrile were obtained from Fisher Scientific.

6.4.2 Synthesis

$Au_{30}(S\text{-}t\text{-}C_4H_9)_{18}$ nanomolecules were synthesized by reacting 0.1 g $HAuCl_4.3H_2O$ to 15 mL of HPLC grade THF. Followed by addition of 87 µL of HS-tBu (1:3 molar ratio) which was stirred at 450 rpm for 15 minutes. An excess of 12 mmols of $NaBH_4$ 0.113 g in 10 mL cold H_2O was added. The reaction was stopped after 1 h then washed with a combination of 5 mL water and 40 mL MeOH, 3 times. ~The crude product 200 mg was combined with 1mL toluene and 1 mL HS-tBu. The mixture of excess thiol and crude nanomaterial were etched at 70 °C for 4 hrs. After etching the product, it was washed again with a combination of 5 mL water and 40 mL MeOH, 3 times. SEC (size exclusion chromatography) was performed in order to separate $Au_{30}(S\text{-}t\text{-}C_4H_9)_{18}$ from the etched mixture SEC was repeated 3-4 times to achieve ~20 mg of pure $Au_{30}(S\text{-}t\text{-}C_4H_9)_{18}$.

6.4.3 Instrumentation

Matrix assisted laser desorption time-of-flight (MALDI-TOF) mass spectrometer was used to acquire mass spectra with DCTB matrix on a Voyager DE PRO mass spectrometer. Compositional analysis was performed with electrospray ionization mass spectra (ESI-MS), collected from Waters Synapt HDMS using THF as the solvent. Temperature dependent UV-vis-NIR absorption measurements were collected with UV-vis-NIR Cary 5000 and JANIS VNF-100 low temperature cryostat using 1-methyltetrahydrofuran as the solvent and Lakeshore Cyotronics temperature controller was used for temperature-dependent absorption measurements.

6.4.4 Single Crystal X-ray Diffraction

Data for both $Au_{30}(S\text{-}t\text{-}Bu)_{18}$ structures ($P2_1/n$ and *P-1*) were collected on beamline 11.3.1 at the Advanced Light Source, Lawrence Berkeley National Laboratory. Samples were mounted on MiTeGen® kapton loops and placed in a 100(2) K nitrogen cold stream provided by an Oxford Cryostream 800 Plus low temperature apparatus on the goniometer head of a Bruker D8 diffractometer equipped with a PHOTON 100 CMOS detector operating in shutterless mode. Diffraction data were collected using synchrotron radiation monochromated using silicon(111) to wavelengths of 0.7293 and 0.7749 Å, respectively. An approximate full sphere of data was collected using a combination of phi and omega scans with scan speeds of 1 second per 4 degrees for the phi scans, and 3 and 5 second per degree for the omega scans at 2theta = 0 and -45, respectively. Additional crystallographic information has been summarized in the SI. Full details can be found in the crystallographic information files provided in the Supplementary Information.

6.4.5 DFT calculations

The optimized structure of the $Au_{30}(S\text{-}t\text{-}C_4H_9)_{18}$ complex was obtained starting from the experimentally determined geometry and performing a local relaxation. The Plane-Wave QuantumEspresso software [6.23] was adopted in conjunction with ultra-soft pseudopotentials [6.24] and the PBE xc-functional. Values of 30 and 300 Rydberg were used as the cutoffs for the selection of the plane wave basis sets for describing the kinetic energy and the electronic density, respectively. One-electron levels were broadened using a Gaussian distribution with σ=0.002 Rydberg.

6.4.6 TDDFT simulations

The TDDFT/B3LYP absorption spectra are the result of a real-time time dependent DFT (RT-TDDFT) simulation, carried out with the CP2K package [6.25]. To reduce the computational effort, the CH3 groups of the tert-butyl moieties were replaced with hydrogen atoms. DVZP primary basis set [6.26], GTH pseudopotentials [6.27] and an auxiliary cpFIT3 basis set as described in Ref. [6.28] were employed in the calculations. Starting from a ground-state calculation, optical response is obtained by subjecting the system to electrical pulses (with a strength of 0.0005 a.u.) in each of the three Cartesian directions and using the time-evolution formalism to follow the electron dynamics. A total of 16.5 femtosec were sampled using a time step of 0.012 femtosec. A time damping of 7.3 femtosec was chosen to broaden the predicted spectrum. The TDDFT/SAOP spectra were calculated at the scalar relativistic ZORA [6.29]level, with the Amsterdam Density Functional (ADF) code [6.30][6.31] which solves the TDDFT equations with the Casida approach [6.32]. The basis set consists of all-electron Slater Type Orbitals (STO) of Triple Zeta plus Polarization (TZP) size for all the atoms, taken from the ADF ZORA database. SAOP exchange-correlation potential [6.22] was used, exhibiting a correct Coulombic asymptotic behavior. 200 lowest eigenvalues of the Casida matrix were extracted. The discrete transitions have been convoluted with Lorentzian functions of 0.15 eV of FWHM.

7 Efficient TDDFT photoabsorption of icosahedral silver and gold bare clusters containing up to 309 atoms

Oscar Baseggio, Martina De Vetta, Giovanna Fronzoni, Mauro Stener, Luca Sementa, Alessandro Fortunelli, Arrigo Calzolari

We apply a recently developed time-dependent density-functional theory (TDDFT) algorithm based on the complex dynamical polarizability to calculate the photoabsorption spectrum of the following series of closed shell icosahedral clusters of increasing size (namely $[M_{13}]^{5+}$, $[M_{55}]^{3-}$, $[M_{147}]^{-}$ and $[M_{309}]^{3+}$ with M = Ag, Au), focusing in particular on their plasmonic response. The new method is shown to be computationally very efficient: it simultaneously retains information on excited state wave function and provides a detailed analysis of the optical resonances, employing the Transition Contribution Map scheme. For silver clusters, a very intense plasmon resonance is found already for $[Ag_{55}]^{3-}$, with a strong coupling among low-energy single-particle configurations. At variance, for gold clusters we do not find a single strong plasmonic peak, but rather many features of comparable intensity, with a partial plasmonic behavior present only for the lowest-energy transitions. Notably, we also find a much greater sensitivity of the optical response of Ag clusters with respect to Au clusters to cluster charge, exchange-correlation (xc-)functional, and basis set, as demonstrated via a detailed comparison between $[Ag_{55}]^{q}$ and $[Au_{55}]^{q}$. The results of the TDDFT algorithm obtained with the complex dynamical polarizability are finally compared with those produced by alternative (real-time evolution or Lanczos) approaches, showing that – upon a proper choice of numerical parameters – an overall nearly quantitative agreement is achieved among all the considered approaches, in keeping with their fundamental equivalence.

7.1 Introduction

The calculation of photoabsorption spectra for large molecules is nowadays considered as a standard task for quantum chemistry, and this has become possible thanks to the accuracy of the Time Dependent Density Functional Theory (TDDFT) formalism, which includes most of the physics of linear optical response phenomenon, as well as its efficient implementations in publicly available quantum chemistry codes.

The most common way to tackle this problem in quantum chemistry consists *firstly* in solving the Kohn-Sham (KS) equations of Density Functional Theory (DFT) by expanding the molecular KS orbitals as linear combinations of atomic functions, and *secondly* to recast the TDDFT equations in a form involving the diagonalization of a matrix Ω according to the density matrix formulation of Casida [7.1]. In this scheme the TDDFT problem is reduced to the extraction of the lowest eigenvalues and eigenvectors of Ω, a matrix whose dimension is the product of the number of occupied and virtual orbitals ($N_{occ} \times N_{virt}$) which can thus be huge for large systems. Such an approach has been implemented in many codes, like for example ADF [7.2][7.3][7.4], and can be made efficient by taking advantages of: (a) the point group molecular symmetry, (b) the Davidson diagonalization iterative algorithm which is well suited for very large matrices, (c) electron density fitting techniques through the use of auxiliary basis functions, and finally (d) massive parallelization. This scheme can be computationally feasible even on very large molecules (up to hundreds of atoms) provided one is interested only in the lowest part of the absorption spectrum. However, due to the intrinsic limitation of the Davidson algorithm, which becomes numerically unstable when too many eigenvalues are requested, the higher-energy part of the spectrum of large molecules is basically inaccessible. This situation is encountered for example in the calculation of the photoabsorption spectra of metal clusters which exhibit plasmonic behaviour, since the clusters are quite large and the plasmons lie at moderately high energy, so that the number of eigenvalues requested is too high to be practicable using the Davidson algorithm. For this reason alternative approaches, based for example on real-time propagation of the wave function [7.5] or on Lanczos chains [7.6] have been considered as possible alternatives to the Casida scheme. These alternative schemes do not suffer of energy limitation issues in the calculation of the spectrum, but loose information on the excited state wave function and therefore cannot support very useful analysis tools which are naturally included in the Casida scheme. Such an analysis allows one to describe electron excitations as a linear combination of one-electron excited configurations and therefore gives a complete description of the photoabsorption spectrum in terms of electronic structure. To avoid the diagonalization bottleneck and simultaneously keep the useful analysis of excitations, recently a new TDDFT algorithm has been proposed [7.7] which extracts the spectrum from the calculation of the complex dynamical polarizability. In this approach the TDDFT equations are projected onto the density fitting auxiliary basis set and therefore the associated numerical problem is recast into the resolution of a non-homogeneous linear system with a dimension much smaller with respect to the Casida approach. The matrix dimension of such linear system is $k \times (N_{occ} + N_{virt})$ instead of $N_{occ} \times N_{virt}$ of the Casida Ω matrix, with k =1.91 or 1.6 for Au and Ag respectively. Moreover, in this new scheme the spectrum at each frequency is obtained as an independent calculation, which makes that the algorithm is easily parallelizable and is feasible essentially for all systems for which a DFT calculation is affordable. The potentialities of this approach are demonstrated in the present work by studying two series of noble metals (Ag and Au) clusters containing up to 309 atoms. It is first shown that the new algorithm is very efficient, especially for the larger clusters that, on the contrary, could not be treated by means standard Casida's approaches. For example in $[Au_{309}]^{3+}$ the linear system dimension is 13596, while the dimension of the Casida Ω matrix would have been around 12 millions. To validate the new approach and to firmly assess the equivalence of different TDDFT schemes, the photoabsorption spectra of Ag_{55} and Au_{55} clusters are also predicted and compared by using CP2K [7.8] and turboTDDFT codes [7.9], which relay on real-time propagation of the wave function and Lanczos chain approaches, respectively.

Finally comparison between the optical response of Ag and Au clusters shows the much greater sensitivity of Ag optical response to both physical and numerical parameters such as the charge state, the exchange-correlation (xc-)functional, and the basis set, due to the intrinsically more free-electron character of Ag and the absence of strong s/d coupling with respect to Au. The availability of an efficient method to treat photoabsorption in large systems opens the way to study the behaviour of Surface Plasmon Resonance (SPR), a typical optical properties of noble metal nanoclusters with many potential applications.

7.2 Theoretical method

The theoretical method as well as its implementation have been described in details previously [7.7], so here we only give a brief description of the salient features and refer the reader to the original work for more information about the algorithm and how to calculate the corresponding matrix elements.

The photoabsorption spectrum $\sigma(\omega)$ is calculated for each value of the photon energy ω, from the imaginary part of the isotropic dynamical polarizability $\alpha(\omega)$:

$$\sigma(\omega) = \frac{4\pi\omega}{c} Im[\alpha(\omega)] \tag{7.2.1}$$

The isotropic dynamical polarizability is calculated for complex frequency, i.e. $\omega = \omega_r + i\omega_i$, where the real part ω_r corresponds to the actual photon frequency (energy) and ω_i is the imaginary part which refers to a broadening of the discrete lines and is interpreted as the excited states finite lifetime [7.10]. For the calculation of the spectrum, the isotropic part of the tensor is actually extracted from its trace: $\alpha(\omega) = \frac{1}{3}\sum_{i=1}^{3} \alpha_{ii}(\omega)$ where the index i runs on the three components x, y and z. The polarizability tensor is obtained from the following expression:

$$\alpha_{zz}(\omega) = \int \rho_z^{(1)}(\omega, \bar{r}) z d\bar{r} \tag{7.2.2}$$

where $\rho_z^{(1)}(\omega, \bar{r})$ is the Fourier component of the given frequency of the first order time dependent density, induced by the external time dependent scalar potential. According to TDDFT, the induced density can be obtained from the dielectric susceptibility $\chi_{KS}(\omega, \bar{r}, \bar{r}')$ of a reference system of non-interacting electrons under the effect of an effective potential $V_{SCF}^{z}(\omega, \bar{r})$ sum of the external potential plus the Coulomb and the response xc-potentials.

This is summarized by the following coupled linear equations:

$$\rho_z^{(1)}(\omega, \bar{r}) = \int \chi_{KS}(\omega, \bar{r}, \bar{r}') V_{SCF}^{z}(\omega, \bar{r}') d\bar{r}' \tag{7.2.3}$$

$$V_{SCF}^{z}(\omega, \bar{r}) = V_{EXT}^{z}(\omega, \bar{r}) + \int \frac{\rho_z^{(1)}(\omega, \bar{r}') d\bar{r}'}{|\bar{r} - \bar{r}'|} + \left.\frac{\partial V_{XC}}{\partial \rho}\right|_{\rho^0} \rho_z^{(1)}(\omega, \bar{r}) \tag{7.2.4}$$

The Adiabatic Local Density Approximation (ALDA) [7.11] is assumed in expression (7.2.4) and $V_{EXT}^{z}(\omega, \bar{r})$ corresponds in practice to the z dipole component. Now expressions (7.2.3) and (7.2.4) can be written in operatorial form:

$$\rho_z^{(1)} = \chi_{KS} V_{SCF}^{z} \tag{7.2.5}$$

$$V_{SCF}^{z} = V_{EXT}^{z} + K \rho_z^{(1)} \tag{7.2.6}$$

where in expression (7.2.6) K stands for the sum of the Coulomb and the XC kernels.

Due to the linearity of (7.2.5) and (7.2.6) it is possible to eliminate V_{SCF}^{z} and to obtain an equation for $\rho_z^{(1)}$, which reads:

$$[1 - \chi_{KS}K]\rho_z^{(1)} = \chi_{KS}V_{EXT}^{z} \tag{7.2.7}$$

Equation (7.2.7) is then represented over the basis set of the auxiliary density fitting functions f_μ. More precisely only a subset of the fitting set is enough to obtain convergent results. Within this representation, the induced density assumes this expression: $\rho_z^{(1)}(\omega, \bar{r}) = \sum_\mu^K f_\mu(\bar{r})b_\mu(\omega)$ and the following non-homogeneous system of linear algebraic equations can be written in the matrix formulation form:

$$[\boldsymbol{S} - \boldsymbol{M}(\boldsymbol{\omega})]\boldsymbol{b} = \boldsymbol{d} \tag{7.2.8}$$

In equation (7.2.8) $\boldsymbol{S}$ is the overlap matrix between fitting functions, $\boldsymbol{b}$ is the unknown vector with the expansion coefficients $b_\mu(\omega)$ of $\rho_z^{(1)}$, $\boldsymbol{d}$ is the frequency dependent vector corresponding to the known non-homogeneous term, whose components are:

$$d_\mu = \langle f_\mu | \chi_{KS}(\omega) | z \rangle \tag{7.2.9}$$

and finally the elements of the frequency dependent matrix $\boldsymbol{M}$ are:

$$M_{\mu\nu} = \langle f_\mu | \chi_{KS}(\omega)K | f_\nu \rangle \tag{7.2.10}$$

In practice, equation (7.2.8) is solved for each value of the photon energy.

For comparison, in the case of the $[Ag_{55}]^{5+}$ and $[Au_{55}]^{5+}$ clusters the photoabsorption spectrum has been calculated with CP2K and QE codes as well.

In the CP2K code [7.8], the time-dependent Kohn-Sham (TDKS) equations are explicitly integrated in time (see next section for computational details), and from the so-produced time-resolved TDKS solution the TDDFT spectrum is obtained via Fourier transform of the time-dependent dipole moment resulting from a small instantaneous electric field perturbation of the system wave function.

In the turboTDDFT code [7.6][7.12], the frequency dependent polarizability is obtained as the trace of the product between the dipole operator and the response density matrix, where the latter is expressed as the solution of the linearized quantum Liouville equation. The specific Lanczos implementation does not require the explicit evaluation of empty (virtual) states, thus reducing the computational cost and allowing for the calculation of extended portions of the spectrum in systems comprising several hundred atoms.

7.3 Computational details

The complex polarizability method has been implemented in a local version of the ADF code. The LB94 [7.13] or the PBE [7.14] exchange-correlation xc-functionals were employed to obtain the KS orbitals and eigenvalues from the KS equations, while the exchange-correlation kernel is approximated by ALDA [7.11] in the TDDFT part taking the derivative of the VWN [7.15] LDA xc-potential. The basis sets as well as the auxiliary density fitting functions employed consist of Slater Type Orbitals (STO) included in the ADF database. The new program allows a simple choice of a subset of the ADF fitting functions, in order to save computer time when some fitting functions are not necessary for an accurate description of the photoabsorption spectrum. Such choice was made with preliminary test calculations on Ag_2 and Au_2. The calculations have been performed at scalar relativistic level with Zero Order Relativistic Approximation (ZORA) [7.16].

In order to give a quantitative idea about the computational efforts and the efficiency of the spectrum calculation from the complex polarizability, for $[Au_{309}]^{3+}$ the SCF procedure employed 10 hours using 16 cores on a Linux Infiniband Cluster with 8-cores Intel Haswell 2.40 GHz processors, while the resolution of the TDDFT inhomogeneous linear system (dim = 13596) employed only 145 seconds using 16 cores for each energy point. Since about one hundred of energy points are enough for a complete description of the spectrum, the TDDFT linear system resolution is comparable to the SCF effort. In addition also matrix elements calculation time should be considered, so in general a TDDFT calculation will be comparable to a geometry optimization in terms of computational cost.

In the CP2K package [7.8], DVZP basis set [7.17], GTH pseudopotentials [7.18] were employed in the calculations. The PBE xc-functional was used in the KS equations and dynamics. Starting from a ground-state calculation, optical response is obtained by subjecting the system to electrical pulses (with a strength of 0.0005 a.u) in each of the three Cartesian directions and using the time-evolution formalism to follow the electron dynamics. A total of 19.3 femtosec were sampled using a time step of 0.012 femtosec. A time damping of 7.3 femtosec was chosen to broaden the predicted spectrum.

TurboTDDFT code is part of the Quantum-ESPRESSO (QE) package [7.9], for the simulation of the ground and excited states of solid state systems, based on (TD)DFT approaches. In the present case, the $[Ag_{55}]^{5+}$ and $[Au_{55}]^{5+}$ clusters have been simulated by using periodically repeated supercells, each including the metallic cluster (i.e. 55 atoms) and a thick layer of vacuum (~18 Å) in the three spatial directions, in order to avoid spurious interactions between adjacent replica. PBE xc-functional was used in solution of both DFT and TDDFT problems. The single particle wavefunctions (charge) were expanded in plane waves up to an energy cutoff of 25 Ry (250 Ry). Atomic potentials were described by using ab initio ultrasoft pseudopotentials of the Vanderbilt type [7.19]. The *4d* (*5d*) electrons of Ag (Au) have been explicitly included in the valence shell. The Brillouin zone of the reciprocal lattice was sampled at the Γ point. A jellium background is inserted to remove divergences in the charged cells, and the Martyna-Tuckerman correction [7.20] to both total energy and self-consistent potential is applied to consider the system as isolated. Optical spectra were obtained by evaluating 10000 Lanczos cycles for each incoming light polarization, and then averaged over the three spatial directions.

7.4 Results and discussions

The behaviour of Surface Plasmon Resonance (SPR), a typical optical properties of noble metal nanoclusters, has been the subject of many studies. SPR starts to appear in systems whose size is beyond about 2 nm, therefore containing more than 150-200 atoms. The size and shape effects are quite important factors which have strong influence on the energy position and the intensity of the SPR. Shape can also be profitably exploited to study SPR behaviour in systems which are elongated in only one dimension (nanowires), thus enabling plasmon-like optical response in clusters containing less than 100 atoms [7.21]. Small size noble metal clusters do not arrange with bulk fcc-structure, since surface tension effects tend to destabilize such configurations, instead they prefer to assume more spherical shapes, like icosahedral or decahedral ones. In this work we have considered only the most symmetric icosahedral structures.

Contrary to bulk systems, where plasmons can be excited only by longitudinal external electric field, in the case of nanoparticles and clusters SPRs can be excited also by transversal incoming fields, i.e. light. Thus, plasmonic features of nanostructures can be easily characterized starting from their optical absorption spectra. Several previous TDDFT studies are available for both silver and gold nanoclusters [7.22]-[7.30], but more specific works on series of icosahedral noble metal clusters are available for silver up to Ag_{55} [7.31] and Ag_{561} atoms [7.32], while for gold up to Au_{55} [7.33] and Au_{1414} [7.34] atoms. Unfortunately in these studies different methods have been employed to treat the largest systems with respect to the smaller ones, in terms of both the exchange-correlation functional and the numerical implementation (Casida like or real time propagation), so that a precise assessment of size-dependence effects is not readily available. The present work consists, instead, in a fully coherent study of metal clusters of both Ag and Au, by using the same method and the same level of accuracy for all the considered sizes. This investigation is also supplemented with an analysis of the electron transitions in terms of one-electron excited configurations, which will be conveniently presented in graphical compact form, according to the bi-dimensional Transition Contribution Map (TCM) plots [7.35].

7.4.1 Clusters geometry

The icosahedral clusters have been built starting with the simple M_{13} system, adding further shells according to MacKay protocol. Cluster structure has not been optimized, but is kept fixed imposing that average interatomic distance is equal to its experiment bulk value – indeed, it has been shown that structural relaxation has only a minor impact on the optical properties of gold clusters [7.36]. In the regular icosahedron two different interatomic distances are defined, the inter-shell (R) and the intra-shell (D) ones, which are connected by the following geometric relation: $\frac{R}{D} = \sqrt{\frac{5+\sqrt{5}}{8}}$. Therefore we have taken $\frac{R+D}{2}$ equal to 2.89 Å and 2.88 Å for Ag and Au clusters respectively.

7.4.2 Photoabsorption of the $[Ag_n]^q$ series

We have considered the first fourth members of the series of icosahedral silver clusters $[Ag_{13}]^{5+}$, $[Ag_{55}]^{3-}$, $[Ag_{147}]^{-}$ and $[Ag_{309}]^{3+}$, the charges have been chosen in order to have closed shell electronic structure, since the complex polarizability method at the moment cannot treat open shells.

The photoabsorption spectra of this series, calculated at the TDDFT level with LB94 [7.13] xc-functional and DZ basis set, are reported in **Figure 7.1**. Apart from the smallest cluster $[Ag_{13}]^{5+}$, all the other ones are characterized by a very strong peak which grows and is red-shifted with increasing cluster size, a behaviour which is typical of plasmon resonance [7.37]. In $[Ag_{55}]^{3-}$ the peak is actually split in two very close

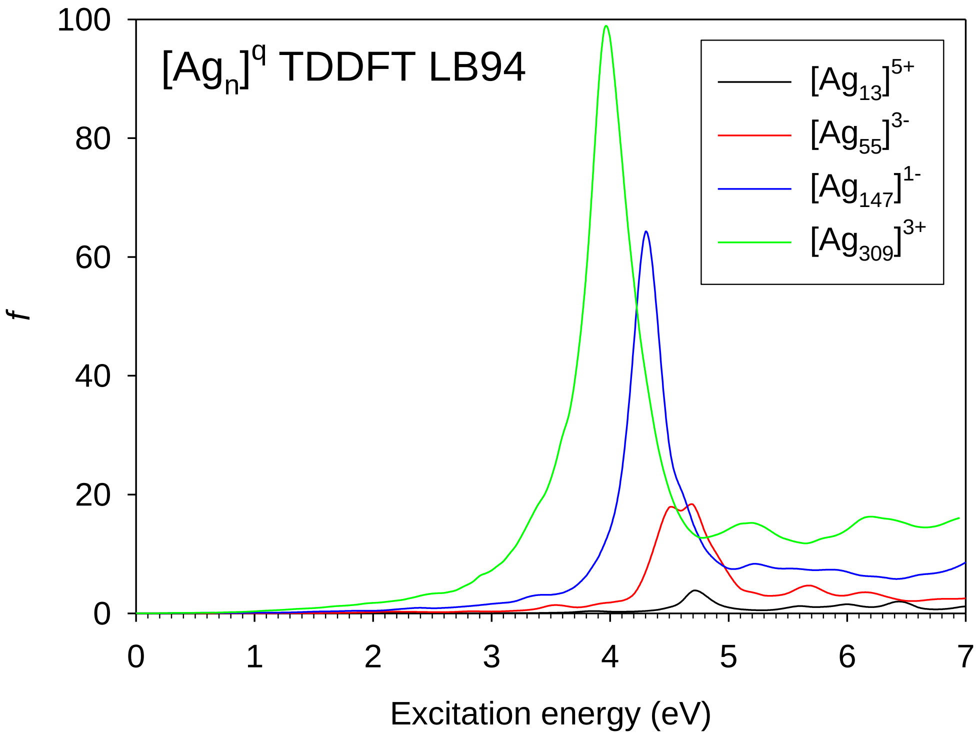

***Figure 7.1** Photoabsorption profiles of [Ag$_{13}$]$^{5+}$, [Ag$_{55}$]$^{3-}$, [Ag$_{147}$]$^{-}$ and [Ag$_{309}$]$^{3+}$ calculated by complex polarizability TDDFT DZ LB94. Imaginary broadening ω_i = 0.15 eV.*

contributions. The energy of the maxima are 4.70 eV, 4.30 eV and 3.95 eV for [Ag$_{55}$]$^{3-}$, [Ag$_{147}$]$^{-}$ and [Ag$_{309}$]$^{3+}$ respectively, so it seems that the energy of the plasmon resonance is still decreasing and has not yet reached its limit value. It is interesting to compare this finding with a previous TDDFT study [7.32] on the same icosahedral silver clusters which had employed a very accurate real-time propagation method and the adiabatic GLLBSC potential [7.38][7.39]. In such a study all the peaks were calculated at lower energies with respect to present work by 0.5-0.2 eV and, more interestingly, a red shift of 0.4 eV was actually found going from Ag$_{55}$ to Ag$_{147}$ which is in good agreement with present calculation, while a very small red shift of only 0.1 eV was found going from Ag$_{147}$ to Ag$_{309}$. The difference for the energy of the maxima between the two calculations are not surprising and can be assigned to the different xc-functional employed. In the previous work [7.32] the energy position of the resonance for Ag$_{147}$

calculated with PBE functional was found at about 3.2 eV, i.e. shifted by 0.6 eV with respect the value calculated at the GLLBSC level (3.8 eV). The calculated spectrum of $[Ag_{55}]^{3-}$ is in good agreement with that calculated by ADF with DZ basis set and LB94 xc-functional reported in ref. [7.31], showing the same double peak shape, although the present spectrum is shifted by about 0.1-0.2 eV to higher energy. To check this point, we have calculated the spectrum (not shown) for $[Ag_{55}]^{3-}$ with the ADF program employing the Casida approach with the geometry of present work and have obtained a perfect agreement with the results produced by the complex polarizability algorithm reported in **Figure 7.1**. We can conclude that this discrepancy is not due to the computational method but rather is an effect of the cluster geometry, which in ref. [7.31] was relaxed in the C_{5v} symmetry.

Besides the strong plasmonic resonance, the calculated spectra do not show other important features, only a weak intensity modulation is apparent for all the clusters above 5 eV. Although in this case the plasmonic behaviour is clear-cut, in general it is very difficult to distinguish between a molecular-like resonance and a plasmon: a general analysis has been suggested by Jacob [7.40] but requires to re-calculate the spectra many times with different values of a coupling parameter λ, so that such procedure can be impractical for very large systems like present ones. For this reason, in order to gain a better insight into the physics that governs the plasmonic features in metal clusters, here we have performed a TCM analysis [7.35] of the spectrum, in correspondence of the maximum of the intensity as reported in **Figure 7.2**. The TCM plots are very convenient 2D representations of the one-electron excited configurations coefficients which contribute to the excited state: each excited determinant corresponds to a point in the plane, the value on the X axis corresponds to the occupied orbital energy while the value on the Y axis corresponds to the unoccupied orbital energy. For each excited determinant a 2D Gaussian function is added, with a weight proportional to its coefficient in the excited state expansion.

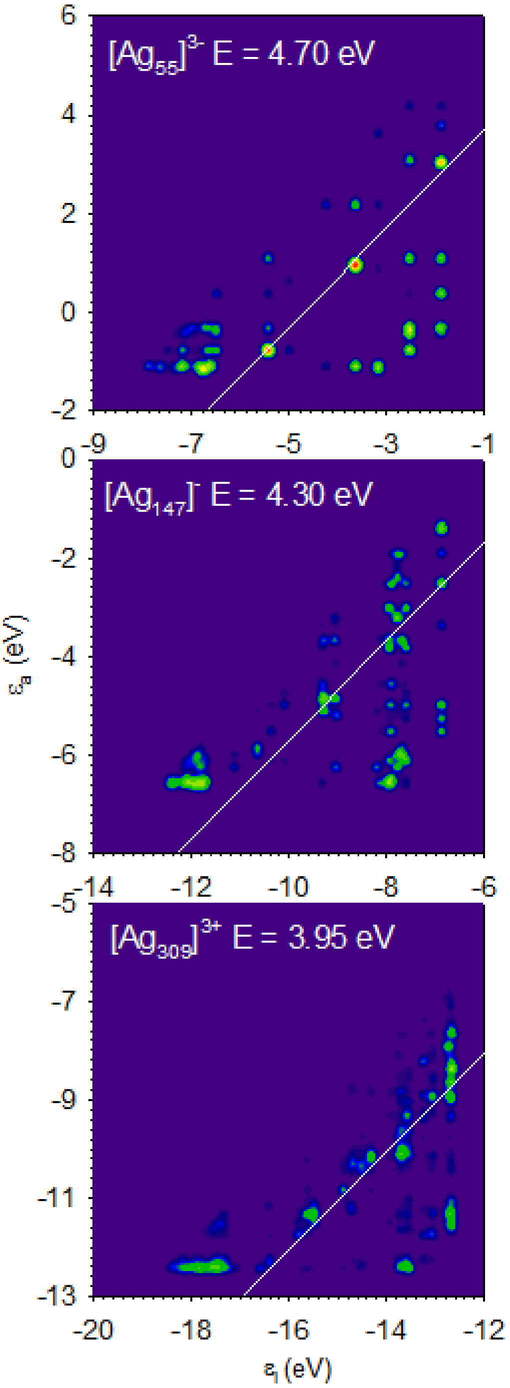

Figure 7.2 *TCM plots for* $[Ag_{55}]^{3-}$*,* $[Ag_{147}]^{-}$ *and* $[Ag_{309}]^{3+}$ *taken at plasmon energies E.* ε_i *(X axis) and* ε_a *(Y axis) refer to occupied and virtual orbital energies. White line corresponds to* $\varepsilon_a - \varepsilon_i = E$*.*

We start the analysis with the $[Ag_{55}]^{3-}$ plasmon at 4.70 eV (upper panel in **Figure 7.2**), in the TCM plot we have also added a white line which corresponds to the unoccupied-occupied orbital eigenvalue difference equal to the excitation energy. In order to read properly the TCM plots, it must be remembered that for Ag clusters the sp band covers all occupied and unoccupied orbitals, while the d band is confined well below the Fermi level (ε_F), see for example the DOS plots of **Figure 7.3** of Ref. [7.32]. In the present case the upper limit of the d band is at -6.2 eV (X axis) that is about 4.7 eV below ε_F. So in the TCM plot of $[Ag_{55}]^{3-}$ all the spots correspond to intraband sp → sp configurations, with the only exception of the region around -7 eV in the X axis which instead corresponds to interband d → sp configurations. Therefore the plasmon consists essentially in an intraband sp → sp excitation. The collective nature of the plasmon can be inferred by the presence of many spots in the TCM, moreover, it is worth noting that three strong spots lie on the white line, which correspond to electron promotion between orbitals whose energy difference matches almost exactly the plasmon energy. On the other hand, there are important contributions coming from configurations having energies well below the plasmon, in particular between -4 eV and -2 eV in the occupied orbitals (X axis) and between -1 eV and 1 eV in the virtual orbitals (Y axis). On the contrary, the configurations having energies above the plasmon excitation play only a minor role: the only important contribution comes from the already identified interband d → sp configurations, along with a few weak ones coming from the sp → sp around 2 eV – 3 eV in the virtual orbitals (Y axis). It is important to discriminate the contributions accordingly to their energy: the presence of contributions with eigenvalue energy difference different with respect to plasmon resonance indicates a strong coupling among them, on the other hand if the eigenvalue energy difference matches the plasmon energy it means that the contributions are almost degenerate with plasmon but not necessarily coupled to it.

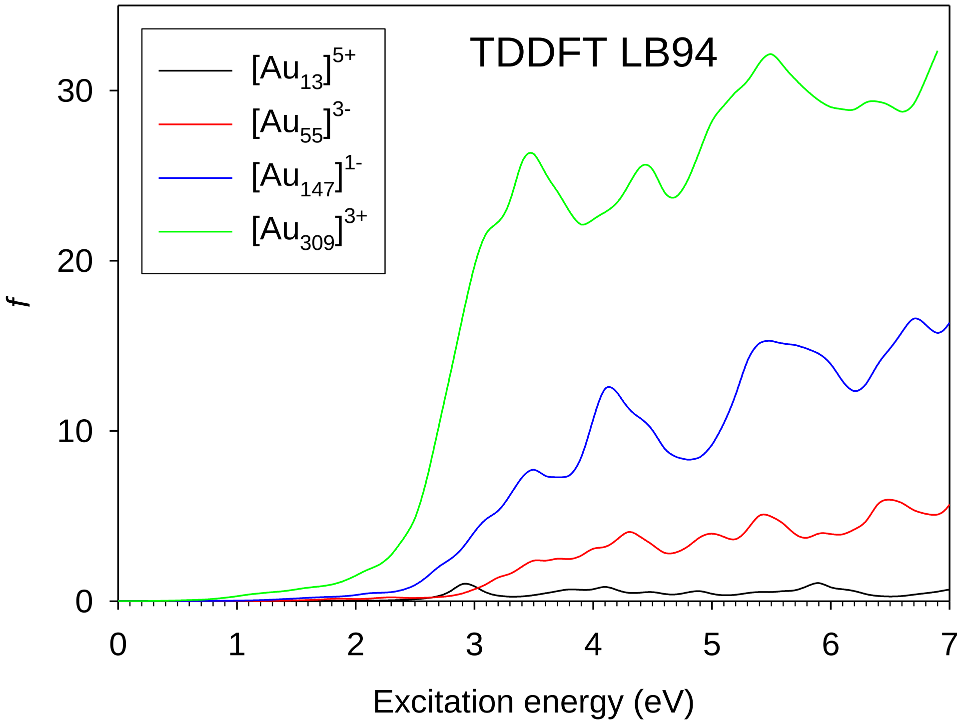

Figure 7.3 *Photoabsorption profiles of* $[Au_{13}]^{5+}$*,* $[Au_{55}]^{3-}$*,* $[Au_{147}]^{-}$ *and* $[Au_{309}]^{3+}$ *calculated by complex polarizability TDDFT DZ LB94. Imaginary broadening* ω_i = *0.15 eV.*

The TCM plots for the plasmons of $[Ag_{147}]^{-}$ and $[Ag_{309}]^{3+}$ at 4.30 eV and 3.95 eV respectively are also reported in **Figure 7.2**, displaying very similar patterns as in $[Ag_{55}]^{3-}$. In both cases the interband d → sp "island" is observed at ca -12 eV in $[Ag_{147}]^{-}$ and ca -18 eV in $[Ag_{309}]^{3+}$ as the occupied orbital energy, is concerned. All the other contributions are pertaining to the sp → sp intraband. Some of them are detected along the white line, indicating quasi-degeneracy between excited configuration and plasmon, ones come from lower energy configurations, indicating strong configuration coupling and therefore a collective behaviour. By comparing the present TCM analysis with previous one on Au_{86} gold nanowire [7.21] and $[Au_{147}]^{-}$ icosahedral clusters [7.7] we notice that the Au_{86} gold nanowire displayed a very strong plasmon peak and the most intense TCM contributions derived from lower energy configurations, indicating strong configuration coupling. On the other hand in $[Au_{147}]^{-}$ cluster the plasmon was much weaker, and only minor contributions were found from low energy configurations. All this is consistent with present analysis.

In addition to the TCM analysis, we have also inspected the resonant part of the first order time dependent perturbed density, that is the imaginary part of the solution of previous equation (7.2.7), calculated at the plasmon energy for the three largest silver clusters. Results are reported in Figure S1 of the Supporting Information. As expected, all the plots display a typical dipolar character, consistent with the classical interpretation of the SPR as density oscillations, this confirms the plasmonic nature of the resonance given above. However, it is worth noticing that it is not possible to extract from the simple perturbed density plots the same amount of information derived from the TMC ones that confirm to be a more powerful analysis tool.

7.4.3 Photoabsorption of the $[Au_n]^q$ series

In parallel to the silver clusters, we have considered the analogue series of icosahedral gold clusters $[Au_{13}]^{5+}$, $[Au_{55}]^{3-}$, $[Au_{147}]^{-}$ and $[Au_{309}]^{3+}$, with the same charge states as in the silver case, so to obtain a closed shell electronic structure for all four clusters. The photoabsorption spectra of the cluster series, calculated at the TDDFT level with LB94 [7.13] xc-functional and DZ basis set, is reported in **Figure 7.3**. The spectra look very different with respect to silver: there is no a leading peak to be easily attributed to a plasmon resonance, but rather a smoothly growing intensity starting around 2 – 3 eV depending on the cluster, followed by a wide modulation displaying maxima at 3.50 eV, 4.40 eV and 5.50 eV for $[Au_{309}]^{3+}$ and 3.50 eV, 4.10 eV and 5.50 eV for $[Au_{147}]^{-}$. For all the three largest gold clusters, the intensity is still growing up to 7 eV, while the absolute intensity is much weaker than for silver cluster by a factor of three. The absence of strong plasmons is not surprising: in a previous work on gold nanowires [7.21] it has been shown that a clear plasmon emerges only when cluster size exceeds 2 nm. In the case of Au_{68} with length 2.02 nm only an incipient weak plasmon was observed, while for Au_{86} with length 2.59 nm a very intense plasmon was found.

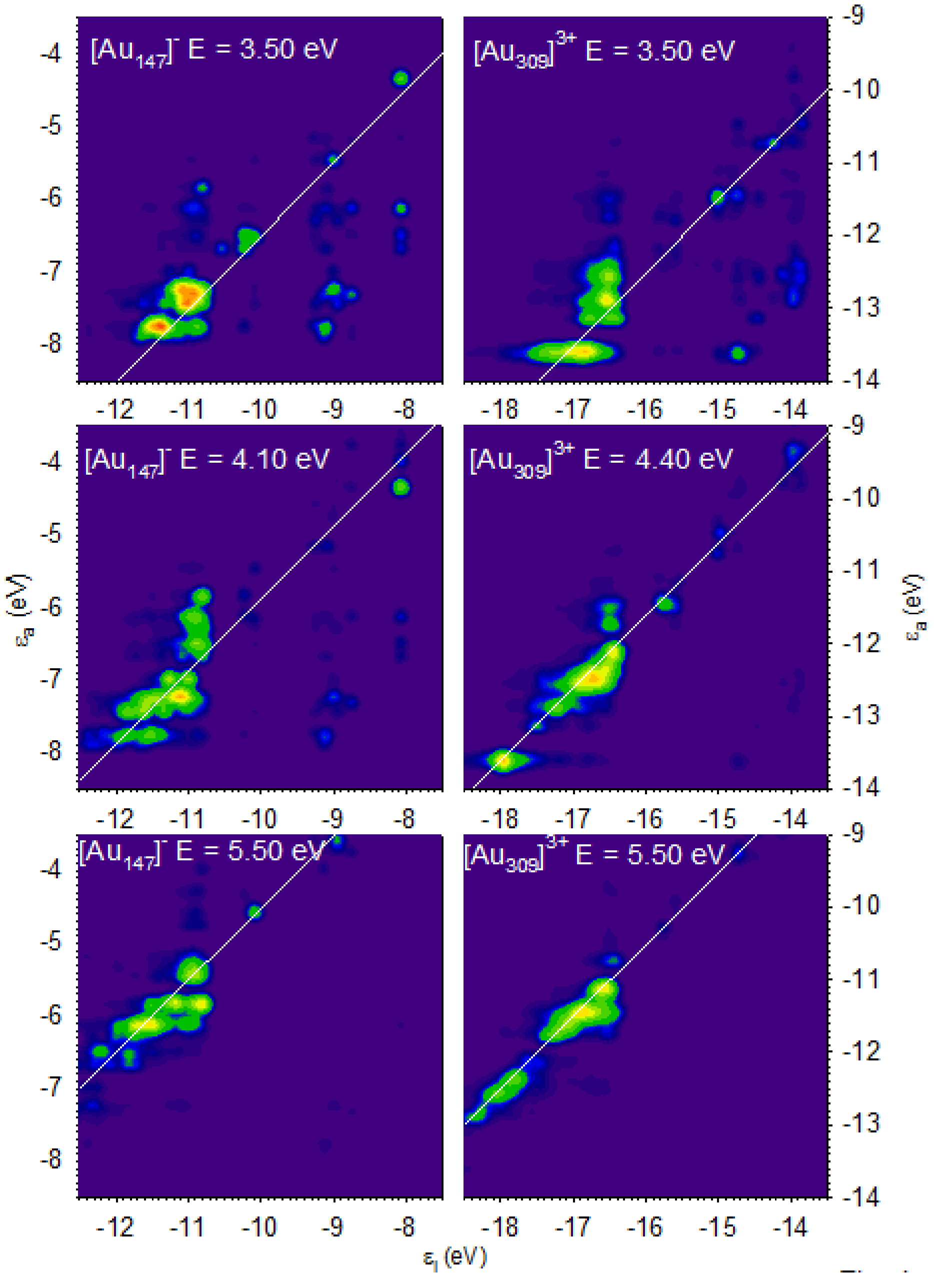

Figure 7.4 *TCM plots for* $[Au_{147}]^-$ *and* $[Au_{309}]^{3+}$ *taken at energies corresponding to photoabsorption maxima E.* ε_i *(X axis) and* ε_a *(Y axis) refer to occupied and virtual orbital energies. White line corresponds to* $\varepsilon_a - \varepsilon_i = E$.

In the present work the distance between the two most distant atoms of $[Au_{309}]^{3+}$ and $[Au_{147}]^{-}$ are 2.25 nm and 1.68 nm respectively, so only a weak plasmon should be expected even for the largest cluster. It is worth noting that $[Au_{147}]^{-}$ has been considered as well in a previous work [7.36], exhibiting a first plasmonic peak found at 2.95 eV, which is consistent with a shoulder found in the present work around 3 eV. In that work it was not possible to go beyond 3.2 eV because the Davidson algorithm implemented in ADF was not practicable to extract a higher number of eigenvalues. Interestingly, the absorption profile of the $[Au_{309}]^{3+}$ cluster also displays a shoulder around 3.2 eV, which is very likely the evolution of the shoulder of $[Au_{147}]^{-}$ at 3 eV.

In order to identify possible plasmonic behaviours, in **Figure 7.4** we have considered the TCM analysis of the three most intense features of $[Au_{147}]^{-}$ and $[Au_{309}]^{3+}$. We start with $[Au_{147}]^{-}$ at 3.50 eV: taking into account (i) that the Au 5d band lies between -10 eV and -12 eV on the occupied orbital energy scale (X axis) and (ii) that the remaining states belong to the 6s6p band, we find that the leading contribution is a d → sp interband transition, with important intraband sp → sp contributions even from lower energies. This suggests that coupling is present and indicates a collective behaviour typical of plasmons, at least to some extent. Going to the next maximum at 4.10 eV, we notice a drastic decrease in the role played by the lower energy configurations and a concomitant increase in the d → sp interband transition character, so in this case the plasmonic behaviour is almost disappeared. Finally at 5.50 eV the coupling is negligible, so this feature does not carry any plasmonic character and can be classified as a pure d → sp interband transition.

Moving to the next cluster $[Au_{309}]^{3+}$ at 3.50 eV, we find again a clear coupling with lower energy configurations, confirming the plasmonic nature of this feature. The next peak at 4.40 eV displays only a very weak coupling that disappears completely at 5.50 eV. We can summarize all these findings saying that the feature at 3.50 eV in both clusters has a definite plasmonic-like nature, which is not pure but hybridized with d → sp interband excitations. Such hybridization is present also in the feature at 4.10 eV of $[Au_{147}]^{-}$.

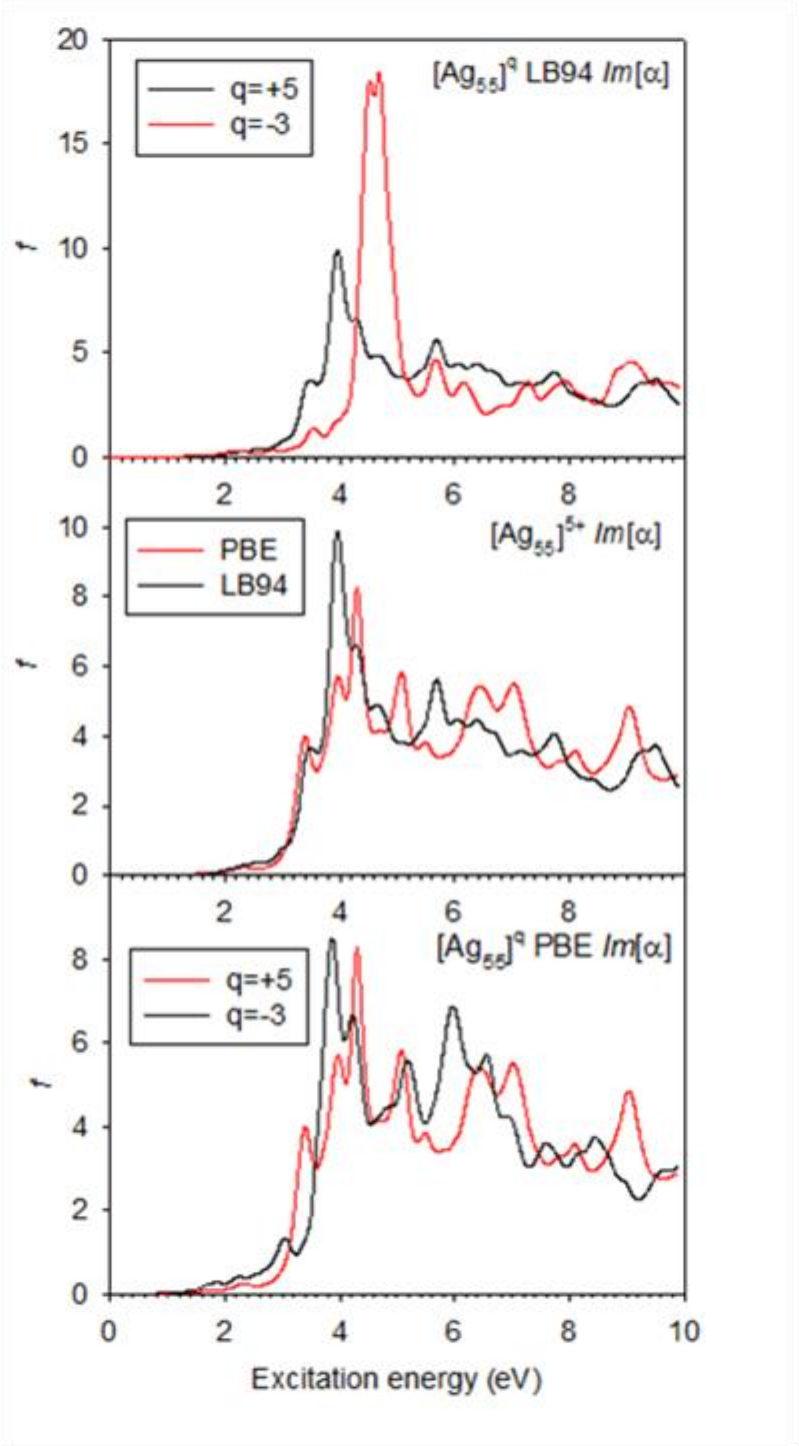

Figure 7.5 *Photoabsorption profiles of [Ag*$_{55}$*]*^{q} *calculated by complex polarizability TDDFT DZ and imaginary broadening* ω_i *= 0.15 eV. Charge and XC are shown in insets.*

We can expect that as the cluster size increases this hybridization should decrease, giving rise to a strong pure plasmon at low energy followed by pure d → sp interband excitations at higher energy.

Moreover we have considered the induced density, reported in Fig. S2 of the Supporting Information. As in the previous case, all of them display the typical dipolar shape, consistent with the plasmon. The only noteworthy features in the perturbed density are a kind of fringes which reduce the dipolar distribution of the density, well apparent in the equatorial faces of $[Au_{309}]^{3+}$ at 4.4 eV and 5.5 eV and to some extent in $[Au_{147}]^{-}$ at 5.5 eV. They might be an indication of a reduced or absent plasmon character. Also in this case the TCM analysis has proven much more informative than the induced density to assess the nature of the spectral features in terms of electronic structure.

7.4.4 Analysis of photoabsorption for $[Ag_{55}]^{q}$

Among the series of silver clusters, we have selected Ag_{55} as an example of a relatively small cluster to be further analysed with other methods and with different schemes in order to assess the importance of the various computational approaches. In **Figure 7.5** we consider the effect of the charge and of the xc-functional. In the upper panel of **Figure 7.5**, the photoabsorption is calculated with the LB94 xc-functional with two different charges: -3 and +5, both of them give a closed shell electronic structure. The charge effect is quite dramatic: while with charge -3 a clear-cut plasmon is observed, the charge +5 destroys the sharp plasmon peak and a broader structure is obtained, whose maximum is red-shifted by about 0.7 eV. A very similar and equally strong charge effect in which the plasmon is quenched was observed in the icosahedral silver cage [7.41] $[Ag_{92}]^{2+}$ when passing from LB94 to the LDA xc-functional [7.15]. This behaviour indicates that the plasmon is not yet ‘stable’, and that an external perturbation is enough to quench it. Nevertheless it should be noted that a change of eight electrons is significant for a cluster containing only 55 atoms.

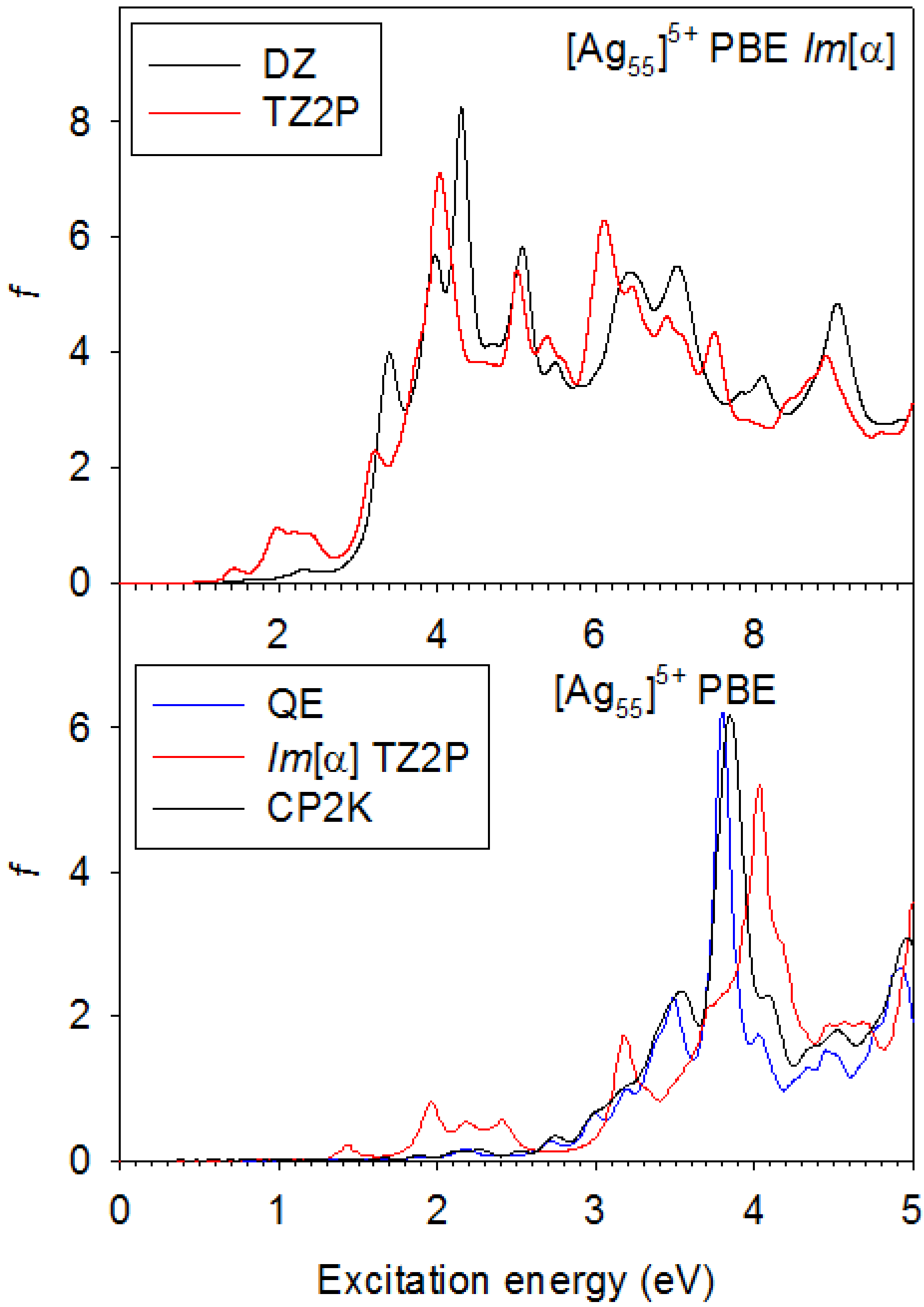

Figure 7.6 *Photoabsorption profiles of* $[Ag_{55}]^{5+}$ *calculated by TDDFT PBE. Upper panel: complex polarizability with imaginary broadening* $\omega_i = 0.15$ *eV. Lower panel: QE, CP2K and complex polarizability with imaginary broadening* $\omega_i = 0.075$ *eV. Basis sets and methods are shown in insets.*

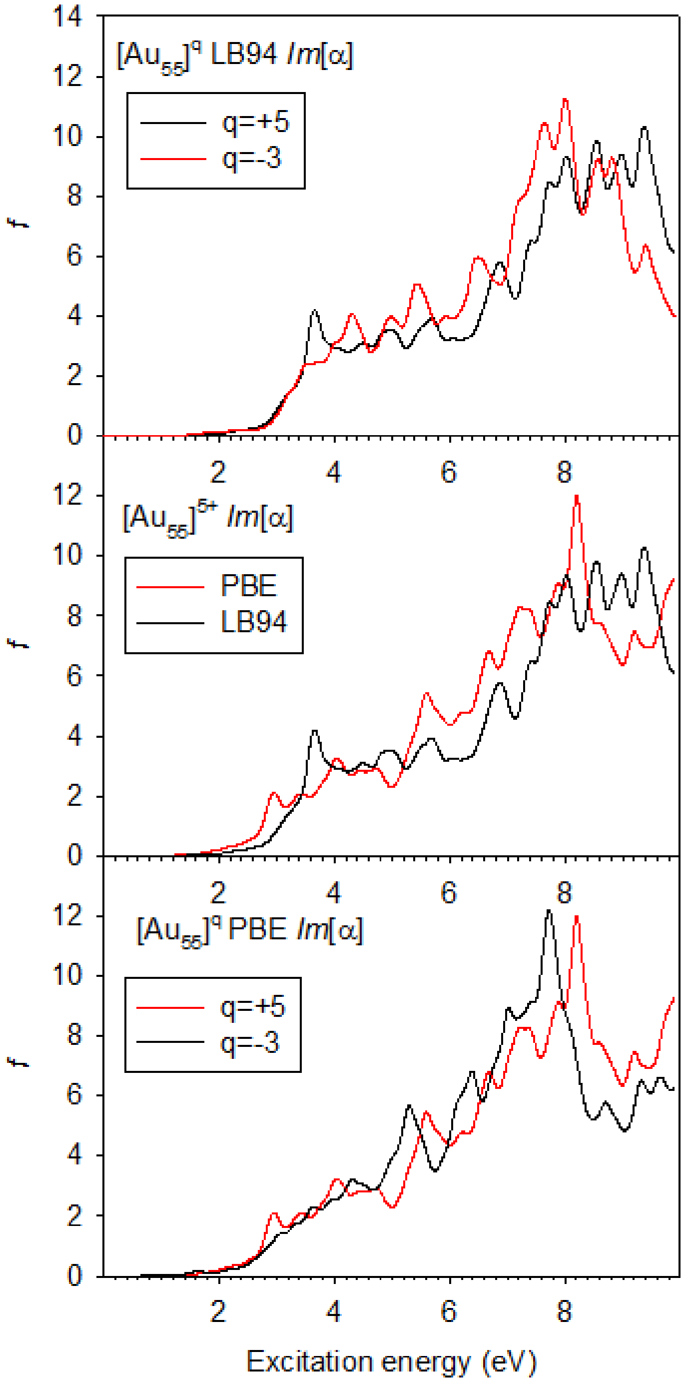

Figure 7.7 *Photoabsorption profiles of* $[Au_{55}]^q$ *calculated by complex polarizability TDDFT DZ and imaginary broadening* ω_i *= 0.15 eV. Charge and XC are shown in insets.*

The effect of the xc-functional on $[Ag_{55}]^{5+}$ is quite modest (central panel) as well as the charge effect using the PBE functional (lower panel). In the upper panel of **Figure 7.6** we considered the effect of the basis set in the case of PBE functional. Only rather modest differences are evident going from DZ to TZ2P set: the most important one being the shift of the maximum of about 0.2 eV to lower energy, as expected due to the greater variational freedom assured by the larger basis set on the excited state wave function. Finally in the lower panel of **Figure 7.6**, the spectra calculated with QE and CP2K have been reported together with that calculated from complex polarizability. The agreement between QE and CP2K is excellent, while the complex polarizability approach slightly overestimates the position of the peak at around 3.9 eV. This disagreement is likely an effect of the basis set: indeed as discussed above a basis set enlargement tends to decrease the peak energy (upper panel) thus going in the direction of the QE and CP2K results.

7.4.5 Analysis of photoabsorption for $[Au_{55}]^q$

In **Figure 7.7** we have performed the same analysis as concerns the charge and the xc-effects for $[Au_{55}]^q$ clusters. At variance with respect to silver, the effects for $[Au_{55}]^q$ are not relevant: the general shape of the profiles does not change qualitatively if the charge or the xc-functional are varied. It is curious that for both LB94 and PBE the change of charge state from -3 to +5 causes a red-shift at low energy and a blue-shift for energies above 6 eV, so the charge effect cannot be simplified as a rigid translation on the energy scale.

In **Figure 7.8** the role of the basis set (upper panel) is considered. Going from DZ to TZ2P a slight intensity decrease is observed for energies below 5 eV, while above 8 eV the profiles look rather different, suggesting that the high energy part of the spectrum is more demanding in terms of basis set requirements (as expected since we enter the continuum part of the spectrum). The comparison among the three methods (QE, CP2K

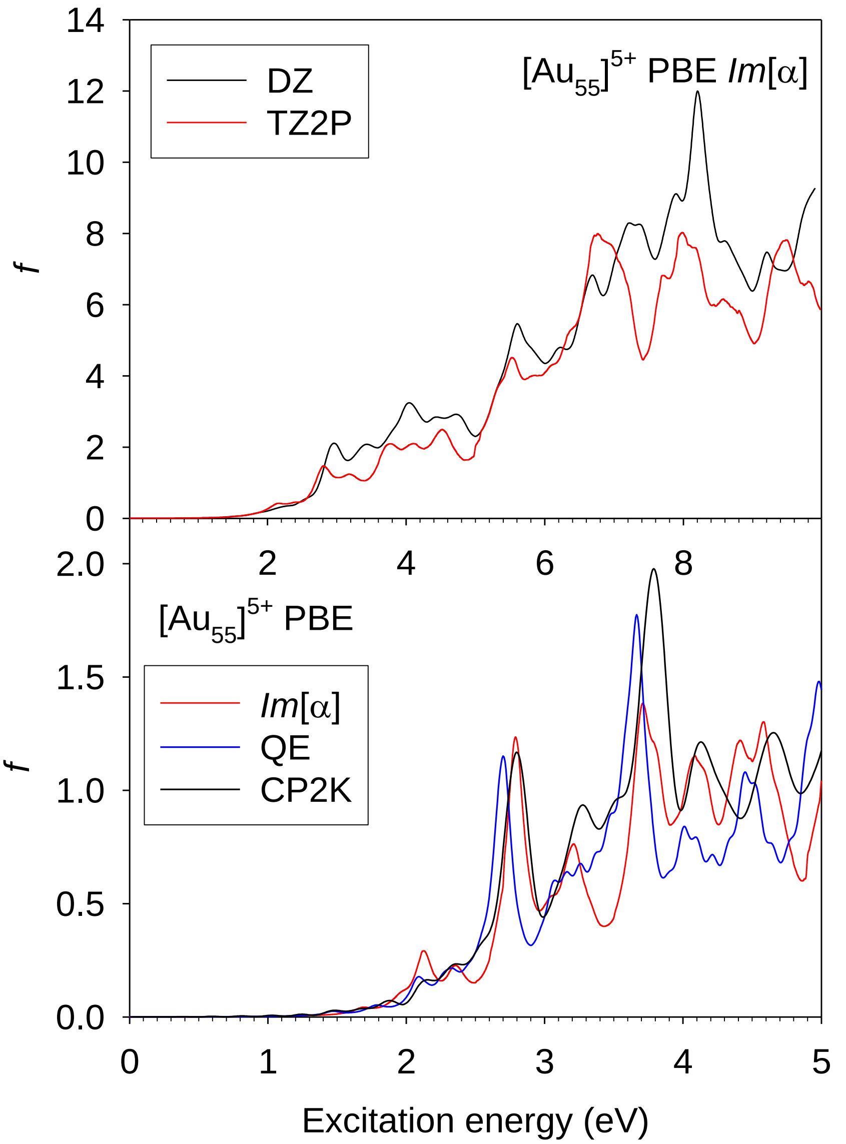

Figure 7.8 *Photoabsorption profiles of [Au$_{55}$]$^{5+}$ calculated by TDDFT PBE. Upper panel: complex polarizability with imaginary broadening ω_i = 0.15 eV. Lower panel: QE, CP2K and complex polarizability with imaginary broadening ω_i = 0.075 eV. Basis sets and methods are shown in insets.*

and complex polarizability) is fair good: for the feature at 2.8 eV the three methods are in excellent agreement with each other, only above 3.2 eV some discrepancies appear, which however do not alter the qualitative shape of the profile. In conclusion we can say that Ag_{55} is much more sensitive than Au_{55} to charge, xc-functional and basis set, due to the plasmon which is present only when LB94 xc-functional with charge -3 are employed. On the other hand for Au_{55} the plasmon is not yet present in full and therefore the spectral differences are consequences of subtle modifications of the electronic structure.

7.5 Conclusions

In this work we have applied a recently developed new TDDFT algorithm [7.7] to a series of closed shell icosahedral Ag and Au clusters, containing from 13 to 309 atoms. The photoabsorption spectrum is extracted from the imaginary part of the complex dynamical polarizability, solving a non-homogeneous linear system and avoiding the diagonalization of the Casida matrix, which represents a problematic step when too many eigenvalues need to be calculated to cover the energy interval of interest. The new method has proven not only to be very efficient, but also very powerful in terms of analysis of the excited state wave function, which has been done employing the 2D TCM scheme. For silver clusters, a very intense plasmon resonance has been found already for $[Ag_{55}]^{3-}$. When cluster size increases the feature gains intensity and is red-shifted, a behaviour typical of plasmon resonances. The TCM analysis identified strong coupling among low energy excited configurations with intraband sp → sp character, while d → sp interband excitations play a minor role. For gold clusters the situation is quite different, as we did not identify a single strong plasmon like in silver clusters, but rather many features of comparable intensity. The TCM analysis revealed that only for the lowest energy features a partial plasmonic behaviour can be singled out, with moderate coupling of low energy excitations together with important interband d → sp excitations. As the energy increases, the coupling with low energy excitations disappears and the features become pure interband d → sp excitations.

The analysis of the spectral features revealed that the photoabsorption in the $[Ag_{55}]^q$ cluster is very sensitive to the cluster charge and choice of xc-functional and basis set. In particular the strong plasmon calculated with LB94 xc-functional and q=3- is suppressed if charge is changed to q=5+ or if the PBE xc-functional is employed. The PBE results obtained with the complex dynamical polarizability compare fairly well with those calculated by using real-time evolution or Lanczos approaches via the QE and CP2K codes. However being so sensitive to physical and computational choices, when using localized basis functions attention needs to be paid to basis set completeness issues as shown by the fact that using the new algorithm only a basis set enlargement from DZ to TZ2P produced a nearly quantitative agreement with both QE and CP2K.

The same analysis for the $[Au_{55}]^q$ cluster shows that in this case the results are much less sensitive to charge, xc-functional and basis set, due to the marginal role played by plasmonic features which do not dominate the spectrum any more. In this case the match among the complex dynamical polarizability, QE and CP2K methods is even better than for the silver homologue.

The efficiency of the complex dynamical polarizability method together with the power of the TCM analysis suggests that further applications to more complex and realistic systems, like for example metal clusters protected by ligands and therefore with reduced symmetry, are feasible and should be able to give an important contribution to rationalize and clarify the many questions still existing in the field and trigger further technological applications.

8 Theoretical photoabsorption spectra of $Au_{144}(SH)_{60}$ at TDDFT level

8.1 Introduction

The $Au_{144}(SH)_{60}$ model cluster has attracted a considerable interest in literature, for the study of the analogue $Au_{144}(SCH_2CH_2Ph)_{60}$ cluster [8.1], such cluster is very stable and robust [8.2], but is not yet characterized by X-ray diffraction, so its structure is simulated with theoretical models, and the simplest corresponds to the $Au_{144}(SH)_{60}$ [8.1].

The theoretical method employed to calculate the photoabsorption spectra has been described in details in chapter 5 [8.3], this cluster has been selected to test the new TDDFT complex polarizability algorithm with a very large system (~200 atoms). In fact with ADF code is possible extract only up to ~3eV of excitation energy in the spectra without introducing numerical errors during the iterative procedure of the Davidson diagonalization (**Figure 8.2**).

8.2 Computational details

The structure employed in the present work is reported in **Figure 8.1**, it has been symmetrised to D5 point group symmetry by Barcaro et al. [8.4] employing the LDA Vxc potential in the geometry optimization.

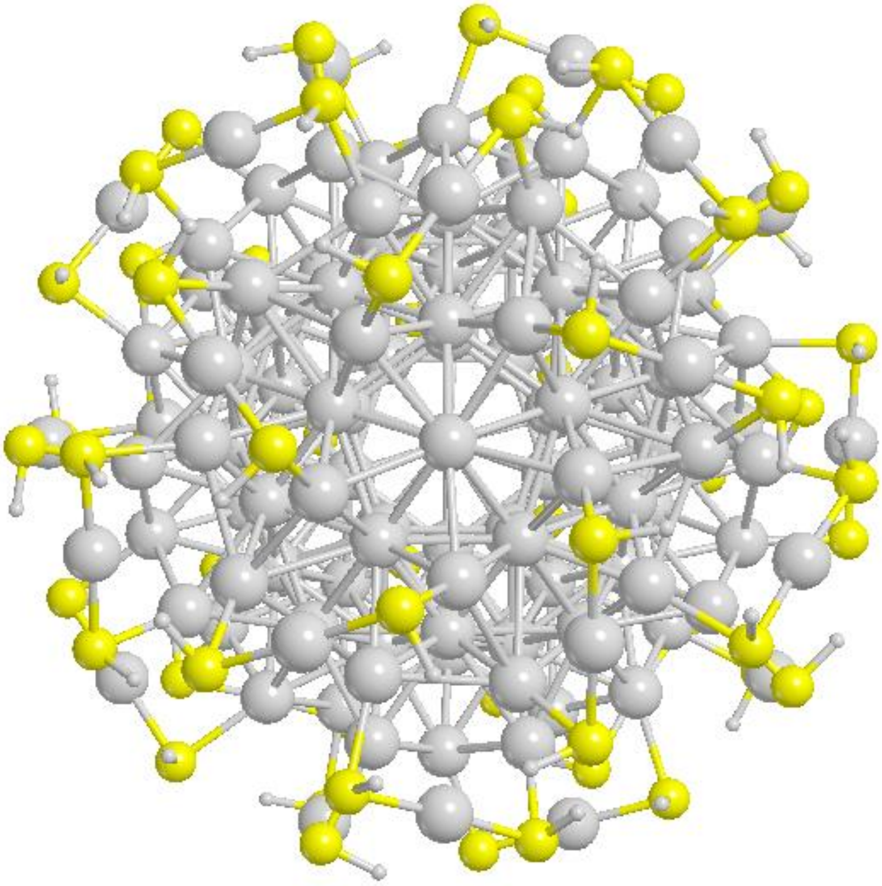

Figure 8.1 *Structure of the* $Au_{144}(SH)_{60}$ *employed in the calculations.*

The complex polarizability method has been implemented in a local version of the ADF code. The LB94 [8.5] or the PBE [8.6] exchange-correlation xc-functionals were employed to obtain the KS orbitals and eigenvalues from the KS equations, while the exchange-correlation kernel is approximated by ALDA [8.7] in the TDDFT part taking the derivative of the VWN [8.8] LDA xc-potential. The basis sets as well as the auxiliary density fitting functions employed consist of Slater Type Orbitals (STO) included in the ADF database. The new program allows a simple choice of a subset of the ADF fitting functions, in order to save computer time when some fitting functions are not necessary for an accurate description of the photoabsorption spectrum. The calculations have been performed at scalar relativistic level with Zero Order Relativistic Approximation (ZORA) [8.9].

8.3 Results and discussion

In **Figure 8.2** is reported the comparison of the calculated spectra at the TDDFT level of $Au_{144}(SH)_{60}$ between ADF code and complex polarizability algorithm, and can be observed the good accord for the low energy interval of the spectra, and the limitation of the Davidson diagonalization.

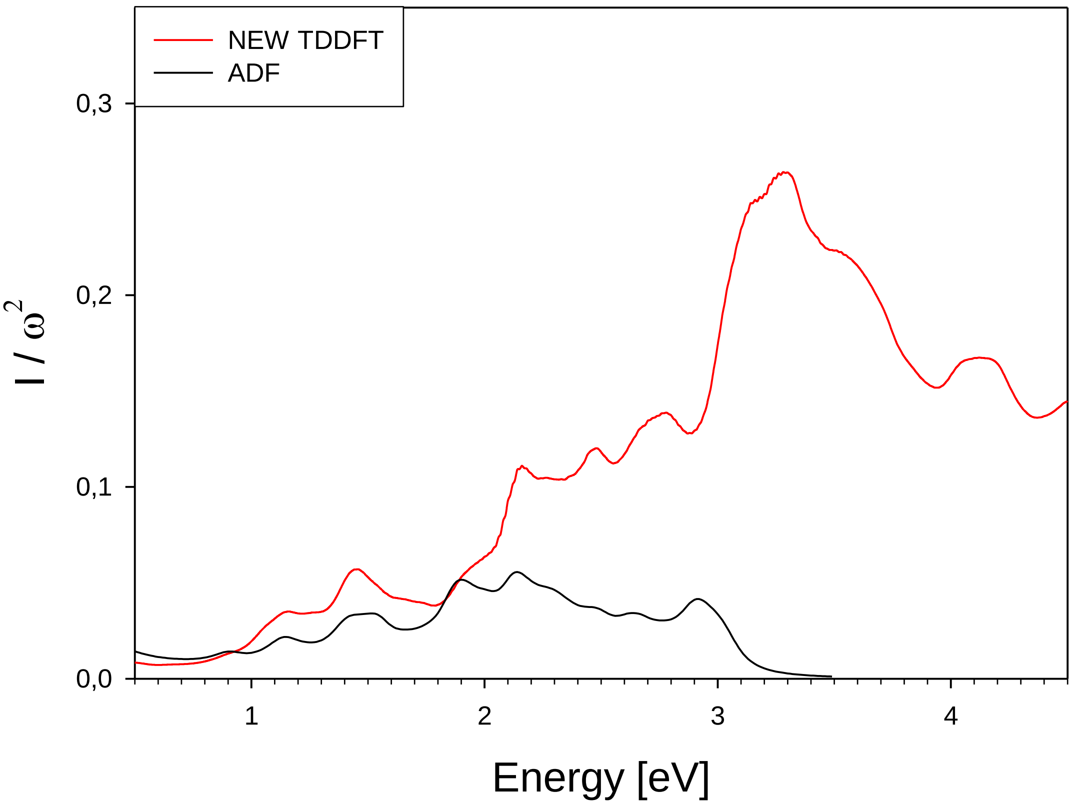

Figure 8.2 *Comparison between the TDDFT calculated spectra of* $Au_{144}(SH)_{60}$ *with ADF and the complex polarizability algorithm; DZ basis set, PBE* V_{XC} *potential, z component.*

From **Figure 8.3** it is apparent that the equivalent x and y components of the absorption spectrum resemble closely z-th dipole component. This happens because the ligands affect the geometry of the cluster, lowering the symmetry group from the icosahedral shape to a less symmetry one, D_5 in this case. The difference between the components is more pronounced at higher energy, where ligands play a more important role, while at low energy the spectrum is governed by absorption of the gold core, which retains largely its icosahedral symmetry. Also the experimental data [8.1] for $Au_{144}(SC_6H_{13})_{60}$ at 77 K is reported for a qualitative comparison.

Both xc-functionals with DZ basis set (**Figure 8.3**) give only a qualitative agreement with the experiment. In particular PBE displays a large jump around 3eV which is not supported by the experimental data. At lower energies both functionals displays weak features which seem to reproduce correctly the experiment. However the latter is characterized by a sudden increase around 1.7eV which is much more broadened in the calculation. The oversimplification of the SC_6H_{13} ligand to the SH one and the uncertainty in the cluster geometry prevent for a more detailed analysis and comparison between theory and experiment.

Finally the calculated spectrum with TZP basis set and LB94 V_{XC} potential simulates very well the experimental data. It presents two weak signals at 1.3 and 1.5eV like the experiment (1.36 and 1.50eV); the theoretical data display a large jump around 1.8eV which is present in experimental data at 1.86 eV. At higher energies the calculated spectrum gives only small differences in intensity distribution and energy with respect to the experiment.

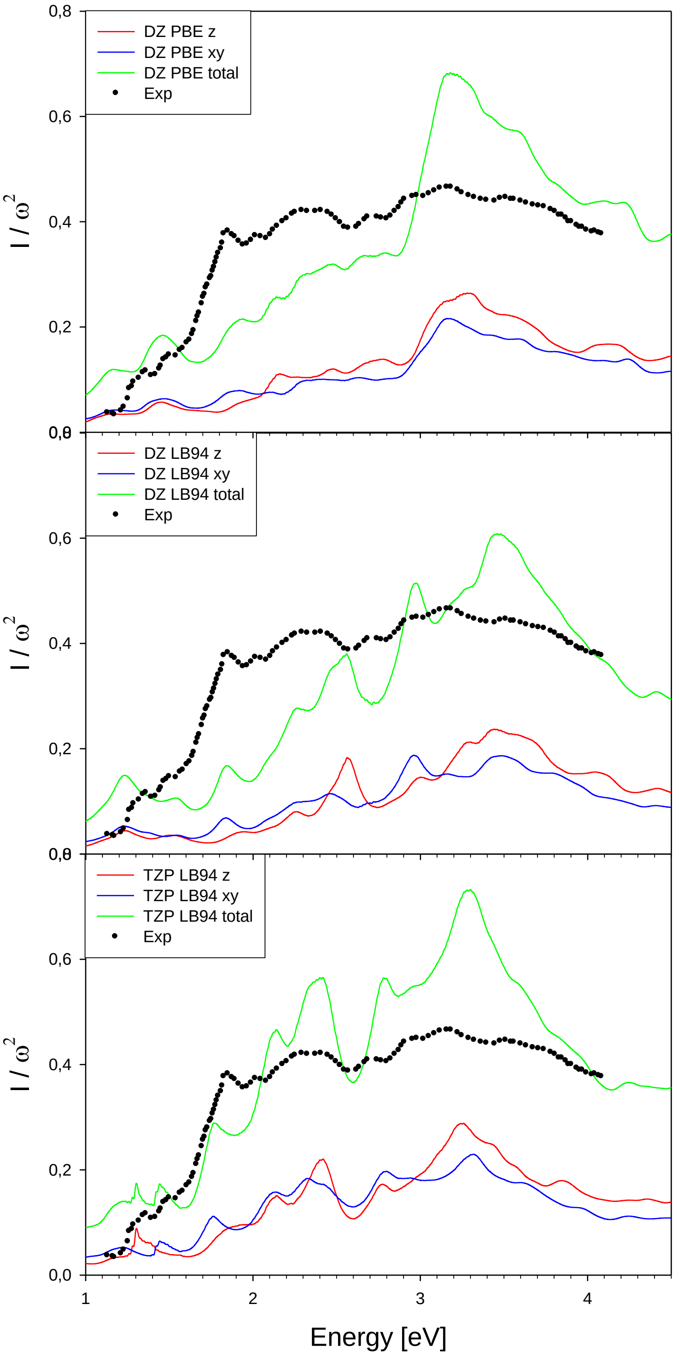

Figure 8.3 *components and total absorption spectra of* $Au_{144}(SH)_{60}$ *calculated with the new TDDFT complex polarizability algorithm. Experimental data of* $Au_{144}(SC_6H_{13})_{60}$ *are reported [8.1]. Upper panel: DZ basis set and PBE XC potential, Central panel: DZ basis set and LB94 XC potential, Lower panel: TZP basis set and LB94 XC potential*

9 Circular dichroism from complex polarizability TDDFT

Oscar Baseggio, Giovanna Fronzoni, Daniele Toffoli, Mauro Stener, work in progress

9.1 Theoretical Method

For a molecule with fixed orientation in the laboratory frame, the Circular Dichroism (CD) of an electronic transition from the ground state $|0\rangle$ to the *n*-th excited state $|n\rangle$ is defined as the difference between the absorbance of left and right circulary polarized light which propagates along the X direction as follows [9.1]:

$$CD = A_L - A_R = 2k\,\mathrm{Im}(\langle 0|\mu_Y|n\rangle\langle n|m_Y|0\rangle + \langle 0|\mu_Z|n\rangle\langle n|m_Z|0\rangle) \tag{9.1.1}$$

Where in (9.1.1) $\boldsymbol{\mu}$ and $\mathbf{m}$ are the electric dipole and magnetic dipole moment operators.

When the molecules are randomly oriented, as in usual solution or gas-phase experiments, expression (9.1.1) must be rotationally averaged, and the Rosenfeld equation is obtained:

$$CD = \frac{4}{3}k\,\mathrm{Im}(\langle 0|\boldsymbol{\mu}|n\rangle \cdot \langle n|\boldsymbol{m}|0\rangle) \tag{9.1.2}$$

The Rotatory Strength is therefore defined as follows:

$$R_{0n} = \mathrm{Im}(\langle 0|\boldsymbol{\mu}|n\rangle \cdot \langle n|\boldsymbol{m}|0\rangle) \tag{9.1.3}$$

Our goal is to calculate (9.1.3) with the complex polarizability algorithm [9.2], so it is convenient to consider the dipole moment induced by an electromagnetic field [9.3][9.4]:

$$\mu'_u = \sum_{\nu} \alpha_{u\nu} E_\nu - \sum_{\nu} \frac{\beta_{u\nu}}{c} \frac{\partial B_\nu}{\partial t} \tag{9.1.4}$$

In (9.1.4) β is the optical rotation tensor which is related to the rotatory strength by the following Sum Over States (SOS) expression:

$$\bar{\beta} = \frac{1}{3} \sum_{u} \beta_{uu} = \frac{2c}{3} \sum_{n} \frac{R_{0n}}{\omega_{0n}^2 - \omega^2} \tag{9.1.5}$$

Therefore we will calculate β and extract R_{0n} from its imaginary part as in conventional photoabsorption. β consists in the electric dipole moment induced by a Time Dependent (TD) magnetic field, so the perturbing Hamiltonian can be written as:

$$H^{(1)} = \frac{1}{2} \left[m_Z e^{-i\omega t} + m_Z^{+} e^{i\omega t} \right] B_Z^0 \tag{9.1.6}$$

Now we can invoke standard Linear Response (LR) theory [9.5] and write down the electric dipole induce by (9.1.6):

$$\Pi(\mu_Z m_Z|\omega) = \lim_{\varepsilon \to 0^+} \sum_{n \neq 0} \left(\frac{\langle 0|\mu_Z|n\rangle\langle n|m_Z|0\rangle}{\omega - \omega_{0n} + i\varepsilon} - \frac{\langle 0|m_Z|n\rangle\langle n|\mu_Z|0\rangle}{\omega + \omega_{0n} + i\varepsilon} \right) \tag{9.1.7}$$

Now consider that the self-adjoint magnetic dipole operator is pure imaginary and assume real wavefunctions:

$$\langle 0|m_Z|n\rangle = \langle n|m_Z|0\rangle^* = -\langle n|m_Z|0\rangle \qquad (9.1.8)$$

In this way equation (9.1.7) becomes:

$$\Pi(\mu_Z m_Z|\omega) = \lim_{\varepsilon\to 0^+} \sum_{n\neq 0} \langle 0|\mu_Z|n\rangle\langle n|m_Z|0\rangle \left(\frac{1}{\omega-\omega_{0n}+i\varepsilon}+\frac{1}{\omega+\omega_{0n}+i\varepsilon}\right) \qquad (9.1.9)$$

So finally:

$$\Pi(\mu_Z m_Z|\omega) = -\int z\rho_Z^{(1)}(r)dr \qquad (9.1.10)$$

Up to now the approach is only formal, since it is not possible to do in practice the infinite sum over all the excited states, but TDDFT can be invoked so the induced density can be calculated with the response of the Kohn-Sham non-interacting systems to the *external magnetic perturbation* plus the conventional potential generated by the response kernel:

$$\begin{aligned}\rho_Z^{(1)}(\omega,\bar{r}) = \sum_{i,a} \varphi_i\varphi_a \, \langle a|m_Z|i\rangle \left(\frac{1}{\omega-\omega_{ia}+i\varepsilon}+\frac{1}{\omega+\omega_{ia}+i\varepsilon}\right)\\ + \int \chi_{KS}\,(\omega,\bar{r},\bar{r}')\, V_{IND}^{Z}(\omega,\bar{r}')d\bar{r}'\end{aligned} \qquad (9.1.11)$$

$$V_{IND}^{Z}(\omega,\bar{r}') = \int \frac{\rho_Z^{(1)}(\omega,\bar{r}')d\bar{r}'}{|\bar{r}-\bar{r}'|} + \left.\frac{\partial V_{XC}}{\partial\rho}\right|_{\rho^{(0)}} \rho_Z^{(1)}(\omega,\bar{r}) \qquad (9.1.12)$$

Now equations (9.1.11) and (9.1.12) can be solved with respect to the induced density and represented over the density fitting set, the following complex linear system must be solved:

$$[\boldsymbol{S}-\boldsymbol{M}(\omega)]\boldsymbol{q}=\boldsymbol{g} \tag{9.1.13}$$

Where in (9.1.13) **g** is a new vector whose elements are:

$$g_\mu=\sum_{k=1}^{P} t_k(\omega)\sum_{\varepsilon_{ia}\in I_k} A^k_{\mu,ia}\langle\varphi_i|m_Z|\varphi_a\rangle \tag{9.1.14}$$

and

$$t_k=\frac{1}{\omega-\omega_{0n}+i\varepsilon}+\frac{1}{\omega+\omega_{0n}+i\varepsilon} \tag{9.1.15}$$

This is quite simple from the computational point of view, since we have already performed the LU decomposition of left hand side of (9.1.13), so we just need only to perform the back-substitution for another column vector, which is computationally irrelevant, only new angular momentum matrix elements must be calculated, which are already available in the debye.f90 routine of ADF.

Once the vector **q** is obtained solving system (9.1.13), accurate polarizability (9.1.10) is calculated, preferably with the MSA [9.2].

Now let’s compare (9.1.4) with (9.1.10):

$$-\frac{\beta_{ZZ}}{c}\frac{\partial B_Z}{\partial t}=\frac{1}{2}\left(\Pi(\mu_Z m_Z|\omega)e^{-i\omega t}+\Pi(\mu_Z m_Z|-\omega)e^{i\omega t}\right) \tag{9.1.16}$$

consider a monochromatic radiation of frequency ω so that the magnetic field is:

$$B_Z=\frac{B_Z^0}{2}\left(e^{-i\omega t}+e^{i\omega t}\right) \tag{9.1.17}$$

$$\frac{\partial B_Z}{\partial t} = \frac{B_Z^0}{2}\left(-i\omega e^{-i\omega t} + i\omega e^{i\omega t}\right) \tag{9.1.18}$$

Therefore we finally find:

$$\beta_{ZZ} = -\frac{ic}{\omega}\Pi(\mu_Z m_Z|\omega) \tag{9.1.19}$$

If we analyse the behaviour of β_{ZZ} (9.1.19) as a function of ω, we find it is real (m_Z operator is pure imaginary), while at resonances it has poles from whose residual the rotatory strength can be extracted, consider one single resonance:

$$\beta_{ZZ} = -\frac{ic}{\omega}\cdot\frac{\langle 0|\mu_Z|n\rangle\langle n|m_Z|0\rangle}{i\varepsilon} \tag{9.1.20}$$

$$\bar{\beta} = -\frac{2icR}{3\omega\varepsilon} \tag{9.1.21}$$

The factor 2 in (9.1.21) derives from an assumed closed shell configuration, so the sum is assumed over spatial orbitals, finally:

$$R = \frac{3\omega\varepsilon}{2c}\mathrm{Im}\left(\bar{\beta}\right) \tag{9.1.22}$$

For finite ε equation (9.1.22) can be directly compared with discrete R spectra calculation smoothed with Lorentzian functions with the same width.

9.2 Implementation

The linear system (9.1.13) is built with one more column (vectors **q** and **g**). **g** is calculated by expression (9.1.14), magnetic moment matrix elements are stored in array rxpij in debye.f90. From **q** with expression (9.1.10) the rotation strength R can be calculated in principle. However it is more convenient and accurate to calculate R with the MSA approach according to the following expression for an electric dipole perturbing field:

$$\beta_{ZZ}(\omega) = \left(-\frac{ic}{\omega}\right)\sum_{i}^{occ}\sum_{a}^{virt}\langle\varphi_i|m_Z|\varphi_a\rangle\,\bar{\bar{P}}_i^a \tag{9.2.1}$$

$$\bar{\bar{P}}_i^a = t_k(\omega)\left[\langle\varphi_i|z|\varphi_a\rangle - \sum_{\mu\tau}^{fit}(A^k)_{ia,\mu}^{+}L_{\mu\tau}b_\tau\right] \tag{9.2.2}$$

If instead a magnetic dipole is considered as a perturbation the following expression is employed:

$$\beta_{ZZ}(\omega) = \left(-\frac{ic}{\omega}\right)\sum_{i}^{occ}\sum_{a}^{virt}\langle\varphi_i|z|\varphi_a\rangle\,\bar{P}_i^a \tag{9.2.3}$$

$$\bar{P}_i^a = t_k(\omega)\langle\varphi_i|m_Z|\varphi_a\rangle + s_k(\omega)\sum_{\mu\tau}^{fit}(A^k)_{ia,\mu}^{+}L_{\mu\tau}q_\tau \tag{9.2.4}$$

Finally, also the electric dipole ‘velocity gauge’ is been implemented, which consists to employ the following expression, which holds for local potential and complete basis, to evaluate electric dipole integrals from linear momentum (derivative) matrix elements:

$$\langle\varphi_a|x|\varphi_i\rangle = \frac{\left\langle\varphi_a\middle|\frac{d}{dx}\middle|\varphi_i\right\rangle}{\varepsilon_a - \varepsilon_i} \tag{9.2.5}$$

So in summary three columns should be employed in linear system (9.1.13), the third is like **b** but calculated in velocity gauge.

The matrix element of the derivative (gradient or nabla) correspond to the array pij in debye.f90

So finally we will have 4 different possibilities to calculate CD spectra: with expression (9.2.1) and (9.2.3) each with length or velocity gauge.

Also the normal photoabsorption calculation has been extended allowing the calculation in both length and velocity gauges.

9.3 Results and Discussion

At the moment we have completed all the implementation as described above, and we have some preliminary results for the chiral helical chain of silver atoms Ag_8. We have taken this system from a previous work [9.6], in particular we have chosen the chain with the bond angle of 150º, the dihedral angle of 10º and interatomic distance of 2.7 Å since it displayed one of the stronger rotation strength among the other chains considered in ref. [9.6]. In **Figure 9.1** we have reported the conventional photoabsorption spectrum, calculated with TZP basis set and LB94 xc-functional, with both ADF program and present complex polarizability algorithm. The chain belongs to the C_2 point group symmetry, so there are two different active dipole components: A (z component) and B (y and z components). The two insets of **Figure 9.1** report the chain from two different view directions, underlying the global shape (left inset from x direction) or the helicity (right inset from z direction, which corresponds to the C_2 binary rotation axis). The agreement between the two methods is fairly nice, only very modest energy shifts around one tenth of eV and intensity deviations for the weak features is apparent, while the most prominent spectral features are very well reproduced.

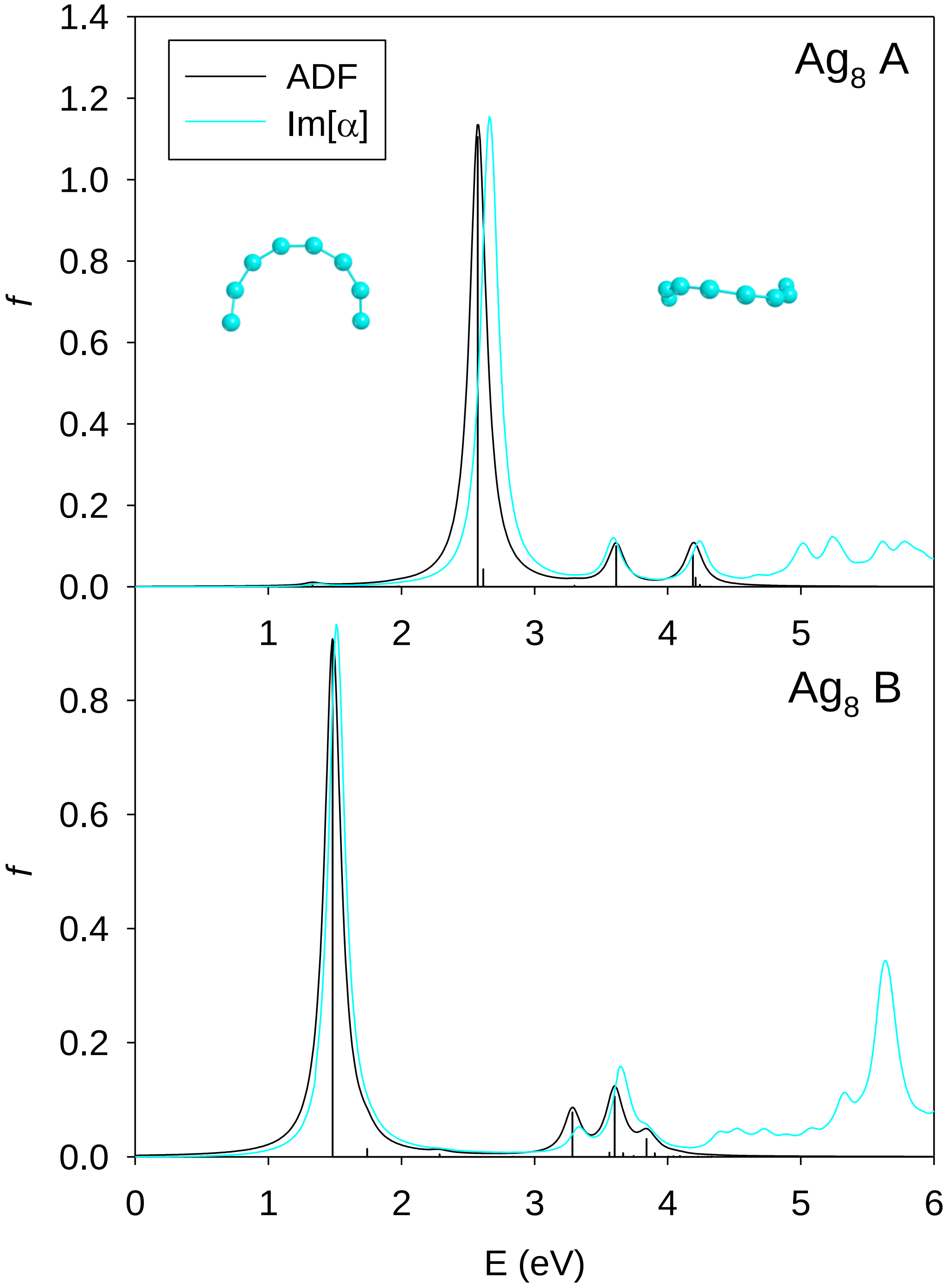

Figure 9.1 *The photoabsorption (f) of Ag*$_8$ *calculated with ADF and from the complex polarizability.*

In **Figure 9.2** the rotation strength (R) is reported for both A and B components, also in this case calculated from the ADF program and from the present new implementation, extracting R from the imaginary part of the optical rotation tensor β. Also in this case the agreement between the two methods is in practice quantitative: the deviations are of the same size as already found for absorption in **Figure 9.1**. It is worth noting that we have calculated R employing both previous expressions (9.2.1)(9.2.2) and (9.2.3)(9.2.4) which furnished the same results, confirming the fundamental equivalence of the expressions. Moreover, since (9.2.1)(9.2.2) and (9.2.3)(9.2.4) are independently calculated each other, this is a safe proof that the new code has been properly debugged. All the results reported in **Figure 9.1** and **Figure 9.2** have been calculated with the length gauge of the dipole operator, we have recalculated them with the velocity gauge but the results were in practice the same so we did not report them in the figure. The match between the two gauges can be expected to worsen in case the basis set quality would be reduced, for example going to DZ which is usually employed when very large clusters are considered. This point will be explored in a further study. Finally it is worth noting that the calculation of R is origin dependent when length gauge is employed, while it is strictly origin invariant for the velocity gauge even for not complete basis set. So the gauge choice will be an important issue which needs to be properly assessed for the calculation of R in large systems with small basis set.

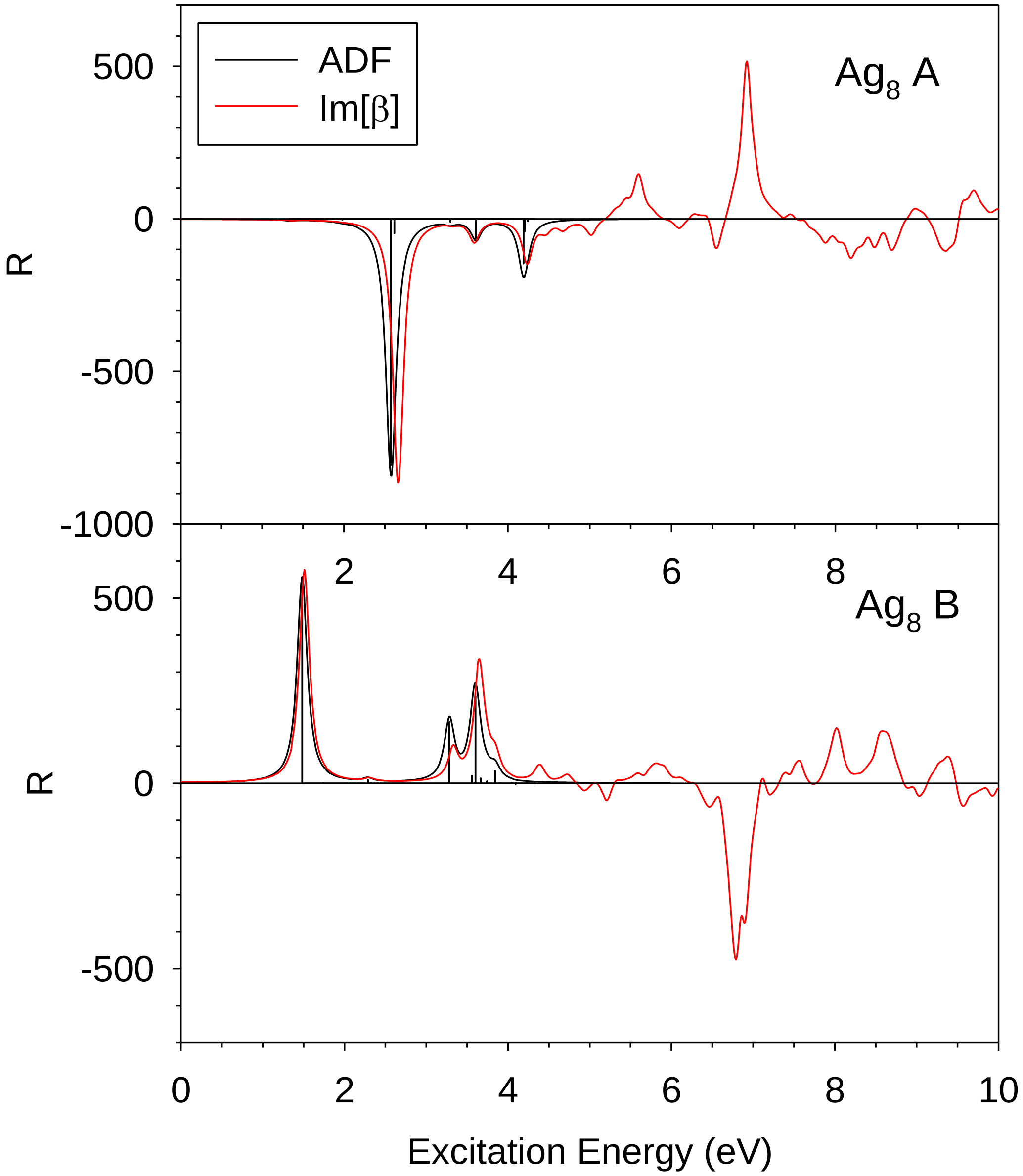

Figure 9.2 *The rotation strength (R) of Ag₈ calculated with ADF and from the complex optical rotation tensor.*

10 Bibliography

Chapter 1

[1.1] A. Bianconi, in X-ray absorption: principles, applications, tecnuiques of EXAFS, SEXAFS and XANES, Koningsberger D. C., Prins R. (Eds.), John Wiley, New York, 1988, p.573

[1.2] J. Stöhr, NEXAFS Spectroscopy, Springer Series in Surface Science, Vol. 25, Springer-Verlag, Berlin – New York, 1992

[1.3] A. Bianconi, Appl. Surf. SCI. 6, 392 (1980)

[1.4] E. L. Shirley, J. Electron Spectrosc. Relat. Phenom, 136 (2004) 77-83

[1.5] A. Bianconi, J. Garcia, M. Benfatto, in Synchrotron radiation in chemistry an biology. 1, Topics in Current Chemistry, Vol. 145, Mandelkow E., Bazin D. (Eds), Springer-Verlag, Berlin Heidelberg, 1988, p.29

[1.6] P. J. Durham, in X-ray absorption: principles, applications, tecnuiques of EXAFS, SEXAFS and XANES, Koningsberger D. C., Prins R. (Eds.), John Wiley, New York, 1988, p.53

[1.7] J. Fink, in Unoccupied electronic states: fundamentals for XANES, EELS, IPS and BIS, Topics in applied physics, Vol. 69, Fuggle J. C., Inglesfield J. E., Andrews P. T. (Eds), Springer-Verlag, Berlin, 1992, p. 203

[1.8] J. L. Dehmer, D. Dill, in Electron-molecule and photon-molecule collisions, Rescigno T. N., McKoy B. V., Schneider B. (Eds), Plenum Press, New York, 1979, p.225

[1.9] J. A. Sheehy, T. J. Gill, C. L. Winstead, R. E. Farren, P. W. Langhoff, J. Chem Phys, 91, 1796 (1989)

[1.10] P. W. Langhoff, in Electron-molecule and photon-molecule collisions, Rescigno T. N., McKoy B. V., Schneider B. (Eds), Plenum Press, New York, 1979, p.183

[1.11] J. Li, X. Li, H.-J. Zhai, and L.-S. Wang, “Au20: A Tetrahedral Cluster,” Science, vol. 299, no. 5608, pp. 864–867, 2003.

[1.12] Z. Zhong, D. Wang, Y. Cui, M. W. Bockrath, and C. M. Lieber, “Nanowire Crossbar Arrays as Address Decoders for Integrated Nanosystems,” Science, vol. 302, no. 5649, pp. 1377–1379, 2003.

[1.13] C. Murphy and N. Jana, “Controlling the aspect ratio of inorganic nanorods and nanowires,” Advanced Materials, vol. 14, no. 1, pp. 80–82, 2002.

[1.14] V. Rodrigues, T. Fuhrer, and D. Ugarte, “Signature of atomic structure in the quantum conductance of gold nanowires,” Phys. Rev. Lett., vol. 85, pp. 4124–4127, Nov 2000.

[1.15] A. Kunzmann, B. Andersson, T. Thurnherr, H. Krug, A. Scheynius, and B. Fadeel, “Toxicology of engineered nanomaterials: Focus on biocompatibility, biodistribution and biodegradation,” Biochimica et Biophysica Acta (BBA) - General Subjects, vol. In Press, Corrected Proof, pp. –, 2010.

[1.16] C. Burda, X. Chen, R. Narayanan, and M. A. El-Sayed, “Chemistry and properties of nanocrystals of different shapes,” Chemical Reviews, vol. 105, pp. 1025–1102, 03 2005

[1.17] C. Zhang, J. Z. Noguez, “Plasmonic optical properties and applications of metal nanostructures,” Plasmonics, vol. 3, pp. 1157–1955, December 2008.

[1.18] Casida, M. E.; C. Jamorski; F. Bohr; J. Guan; D. R. Salahub (1996). S. P. Karna and A. T. Yeates, ed. Theoretical and Computational Modeling of NLO and Electronic Materials. Washington, D.C.: ACS Press. p. 145–

[1.19] G. Barcaro, L. Sementa, A. Fortunelli and M. Stener, Physical Chemistry Chemical Physics, 2015, DOI: 10.1039/C5CP00498E

Chapter 2

[2.1] R. G. Parr, W. Yang, ”Density Functional Theory of Atoms and Molecules”, Oxford University Press, New York 1989

[2.2] P. Hohenberg, W. Kohn, Phys. Rev., 136 (1964) B864

[2.3] Ligneres, Vincent L.; Emily A. Carter (2005). "An Introduction to Orbital Free Density Functional Theory". In Syndey Yip. Handbook of Materials Modeling. Springer Netherlands. pp. 137–148

[2.4] W. Kohn, L. J. Sham, Phys. Rev., 140 (1965) A1133

[2.5] R. van Meer, O. V. Gritsenko, and E. J. Baerends, J. Chem. Theory Comput., 2014, 10 (10), pp 4432–4441

[2.6] J. C. Slater, Adv. Quant. Chem., 6 (1972) 1.

[2.7] D. A. Liberman, Phys. Rev. B, 62 (2000-I) 6851

[2.8] J. F. Janak, Phys. Rev. B, 18 (1978) 7165

[2.9] J. C. Slater, K. H. Johnsson, Phys. Rev. B, 18 (1978) 7165

[2.10] M. Leetman, M. P. Ljungberg, A. Lyubartsev, A. Nilsson, L. G. M. Petersson, J. Electron Spectrosc. Relat. Phenom., 177 (2010) 135

[2.11] L. Triguero, L. G. M. Pettersson, H. Ågren, Phys. Rev. B, 58 (1998) 8097

[2.12] J. C. Slater, K. H. Johnsson, Phys. Rev. B, 5 (1972) 844

[2.13] G. Diercksen, R. McWeeny, J. Chem. Phys, 44, (1966) 3554

[2.14] E. Runge, E. K. U. Gross, Phys. Rev. Lett., 52 (1984) 997

[2.15] O. Baseggio, G. Fronzoni, M. Stener; J. Chem. Phys.; 2015, 143, 024106.

[2.16] E. K. U. Gross and W. Kohn, “Time-dependent density-functional theory”, Adv. Quantum Chem. 21, 255 (1990)

[2.17] E. J. Baerends, D. E. Ellis, P. Roos, Chem. Phys., 2 (1973) 41

[2.18] C. Fonseca Guerra, J. G. Snijders, G. Te Velde, E. J. Baerends, Theor. Chem. Acc., 99 (1998) 391

[2.19] Kenneth G. Dyall; Knut Fægri, Jr.; Introduction in Introduction to Relativistic Quantum Chemistry; Oxford University Press, 2007

[2.20] E. van Lenthe, E. J. Baerends; J. Comput. Chem., 2006, 24 (9), 1142-1156

[2.21] F. Wang, T. Ziegler, E. van Lenthe, S. Van Gisbergen, E. J. Bearends; J. Chem. Phys., 2005, 122 (20), 204103

[2.22] Koch W., Holthausen M.C.; A Chemist's Guide to Density Functional Theory, Wiley-VCH, Weinheim, 2000

[2.23] S. Malola, L. Lehtovaara, J. Enkovaara, and H. Hakkinen, ACS Nano 7, 10263 (2013).

[2.24] G. D. Mahan and K. R. Subbaswamy, Local Density Theory of Polarizability (Plenum Press, New York, 1990).

[2.25] M. Stener, P. Decleva, and A. Lisini, J. Phys. B: At., Mol. Opt. Phys. 28, 4973 (1995).

[2.26] M. Stener and P. Decleva, J. Chem. Phys. 112, 10871 (2000).

[2.27] S. Bernadotte, F. Evers, and C. R. Jacob, J. Phys. Chem. C 117, 1863 (2013).

[2.28] B. Gao, K. Ruud, and Y. Luo, J. Phys. Chem. C 118, 13059 (2014).

[2.29] L. Bursi, A. Calzolari, S. Corni, and E. Molinari, ACS Photonics 1, 1049 (2014).

Chapter 3

[3.1] J. Stöhr, NEXAFS Spectroscopy (Springer Verlag, Berlin, 1992).

[3.2] H. Ågren, V. Carravetta, O. Vahtras, and L. G. M. Pettersson, Chem. Phys. Lett. 222, 75 (1994).

[3.3] M. Stener, A. Lisini, and P. Decleva, Chem. Phys. 191, 141 (1995).

[3.4] L. Triguero, L. G. M. Pettersson, and H. Ågren, Phys. Rev. B 58, 8097 (1998).

[3.5] M. Stener, G. Fronzoni, and M. de Simone, Chem. Phys. Lett. **373**, 115 (2003).

[3.6] N. A. Besley and F. A. Asmuruf, Phys. Chem. Chem. Phys. **12**, 12024 (2010)

[3.7] W. Eberhardt, R. P. Haelbich, M. Iwan, E. E. Koch, and C. Kunz, Chem. Phys. Lett. **40**, 180 (1976)

[3.8] A. P. Hitchcock and C. E. Brion, J. Electron Spectrosc. Relat. Phenom. **10**, 317 (1977).

[3.9] Y. Ma, F. Sette, G. Meigs, S. Modesti, and C. T. Chen, Phys. Rev. Lett. **63**, 2044 (1989).

[3.10] O. Plashkevych, T. Privalov, H. Ågren, V. Carravetta, and K. Ruud, Chem. Phys. **260**, 11 (2000).

[3.11] A. Lisini, G. Fronzoni, and P. Decleva, J. Phys. B: At., Mol. Opt. Phys. **21**, 3653 (1988).

[3.12] M. Stener, A. Lisini, and P. Decleva, J. Electron Spectrosc. Relat. Phenom. **69**, 197 (1994).

[3.13] U. Gelius, S. Svensson, H. Siegbahn, E. Basilier, A. Faxalv, and K. Siegbahn, Chem. Phys. Lett. 28, 1 (1974).

[3.14] U. Hergenhahn, J. Phys. B: At. Mol. Phys. 37, R89 (2004).

[3.15] B. Apicella, R. Barbella, A. Ciajolo, and A. Tregrossi, Combust. Sci. Technol. 174(11–12), 309 (2002).

[3.16] B. Apicella, A. Carpentieri, M. Alfè, R. Barbella, A. Tregrossi, P. Pucci, and A. Ciajolo, Proc. Combust. Inst. 31(1), 547 (2007).

[3.17] H. Wang, Proc. Combust. Inst. 33, 41 (2011).

[3.18] A. D'Anna, Proc. Combust. Inst. 32(1), 593 (2009).

[3.19] H. Bockhorn, A. D'Anna, A. F. Sarofim, and H.Wang, Combustion Generated Fine Carbonaceous Particles, Proceedings of an International Workshop held in Villa Orlandi, Anacapri, May 13–16, 2007 (KIT Scientific Publishing, 2007).

[3.20] U. von Barth and G. Grossman, Solid State Commun. 32, 645 (1979).

[3.21] U. von Barth and G. Grossmann, Phys. Rev. B 25, 5150 (1982).

[3.22] T. Privalov, F. Gel'mukhanov, and H. Ågren, Phys. Rev. B 64, 165115 (2001).

[3.23] T. Privalov, F. Gel'mukhanov, and H. Ågren, Phys. Rev. B 64, 165116 (2001).

[3.24] A. D. Becke, Phys. Rev. A 38, 3098 (1988).

[3.25] A. D. Becke, J. Chem. Phys. 98, 5648 (1993).

[3.26] C. Lee, W. Yang, and R. G. Parr, Phys. Rev. B 37, 785 (1988).

[3.27] M. J. Frisch, G. W. Trucks, H. B. Schlegel et al., Gaussian 09, Revision C.01, Gaussian, Inc., Wallingford, CT, 2009.

[3.28] J. P. Perdew, Phys. Rev. B 33, 8822 (1986).

[3.29] G. te Velde, F. M. Bickelhaupt, E. J. Baerends, C. Fonseca Guerra, S. J. A. van Gisbergen, J. G. Snijders, and T. Ziegler, J. Comput. Chem. 22, 931 (2001).

[3.30] C. Fonseca Guerra, J. G. Snijders, G. te Velde, and E. J. Baerends, Theor. Chem. Acc. 99, 391 (1998).

[3.31] E. J. Baerends, T. Ziegler, J. Autschbach, D. Bashford, A. Bárces, F. M. Bickelhaupt, C. Bo, P. M. Boerrigter, L. Cavallo, D. P. Chong et al., ADF2010, SCM, Theoretical Chemistry, Vrije Universiteit, Amsterdam, The Netherlands, 2010, see http://www.scm.com.

[3.32] P. S. Bagus, Phys. Rev. 139, 619 (1965).

[3.33] L. Triguero, O. Plashkevych, L. G. M. Pettersson, and H. Ågren, J. Electron Spectrosc. Relat. Phenom. 104, 195 (1999).

[3.34] T. Ziegler, A. Rauk, and E. J. Baerends, Theor. Chim. Acta 43, 261 (1977).

[3.35] P. Macak, Y. Luo, and H. Ågren, Chem. Phys. Lett. 330, 447 (2000).

[3.36] G. Tian, S. Duan, W. Hua, and Y. Luo, DynaVib, Version 1.0, Royal Institute of Technology, Sweden, 2012.

[3.37] I. Minkov, F. Gel'Mukhanov, R. Friedlein, W. Osikowicz, C. Suess, G. Ohrwall, S. L. Sorensen, S. Braun, R. Murdey, W. R. Salaneck et al., J. Chem. Phys. 121, 5733 (2004).

[3.38] W. Hua, G. Tian, G. Fronzoni, X. Li, M. Stener, and Y. Luo, J. Phys. Chem. A 117, 14075 (2013).

[3.39] W. Hua, J. D. Biggs, Y. Zhang, D. Healion, H. Ren, and S. Mukamel, J. Chem. Theory Comput. 9, 5479 (2013).

[3.40] I. Minkov, F. Gelmukhanov, H. Ågren, R. Friedlein, C. Suess, and W. R. Salaneck, J. Phys. Chem. A 109, 1330 (2005).

[3.41] X. Chen, G. Tian, Z. Rinkevicius, O. Vahtras, Z. Cao, H. Ågren, and Y. Luo, Chem. Phys. 405, 40 (2012).

[3.42] H. Ren, J. D. Biggs, and S. Mukamel, J. Raman Spectrosc. 44, 544 (2013).

[3.43] R. Blyth, R. Delaunay, M. Zitnik, J. Krempasky, R. Krempaska, J. Slezak, K. Prince, R. Richter, M. Vondracek, R. Camilloni, L. Avaldi, M. Coreno, G. Stefani, C. Furlani, M. de Simone, S. Stranges, and M.-Y. Adam, J. Electron Spectrosc. Relat. Phenom. 101–103, 959 (1999).

[3.44] O. Plekan, V. Feyer, R. Richter, M. Coreno, M. de Simone, K. Prince, A. Trofimov, E. Gromov, I. Zaytseva, and J. Schirmer, Chem. Phys. 347, 360 (2008).

[3.45] R. Boschi, J. N. Murrel, and W. Schmidt, Discuss. Faraday Soc. 54, 116 (1972). 044313-9 Fronzoni et al. J. Chem. Phys. 141, 044313 (2014)

[3.46] M. S. Deleuze, J. Chem. Phys. 116, 7012 (2002).

[3.47] R. Boschi and W. Schmidt, Tetrahedron Lett. 25, 2577 (1972).

[3.48] M. S. Deleuze, J. Phys. Chem. A 108, 9244 (2004).

[3.49] T. D. Thomas and R. W. Shaw, Jr., J. Electron Spectrosc. Relat. Phenom 5, 1081 (1974).

[3.50] M. Tronc, G. C. King, and F. H. Read, J. Phys. B: At. Mol. Phys. 12, 137 (1979).

[3.51] M. Tronc, G. C. King, and F. H. Read, J. Phys. B: At. Mol. Phys. 13, 999 (1980).

[3.52] O. Takahashi and L. G. M. Pettersson, J. Chem. Phys. 121, 10339 (2004).

[3.53] H. Li, W. Hua, Z. Lin, and Y. Luo, J. Phys. Chem. B 116, 12641 (2012).

[3.54] V. Myrseth, K. J. Børve, K. Wiesner, M. Bässler, S. Svensson, and J. Sæthre, Phys. Chem. Chem. Phys. 4, 5937 (2002).

[3.55] A. Allouche, J. Comput. Chem. 32, 174 (2011).

Chapter 4

[4.1] J. Roncali *Chem. Rev.* 1992, 92, 711-738.

[4.2] J. Roncali *Chem. Rev.* 1997, 97, 173-206.

[4.3] A. Mishra, C. Ma, P. Bauerle, *Chem. Rev.* 2009, 109, 1141−1276.

[4.4] T. W. Kelley, P. F. Baude, C. Gerlach, D. E. Ender, D. Muyres, M. A. Haase, D. E. Vogel, S. D. Theiss, *Chem. Mater.* 2004, 16, 4413−4422.

[4.5] G. R. Hutchison, M. A. Ratner, T. J. Marks, J. Am. Chem. Soc. 2005, 127, 16866-16881.

[4.6] T. A. Skotheim, Ed.; Dekker ***Handbook of Conducting Polymers*** New York, 1986; Vols. 1 and 2

[4.7] G. Barbarella, M. Melucci and G. Sotgiu, *Adv. Mater.*, 2005, 17, 1581-1593.

[4.8] J. E. Chadwick, B. E. Kohler, *J. Phys. Chem.* 1994, 98, 3631-3637.

[4.9] E. Ortí, P. M. Viruela, J. Sánchez-Marín, F. Tomás, *J. Phys. Chem.* 1995, 99, 4955-4963.

[4.10] D. Jones, M. Guerra, L. Favaretto, A. Modelli, M. Fabrizio, G. Distefano, *J. Phys. Chem.* 1990, 94, 5761-5766.

[4.11] M. Rubio, M. Merchán, E. Ortí, *Chem. Phys. Chem.* 2005, 6, 1357-1368.

[4.12] A. Prlj, B. F. E. Curchod, A. Fabrizio, L. Floryan, and C. Corminboeuf *J. Phys. Chem. Lett.* 2015, 6, 13−21.

[4.13] R. R. Blyth, R. Delaunay, M. Zitnik, J. Krempasky, R. Krempaska, J. Slezak, K. C. Prince, R. Richter, M. Vondracek, R. Camilloni, et al. J. Electron Spectrosc. Relat. Phenom. 1999, 101−103, 959−964.

[4.14] N. Mårtensson, P. Balzer, P. Bruhwiler, J. Forsell, A. Nilsson, A. Stenborg, and B. Wannberg, J. Electron Spectrosc. Relat. Phenom. 70, 117–128 (1994).

[4.15] M. Tronc, G. C. King, and F. H. Read, Journal of Physics B: Atomic and Molecular Physics 12, 137 (1979).

[4.16] M. Tronc, G. C. King, and F. H. Read, Journal of Physics B: Atomic and Molecular Physics 13, 999 (1980).

[4.17] S. H. Vosko, L. Wilk and M. Nusair, Can. J. Phys. **58**, 1200 (1980).

[4.18] G. te Velde, F. M. Bickelhaupt, E. J. Baerends, C. Fonseca Guerra, S. J. A. van Gisbergen, J. G. Snijders, and T. Ziegler, J. Comput. Chem. **22**, 931 (2001).;

[4.19] C. Fonseca Guerra, J. G. Snijders, G. te Velde, and E. J. Baerends, Theor. Chem. Acc. **99**, 391 (1998).

[4.20] E. J. Baerends, T. Ziegler, J. Autschbach, D. Bashford, A. B´arces, F. M. Bickelhaupt,C. Bo, P. M. Boerrigter, L. Cavallo, D. P. Chong, et al., *ADF2010*, SCM, TheoreticalChemistry, Vrije Universiteit, Amsterdam, The Netherlands, http://www.scm.com.

[4.21] J. P. Perdew, Phys. Rev. B **33**, 8822 (1986).

[4.22] L. Triguero, L. G. M. Pettersson, and H. Ågren, Phys. Rev. B **58**, 8097 (1998).

[4.23] U. von Barth and G. Grossman, Solid State Commun. **32**, 645 (1979); U. von Barth and G. Grossmann, Phys. Rev. B **25**, 5150 (1982).

[4.24] T. Privalov, F. Gel'mukhanov, and H. Ågren, Phys. Rev. B **64**, 165115 (2001); T. Privalov, F. Gel'mukhanov, and H. Ågren, Phys. Rev. B **64**, 165116 (2001).

[4.25] J. Stöhr, *NEXAFS Spectroscopy* (Springer Verlag, Berlin, 1992).

[4.26] J. P. Perdew, Phys. Rev. B **33**, 8822 (1986); P. S. Bagus, Phys. Rev. **139**, 619 (1965).

[4.27] A. Hitchcock, J.A. Horsley, J. Stöhr, J. Chem. Phys. **85** (1986) 4835;

[4.28] P. Väterlein, M. Schmelzer, J. Taborski, T. Krause, F. Viczian, M. Bäßler, R. Fink, E. Umbach, W. Wurth, Surf. Science **452** (2000) 20

[4.29] A. Giertz, M. Bässler, O. Björneholm, H. Wang, R. Feifel, C. Miron, L. Karlsson, S. Svensson JCP 117 (2002) 7587

[4.30] G. A. Diaz-Quijada, N. Weinberg, S. Holdcroft, B. M. Pinto, J. Phys. Chem. A, 2002, **106**, 1266

[4.31] M. Rubio, M. Merch, E. Ort, ChemPhysChem, 2005, **6**, 1357-1368

[4.32] A. Baiardi, M. Mendolicchio, V. Barone, G. Fronzoni, G. A. Cardenas Jimenez, M. Stener, C. Grazioli, M. de Simone and M. Coreno, J. Chem. Phys. **143**, 204102 (2015)

[4.33] G. Fronzoni, O. Baseggio, M. Stener, W. Hua, G. Tian, Y. Luo, B. Apicella, M. Alfé, M. de Simone, A. Kivimäki, and M. Coreno, The Journal of Chemical Physics **141**, 044313 (2014)

Chapter 5

[5.1] M. E. Casida, in Recent Advances in Density-Functional Methods, edited by D. P. Chong (World Scientific, Singapore, 1995), p. 155.

[5.2] E. J. Baerends, D. E. Ellis, and P. Ros, Chem. Phys. 2, 41 (1973).

[5.3] C. Fonseca Guerra, J. G. Snijders, G. te Velde, and E. J. Baerends, Theor. Chem. Acc. 99, 391 (1998).

[5.4] S. J. A. van Gisbergen, J. G. Snijders, and E. J. Baerends, Comput. Phys. Commun. 118, 119 (1999).

[5.5] R. Ahlrichs, M. Bar, M. Haser, H. Horn, and C. Kolmel, Chem. Phys. Lett. 162, 165 (1989).

[5.6] K. Yabana and G. F. Bertsch, Phys. Rev. B 54, 4484 (1996).

[5.7] M. A. L. Marques, A. Castro, G. F. Bertsch, and A. Rubio, Comput. Phys. Commun. 151, 60 (2003).

[5.8] A. Castro, M. A. L. Marques, D. Varsano, F. Sottile, and A. Rubio, C. R. Phys. 10, 469 (2009).

[5.9] H.-Ch. Weissker and C. Mottet, Phys. Rev. B 84, 165443 (2011).

[5.10] X. Lopez-Lozano, H. Barron, C. Mottet, and H.-C. Weissker, Phys. Chem. Chem. Phys. 16, 1820 (2014).

[5.11] B. Walker, A. M. Saitta, R. Gebauer, and S. Baroni, Phys. Rev. Lett. 96, 113001 (2006).

[5.12] B. Walker and R. Gebauer, J. Chem. Phys. 127, 164106 (2007).

[5.13] D. Rocca, R. Gebauer, Y. Saad, and S. Baroni, J. Chem. Phys. 128, 154105 (2008).

[5.14] P. Ghosh and R. Gebauer, J. Chem. Phys. 132, 104102 (2010).

[5.15] S. Grimme, J. Chem. Phys. 138, 244104 (2013).

[5.16] C. Bannwarth and S. Grimme, Comput. Theor. Chem. 1040, 45 (2014).

[5.17] T. J. Zuehlsdorff, N. D. M. Hine, J. S. Spencer, N. M. Harrison, D. J. Riley, and P. D. Haynes, J. Chem. Phys. 139, 064104 (2013).

[5.18] S. Malola, L. Lehtovaara, J. Enkovaara, and H. Hakkinen, ACS Nano 7, 10263 (2013).

[5.19] M. Noda, K. Ishimura, K. Nobusada, K. Yabana, and T. Boku, J. Comput. Phys. 265, 145 (2014).

[5.20] K. Iida, M. Noda, K. Ishimura, and K. Nobusada, J. Phys. Chem. A 118, 11317 (2014).

[5.21] M. Pavanello, J. Chem. Phys. 138, 204118 (2013).

[5.22] R. Kevorkyants, H. Eshius, and M. Pavanello, J. Chem. Phys. 141, 044127 (2014).

[5.23] M. Valiev, E. J. Bylaska, N. Govind, K. Kowalski, T. P. Straatsma, H. J. J. van Dam, D.Wang, J. Nieplocha, E. Apra, T. L.Windus, andW. A. de Jong, Comput. Phys. Commun. 181, 1477 (2010).

[5.24] J. Kauczor, P. Jorgensen, and P. Norman, J. Chem. Theory Comput. 7, 1610 (2011).

[5.25] E. K. U. Gross and W. Kohn, “Time-dependent density-functional theory”, Adv. Quantum Chem. 21, 255 (1990).

[5.26] A. Ipatov, A. Hesselmann, and A. Gorling, Int. J. Quantum Chem. 110, 2202 (2010).

[5.27] G. D. Mahan and K. R. Subbaswamy, Local Density Theory of Polarizability (Plenum Press, New York, 1990).

[5.28] M. Stener, P. Decleva, and A. Lisini, J. Phys. B: At., Mol. Opt. Phys. 28, 4973 (1995).

[5.29] M. Stener and P. Decleva, J. Chem. Phys. 112, 10871 (2000).

[5.30] M. Stener, G. Fronzoni, D. Toffoli, and P. Decleva, Chem. Phys. 282, 337 (2002).

[5.31] R. Van Leeuwen and E. J. Baerends, Phys. Rev. A 49, 2421 (1994).

[5.32] S. H. Vosko, L. Wilk, and M. Nusair, Can. J. Phys. 58, 1200 (1980).

[5.33] S. Bernadotte, F. Evers, and C. R. Jacob, J. Phys. Chem. C 117, 1863 (2013).

[5.34] B. Gao, K. Ruud, and Y. Luo, J. Phys. Chem. C 118, 13059 (2014).

[5.35] L. Bursi, A. Calzolari, S. Corni, and E. Molinari, ACS Photonics 1, 1049 (2014).

[5.36] G. M. Piccini, R. W. A. Havenith, R. Broer, and M. Stener, J. Phys. Chem. C 117, 17196 (2013).

[5.37] N. Durante, A. Fortunelli, M. Broyer, and M. Stener, J. Phys. Chem. C 115, 6277 (2011).

[5.38] J. Kauczor and P. Norman, J. Chem. Theory Comput. 10, 2449 (2014).

Chapter 6

[6.1] Whetten, R. L.; Khoury, J. T.; Alvarez, M. M.; Murthy, S.; Vezmar, I.; Wang, Z. L.; Stephens, P. W.; Cleveland, C. L.; Luedtke, W. D.; Landman, U. *Adv. Mater.* **1996**, *8*, 428.

[6.2] Parker, J. F.; Fields-Zinna, C. A.; Murray, R. W. *Acc. Chem. Res.* **2010**, *43*, 1289.

[6.3] Heaven, M. W.; Dass, A.; White, P. S.; Holt, K. M.; Murray, R. W. *J. Am. Chem. Soc.* **2008**, *130*, 3754.

[6.4] Chaki, N. K.; Negishi, Y.; Tsunoyama, H.; Shichibu, Y.; Tsukuda, T. *J. Am. Chem. Soc.* **2008**, *130*, 8608.

[6.5] Weissker, H. C.; Escobar, H. B.; Thanthirige, V. D.; Kwak, K.; Lee, D.; Ramakrishna, G.; Whetten, R. L.; López-Lozano, X. *Nat Commun* **2014**, *5*.

[6.6] Offord, D. A.; John, C. M.; Linford, M. R.; Griffin, J. H. *Langmuir* **1994**, *10*, 883.

[6.7] Krommenhoek, P. J.; Wang, J.; Hentz, N.; Johnston-Peck, A. C.; Kozek, K. A.; Kalyuzhny, G.; Tracy, J. B. *Acs Nano* **2012**, *6*, 4903.

[6.8] Nishigaki, J.-i.; Tsunoyama, R.; Tsunoyama, H.; Ichikuni, N.; Yamazoe, S.; Negishi, Y.; Ito, M.; Matsuo, T.; Tamao, K.; Tsukuda, T. *J. Am. Chem. Soc.* **2012**, *134*, 14295.

[6.9] Crasto, D.; Dass, A. *J. Phys. Chem. C.* **2013**, *117*, 22094.

[6.10] Crasto, D.; Malola, S.; Brosofsky, G.; Dass, A.; Häkkinen, H. *J. Am. Chem. Soc.* **2014**, *136*, 5000.

[6.11] Yang, H.; Wang, Y.; Edwards, A. J.; Yan, J.; Zheng, N. *Chem. Commun.* **2014**, *50*, 14325.

[6.12] Hesari, M.; Workentin, M. S. *J. Mater. Chem. C.* **2014**, *2*, 3631.

[6.13] Nimmala, P. R.; Theivendran, S.; Barcaro, G.; Sementa, L.; Kumara, C.; Jupally, V. R.; Apra, E.; Stener, M.; Fortunelli, A.; Dass, A. *J. Phys. Chem. Lett.* **2015**, *6*, 2134.

[6.14] Nimmala, P. R.; Dass, A. *J. Am. Chem. Soc.* **2014**, *136*, 17016.

[6.15] Nimmala, P. R.; Dass, A. *J. Am. Chem. Soc.* **2011**, *133*, 9175.

[6.16] Zeng, C.; Li, T.; Das, A.; Rosi, N. L.; Jin, R. *J. Am. Chem. Soc.* **2013**, *135*, 10011.

[6.17] van der Sluis, P.; Spek, A. L. *Acta. Cryst.* **1990**, *A46*, 194.

[6.18] Spek, A. L. *Acta. Cryst.* **2003**, *36*, 7.

[6.19] Perdew, J. P.; Burke, K.; Ernzerhof, M. *Phys. Rev. Lett.* **1996**, *77*, 3865.

[6.20] Becke, A. D. *J. Chem. Phys.* **1993**, *98*, 5648.

[6.21] Stephens, P. J.; Devlin, F. J.; Chabalowski, C. F.; Frisch, M. J. *J. Phys. Chem.* **1994**, *98*, 11623.

[6.22] Gritsenko, O. V.; Schipper, P. R. T.; Baerends, E. J. *Chem. Phys. Lett.* **1999**, *302*, 199.

[6.23] Giannozzi, P.; et.al. *J. Phys.: Condens. Matter* **2009**, *21*, 395502.

[6.24] Vanderbilt, D. *Phys. Rev. B.* **1990**, *41*, 7892.

[6.25] Lippert, G.; Hutter, J.; Parrinello, M. *Theor. Chem. Acc.* **1999**, *103*, 124.

[6.26] VandeVondele, J.; Hutter, J. *J. Chem. Phys.* **2007**, *127*, 114105.

[6.27] Hartwigsen, C.; Goedecker, S.; Hutter, J. *Phys. Rev. B.* **1998**, *58*, 3641.

[6.28] Guidon, M.; Hutter, J.; VandeVondele, J. *Journal of Chemical Theory and Computation* **2010**, *6*, 2348.

[6.29] van Lenthe, E.; Baerends, E. J.; Snijders, J. G. *J. Chem. Phys.* **1993**, *99*, 4597.

[6.30] Baerends, E. J.; Ellis, D. E.; Ros, P. *Chem. Phys.* **1973**, *2*, 41.

[6.31] Fonseca Guerra, C.; Snijders, J. G.; te Velde, G.; Baerends, E. J. *Theor. Chem. Acc.* **1998**, *99*, 391.

[6.32] Casida, M. E. In *Recent Advances in Density-Functional Methods*; Chong, D. P., Ed.; World Scientific: Singapore, 1995, p 155. A

Chapter 7

[7.1] Casida, M. E. Recent Advances in Density-Functional Methods, D. P. Chong, ed. (World Scientific, Singapore, 1995) p. 155.

[7.2] E. J. Baerends, D. E. Ellis and P. Ros, Chem. Phys. **2**, 41 (1973).

[7.3] C. Fonseca Guerra, J. G. Snijders, G. te Velde, and E. J. Baerends, Theor. Chem. Acc. **99**, 391 (1998).

[7.4] S. J. A. van Gisbergen, J. G. Snijders and E. J. Baerends, Computer Phys. Comm. **118**, 119 (1999).

[7.5] K. Yabana and G. F. Bertsch, Phys. Rev. B **54**, 4484 (1996).

[7.6] B. Walker, A. M. Saitta, R. Gebauer and S. Baroni, Phys. Rev. Lett. 96 113001 (2006).

[7.7] Oscar Baseggio, Giovanna Fronzoni and Mauro Stener "A New Time Dependent Density Functional Algorithm for Large Systems and Plasmons in Metal Clusters", J. Chem. Phys., 143 (2015) 024106.

[7.8] Lippert, G.; Hutter, J.; Parrinello, M. *Theor. Chem. Acc*. **1999**, *103*, 124-140.

[7.9] Giannozzi, P. et al. *J. Phys.: Condens. Matter* **2009**, *21*, 395502

[7.10] L. Jensen, J. Autschbach, and G. C. Schatz, J. Chem. Phys., 122 (2005) 224115.

[7.11] Gross, E. K. U.; Kohn, W. Time-Dependent Density-Functional Theory. Adv. Quantum. Chem. **21**, 255 (1990).

[7.12] Malcioglu, O.; Gebauer, R.; Rocca, D.; Baroni, S., *Compt. Phys. Commun.*, **2011**, *182* 1744–1754

[7.13] R. Van Leeuwen and E. J. Baerends, Phys. Rev. A **49**, 2421 (1994).

[7.14] J. P. Perdew, K. Burke and M. Ernzerhof, Generalized Gradient Approximation Made Simple, Physical Review Letters 77, 3865 (1996)

[7.15] S. H. Vosko, L. Wilk, M. Nusair, Can. J. Phys. **58**, 1200 (1980).

[7.16] van Lenthe, E.; Baerends, E. J.; Snijders, J. G. Relativistic regular two-component Hamiltonians. *J. Chem. Phys.* **1993**, *99*, 4597-4610

[7.17] VandeVondele, J.; Hutter, J. *J. Chem. Phys*. **2007**, *127* , 114105.

[7.18] Hartwigsen, C.; Goedecker, S.; Hutter, J. *Phys. Rev. B*. **1998**, *58*, 3641-3662.

[7.19] Vanderbilt, D. *Phys. Rev. B* **1990**, *41*, R7892–R7895

[7.20] Martyna, J. G.; Tuckerman, M.E.; *J. Chem. Phys.* **1999**, *110*, 2810

[7.21] G. M. Piccini, R. W. A. Havenith, R. Broer and M. Stener, J. Phys. Chem. C **117**, 17196 (2013).

[7.22] Johnson, Hannah E.; Aikens, Christine A. JOURNAL OF PHYSICAL CHEMISTRY A Volume: 113 Issue: 16 Pages: 4445-4450 (2009)

[7.23] Aikens, Christine M.; Li, Shuzhou; Schatz, George C. JOURNAL OF PHYSICAL CHEMISTRY C Volume: 112 Issue: 30 Pages: 11272-11279 (2008)

[7.24] Guidez, Emilie B.; Aikens, Christine M. NANOSCALE Volume: 4 (2012) Issue: 14 Pages: 4190-4198

[7.25] Guidez, Emilie B.; Aikens, Christine M. JOURNAL OF PHYSICAL CHEMISTRY C Volume: 117 Issue: 23 Pages: 12325-12336 (2013)

[7.26] Rabilloud, Franck JOURNAL OF CHEMICAL PHYSICS Volume: 141 Issue: 14 Article Number: 144302 Published: OCT 14 2014

[7.27] Harb, M.; Rabilloud, F.; Simon, D.; et al. JOURNAL OF CHEMICAL PHYSICS Volume: 129 Issue: 19 Article Number: 194108 Published: NOV 21 2008

[7.28] Weissker, H-Ch; Mottet, C. PHYSICAL REVIEW B Volume: 84 Issue: 16 Article Number: 165443 Published: OCT 24 2011

[7.29] Lopez-Lozano, Xochitl; Barron, Hector; Mottet, Christine; et al. PHYSICAL CHEMISTRY CHEMICAL PHYSICS Volume: 16 Issue: 5 Pages: 1820-1823 Published: 2014

[7.30] Weissker, Hans-Christian; Lopez-Lozano, Xochitl PHYSICAL CHEMISTRY CHEMICAL PHYSICS Volume: 17 Issue: 42 Pages: 28379-28386 Published: 2015

[7.31] Gyun-Tack Bae and Christine M. Aikens, J. Phys. Chem. C 116 (2012) 10356

[7.32] M. Kuisma, A. Sakko, T. P. Rossi, A. H. Larsen, J. Enkovaara, L. Lehtovaara and T. T. Rantala, Phys. Rev. B 91 (2015) 115431.

[7.33] Gyun-Tack Bae and Christine M. Aikens, J. Phys. Chem. C 119 (2015) 23127-23137.

[7.34] K. Iida, M. Noda, K Ishimura and K. Nobusada, J. Phys. Chem. A **118**, 11317 (2014).

[7.35] Sami Malola, Lauri Lehtovaara, Jussi Enkovaara and Hannu Häkkinen, ACS Nano 7 10263 (2013).

[7.36] Nicola Durante, Alessandro Fortunelli, Michel Broyer, and Mauro Stener, J. Phys. Chem. C 2011, 115, 6277–6282

[7.37] Liebsch, A. *Phys. Rev. B* **1993**, *48*, 11317-11328.

[7.38] M. Kuisma, J. Ojanen and T. T. Rantala, Phys. Rev. B 82 (2010) 115106

[7.39] O. Gritsenko, R. van Leeuwen, E. van Lenthe and E. J. Baerends, Phys. Rev. A 51 (1995) 1944.

[7.40] S. Bernadotte, F. Evers, C. R. Jacob, J. Phys. Chem. C **117**, 1863 (2013).

[7.41] Barcaro, G.; Sementa, L.; Fortunelli, A.; Stener, M. *J. Phys. Chem. C* **2014**, *118*, 12450 - 12458.

Chapter 8

[8.1] H.-Ch. Weissker, H. B. Escobar, V. D. Thanthirige, K. Kwak, D. Lee, G. Ramakrishna, R. L. Whetten, X. Lopez-Lozano; Nature Comm.; 2014, 5, 4785.

[8.2] A. Dass, S. Theivendran, P. Nimmala, C. Kumara, V. Jupally, A. Fortunelli, L. Sementa, G. Barcaro, X. Zuo, B. C. Noll, J. Am. Chem. Soc.; 2015, 137, 4610-4613.

[8.3] O. Baseggio, G. Fronzoni and M. Stener, J. Chem. Phys., 143 (2015) 024106.

[8.4] G. Barcaro, L. Sementa, A. Fortunelli, M. Stener; Nanoscale, 17 (2014), 8166-7

[8.5] R. Van Leeuwen and E. J. Baerends, Phys. Rev. A **49**, 2421 (1994).

[8.6] J. P. Perdew, K. Burke and M. Ernzerhof, Generalized Gradient Approximation Made Simple, Physical Review Letters 77, 3865 (1996)

[8.7] Gross, E. K. U.; Kohn, W. Time-Dependent Density-Functional Theory. Adv. Quantum. Chem. **21**, 255 (1990).

[8.8] S. H. Vosko, L. Wilk, M. Nusair, Can. J. Phys. **58**, 1200 (1980).

[8.9] E. van Lenthe, E. J. Baerends, J. G. Snijders, *J. Chem. Phys.* **1993**, *99*, 4597-4610

Chapter 9

[9.1] A. Rodger and B. Nordén, “Circular Dichroism & Linear Dichroism”, Oxford Univerisity Press, Oxford, 1997.

[9.2] O. Baseggio, G. Fronzoni and M. Stener, J. Chem. Phys. 143 (2015) 024106.

[9.3] J. Autschbach and T. Ziegler, J. Chem. Phys. 116 (2002) 891.

[9.4] A. D. Buckingham, Adv. Chem. Phys. 12 (1967) 107.

[9.5] R. McWeeny, Methods of Molecular Quantum Mechanics, Academic Press, 1989.

[9.6] N. V. Karimova and C. M. Aikens, J. Phys. Chem. A 119 (2015) 8163-8173.

Publications

G. Fronzoni, O. Baseggio, M. Stener, W. Hua, G. Tian, Y. Luo, B. Apicella, M. Alfé, M. de Simone, A. Kivimäki, and M. Coreno, Vibrationally resolved high-resolution NEXAFS and XPS spectra of phenanthrene and coronene, The Journal of Chemical Physics 141, 044313 (2014);

O. Baseggio, G. Fronzoni, M. Stener, A new time dependent density functional algorithm for large systems and plasmons in metal clusters, The Journal of Chemical Physics 143, 024106 (2015);

Amala Dass, Tanya Jones, Milan Rambukwella, David Crasto, Kevin J. Gagnon, Luca Sementa, Martina De Vetta, Oscar Baseggio, Edoardo Aprà, Mauro Stener, Alessandro Fortunelli, Crystal Structure and Theoretical Analysis of Green Gold $Au_{30}(S\text{-}tBu)_{18}$ *Nanomolecules and its Relation to* $Au_{30}S(S\text{-}tBu)_{18}$*, The Journal of Physical Chemistry C, DOI: 10.1021/acs.jpcc.6b00062*

Oscar Baseggio, Martina De Vetta, Giovanna Fronzoni, Mauro Stener, Luca Sementa, Alessandro Fortunelli, Arrigo Calzolari, Photoabsorption of icosahedral noble metal clusters: an efficient TDDFT approach to large scale systems, Journal of Chemical Theory and Computation, submitted

Oscar Baseggio, Martina De Vetta, Giovanna Fronzoni, Mauro Stener, Alessandro Fortunelli, A new Time Dependent Density Functional Method for molecular plasmonics: formalism, implementation and the $Au_{144}(SH)_{60}$ *case study, International Journal of Quantum Chemistry, submitted*

Ringraziamenti:

Il mio primo ringraziamento non può non andare al professor Mauro Stener per tutto quello che ha fatto per me in questi anni; per la sua competenza, la sua disponibilità e la sua fiducia nei miei confronti; grazie per la splendida opportunità che mi ha concesso.

Vorrei ringraziare tutto il gruppo di chimica teorica e computazionale e in particolare la professoressa Giovanna Fronzoni per l'accoglienza e la gentilezza che avete sempre avuto nei miei confronti. Mi sento veramente onorato e fortunato ad aver lavorato in un gruppo così valido sia dal punto di vista lavorativo che da quello umano.

Un sentito grazie va a tutte le persone passate per l'ufficio 465, anche se per brevi periodi rimarrete sempre nei ricordi che mi legano a questo posto, ringrazio il dott. Nicola Quadri che ormai condivide con me l'ufficio da un anno, grazie per rendere meno drammatico il lunedì mattina, guardare insieme le sintesi di Daniel Rizzo ormai è diventato un appuntamento imperdibile.

Un ringraziamento a tutti i membri del gruppo pranzo c11 anche se molti ormai sono lontani da Trieste, perché mangiare in compagnia è sempre bellissimo se poi lo fai con persone meravigliose, diventa uno dei momenti più belli della giornata.

Un grazie a tutti gli amici pendolari, fare due viaggi in treno al giorno è uno dei mali della nostra epoca, avere delle persone che soffrono insieme a te rende tutto meno faticoso e stressante, un grazie particolare va ai Pendolacidi perché se la malasorte ti rende amico allora sarà sicuramente un'amicizia indistruttibile. Inoltre vorrei modificare un famoso detto in: "La pazienza è la virtù dei pendolari".

Un ringraziamento va a tutti gli amici di vecchia e nuova data, grazie per rendere la mia vita migliore, grazie per i momenti passati insieme e per quelli che ancora devono venire. Sono veramente fortunato ad avere accanto a me delle bellissime persone come voi.

Due persone molto speciali mi hanno veramente aiutato in questo percorso, abbiamo iniziato come colleghi e siamo diventati Amici. Renato e Aurora il tempo passato con voi è sempre una meraviglia (anche meglio senza Aurora, grazie Zagabria). Come non ricordare le avventure di Aurora contro le creature mitologiche che infestano le sue case, i drammi di Renato per il Fantacalcio, le testate degli anziani, i detti triestini alla romana, le anZie, il Puzlaiz, le partite di tennis e gli spettacoli teatrali; per questi ed altri miliardi di motivi …. Ve la sto facendo sudare quella parolina … Grazie.

Un grazie alla mia Famiglia per essermi stata sempre vicino, avermi supportato ed avermi aiutato in qualsiasi momento, senza farmi mai mancare niente.

Questa tesi è dedicata alla persona che più di tutte mi conosce e mi ha aiutato, mia moglie Sara, senza di te tutto questo non sarebbe stato possibile. Molte persone m’invidiano che non sono mai ansioso o teso, ma non sanno che in verità il mio segreto sei tu che riesci sempre a tranquillizzarmi e a ridimensionare i problemi che sembrano insormontabili. Grazie mille.